

Low-Dimensional Carbon Nanomaterials 2012

Guest Editors: Teng Li, Sulin Zhang, Vivek Shenoy, and Jianyu Huang





Low-Dimensional Carbon Nanomaterials 2012

Journal of Nanomaterials

Low-Dimensional Carbon Nanomaterials 2012

Guest Editors: Teng Li, Sulin Zhang, Vivek Shenoy,
and Jianyu Huang



Copyright © 2012 Hindawi Publishing Corporation. All rights reserved.

This is a special issue published in "Journal of Nanomaterials." All articles are open access articles distributed under the Creative Commons Attribution License, which permits unrestricted use, distribution, and reproduction in any medium, provided the original work is properly cited.

Editorial Board

Katerina E. Aifantis, Greece
Nageh K. Allam, USA
Margarida Amaral, Portugal
Xuedong Bai, China
Lavinia Balan, France
Enrico Bergamaschi, Italy
Theodorian Borca-Tasciuc, USA
C. Jeffrey Brinker, USA
Christian Brosseau, France
Xuebo Cao, China
Shafiul Chowdhury, USA
Kwang-Leong Choy, UK
Cui ChunXiang, China
Miguel A. Correa-Duarte, Spain
Shadi A. Dayeh, USA
Claude Estourns, France
Alan Fuchs, USA
Lian Gao, China
Russell E. Gorga, USA
Hongchen Chen Gu, China
Mustafa O. Guler, Turkey
John Zhanhu Guo, USA
Smrati Gupta, Germany
Michael Harris, USA
Zhongkui Hong, China
Michael Z. Hu, USA
David Hui, USA
Y.-K. Jeong, Republic of Korea
Sheng-Rui Jian, Taiwan
Wanqin Jin, China
Rakesh K. Joshi, UK
Zhenhui Kang, China
Fathallah Karimzadeh, Iran
Alireza Khataee, Iran

Do Kyung Kim, Korea
Alan K. T. Lau, Hong Kong
Burtrand Lee, USA
Jun Li, Singapore
Benxia Li, China
Xing-Jie Liang, China
Shijun Liao, China
Gong Ru Lin, Taiwan
J. -Y. Liu, USA
Tianxi Liu, China
Jue Lu, USA
Songwei Lu, USA
Daniel Lu, China
Ed Ma, USA
Gaurav Mago, USA
Santanu K. Maiti, India
Sanjay R. Mathur, Germany
Vikas Mittal, UAE
Weihai Ni, Germany
Sherine Obare, USA
Atsuto Okamoto, Japan
Abdelwahab Omri, Canada
Edward Andrew Payzant, USA
Kui-Qing Peng, China
Anukorn Phuruangrat, Thailand
Suprakas Sinha Ray, South Africa
Ugur Serincan, Turkey
Huaiyu Shao, Japan
Donglu Shi, USA
Vladimir Sivakov, Germany
Marinella Striccoli, Italy
Bohua Sun, South Africa
Saikat Talapatra, USA
Nairong Tao, China

Titipun Thongtem, Thailand
Somchai Thongtem, Thailand
Alexander Tolmachev, Ukraine
Valeri P. Tolstoy, Russia
Tsung-Yen Tsai, Taiwan
Takuya Tsuzuki, Australia
Raquel Verdejo, Spain
Mat U. Wahit, Malaysia
Zhenbo Wang, China
Ruibing Wang, Canada
Shiren Wang, USA
Cheng Wang, China
Yong Wang, USA
Jinquan Wei, China
Ching-Ping Wong, Hong Kong
Xingcai Wu, China
Guodong Xia, Hong Kong
Zhi Li Xiao, USA
Ping Xiao, UK
Yangchuan Xing, USA
Shuangxi Xing, China
N. Xu, China
Doron Yadlovker, Israel
Yingkui Yang, China
Khaled Youssef, USA
Kui Yu, Canada
William W. Yu, USA
Haibo Zeng, China
Tianyou Zhai, Japan
Renyun Zhang, Sweden
Yanbao Zhao, China
Lianxi Zheng, Singapore
Chunyi Zhi, Hong Kong

Contents

Growth Mechanism of a Hybrid Structure Consisting of a Graphite Layer on Top of Vertical Carbon Nanotubes, Nicolo' Chiodarelli, Cigang Xu, Olivier Richard, Hugo Bender, Alexander Klekachev, Mike Cooke, Marc Heyns, Stefan De Gendt, Guido Groeseneken, and Philippe M. Vereecken
Volume 2012, Article ID 130725, 10 pages

Measuring of Electrical Properties of MWNT-Reinforced PAN Nanocomposites, Sliman Almuhammed, Nabyl Khenoussi, Laurence Schacher, Dominique Adolphe, and Henri Balard
Volume 2012, Article ID 750698, 7 pages

The Synthesis of Peculiar Structure of Springlike Multiwall Carbon Nanofibers/Nanotubes via Mechanochemical Method, Sahebali Manafi, Mohammad Reza Rahimipour, Iman Mobasherpour, and Atefeh Soltanmoradi
Volume 2012, Article ID 803546, 8 pages

Study on Carbon Nanocomposite Counterelectrode for Dye-Sensitized Solar Cells, Yiming Chen, Haiyan Zhang, Yuting Chen, and Jiapeng Lin
Volume 2012, Article ID 601736, 6 pages

Electric Double-Layer Capacitor Fabricated with Addition of Carbon Nanotube to Polarizable Electrode, Yoshiyuki Show
Volume 2012, Article ID 929343, 8 pages

Estimating the Thermal Conductivities and Elastic Stiffness of Carbon Nanotubes as a Function of Tube Geometry, Z. H. Zhang, N. Yu, and W. H. Chao
Volume 2012, Article ID 939806, 8 pages

Large-Scale Integrated Carbon Nanotube Gas Sensors, Joondong Kim
Volume 2012, Article ID 741647, 13 pages

Properties of Reaction Intermediates from Unzipping Nanotubes via the Diketone Formation: A Computational Study, Takashi Yumura and Toshiyuki Kanemitsu
Volume 2012, Article ID 612672, 10 pages

Nanopore-Based DNA Analysis via Graphene Electrodes, Qing Zhao, Yang Wang, Jianjin Dong, Lina Zhao, X. F. Rui, and Dapeng Yu
Volume 2012, Article ID 318950, 5 pages

Dry-Transfer of Aligned Multiwalled Carbon Nanotubes for Flexible Transparent Thin Films, Matthew Cole, Pritesh Hiralal, Kai Ying, Chi Li, Yan Zhang, Kenneth Teo, Andrea Ferrari, and William Milne
Volume 2012, Article ID 272960, 8 pages

Improving the RF Performance of Carbon Nanotube Field Effect Transistor, S. Hamieh
Volume 2012, Article ID 724121, 7 pages

An Investigation on the Formation of Carbon Nanotubes by Two-Stage Chemical Vapor Deposition, M. S. Shamsudin, M. F. Achoi, M. N. Asiah, L. N. Ismail, A. B. Suriani, S. Abdullah, S. Y. S. Yahya, and M. Rusop
Volume 2012, Article ID 972126, 5 pages



The Effects of Radial Compression on Thermal Conductivity of Carbon and Boron Nitride Nanotubes,

Haijun Shen

Volume 2012, Article ID 756791, 4 pages

Critical Dispersion Distance of Silicon Nanoparticles Intercalated between Graphene Layers, Shuze Zhu,

Jason Galginaitis, and Teng Li

Volume 2012, Article ID 375289, 4 pages

Effects of Surface Modification of MWCNT on the Mechanical and Electrical Properties of Fluoro Elastomer/MWCNT Nanocomposites, Tao Xu and Jinghui Yang

Volume 2012, Article ID 275637, 9 pages

Fabrication of Microscale Carbon Nanotube Fibers, Gengzhi Sun, Yani Zhang, and Lianxi Zheng

Volume 2012, Article ID 506209, 10 pages

Research Article

Growth Mechanism of a Hybrid Structure Consisting of a Graphite Layer on Top of Vertical Carbon Nanotubes

Nicolo' Chiodarelli,^{1,2} Cigang Xu,³ Olivier Richard,¹ Hugo Bender,¹
Alexander Klekachev,^{1,4} Mike Cooke,³ Marc Heyns,^{1,5} Stefan De Gendt,^{1,6}
Guido Groeseneken,^{1,2} and Philippe M. Vereecken^{1,7}

¹ imec, Kapeldreef 75, 3001 Leuven, Belgium

² Department of Electrical Engineering, K.U. Leuven, Kasteelpark Arenberg 1, 3001 Leuven, Belgium

³ Oxford Instruments Plasma Technology, North End, Yatton, Bristol BS49 4AP, UK

⁴ Department of Physics and Astronomy, K.U. Leuven, Celestijnenlaan 200D, 3001 Leuven, Belgium

⁵ Metallurgy and Materials Engineering Department, K.U. Leuven, Kasteelpark Arenberg 44, 3001 Leuven, Belgium

⁶ Chemistry Department, K.U. Leuven, Celestijnenlaan 200f, Bus 2404, 3001 Leuven, Belgium

⁷ Centre for Surface Chemistry and Catalysis (COK), K.U. Leuven, Kasteelpark Arenberg 23, 3001 Leuven, Belgium

Correspondence should be addressed to Philippe M. Vereecken, vereeck@imec.be

Received 14 October 2011; Accepted 3 June 2012

Academic Editor: Jianyu Huang

Copyright © 2012 Nicolo' Chiodarelli et al. This is an open access article distributed under the Creative Commons Attribution License, which permits unrestricted use, distribution, and reproduction in any medium, provided the original work is properly cited.

Graphene and carbon nanotubes (CNTs) are both carbon-based materials with remarkable optical and electronic properties which, among others, may find applications as transparent electrodes or as interconnects in microchips, respectively. This work reports on the formation of a hybrid structure composed of a graphitic carbon layer on top of vertical CNT in a single deposition process. The mechanism of deposition is explained according to the thickness of catalyst used and the atypical growth conditions. Key factors dictating the hybrid growth are the film thickness and the time dynamic through which the catalyst film dewets and transforms into nanoparticles. The results support the similarities between chemical vapor deposition processes for graphene, graphite, and CNT.

1. Introduction

Graphene and carbon nanotubes (CNTs) are carbon allotropes with similar and exceptional optical and electronic properties [1] which can find applications as electronic or optoelectronic devices such as interconnects [2, 3], transparent electrodes [4], photodiodes [5], photodetectors [6], or solar cells [7]. The similarity in their properties derives from the identical atomic structure consisting of sp²-hybridized carbon atoms arranged in a hexagonal lattice and from the fact that the band structure of CNT is derived from that of graphene simply by confining the electronic wave functions to a smaller portion of a graphene plane [8].

Moreover, their manufacturing process is similar since CNT [9–12] and graphene [13–15] can be deposited via catalytic chemical vapor deposition (CVD) by exploiting

the catalyzed decomposition reaction between a carbon precursor (acetylene for example) and a catalyst of the iron group (Ni, Co, or Fe). More specifically, the catalyst provides active sites for adsorption and decomposition of the precursor molecule and a template to organize the adsorbed and/or dissolved carbon into graphitized structures. The main difference between the two processes lies in the shape of the template; that is, a nanoparticle in the case of one-dimensional CNT or carbon nanofiber and a film (infinite large particle) in the case of two-dimensional graphene.

In this work, the link between graphene and CNT is further investigated by studying and explaining the formation mechanism of a hybrid structure consisting of graphitic layers on top of CNT. This peculiar structure is receiving increasing interest in the scientific community [3, 16–18] since it basically shows that an horizontal top electrode of

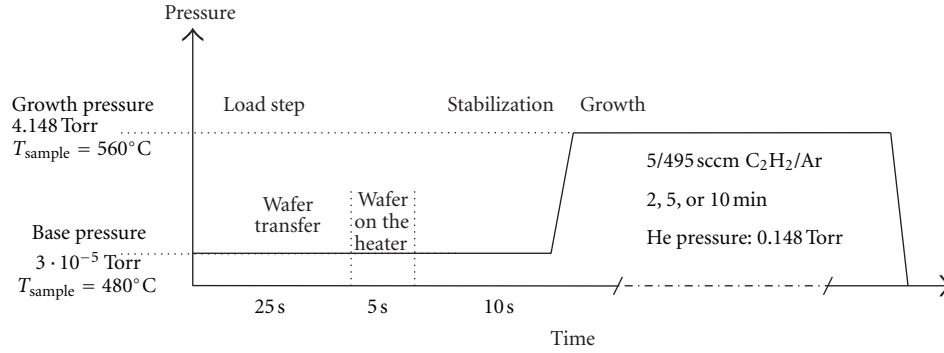


FIGURE 1: Scheme of growth recipes and tool operations. During the first load step of 30 s, samples are transferred into the chamber at base pressure. A 10 s stabilization step is used for stabilizing sample temperature. The last growth step occurs in C_2H_2/Ar mixture (5/495 sccm) at a total pressure of 4.148 Torr and for 2, 5, or 10 minutes. Helium partial pressure is 0.148 Torr.

graphite can be deposited over vertical CNT in a single process step at low temperature whereas most of the times the two materials are deposited with independent stand-alone processes at high temperature. For instance, a horizontal top electrode in graphite could serve for interconnections [3] as a protective carbon cap for the CNT underneath or as self-formed large area electrode to contact the carbon nanotubes [18]. Clearly, the coexistence of both graphite and CNT in a unique process window would offer advantages in terms of manufacturability using a relatively inexpensive single-step process.

In this work, the key factors dictating the process window for growing the hybrid structure are identified in the film thickness, studied here in a relatively narrow range, and the time dynamic through which the catalyst film dewets and transforms into nanoparticles (also dependent, among other factors, on the film thickness). A based growth mechanism is identified for the growth of the hybrid structure on TiN as observed in [17] but not in [3]. Its formation appears catalyst independent since the hybrid structure has been observed for Co and Ni on TiN (this work and [3, 17]), Ni on Ti [16], or for Fe on SiO_2 [18]. Finally, based on the observations of catalyst debris near the base or inside the CNT, we agree with the qualitative idea that the CNTs underneath the structure form as a result of a catalyst in a viscous liquid-like state of high mobility over the underlying metallic substrate [17].

2. Experimental

Nickel and cobalt films of different thicknesses were deposited on a blanket 70 nm TiN/100 nm SiO_2/p -Si stack by physical vapor deposition (PVD). The amount of material deposited by PVD was first calibrated on SiO_2 test wafers and measured using Rutherford backscattering (RBS). The depth of the test films measured by RBS was $1.24 \cdot 10^{16}$ atoms·cm $^{-2}$, $2 \cdot 10^{16}$ atoms·cm $^{-2}$ for nickel and $1.02 \cdot 10^{16}$ atoms·cm $^{-2}$, $1.75 \cdot 10^{16}$ atoms·cm $^{-2}$ for cobalt, respectively. These data correspond to an equivalent thickness of about 1.3 nm and 2.2 nm for nickel and 1.1 nm and 1.9 nm for cobalt, respectively. Moreover, a film with an equivalent thickness of 5 nm was also included in the set of experiments.

In a typical growth experiment, a sample of each was loaded together. Pieces of 2 by 2 cm were placed next to each

other in the center of a carrier wafer and processed in a plasma-lab CVD tool from Oxford Instrument consisting of a main deposition chamber with a heating stage of graphite connected to a load lock stage by a robot. Gasses are top injected into the main chamber via showerhead gas inlets in the top electrode.

As the exact sequence of tool operations during the growth experiments is important for the interpretation of the results, the growth recipe and the tool operations will be described in detail and are schematically represented in Figure 1 for clarity. All recipes begin with a load step where the samples are automatically transferred from the load lock into the main chamber in about 30 s. As soon as the carrier wafer is in contact with the heater in the last 5 s of the load step, the sample temperature rapidly increases to approximately $T_{BP} = 480^\circ C$, which is the sample temperature at the chamber base pressure of $3 \cdot 10^{-5}$ Torr.

For temperature stabilization, the samples were left for 10 s (stabilization step) in the chamber at base pressure. Then, the growth step begins and a 5/495 sccm C_2H_2/Ar mixture was introduced into the chamber up to the process pressure of 4.148 Torr. Helium was also present in the chamber at this stage at a partial pressure of 0.148 Torr. As a result of the pressure increase, the sample temperature rapidly increases to about $T_{growth} = 560^\circ C$. Note that, except for the loading and stabilization steps, no extra heat treatment or catalyst activation step was done.

For all experiments, the growth step consisted only of the operations described above, except for the fact that the growth time was varied for 2, 5, and 10 minutes. After growth, the samples were characterized by SEM and TEM. For TEM analysis samples were sonicated in isopropanol for 10 minutes and few droplets of the solution were deposited on a carbon lacey copper grid and dried. The analysis was done with a HRTEM Tecnai F30 operating at 200 kV to limit damage to the CNT during beam exposure.

3. Results

Figure 2 shows the growth results for cobalt and nickel films with increasing film thickness after 5 minutes of growth time. Dense CNT mats were obtained for layers below 1.3 nm,

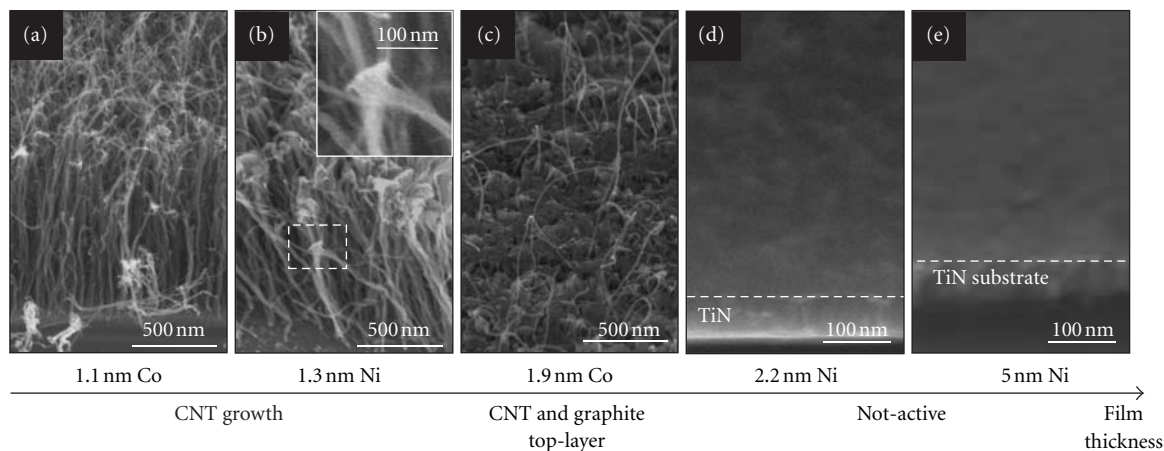


FIGURE 2: SEM pictures of different carbon nanostructures grown from thin nickel and cobalt films with different initial catalyst thickness in mixture of 5/495 sccm C_2H_2/Ar for 5 min at 4.148 Torr. (a) CNT from 1.1 nm Co, (b) CNT from 1.3 nm Ni. The inset shows a CNT with a particularly tapered tip; (c) CNT with a top porous carbon layer grown from 1.9 nm Co; (d) and (e) no growth of carbon structures from 2.2 nm and 5 nm Ni.

while no CNTs were observed for films equal to and thicker than 2.2 nm, under the presented growth conditions. For the intermediate film thickness of 1.9 nm, CNT growth was also observed but an atypical layer can be distinguished on top of the CNT (Figure 2(c)). This top layer appears to be porous and some elongated CNTs extend through the pores. For a film thickness of 1.3 nm, a peculiar tapered shape was found near the top of the CNT mat, showing a broadening towards a platform shape on top of the CNT (inset in Figure 2(b)).

To study the type of structures in more detail, TEM analysis was done on the 1.1-Co, 1.3-Ni, and 1.9-Co samples. In all cases (Figures 3 and 4), the structures consist of multiwalls CNT with diameters 10.8 ± 3.4 nm for 1.1-Co, 13.1 ± 5.1 nm for 1.3-Ni, and 12.7 ± 5.0 nm for the 1.9-Co samples as measured by SEM.

For the thinnest 1.1 nm film, cobalt nanoparticles are located mostly at the extremities of the tubes (Figure 3(a)) whereas only a few were found in the interior of the tube. Similarly, the 1.3-Ni sample had particles at the tube extremities but the amount of particles found inside the tube interior was larger in this case. Figure 3(d) shows a detail of the tapered platform-like shape which was observed with SEM at the tip of some CNT (inset of Figure 2(b)). As for the 1.9-Co sample, a crust has formed on top of the CNT but isolated to a single or a few interconnected CNT in contrast to the closed (porous) layer formed on the 1.9-Co sample in Figure 2(c).

In the 1.9-Co sample, the crusty top layer indeed connects the tips of all neighboring CNTs as confirmed by the TEM image in Figure 4(a). Underneath the crust, straight multiwall CNTs are present as shown at high magnification in Figures 4(b) and 4(c). Note that under different growth conditions, carbon nanofibers were found underneath similarly crusted top layers [19]. The fact that the CNTs are still connected to the top layer allows us to unambiguously locate the root of the tubes. From TEM, it follows that a cobalt nanoparticle sits at the base or root of

the CNT. Arrows in Figure 4(a) indicate the particles in the tubes and a high-resolution image of a cobalt nanoparticle at the root of one CNT are shown in Figure 4(e).

For the 1.9-Co sample, nanoparticles are also in the core of some tubes (Figure 4(d)). In particular, comparing the inner particles among the samples, their number and size seem to increase according to the initial catalyst thickness: few and smaller nanoparticles for the 1.1-Co sample meanwhile numerous and larger nanoparticles in the 1.3-Ni and 1.9-Co samples. Note that the interior “particles” can be quite elongated to rod-like structures (see Figures 3(e) and 4(d)) and in some cases even long nanowires suggesting the formation of metal filaments during growth.

Figure 5 shows high-resolution TEM images of the top-layer for 1.9-Co samples. Multiple layers of graphene form the graphitic top layer or crust (Figures 5(a) and 5(b)). Even though the TEM shows only clearly the graphene sheets at the very surface, they appear to extend much further but their visualization is difficult because of overlapping. The global structure looks entangled without long range order (polycrystalline). Small and elongated nanoparticles are found right below the graphitic top-layer; that is, in the tapered transition region between the planar graphite layer and the vertical CNT. The tapered shape is then formed by graphitic encapsulation of these catalyst particles, some of which are trapped into this transition layer, others already in the CNT below.

Figure 6 shows the Raman spectra of the samples analyzed so far (from Figure 2 to Figure 5). The spectra are reproducible and representative since they appear identical for different spots over the same sample.

The samples with CNT only (1.1-Co) and with CNT and a graphitic layer on top (1.9-Co) exhibit identical Raman spectra. This is probably due not only to the fact that the spectra of graphite and MWCNT of large diameter have strong similarities but also depends on the penetration depth of the laser in our setup using a wavelength of 632 nm and a

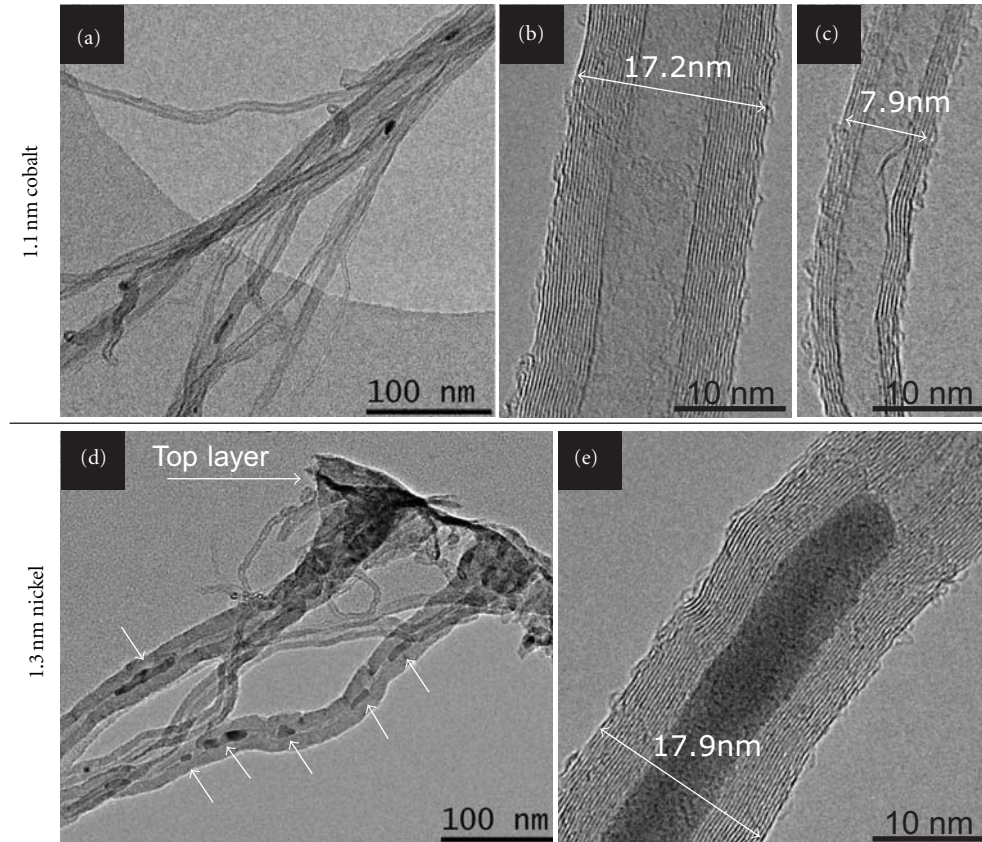


FIGURE 3: TEM of the carbon structures from 1.1 nm cobalt (top row, images (a), (b), (c)) and 1.3 nm nickel (bottom row, images (d) and (e)); (a) CNT at low magnification; (b) large CNT with 16 walls (b) small CNT with 6 walls; (d) carbon top layer at the CNT's tip; numerous particles inside the CNT highlighted by arrows; (e) CNT with a particularly large particle inside.

1 μm laser spot. For instance, a peak for silicon at 500 cm^{-1} is present in the spectra of the samples without CNT (2.2 nm and 5 nm) suggesting that the probed thickness is likely in the order of a hundred of nanometers as SiO_2 is separated from the samples surface by a 70 nm thick layer of TiN. The top graphite layer, instead, is expected only few nanometers thick (from TEM) so large part of the Raman signal originates from the MWCNT underneath.

In all the samples, the typical features of graphitic materials are present in the first-order Raman spectra: that is, D and G bands at $\approx 1350\text{ cm}^{-1}$ and $\approx 1580\text{ cm}^{-1}$, respectively. Considering the pronounced shoulder in the D peak at about 1100 cm^{-1} and the fact that the D and G bands merge in the region between 1350 cm^{-1} , and $\approx 1580\text{ cm}^{-1}$ it is concluded that the samples contain some degree of disorder. In fact, the TEM images of the graphite top layer (Figure 5) revealed a polycrystalline structure made of small domains of undulated fringes continuous over a length of few nanometers only. The edges of each domain can be considered as defects which contribute to the broadening of the D and G peaks as discussed in [20]. For graphitic materials with defects, a D' peak is also expected at 1620 cm^{-1} but it is not distinguishable here probably because buried in the G band as also expected for nanocrystalline graphite when small grains are present [21].

Similar arguments can also be applied to the samples with MWCNT even if broad G and D peaks are more typical because of the parallel contribution of several walls with different diameters. In particular, some degree of disorder in the structure of the tubes can be inferred from the shoulder at 2950 cm^{-1} [22]. Moreover, we noticed that the Raman spectra here reported are similar to those in [23] which were obtained for defective MWCNT and also to the spectra measured in previous works [24] on MWCNT grown at 470°C and 400°C . In this latter case, the quality of the MWCNT was quantified by extracting the electrical resistivity. The result showed indeed that those MWCNT behaved as diffusive conductors for a length of few hundred of nanometers, namely, as a material with some degree of disorder or imperfections. The 2D peak [25] at $\approx 2700\text{ cm}^{-1}$ is an overtone of the D peak also present in graphite and CNT; however, for what mentioned above, it is believed not to originate from the graphite top layer.

The point of major interest for our discussion is that the D and G peaks also appear for samples without CNT (2.2-Ni and 5-Ni) and which looked inactive in the SEM of Figure 2(d) and Figure 2(e). In particular, since the G peak originates from sp^2 carbon domains [23], we conclude that for these samples some graphitic carbon is deposited on the

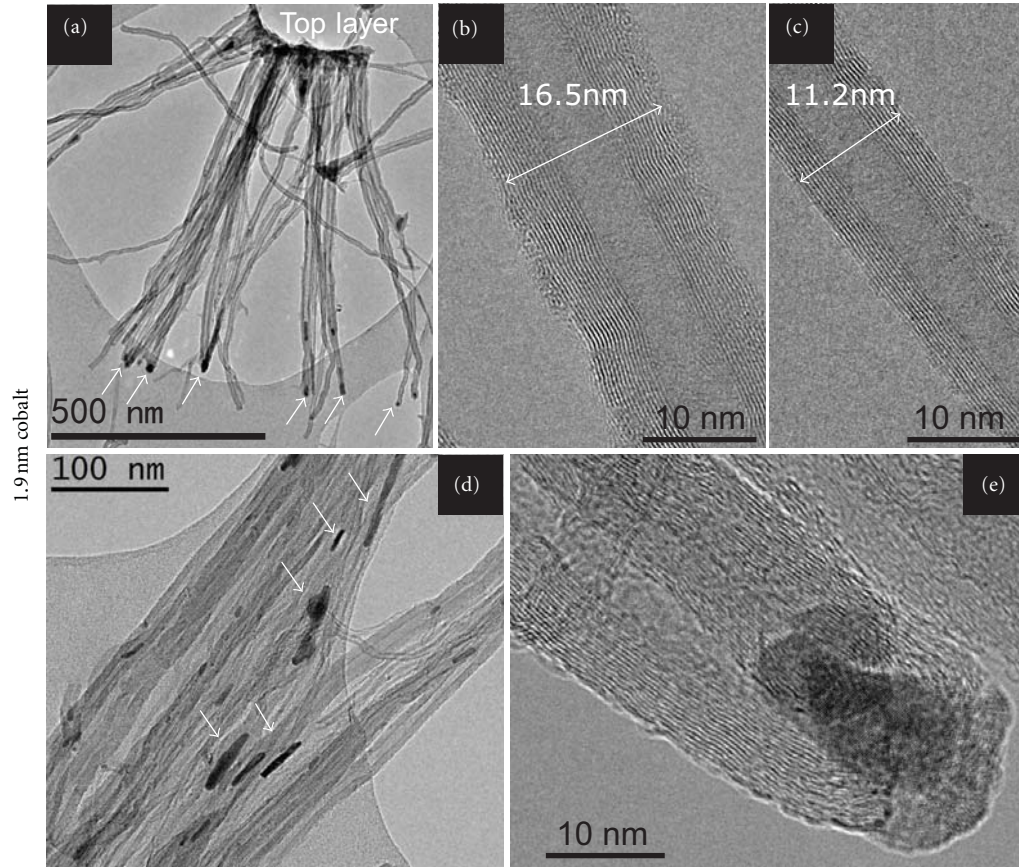


FIGURE 4: TEM of the carbon structures from 1.9 nm cobalt; (a) low-magnification image showing the presence of a large top layer on top of CNT; arrows indicate nanoparticles at the root of the CNT; (b) large CNT with 17 walls; (c) small CNT with 8 walls; (d) nanoparticles inside the CNTs as indicated by arrows; (e) nanoparticle at the tube root.

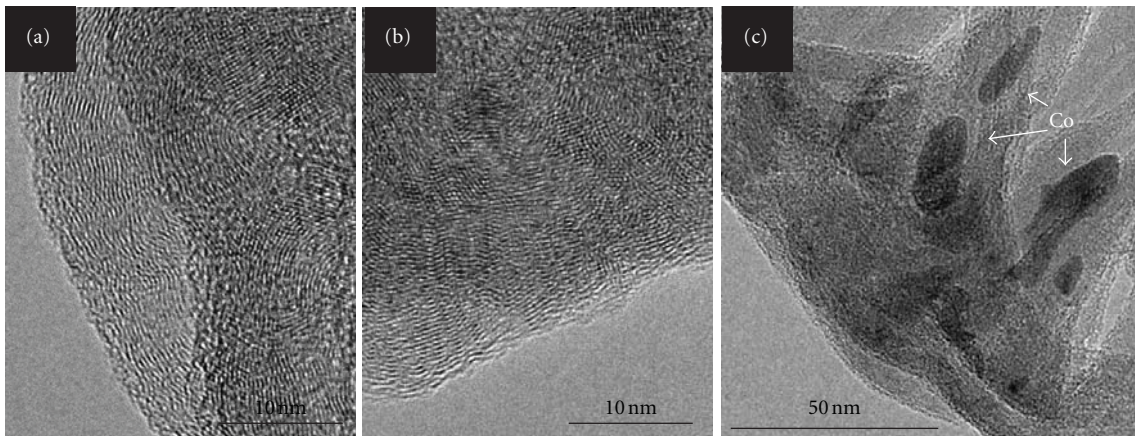


FIGURE 5: High-magnification TEM images of the top layer on the CNT grown from 1.9 nm Co. (a) and (b): graphitic carbon on the crest of the top layer; (c) lower-magnification picture showing elongated cobalt nanoparticles present right below the top layer.

catalyst in the early stage of the growth recipe even if CNT did not form.

The CNT length and consequently the height of the graphite top-layer increase linearly with growth time as shown in Figure 7(a). From the slope, a growth rate of 136 nm/min was found. The intersection with the time axis

suggests an incubation time of about 20 s before the graphite layer is lifted off by the CNT. The top-layer morphology did not change significantly with growth time as ascertained from the SEM images in Figures 7(b) and 7(c).

To assess the effect of pretreatment time [17] on thicker films, the 10 s stabilization step was extended to 2 minutes

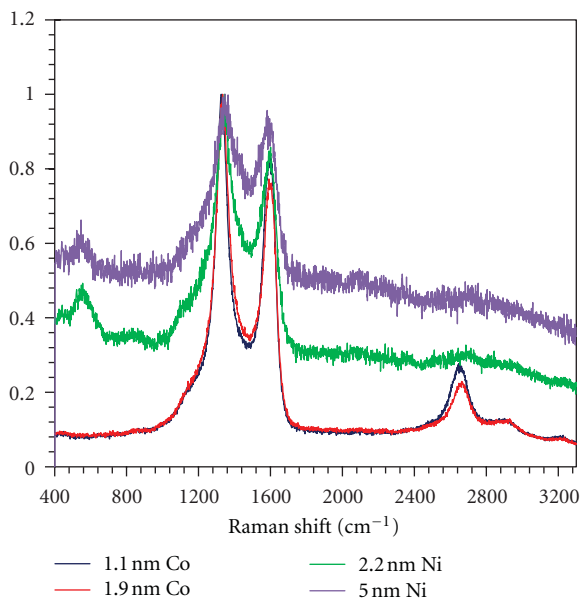


FIGURE 6: Raman spectra (normalized to the D band) of samples with nickel and cobalt films of different catalyst thickness grown in mixture of 5/495 sccm C_2H_2/Ar for 5 min at 4.148 Torr (same series as in Figure 2).

which is equivalent to a thermal pretreatment of 2 min and 10 s at $480^\circ C$ in vacuum ($\approx 10^{-5}$ Torr) before the introduction of acetylene gas for growth. The remainder of the growth recipe was kept the same. The results for the 1.9-Co and 2.2-Ni are presented in Figures 8(a) and 8(b). CNT growth was now observed in both cases without formation of any graphitic layer on top. The 5-Ni film still did not show any growth but after the thermal pretreatment was further extended to 10 minutes, CNTs under large patches of a graphitic top layer were achieved also on this sample (not shown here). Figure 8(c), instead, shows that CNT with a graphite top layer can also be grown in patterned structures using 1.3 nm of Ni and the same recipe without pretreatment used to grow the structures in Figure 2(b).

4. Discussion

The atypical structure observed in the 1.9-Co sample of Figure 4 basically consists of two components: a 2D graphitic top layer on top and a mat of 1D CNT underneath. It is here explained by the interaction between acetylene and the surface of the catalyst template which dynamically changes shape during the process; that is, from a planar film to distributed nanoparticles with possible formation of nanofilaments [28] as the first graphitic layer lifts off from the surface. Note that the term “nanoparticles” has to be seen in a broader sense in this case, namely, as a nucleation center for a CNT (e.g., extrusion in the metal film) which does not have a welldefined distribution in size and density as in the case of CNT growth with a controlled pretreatment or film dewetting step. The necessary conditions are discussed in more detail in the following.

For the decomposition reaction to occur, the catalyst template must be in its “active” state. In catalytic CVD of CNT, a pretreatment step is commonly needed to activate the nickel, cobalt, or iron catalyst. It is believed that the pure metallic form is the most active state for the decomposition of acetylene (access to the transition metal d-orbitals) [29–31]. Reactive reducing gasses like H_2 or NH_3 are typically used to facilitate reduction of the native oxide, especially for those catalysts whose oxides are more difficult to reduce, like iron [29–31]. However, in the case of nickel and cobalt, the oxide reduction or removal is much easier which explains their higher reactivity at lower temperature [12, 31, 32]. For example, in [31], peaks in the XPS graph corresponding to metallic nickel were found at relatively low temperatures in vacuum.

In the first series of experiments, no dedicated pretreatment step was deliberately done. As CNT growth was still observed for the 1.1-Co and 1.3-Ni samples (Figures 2(a) and 2(b)), it can be concluded that the conditions used were sufficient for the activation of the catalyst. Activation may occur either in vacuum, namely, during the sequence of load, stabilization, and purge steps (40 s at 10^{-5} Torr of base pressure and $T_{sample} = 480^\circ C$) or, more likely, during the very early seconds of the growth step where acetylene or the H_2 present as a product of its thermal decomposition can both help the reduction of NiO.

Whether or not CNTs were formed (without a graphitic layer) was dependent on the pretreatment time. Indeed, it is generally accepted that catalyst nanoparticles are needed for CNT growth. Catalyst nanoparticles are typically formed by thermal [33–35] or plasma anneal [10, 36, 37] of thin catalyst films. Because of the larger energy available at high temperatures, the catalyst atoms become mobile which can lead dewetting of the film [38].

The results found here indicate that the time scale at which a film dewets and transforms into nanoparticles is strongly related to the initial film thickness. In fact, only the thinnest films (< 1.3 nm) gave CNT when a short (process intrinsic) pretreatment of 40 s was done (Figures 2, 3, and 4). In the case of 1.1 nm Co, this is because either the film was thin enough to break with a 40 s pretreatment either because it was already discontinuous after deposition. The 1.3 nm Ni film, instead, showed small graphitic patches after the 40 s pretreatment. Since a graphitized top layer was observed for the same film in patterned structures (see Figure 7(c)), this film must have been initially continuous (see [26, 27] for details about the patterned structures). In this case, film breakup occurs during the 40 s pretreatment step, although partially complete.

Thicker films either gave CNT with a graphite layer on top (1.9-Co) or were inactive (2.2-Ni and 5-Ni) with only a 40s pretreatment. However, when the vacuum anneal pretreatment time was increased to 2 min also the 1.9-Co and 2.2-Ni yielded CNT without the graphitic layer indicating that the catalyst film was completely transformed into nanoparticles (Figures 8(a) and 8(b)). Even the 5 nm thick Ni film could eventually be broken into large patches after 10 min of vacuum anneal. Note that the assistance of plasma and reducing gasses may aid the dewetting of thick films [9].

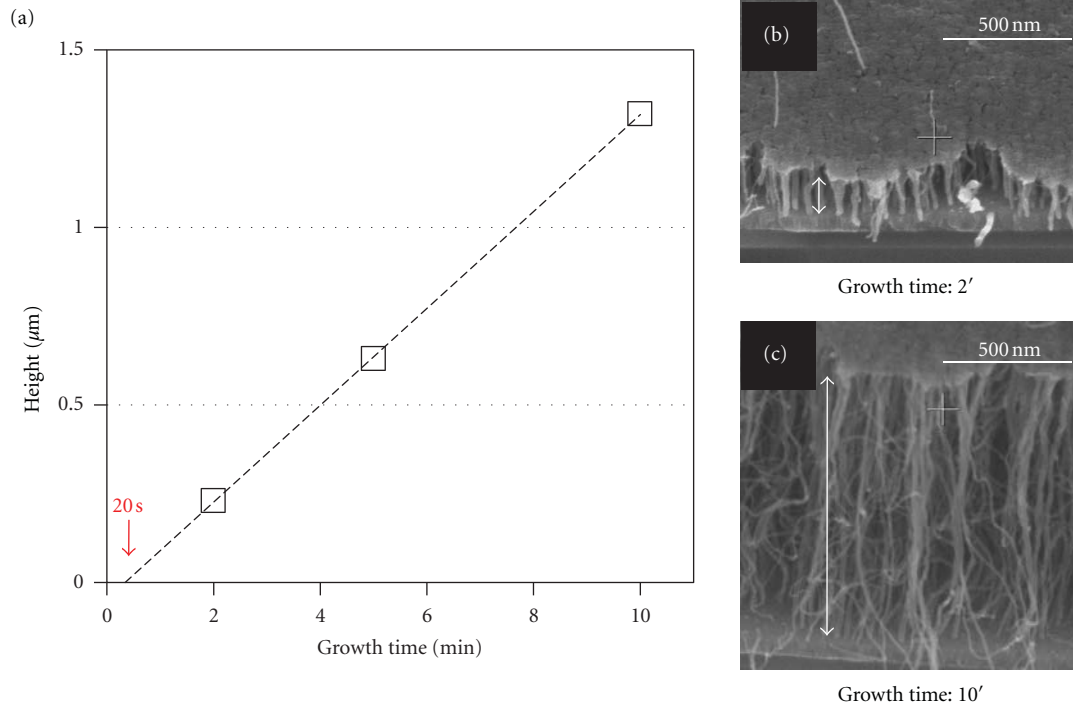


FIGURE 7: (a) Height of the CNT graphite hybrid structure from 1.9 nm Co in function of the growth time. The extrapolated line intersects the x -axis at 20 s (incubation time); (b) and (c) SEM pictures of CNT with graphite top layer grown for, respectively, 2 and 10 minutes. Acetylene was introduced in the chamber at time $t = 0$ of the graph.

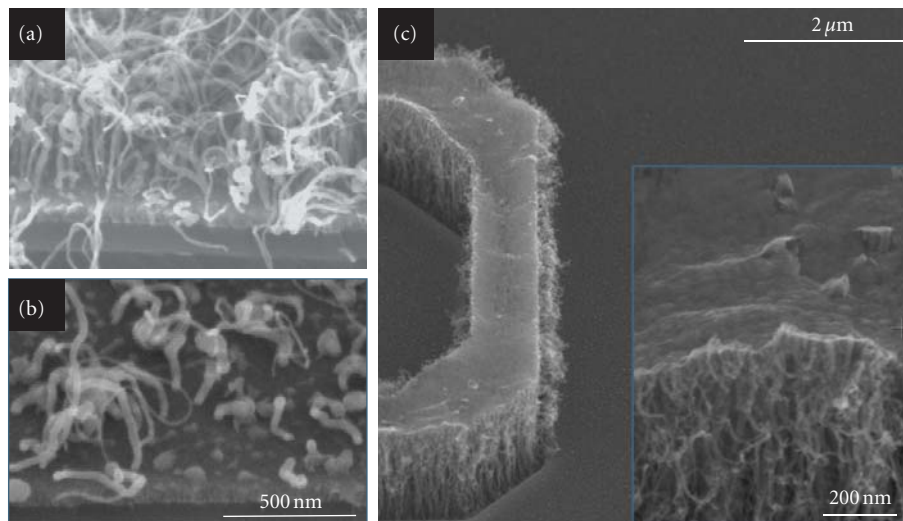


FIGURE 8: (a) CNT grown from a 1.9 nm Co film and (b) from a 2.2 nm Ni film after 2 minute thermal pretreatment (same scale). For both, thermal pretreatment of 2' 10 s in vacuum ($T_{\text{sample}} = 480^{\circ}\text{C}$) and growth step in 5/10/495 sccm $\text{C}_2\text{H}_2/\text{He}/\text{Ar}$ at 4.148 Torr for 5 min ($T_{\text{sample}} = 560^{\circ}\text{C}$); (c) top layer visible on top of patterned structures with 1.3 nm Ni deposited. No pretreatment was used in this case. Details on the patterned structures of c are in [26, 27].

Thus far, we have confirmed the notion that CNTs are formed only when nanoparticles are present before the growth step commences. Now, we will discuss the intermediate phase where the carbon precursor gas (acetylene) is introduced when the catalyst film is still, at least partly, intact. Indeed, the reshaping dynamic for films thicker than 1.3 nm

occurs on a time scale of minutes. Hence, when acetylene is introduced in the chamber immediately after the load and stabilization steps, as for Figure 2, little time is left for these films to transform into nanoparticles. In the 2.2 nm and 5 nm Ni films, no growth at all was observed after 40 s of pretreatment. As the catalyst is active, though, these layers

have been covered by a graphitic coating as confirmed by the presence of D and G peaks in the Raman spectra (Figure 6).

The 1.9 nm Co sample has a thickness intermediate to the extreme cases mentioned above. It is sufficiently thick to be continuous after its deposition but still sufficiently thin to fragment into nanoparticles when the pretreatment time allows for it. The incubation time of 20 s observed in Figure 7(a) indicates that CNT growth does not occur immediately after the introduction of acetylene. Hence, the film retains its 2D film-like shape during the whole load and stabilization steps and at least for the first seconds of the growth steps. Because the catalyst is active, the decomposition of acetylene can occur and a graphitic layer is formed on the surface of the film at this stage, similarly to what happens in catalyzed deposition processes of graphene [39].

At this stage, film fragmentation proceeds and after about 20 s CNT growth can start. Consequently, the top layer is lifted by the CNT structures growing underneath. Theoretical calculations showed that graphitized structures have low adhesion to nickel (100) [40] and Ni (111) [41] surfaces which supports the idea that the fragmentation of the underlying catalyst film can occur without being hampered by the graphite top layer. Note also that CNT growth might start either from nanoparticles as well as from sharp protrusions which form during the dynamic reshaping of the catalyst film under the graphite layer. In this latter case, metal filaments encapsulated in graphene sheets are observed at the bottom of the CNT like in Figure 4(a).

This seems a direct consequence of the fact that catalyst saturated with carbon appears in a viscous semiliquid state [42, 43] suggesting facilitated reshaping. Metal atoms in this phase are much more mobile than in pure metal which leads the catalyst to easily deform into elongated shapes [28]. For example, elongation and reshaping of catalyst nanoparticles has been observed at the initial stages of CNT growth with in situ TEM [44, 45]. Hence, reshaping of the catalyst template can be facilitated by carbon; that is, after introducing acetylene in the chamber. Furthermore, the semi liquid carbon-saturated catalyst state explains how the CNTs end up partly filled with metal especially near the top layer where growth started.

A few remarks should be pointed out regarding the catalyst particles formed during this dynamic process. It is often mentioned that the CNT diameter closely matches that of the original nanoparticle. In particular, for MWCNT, a 1 : 1 correlation between particle's and CNT's diameters was observed in [46, 47] but not [48]. This rule does not apply here as the amount of catalyst found inside the CNT as debris is large and cannot originate from a single nanoparticle with the same diameter of the tube. It seems more plausible that CNTs start growing from particular nucleation points on a larger patch of catalyst. Because of its semiliquid state, the excess of metal is encapsulated in the final CNT and appears in its interior as nanoparticles. This is a major difference compared to most of reported literature data on CNT where the growth recipes had dedicated pretreatments to properly break the catalyst into well-defined nanoparticles.

As catalyst is observed at the CNT root as well as right below the top layer (Figure 5(c)), the CNT growth mechanism is not evident. Nevertheless, the fact that several elongated particles are observed at the CNT root suggests a strong catalyst substrate interaction sufficient to maintain the catalyst, or part of it, anchored to the substrate. The remaining excess of catalyst is dispersed along the entire tube's length as debris. This picture would lead us to propose a base growth mechanism as observed in literature for the Fe-TiN system [10] or for Ni-TiN systems [49–51]. The presence of pores in the top layer could suggest that these are the preferred channels through which the gas can reach the bottom substrate for feeding the catalyst reaction at the CNT base.

Our results have striking similarities with [3, 16–18]. Although the authors investigated the process window for different catalyst thickness and growth temperatures, a similar trend to that reported in Figure 2 can be deduced. In particular, a transition between CNT growth only, the growth of a graphite top layer on CNT, and no growth at all is observed when increasing catalyst thickness [16, 18]. The process window for the hybrid graphite/CNT structure strongly depends on the capability of the catalyst to retain its film shape when the gas precursor is inserted into the chamber and to dewet during the subsequent instants. Hence, at high temperature, thicker catalyst films or growth recipes without pretreatments [3, 16–18] should be used to guarantee the formation of the graphite layer before the film dewets. At lower temperature [17], instead, thinner films or mild pretreatments can be used so to increase the catalyst mobility and guarantee that after some time the film dewets yielding CNT.

5. Conclusions

The growth of an atypical structure composed of CNT with a graphite top layer has been observed and studied. To summarize, the following four conditions have to be satisfied for the formation of this type of structure.

- (1) The catalyst has to be active.
- (2) The catalyst must initially be a continuous film.
- (3) The carbon source has to be introduced before the catalyst has reshaped into nanoparticles.
- (4) The thickness of the catalyst layer and the growth conditions have to be tuned such that the catalyst film retains its 2D shape during the first seconds of the growth but then it is sufficiently mobile to dynamically evolve into distributed nanoparticles.

The first three conditions allow for the formation of a graphitic layer on top of the catalyst film in a similar way to what reported in literature for catalytic deposition processes of graphite/graphene. When also the fourth condition is satisfied, then nanoparticles or patches of catalyst can reshape underneath the graphitic top layer to initiate CNT growth. Consequently, the top layer is lifted up by the underlying CNT [17]. In this phase, excess of catalyst can break and remain in the tubes interior as particles.

Satisfying conditions 2, 3, and 4 all together is not straightforward as the dynamic a film transforms into nanoparticles was found to largely depend on the initial film thickness and temperature used. Very thin films, in fact, either are discontinuous after deposition so that condition 2 cannot be satisfied or break very quickly making condition 3 difficult to satisfy experimentally. Very thick films, instead, may not break at all making condition 4 incomplete. This explains the narrow process window for film thickness in which CNT and the graphite top layer are observed (Figure 2) under the growth conditions used: 1.9 nm for cobalt blanket films and 1.3 nm for Ni patterned samples. Note that this type of structure was observed for both nickel and cobalt but other catalysts might possibly be used probably in a different process window.

The result reported strength the clear correlation between deposition process of graphite and CNT. By improving the control on the dynamic of catalyst breakage and most likely by carefully tuning the growth conditions, it could be possible to achieve a well-defined transition between the growth of graphene or graphite on top of CNT. Such hybrid structures might be of relevant importance for electronic and optical applications such as carbon-based interconnects, field emitters, sensors, NEMs, and optical devices.

Acknowledgments

The authors would like to thank Francesca Clemente for support with Raman spectroscopy. The EU projects CARBONCHIP (NMP4-CT-2006-016475), TECHNO TUBES (NMP2-LA-2009-228579), and the METACEL project (IWT-SBO project 060031) funded by IWT-Vlaanderen are acknowledged for financial support. Nicolo' Chiodarelli has this current address (CEA LITEN/DTNM/LCRE, 17 rue des Martyrs, 38054 Grenoble, France).

References

- [1] P. Avouris, Z. Chen, and V. Perebeinos, "Carbon-based electronics," *Nature Nanotechnology*, vol. 2, no. 10, pp. 605–615, 2007.
- [2] N. Chiodarelli, S. Masahito, Y. Kashiwagi et al., "Measuring the electrical resistivity and contact resistance of vertical carbon nanotube bundles for application as interconnects," *Nanotechnology*, vol. 22, no. 8, Article ID 085302, 2011.
- [3] D. Kondo, S. Sato, and Y. Awano, "Self-organization of novel carbon composite structure: graphene multi-layers combined perpendicularly with aligned carbon nanotubes," *Applied Physics Express*, vol. 1, no. 7, Article ID 074003, 2008.
- [4] S. Bae, H. Kim, Y. Lee et al., "Roll-to-roll production of 30-inch graphene films for transparent electrodes," *Nature Nanotechnology*, vol. 5, no. 8, pp. 574–578, 2010.
- [5] J. Lefebvre, D. G. Austing, J. Bond, and P. Finnie, "Photoluminescence imaging of suspended single-walled carbon nanotubes," *Nano Letters*, vol. 6, no. 8, pp. 1603–1608, 2006.
- [6] M. Freitag, Y. Martin, J. A. Misewich, R. Martel, and P. Avouris, "Photoconductivity of single carbon nanotubes," *Nano Letters*, vol. 3, no. 8, pp. 1067–1071, 2003.
- [7] J. Wei, Y. Jia, Q. Shu et al., "Double-walled carbon nanotube solar cells," *Nano Letters*, vol. 7, no. 8, pp. 2317–2321, 2007.
- [8] J. W. Mintmire and C. T. White, "Electronic and structural properties of carbon nanotubes," *Carbon*, vol. 33, no. 7, pp. 893–902, 1995.
- [9] M. Chhowalla, K. B. K. Teo, C. Ducati et al., "Growth process conditions of vertically aligned carbon nanotubes using plasma enhanced chemical vapor deposition," *Journal of Applied Physics*, vol. 90, no. 10, pp. 5308–5317, 2001.
- [10] S. Esconjauregui, B. C. Bayer, M. Fouquet et al., "Growth of high-density vertically aligned arrays of carbon nanotubes by plasma-assisted catalyst pretreatment," *Applied Physics Letters*, vol. 95, no. 17, Article ID 173115, 2009.
- [11] G. D. Nessim, A. J. Hart, J. S. Kim et al., "Tuning of vertically-aligned carbon nanotube diameter and areal density through catalyst pre-treatment," *Nano Letters*, vol. 8, no. 11, pp. 3587–3593, 2008.
- [12] M. Cantoro, S. Hofmann, C. Mattevi et al., "Plasma restructuring of catalysts for chemical vapor deposition of carbon nanotubes," *Journal of Applied Physics*, vol. 105, no. 6, Article ID 064304, 2009.
- [13] S. Kumar, N. McEvoy, T. Lutz et al., "Low temperature graphene growth," *ECS Transactions*, vol. 19, no. 5, pp. 175–181, 2009.
- [14] A. Reina, X. Jia, J. Ho et al., "Large area, few-layer graphene films on arbitrary substrates by chemical vapor deposition," *Nano Letters*, vol. 9, no. 1, pp. 30–35, 2009.
- [15] K. S. Kim, Y. Zhao, H. Jang et al., "Large-scale pattern growth of graphene films for stretchable transparent electrodes," *Nature*, vol. 457, no. 7230, pp. 706–710, 2009.
- [16] C. C. Chuang, W. L. Liu, W. J. Chen, and J. H. Huang, "Growth of graphite film over the tops of vertical carbon nanotubes using Ni/Ti/Si substrate," *International Journal of Minerals, Metallurgy and Materials*, vol. 16, no. 1, pp. 128–134, 2009.
- [17] V. Jousseau, J. Cuzzocrea, N. Bernier, and V. T. Renard, "Few graphene layers/carbon nanotube composites grown at complementary-metal-oxide-semiconductor compatible temperature," *Applied Physics Letters*, vol. 98, no. 12, Article ID 123103, 2011.
- [18] S. Das, R. Seelaboyina, V. Verma et al., "Synthesis and characterization of self-organized multilayered graphene-carbon nanotube hybrid films," *Journal of Materials Chemistry*, vol. 21, no. 20, pp. 7289–7295, 2011.
- [19] A. Romo-Negreira, D. J. Cott, A. S. Verhulst et al., "Growth and integration of high-density CNT for BEOL interconnects," in *Proceedings of the Materials Research Society Symposium Proceedings*, vol. 1079, 2008.
- [20] A. C. Ferrari, "Raman spectroscopy of graphene and graphite: disorder, electron-phonon coupling, doping and nonadiabatic effects," *Solid State Communications*, vol. 143, no. 1-2, pp. 47–57, 2007.
- [21] A. C. Ferrari and J. Robertson, "Interpretation of Raman spectra of disordered and amorphous carbon," *Physical Review B*, vol. 61, no. 20, pp. 14095–14107, 2000.
- [22] M. A. Pimenta, G. Dresselhaus, M. S. Dresselhaus, L. G. Cançado, A. Jorio, and R. Saito, "Studying disorder in graphite-based systems by Raman spectroscopy," *Physical Chemistry Chemical Physics*, vol. 9, no. 11, pp. 1276–1291, 2007.
- [23] Y. A. Kim, T. Hayashi, K. Osawa, M. S. Dresselhaus, and M. Endo, "Annealing effect on disordered multi-wall carbon nanotubes," *Chemical Physics Letters*, vol. 380, no. 3-4, pp. 319–324, 2003.
- [24] N. Chiodarelli, *Integration of carbon nanotubes as future interconnects for sub-32 nm technologies [Ph.D. thesis]*, Katholieke Universiteit Leuven, Leuven, Belgium, 2011.

- [25] M. S. Dresselhaus, G. Dresselhaus, R. Saito, and A. Jorio, "Raman spectroscopy of carbon nanotubes," *Physics Reports*, vol. 409, no. 2, pp. 47–99, 2005.
- [26] N. Chiodarelli, K. Kellens, D. J. Cott et al., "Integration of vertical carbon nanotube bundles for interconnects," *ECS Transactions*, vol. 19, no. 24, pp. 11–24, 2009.
- [27] N. Chiodarelli, Y. Li, D. J. Cott et al., "Integration and electrical characterization of carbon nanotube via interconnects," *Microelectronic Engineering*, vol. 88, no. 5, pp. 837–843, 2011.
- [28] X. Chen, R. Wang, J. Xu, and D. Yu, "TEM investigation on the growth mechanism of carbon nanotubes synthesized by hot-filament chemical vapor deposition," *Micron*, vol. 35, no. 6, pp. 455–460, 2004.
- [29] C. Mattevi, C. T. Wirth, S. Hofmann et al., "In-situ X-ray photoelectron spectroscopy study of catalyst-support interactions and growth of carbon nanotube forests," *Journal of Physical Chemistry C*, vol. 112, no. 32, pp. 12207–12213, 2008.
- [30] A. Okita, A. Ozeki, Y. Suda et al., "Analysis of oxidation state of multilayered catalyst thin films for carbon nanotube growth using plasma-enhanced chemical vapor deposition," *Japanese Journal of Applied Physics, Part 1*, vol. 45, no. 10 B, pp. 8323–8329, 2006.
- [31] S. Hofmann, R. Blume, C. T. Wirth et al., "State of transition metal catalysts during carbon nanotube growth," *Journal of Physical Chemistry C*, vol. 113, no. 5, pp. 1648–1656, 2009.
- [32] A. M. Cassell, Q. Ye, B. A. Cruden et al., "Combinatorial chips for optimizing the growth and integration of carbon nanofibre based devices," *Nanotechnology*, vol. 15, no. 1, pp. 9–15, 2004.
- [33] E. Terrado, I. Tacchini, A. M. Benito, W. K. Maser, and M. T. Martínez, "Optimizing catalyst nanoparticle distribution to produce densely-packed carbon nanotube growth," *Carbon*, vol. 47, no. 8, pp. 1989–2001, 2009.
- [34] S. Hermann, R. Ecke, S. Schulz, and T. Gessner, "Controlling the formation of nanoparticles for definite growth of carbon nanotubes for interconnect applications," *Microelectronic Engineering*, vol. 85, no. 10, pp. 1979–1983, 2008.
- [35] S. Pisana, M. Cantoro, A. Parvez, S. Hofmann, A. C. Ferrari, and J. Robertson, "The role of precursor gases on the surface restructuring of catalyst films during carbon nanotube growth," *Physica E*, vol. 37, no. 1–2, pp. 1–5, 2007.
- [36] A. Malesevic, H. Chen, T. Hauffman, A. Vanhulsel, H. Terryn, and C. V. Haesendonck, "Study of the catalyst evolution during annealing preceding the growth of carbon nanotubes by microwave plasma-enhanced chemical vapour deposition," *Nanotechnology*, vol. 18, no. 45, Article ID 455602, 2007.
- [37] S. C. Chang, T. C. Lin, T. S. Li, and S. H. Huang, "Carbon nanotubes grown from nickel catalyst pretreated with H₂/N₂ plasma," *Microelectronics Journal*, vol. 39, no. 12, pp. 1572–1575, 2008.
- [38] Y. Wang, Z. Luo, B. Li et al., "Comparison study of catalyst nanoparticle formation and carbon nanotube growth: support effect," *Journal of Applied Physics*, vol. 101, no. 12, Article ID 124310, 2007.
- [39] J. Lahiri, T. Miller, L. Adamska, I. I. Oleynik, and M. Batzill, "Graphene growth on Ni(111) by transformation of a surface carbide," *Nano Letters*, vol. 11, no. 2, pp. 518–522, 2011.
- [40] H. Amara, C. Bichara, and F. Ducastelle, "Interaction of carbon clusters with Ni(1 0 0): application to the nucleation of carbon nanotubes," *Surface Science*, vol. 602, no. 1, pp. 77–83, 2008.
- [41] H. Amara, C. Bichara, and F. Ducastelle, "Formation of carbon nanostructures on nickel surfaces: a tight-binding grand canonical Monte Carlo study," *Physical Review B*, vol. 73, no. 11, Article ID 113404, pp. 1–4, 2006.
- [42] A. R. Harutyunyan, T. Tokune, and E. Mora, "Liquid as a required catalyst phase for carbon single-walled nanotube growth," *Applied Physics Letters*, vol. 87, no. 5, Article ID 051919, 2005.
- [43] A. R. Harutyunyan, E. Mora, T. Tokune et al., "Hidden features of the catalyst nanoparticles favorable for single-walled carbon nanotube growth," *Applied Physics Letters*, vol. 90, no. 16, Article ID 163120, 2007.
- [44] S. Helveg, C. López-Cartes, J. Sehested et al., "Atomic-scale imaging of carbon nanofibre growth," *Nature*, vol. 427, no. 6973, pp. 426–429, 2004.
- [45] S. Hofmann, R. Sharma, C. Ducati et al., "In situ observations of catalyst dynamics during surface-bound carbon nanotube nucleation," *Nano Letters*, vol. 7, no. 3, pp. 602–608, 2007.
- [46] A. Romo-Negreira, D. J. Cott, S. De Gendt, K. Maex, M. M. Heyns, and P. M. Vereecken, "Electrochemical tailoring of catalyst nanoparticles for CNT spatial-dimension control," *Journal of the Electrochemical Society*, vol. 157, no. 3, pp. K47–K51, 2010.
- [47] A. R. Harutyunyan, T. Tokune, E. Mora, J. W. Yoo, and A. J. Epstein, "Evolution of catalyst particle size during carbon single walled nanotube growth and its effect on the tube characteristics," *Journal of Applied Physics*, vol. 100, no. 4, Article ID 044321, 2006.
- [48] C. Lu and J. Liu, "Controlling the diameter of carbon nanotubes in chemical vapor deposition method by carbon feeding," *Journal of Physical Chemistry B*, vol. 110, no. 41, pp. 20254–20257, 2006.
- [49] J. B. A. Kpetsu, P. Jedrzejowski, C. Côté et al., "Influence of Ni catalyst layer and TiN diffusion barrier on carbon nanotube growth rate," *Nanoscale Research Letters*, vol. 5, no. 3, pp. 539–544, 2010.
- [50] W. P. Wang, H. C. Wen, S. R. Jian et al., "The effects of hydrogen plasma pretreatment on the formation of vertically aligned carbon nanotubes," *Applied Surface Science*, vol. 253, no. 23, pp. 9248–9253, 2007.
- [51] S. R. Jian, "Effects of H₂ plasma pretreated Ni catalysts on the growth of carbon nanotubes," *Materials Chemistry and Physics*, vol. 115, no. 2–3, pp. 740–743, 2009.

Research Article

Measuring of Electrical Properties of MWNT-Reinforced PAN Nanocomposites

Sliman Almuhammed, Nabyl Khenoussi, Laurence Schacher, Dominique Adolphe, and Henri Balard

*Laboratoire de Physique et Mécanique Textiles EAC 7189 CNRS/UHA ENSISA,
11 rue Alfred Werner F-68093 Mulhouse Cedex, France*

Correspondence should be addressed to Sliman Almuhammed, sliman.al-muhamed@uha.fr

Received 18 October 2011; Accepted 2 April 2012

Academic Editor: Sulin Zhang

Copyright © 2012 Sliman Almuhammed et al. This is an open access article distributed under the Creative Commons Attribution License, which permits unrestricted use, distribution, and reproduction in any medium, provided the original work is properly cited.

Nano-web sheets of polyacrylonitrile (PAN) reinforced by carbon nanotubes (CNT) were prepared by electrospinning process. Multi wall nanotubes (MWNT) were dispersed mechanically by high shear mixing using a homogenizer device. It has been found that the spinning solution presented an electrical percolation threshold less than 0.5 wt.% of MWNT. Electrical volume and surface conductivity of the obtained nano-webs was studied by measuring the electrical volume resistance and surface resistance thanks to home-made plate electrodes. Scanning electron microscope (SEM) has been used to characterize the nano-web sheets produced. The average filament diameters range from 320 to 750 nm depending on the concentration of CNT and of PAN. From an electrical point of view, it has been observed that the electrical volume conductivity increases by about six orders of magnitude from 2×10^{-12} S/m for pristine PAN to 4×10^{-6} S/m for PAN charged by MWNT. Increasing the pressure on the specimen induces an exponential decrease of the volume resistivity while surface resistivity shows no significant changes, neither between pristine PAN and reinforced nano-webs, nor among reinforced nano-web in relation to MWNT concentration (in the limit of the study). This observed behavior is very interesting in the context of sensor developments.

1. Introduction

Carbon nanotubes (CNTs) are a new shape of carbon, first identified by Iijima in 1991 [1]. Since their discovery, they have attracted a great interest in research field and in industrial applications as well, owing to their magnificent thermal, electrical, and mechanical properties [2–4]. The electrical properties of carbon nanotubes are to a large extent derived from their 1D character and peculiar electronic structure of graphite [5]. In addition, they can carry the highest current density of any known material, measured as high as 10^9 A/cm² [6].

To employ CNTs as effective reinforcement in polymer nanocomposites, the proper dispersion and appropriate interfacial adhesion between the CNTs and polymer matrix have to be guaranteed [7]. There is a sizable volume of literature on the techniques developed for CNT dispersion in

polymer matrix [8–11]. These techniques can be classified into two distinct approaches: the mechanical approach, such as ball milling, ball milling followed by ultrasonication, and high shear mixing, and the chemical approach designed to alter the surface energy of the solids. Chemical methods use surface functionalization of CNT to improve their chemical compatibility with the target medium (solvent or polymer solution/melt), that is, to enhance wetting or adhesion characteristics and reduce their tendency to agglomerate. Chemical treatments include boiling in acids (H₂SO₄ + HNO₃), soaking in concentrated acids under ultrasonication, and annealing at high temperature followed by boiling in concentrated acids [12, 13].

Their high aspect ratio makes carbon nanotubes capable of possessing a percolation threshold at low CNT loading in nanoweb [14]. Du et al. [15] have studied the influence of loading percentage of single-wall carbon nanotubes

(SWNTs) on the rheological properties of CNT-reinforced poly(methyl methacrylate), PMMA, nanocomposites. Their rheological and electrical measurements were performed on solid aligned and unaligned composite reinforced by CNT specimens prepared by the coagulation method. They found that the threshold of rheological percolation (0.12 wt.%) is significantly smaller than the threshold of electrical percolation (0.39 wt.%). Ounaies et al. [16] have investigated the electrical properties of SWNT-reinforced polyimide (aromatic colorless polyimide, CP2) composites prepared by in situ polymerization under sonication. The volume electrical conductivity of pristine CP2 polyimide was about 6.3×10^{-18} S/cm. A sharp increase of the volume conductivity value of solid samples was observed between 0.02 and 0.1 vol.% in solution, where the conductivity changed from 3×10^{-17} to 1.6×10^{-8} S/cm. Kota et al. [17] have studied the electrical and rheological percolation of MWNT-reinforced polystyrene composite prepared by a solvent evaporation method. They found that the volume conductivity of pure polystyrene is about 10^{-20} S/m, but adding MWNTs increased the volume conductivity of the composites by 20 orders of magnitude, approaching a value of about 1 S/m at 8 vol.% loading percentage of MWNTs in solution. Guo et al. [18] have investigated polyacrylonitrile (PAN)/carbon nanotube composites prepared by a solvent evaporation method and their reinforcement efficiency using different types of CNT, including single wall carbon nanotubes (SWNTs), double-wall carbon nanotubes (DWNTs), multiwall carbon nanotubes (MWNTs), and vapor-grown carbon nanofibers (VGCNFs). It was found that PAN/SWNT films at 20 wt.% exhibit the highest surface electrical conductivity among all composite films prepared with the same loading of CNT forms. Ra et al. [19] have researched the influence of MWNT on morphological and electrical conductivity of carbonized PAN nanofibers produced by electrospinning process. They discovered that the surface electrical conductivity of the carbonized PAN/MWNT aligned nanofiber sheets is highly anisotropic, and they pointed out that the percolation threshold was not reached, even at 10 wt.% of MWNT loading percentage.

Although an electrical percolation threshold volume of polymer/CNT composites can be reached for a low loading percentage of CNT, obtaining percolated nanocomposite of a polymer charged by CNTs with a very low concentration of treated carbon nanotubes is an interesting challenge.

Our study is focused on the use of electrospinning device in order to obtain a nanoweb of PAN charged with MWNT. Two different conductivities are measured: volume and surface ones. The fact that volume and surface electrical behaviors could be different will present advantages for sensor and actuator applications and developments.

2. Experimental

2.1. Materials. Polyacrylonitrile (PAN) with molecular weight $M_w = 150000 \text{ g} \cdot \text{mol}^{-1}$ was supplied by Sigma-Aldrich (France). N,N-Dimethylformamide pure (DMF) (impurities less than 152 ppm in which water is less than 50 ppm) was



FIGURE 1: Electrospinning setup.

purchased from Fisher Scientific (France). Purified multiwall carbon nanotubes was prepared by vapor deposition on a catalytic support, supplied by Arkema (France). The purity of MWNT is about 93% with a mean external diameter of 11 nm and a thickness of about 3.2 ± 1 nm.

2.2. Protocol of Work

2.2.1. Preparing Solutions and Electrospinning Parameters. Six dispersions of multiwall carbon nanotubes in DMF with different loading percentages (0.2, 0.4, 0.5, 0.7, 1.0, and 1.5 wt.%) were prepared using high shear homogenizer from IKA (France) with the following conditions: 18 000 rpm during 15 min. In order to avoid overheating nanotubes due to high shear mixing, an aqueous bath was used for this purpose. Then, samples were ultrasonicated for 30 min at 50°C .

To prepare the charged colloids to be electrospun, proper quantities of PAN equivalent to a concentration of 10 wt.% were added to the treated dispersions of MWNTs in DMF. Samples were stirred for 24 h at 70°C to insure the homogeneity of the final spinning polymeric solutions.

The prepared solution was, then, electrospun by means of an electrospinning setup manufactured at LPMT (France), (see Figure 1). This setup is based on the vertical projection of polymeric solution, where this later is fed to a syringe using a pump located outside the electrospinning cabin. The electrospinning process is carried out between the tip of the needle, which is connected to the positive output of a high-voltage-supplier-type (Heinzinger) LNC 30 kV, and a grounded plate of copper covered with a foil of aluminum.

Table 1 gives the parameters of the electrospinning process. The sheets produced were characterized by scanning electron microscopy type (SEM, Hitachi S-2360N). Figure 2 shows a SEM micrograph of pristine PAN and CNT-reinforced PAN nanocomposites, respectively, charged with 0.2, 0.4, 0.5, 0.7, 1.0, and 1.5 wt.% of MWNTs. On these photos, 50 different fibers of each specimen were measured by using Photoshop 6.0 ME in order to evaluate their diameters.

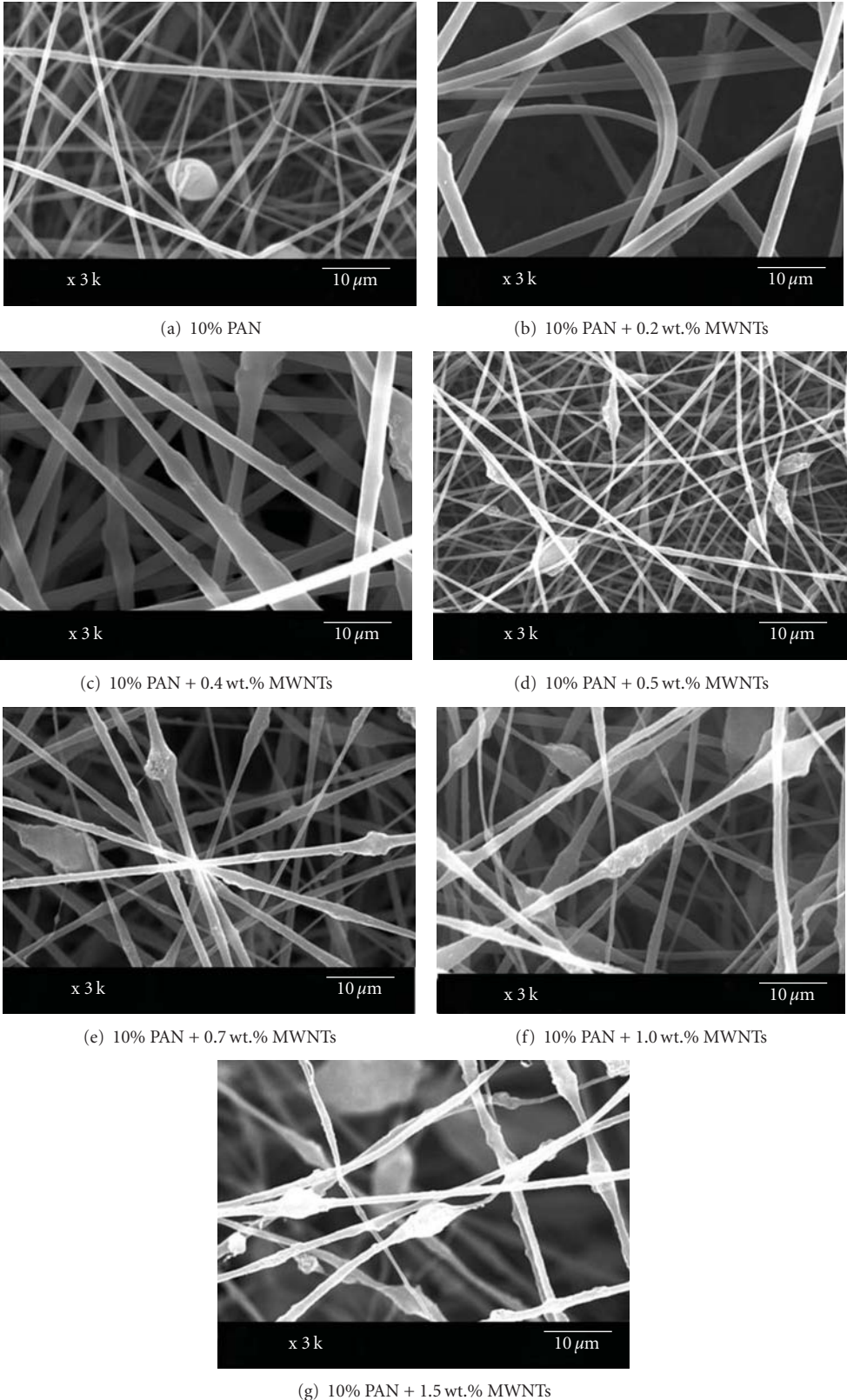


FIGURE 2: SEM micrograph of (a) 10% PAN and CNT-reinforced PAN electrospun nanocomposites with (b) 0.2 wt.%, (c) 0.4 wt.%, (d) 0.5 wt.%, (e) 0.7 wt.%, (f) 1.0 wt.%, and (g) 1.5 wt.% loading percentage of MWNTs.

TABLE 1: Parameters of electrospinning process.

	10% PAN	10% PAN 0.2% CNT	10% PAN 0.4% CNT	10% PAN 0.5% CNT	10% PAN 0.7% CNT	10% PAN 1.0% CNT	10% PAN 1.5% CNT
Voltage (kV)	11	12	12.5	11	14	14	12
Gap needle collector (cm)	30	30	30	30	30	30	30
Feed rate (mL/h)	0.354	0.212	0.212	0.283	0.424	0.424	0.283
Period of spinning (min)	60	60	60	60	60	60	60

2.2.2. Preparing Electrospun Specimens for Resistance Measurements. A set of three specimens of each electrospun sheet was cut in dimensions of 2×2 cm for measuring the volume resistance, and another set composed of three specimens was also cut in dimensions of 2×6 cm for measuring the surface resistance. Surface and volume resistance were measured up to the American standard ASTM D 257-61 by using an assembly of plate electrodes. Table 2 illustrates the parameters of electrical resistance measurements. An assembly of loads was also used to study the effect of compression on resistivity, as shown in Figure 3.

3. Results and Discussion

3.1. Influence of CNT on the Morphology of Nanofibers. Electrospun fibers of 10% PAN have a mean diameter of 568 nm, and reinforced fibers have average diameters that range from 325 to 795 depending on the percentage of MWNTs, as shown in Figure 4. It can be assumed that adding CNT will increase the conductivity of the solution that leads to accelerating the jet and therefore reduces the diameter of filaments. In the case of 0.5 wt.% MWNTs, this phenomenon is observed. With higher MWNT concentrations, this behavior comes from a competing effect between the previous described phenomenon and the size of MWNT aggregates that still are not dispersed and generate coarse diameter.

3.2. Percolation Threshold of Reinforced Nanocomposites and the Influence of CNT on Volume Resistivity of Nanocomposites. Figure 5 illustrates the relationship of electrical volume conductivity in S/m of pristine PAN (at 0% loading percentage of CNT) and CNT-reinforced PAN nanocomposites. According to the results obtained, it is obvious that CNT-reinforced PAN nanofibers have a clear percolation threshold between 0.4 and 0.5 wt.% loading percent of carbon nanotubes. The volume conductivity of less than 0.5 wt.% shows no significant change compared to the initial status, that is, PAN nanofibers with no reinforcement, while the conductivity after adding 0.5 wt.% or more increases by five orders of magnitude from 1.85×10^{-11} S/m at loading percent of 0.4 wt.% of CNT to 4.15×10^{-6} S/m at 0.5 wt.% of CNT. This means that the electrical state of the material (nanocomposite) has changed from an insulative material (where conductivity equals or less than 1×10^{-11} S) into static

dissipative material (where conductivity is between 1×10^{-4} S and 1×10^{-11} S) [20].

On the other hand, plotting the volume resistivity values of the mentioned nanocomposites after percolation threshold, as shown in Figure 6, reveals that the volume resistivity of the nanocomposite decreases exponentially when a load is applied. It can be concluded from this result that these nanocomposites can be used as pressure sensors and could be integrated into an electrical circuit in the context of smart textile applications.

3.3. Influence of CNT on Surface Resistivity of Nanocomposites.

Figure 7 shows a comparison of surface electrical resistivity of the 7 produced nanowebs. It can be noted that there is no significant change in the values of surface resistivity among all specimens; that is, both pristine PAN electrospun fibers and CNT-reinforced fibers have surface resistivities of the same magnitude (teraohm). On the other hand, there is no significant change in surface resistivity in relation to the applied load (Figure 7).

These results can be explained by two approaches: the first one is “electron hopping or tunneling,” and the second one is “the percolation threshold theory.” When the percolation threshold is reached, a conducting path of conclusions is formed, where a distinct distance between fillers is reached. Then, when the fillers are close enough but are not in direct physical contact, hopping or even tunneling [21] occurs. According to the percolation threshold, electrical conductivity σ_{dc} is fitted by

$$\sigma_{dc} \propto (P - P_c)^\mu, \quad P > P_c, \quad (1)$$

where P is the MWNT mass fraction, P_c is the threshold of electrical conductivity percolation, and μ is the critical exponent.

Concerning the conductivity of percolation clusters, there is no current below P_c that passes in the volume direction of the sample, while σ_{dc} increases exponentially by the low power indicated in formula (1). Within this mechanism, carbon nanotubes should be in direct contact so that they form a continuous conducting path [22–24].

Increasing the applied load decreases the distance between fibers more and more, and taking into consideration that carbon nanotubes exist both inside and outside of the surface of fiber [25], this enhances the formation of conducting networks which states the presence of direct contact between embedded MWNTs. In this case, the percolation theory is dominant.

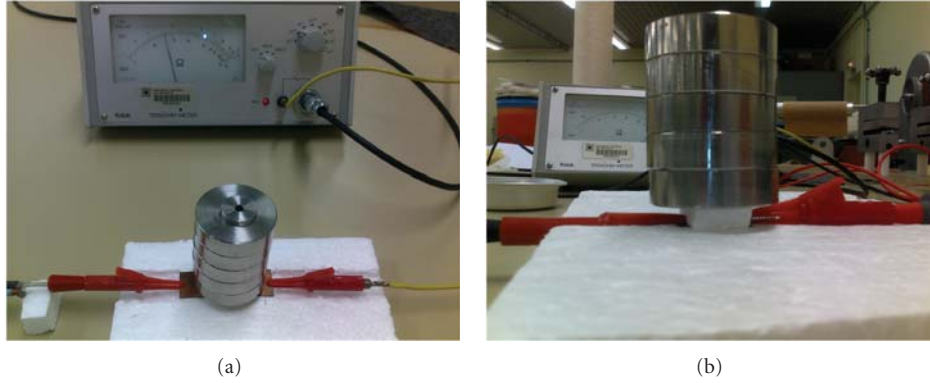


FIGURE 3: Setup for measuring the surface (a) and volume (b) resistances in relation to applied load.

TABLE 2: Parameters of electrical resistance measurements.

Shape and dimensions of specimen	Type and dimensions of electrodes	Conditioning of specimen	Test conditions	Applied voltage	Time of electrification
Square 2×2 cm Rectangular 2×6 cm	Plates of copper metalized by gold 2×2 cm	No cleaning No predrying 24 h of conditioning	$20 \pm 2^\circ\text{C}$ $60 \pm 2\% \text{ RH}$	Surface resistance: 500 V Volume resistance: 10 V	2 min

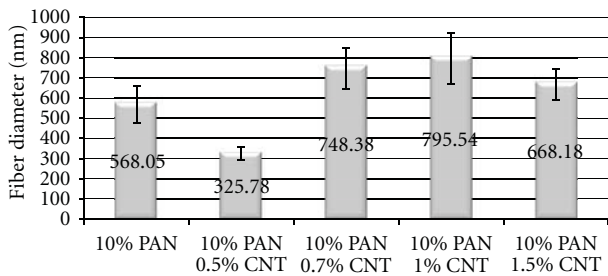


FIGURE 4: Fiber average diameters of CNT-reinforced PAN nanocomposites.

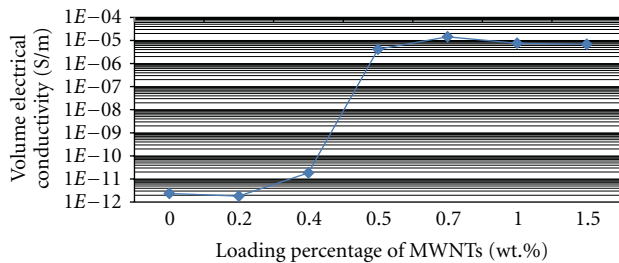


FIGURE 5: Volume conductivity of 10% CNT-reinforced PAN composite with different loading percentage of MWNTs.

Figure 6 reveals that the curves reached asymptotical values when the applied load is greater than 65 g (i.e., 2.5 kPa, where the active area of specimen is about 2.56 cm²).

This means that a saturation value of percolated charges network has been attained. These results offered the possibility of using this nanocomposite of CNT-reinforced PAN (after percolation value) as a pressure sensor for low pressure applications.

The surface resistivity behavior can be explained as follows.

The carbon nanotubes are distributed inside and on the surface of the fiber [25]. In this case, the percolation threshold (P_c) for surface conductivity has not been reached; therefore, within the theory of percolation theory, the conducted network path is not formed.

4. Conclusion

Nanowebs of PAN nanofibers reinforced with MWNTs were produced by means of electrospinning. It was found that adding carbon nanotubes will reduce the diameter of nanofibers when they are well dispersed and when all process and ambience parameters are fully controlled. The reinforced nanofibers obtained possess an electrical volume percolation threshold at very low loading percentage of MWNTs corresponding to 0.5 wt.%. Simultaneously, the surface electrical percolation threshold has not been reached even for a concentration of 1.5 wt.%. An exponential relationship between the mechanical pressure applied and the volume conductivity was observed experimentally by assuming that the electrospun nanoweb of PAN reinforced with MWNTs could be used as a pressure sensor.

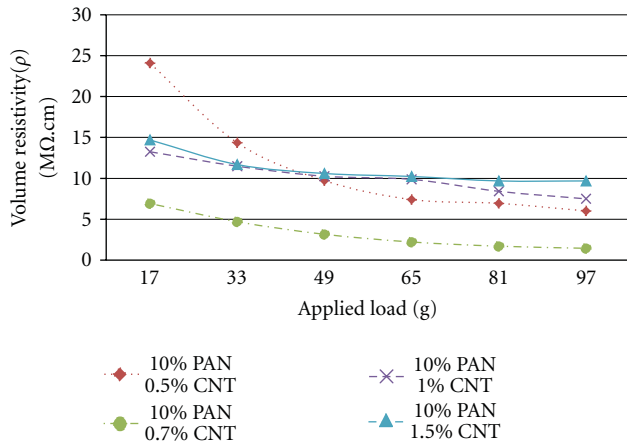


FIGURE 6: Volume resistivity of 10% CNT-reinforced PAN composite with different (wt) loading percentage of MWNTs after percolation threshold at 0.5 wt.%.

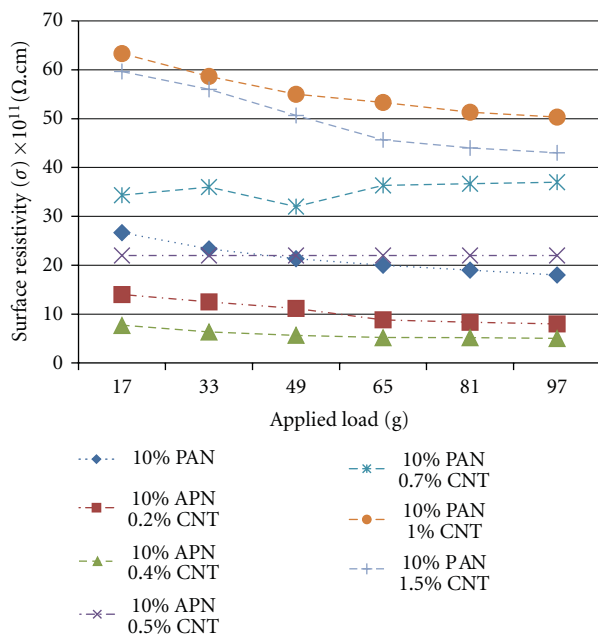


FIGURE 7: Surface resistivity of 10% CNT-reinforced PAN composite.

Perspectives

Additional characterization techniques, like TEM, Raman spectroscopy, and so forth, will be used quantitatively and qualitatively to characterize the nanowebs produced. In addition, a new device that enhances the distribution of carbon nanotubes on the surface of the fibers can be envisaged. Moreover, the increase of the MWNT concentration in order to obtain percolation threshold of the surface conductivity has to be implemented.

Acknowledgments

The research team has no financial nor commercial relations with any of the commercial identities mentioned in this paper. The authors thank Craig Hamilton for proofreading the paper.

References

- [1] S. Iijima, "Helical microtubules of graphitic carbon," *Nature*, vol. 354, no. 6348, pp. 56–58, 1991.
- [2] A. G. Mamalis, L. O. G. Vogtländer, and A. Markopoulos, "Nanotechnology and nanostructured materials: trends in carbon nanotubes," *Precision Engineering*, vol. 28, no. 1, pp. 16–30, 2004.
- [3] S. H. Nahm, "Tensile test of carbon nanotube using manipulator in scanning electron microscope," in *The 3th Korea-US NanoForum, Korea*, 2006.
- [4] S. J. Tans, A. R. M. Verschueren, and C. Dekker, "Room-temperature transistor based on a single carbon nanotube," *Nature*, vol. 393, no. 6680, pp. 49–52, 1998.
- [5] R. Khare and S. Bose, "Carbon nanotube based composites—a review," *Journal of Minerals & Materials Characterization & Engineering*, vol. 40, no. 1, pp. 31–46, 2005.
- [6] B. Q. Wei, R. Vajtai, and P. M. Ajayan, "Reliability and current carrying capacity of carbon nanotubes," *Applied Physics Letters*, vol. 79, no. 8, pp. 1172–1174, 2001.
- [7] P. C. Ma, N. A. Siddiqui, G. Marom, and J. K. Kim, "Dispersion and functionalization of carbon nanotubes for polymer-based nanocomposites: a review," *Composites Part A*, vol. 41, no. 10, pp. 1345–1367, 2010.
- [8] O. Breuer and U. Sundararaj, "Big returns from small fibers: a review of polymer/carbon nanotube composites," *Polymer Composites*, vol. 25, no. 6, pp. 630–645, 2004.
- [9] X. L. Xie, Y. W. Mai, and X. P. Zhou, "Dispersion and alignment of carbon nanotubes in polymer matrix: a review," *Materials Science and Engineering R*, vol. 49, no. 4, pp. 89–112, 2005.
- [10] M. Moniruzzaman and K. I. Winey, "Polymer nanocomposites containing carbon nanotubes," *Macromolecules*, vol. 39, no. 16, pp. 5194–5205, 2006.
- [11] B. Fiedler, F. H. Gojny, M. H. G. Wichmann, M. C. M. Nolte, and K. Schulte, "Fundamental aspects of nano-reinforced composites," *Composites Science and Technology*, vol. 66, no. 16, pp. 3115–3125, 2006.
- [12] P. C. Ma, N. A. Siddiqui, G. Marom, and J. K. Kim, "Dispersion and functionalization of carbon nanotubes for polymer-based nanocomposites: a review," *Composites Part A*, vol. 41, no. 10, pp. 1345–1367, 2010.
- [13] Y. Wang, J. Wu, and F. Wei, "A treatment method to give separated multi-walled carbon nanotubes with high purity, high crystallization and a large aspect ratio," *Carbon*, vol. 41, no. 15, pp. 2939–2948, 2003.
- [14] G. Hu, C. Zhao, S. Zhang, M. Yang, and Z. Wang, "Low percolation thresholds of electrical conductivity and rheology in poly(ethylene terephthalate) through the networks of multi-walled carbon nanotubes," *Polymer*, vol. 47, no. 1, pp. 480–488, 2006.
- [15] F. Du, R. C. Scogna, W. Zhou, S. Brand, J. E. Fischer, and K. I. Winey, "Nanotube networks in polymer nanocomposites: rheology and electrical conductivity," *Macromolecules*, vol. 37, no. 24, pp. 9048–9055, 2004.

- [16] Z. Ounaies, C. Park, K. E. Wise, E. J. Siochi, and J. S. Harrison, "Electrical properties of single wall carbon nanotube reinforced polyimide composites," *Composites Science and Technology*, vol. 63, no. 11, pp. 1637–1646, 2003.
- [17] A. K. Kota, B. H. Cipriano, M. K. Dueterberg et al., "Electrical and rheological percolation in polystyrene/MWCNT nanocomposites," *Macromolecules*, vol. 40, no. 20, pp. 7400–7406, 2007.
- [18] H. Guo, M. L. Minus, S. Jagannathan, and S. Kumar, "Polyacrylonitrile/carbon nanotube composite films," *ACS Applied Materials and Interfaces*, vol. 2, no. 5, pp. 1331–1342, 2010.
- [19] E. J. Ra, K. H. An, K. K. Kim, S. Y. Jeong, and Y. H. Lee, "Anisotropic electrical conductivity of MWCNT/PAN nanofiber paper," *Chemical Physics Letters*, vol. 413, no. 1–3, pp. 188–193, 2005.
- [20] ESDA, *ESD Association Advisory for Electrostatic Discharge Terminology*, ESD Association, 2009.
- [21] Z. Ounaies, C. Park, K. E. Wise, E. J. Siochi, and J. S. Harrison, "Electrical properties of single wall carbon nanotube reinforced polyimide composites," *Composites Science and Technology*, vol. 63, no. 11, pp. 1637–1646, 2003.
- [22] F. Du, R. C. Scogna, W. Zhou, S. Brand, J. E. Fischer, and K. I. Winey, "Nanotube networks in polymer nanocomposites: rheology and electrical conductivity," *Macromolecules*, vol. 37, no. 24, pp. 9048–9055, 2004.
- [23] A. K. Kota, B. H. Cipriano, M. K. Dueterberg et al., "Electrical and rheological percolation in polystyrene/MWCNT nanocomposites," *Macromolecules*, vol. 40, no. 20, pp. 7400–7406, 2007.
- [24] S. H. Liao, C. Y. Yen, C. C. Weng et al., "Preparation and properties of carbon nanotube/polypropylene nanocomposite bipolar plates for polymer electrolyte membrane fuel cells," *Journal of Power Sources*, vol. 185, no. 2, pp. 1225–1232, 2008.
- [25] E. J. Ra, K. H. An, K. K. Kim, S. Y. Jeong, and Y. H. Lee, "Anisotropic electrical conductivity of MWCNT/PAN nanofiber paper," *Chemical Physics Letters*, vol. 413, no. 1–3, pp. 188–193, 2005.

Research Article

The Synthesis of Peculiar Structure of Springlike Multiwall Carbon Nanofibers/Nanotubes via Mechanochemical Method

Sahebali Manafi,¹ Mohammad Reza Rahimpour,² Iman Mobasherpour,²
and Atefeh Soltanmoradi¹

¹Department of Ceramics, Islamic Azad University, Shahrood Branch, Shahrood, Iran

²Materials and Energy Research Center, P.O. Box 14155-4777, Tehran, Iran

Correspondence should be addressed to Sahebali Manafi, ali_manafi2005@yahoo.com

Received 26 September 2011; Accepted 14 April 2012

Academic Editor: Jianyu Huang

Copyright © 2012 Sahebali Manafi et al. This is an open access article distributed under the Creative Commons Attribution License, which permits unrestricted use, distribution, and reproduction in any medium, provided the original work is properly cited.

Mechanochemical (MT) method is one of the methods used for large-scale production of carbon nanotubes/nanofibers. The different peculiar morphologies of carbon allotropes are introduced with an extraordinary structure for the first time by MT method. In this paper, the influence of milling time and annealing temperature on the crystallinity and morphology of the synthesized nanopowders was investigated. Surprisingly, in this investigation, we report the synthesis of springlike multiwalled carbon nanofibers (S-MWCNFs) by a two-step annealing of milled graphite in an Ar atmosphere. On the other hand, the MT method could be used for the preparation of suitable structures with applications in nanocomposite materials, which is an important task in the era of nanotechnology.

1. Introduction

Carbon nanotubes have attracted considerable interest since their discovery by Iijima in 1991 [1]. Carbon nanotubes have aroused great interest recently because of their unique physical properties, which span a wide range from structural to electronic. For example, nanotubes have a low weight and high elastic modulus, and thus they are predicted to be the strongest fibers and widely touted as attractive candidates for use as fillers in composite materials due to their extremely high Young's modulus, stiffness, and flexibility [2–6]. These latter applications will require vast quantities of nanotubes at competitive prices to be economically feasible. Moreover, reinforcing applications may not require ultrahigh purity nanotubes. On the other hand, functionalization of nanotubes to facilitate interfacial bonding within composites will naturally introduce defects into the tube walls; lessening morphologies are needed for specified applications of CNTs. For instance, usually it is needed to prepare knotted CNTs to improve in rich interfacial adhesion, which can lead to nanotube aggregation within the matrix composites. So, there are many methods of producing these nanomaterials,

including electric arc discharge [1, 7], laser evaporation [8], chemical vapor deposition (CVD), catalytic CVD [9–19], hydrothermal treatment [20], and mechanochemical process in which graphite powders were first mechanically ground at room temperature and then annealed at 1400°C [21], but little is known about the possibilities of mechanochemical processing aimed to the synthesis of carbon nanostructures in different conditions. Although significant research progress has been made to synthesize carbon nanomaterials, but developing an easy approach to large-scale production of carbon nanotubes has still been limited to date. On the other hand, most of the synthesizing methods are complicated and uncontrollable. More recently, we have suggested that using washable supported catalysts is accompanied by valuable advantages and with an extraordinary structure [22–28]. Herein, we use an efficient method for the controlled synthesis of multiwall carbon nanotubes/nanofibers by mechanical activation-assisted annealed process. springlike MWCNFs and MWCNTs were fabricated with advantages of mass production, low cost, and high yield without adding any presynthesized Fe/Co/Ni nanocatalysts. Finally, we report a simple and convenient synthesis method of CNFs/CNTs with

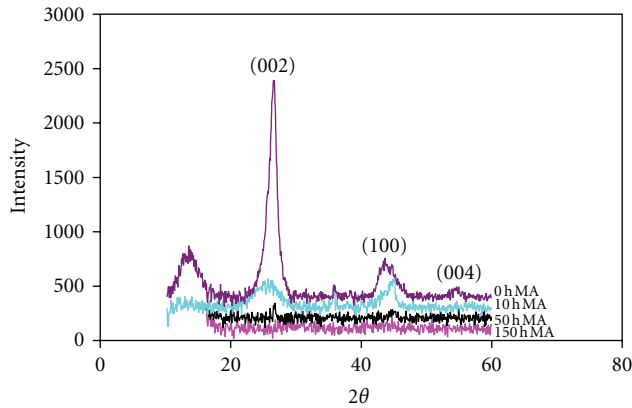
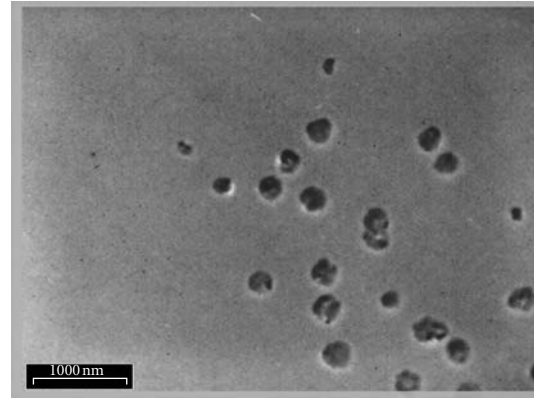


FIGURE 1: The X-ray diffraction spectra of mechanically alloyed graphite powders at different milling times: 0 h, 10 h, 60 h and 160 h.

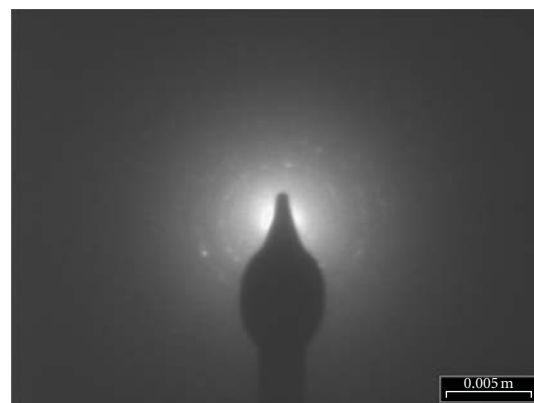
outstanding morphology structure. This method needs no complicated process, relatively low cost and economically.

2. Experimental Procedures

Elemental graphite flakes ($99.9\% < 100 \mu\text{m}$) with a purity of 99.8% were mechanically ground in a purified argon atmosphere. Four grams with ten steel balls of diameter 15 mm were used in the mechanical activation (MA) process. The ball-to-powder weight ratio was kept at 20:1. Mechanical activation was carried out at ambient temperature and at a rotational speed (cup speed) of 700 rpm in a planetary ball mill. The mechanical activation (MA) process was interrupted at regular intervals with a small amount of the MAed powder taken out from the vial to study changes in the microstructures at selected milling duration. On the other hand, mechanical activation was carried out in a planetary ball mill that was directly connected to a closed glove box. In order to avoid oxidization, loading and unloading of powders were operated in a glove box under high pure argon atmosphere. The final gas pressure in the vial was kept to be 0.1 MPa. The Fe/Cr contents of the final sample introduced from the milling media and the starting materials were measured by the inductively coupled plasma (ICP) method. Meanwhile, we removed Fe/Cr contamination by treatment with a 30 mL aqueous solution containing 2 mL of hydrochloric acid (36.5 wt.%), 5 mL of H_2O_2 (30 wt.%), and 20 mL of distilled water ($\text{HCl} : \text{H}_2\text{O}_2 : \text{H}_2\text{O} = 2 : 5 : 20 \text{ V/V}$) at room temperature for 12 h. After full amorphization, one-step and two-step annealing were applied on MAed graphite to investigate the grain growth during the heat treatment. The crystal phase was determined with powder X-ray diffraction. For these experiments, a Siemens diffractometer (30 kV and 25 mA) with the $\text{K}\alpha_1$ radiation of copper ($\lambda = 1.5406 \text{ \AA}$), was used. The structural and compositional information of the product materials was obtained with scanning electron microscopy (SEM, Philips XL30), energy dispersive X-ray spectroscopy (SEM/EDX, XL30), field emission transmission electron microscopy, and selected area electron diffraction (FETEM/SAED, Philips CM200 transmission electron



(a)



(b)

FIGURE 2: Mechanically milled powder by a mechanical activation via planetary mill: (a) transmission electron microscope (TEM) and (b) selected area electron diffraction pattern (SAED).

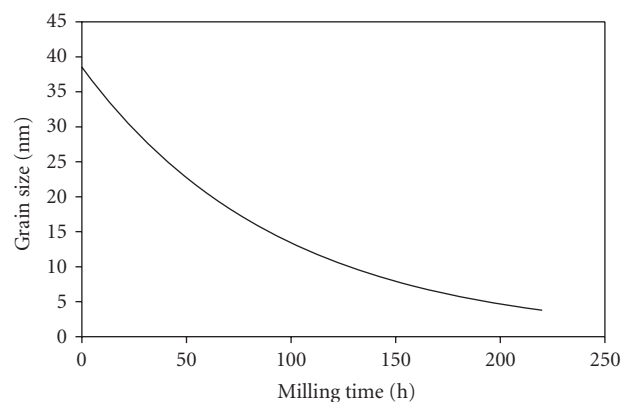


FIGURE 3: The grain size of graphite as function of mechanical activation times.

microscope operated at 200 kV). Specific surface areas (SSAs) of carbon/carbon nanotubes were also measured by the Brunauer-Emmett-Teller (BET) method. The BET surface areas, S_{BET} , of the samples were determined from N_2 adsorption-desorption isotherms obtained at 77 K using an

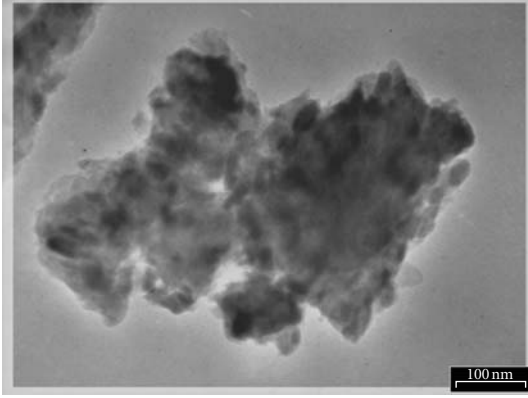


FIGURE 4: MAed graphite powders for 150 h in argon gas atmosphere.

ASAP 2010 surface area analyzer. The Brunauer-Emmett-Teller (BET) method is the most widely used procedure for the determination of the surface areas of solid materials and involves the use of the BET equation:

$$\frac{1}{W[(P_0/P) - 1]} = \frac{1}{W_m C} + \frac{C - 1}{W_m C} \left(\frac{P}{P_0} \right), \quad (1)$$

in which W is the weight of gas adsorbed at a relative pressure of P/P_0 , and W_m is the weight of adsorbate constituting one monolayer of surface coverage. The term C , the BET C constant, is related to the energy of adsorption in the first adsorbed layer, and consequently, its value is an indication of the magnitude of the adsorbent-adsorbate interactions. When the range of P/P_0 is 0.05–0.35, a line will be obtained. Through the slope and intercept, the adsorbate monolayer saturation amount (V_m) can be obtained. The BET surface area equation is

$$S_{\text{BET}} = V_m N_0 \frac{\sigma}{22400 W}, \quad (2)$$

where N_0 is Avogadro's number and σ is the cross-sectional area of a single molecule. Raman spectra were taken at room temperature under ambient condition using an Almega Raman spectrometer with an Ar^+ at an excitation wavelength of 514.5 nm. The crystalline size, D , was estimated by Williamson-Hall [29]:

$$\beta \cos \theta = 2\varepsilon \sin \theta + 0.9 \frac{\lambda}{D}, \quad (3)$$

where λ is the wavelength of the X-ray, β the full width at half maximum (FWHM), θ the Bragg angle, and ε the micro-strain.

3. Results and Discussion

XRD patterns of graphite powder mechanically mixed in argon atmosphere for several activation times are shown in Figure 1. Further milling (after 150 h MA) caused no change in XRD patterns except the broadening of the peaks. So, this broadening can be attributed to the decrease of grain size and

increasing of strain in the lattice. In general, we can conclude that this method is a very successful method for amorphous of graphite powders by mechanical activation (MA).

The constitution of this starting powder corresponds to the elemental graphite powder and so, the diffraction intensities drastically decreased after mechanical activation (MA). The diffraction peaks corresponding to the graphite (particularly the peak at about $2\theta = 26.6^\circ$) almost disappeared at an activating time of 10 h. The crystallite size of the graphite after mechanical activation for 5 h is approximately $D = 30.1$ nm, where that before MA is approximately $D = 31.1$ (Table 1). An additional MA process in the argon atmosphere (Figure 1) in which, diffraction intensities corresponding to the graphite decrease gradually with increasing activating time at the diffraction peaks at around $2\theta = 26.6^\circ$ cannot be eliminated after an activating time of 100 h, suggesting that the formation of an amorphous-like phase or very fine particles has been strongly enhanced in the argon atmosphere after an activating time of 150 h. Figure 2 shows the transmission electron micrograph (Figure 2(a)) and selected area electron diffraction pattern (Figure 2(b)) of graphite nanostructures synthesizing according to the method described previously. It is readily observed that the nanostructures are in a high ultrafine dispersion and the average crystalline size is 10 nm. The electron diffraction (ED) pattern of the MAed graphite (Figure 2(b)) exhibits two very weak diffuse rings, indicating highly disordered wall in milled graphite. On the other hand, the electron diffraction pattern reveals that the carbon nanostructures have an amorphous structure. At the same time, this result is consistent with the X-ray diffraction (XRD) pattern. We believe that the very small size and the amorphous structure are due to the high-energy ball milling of the graphite powders activated by planetary mill. Also, Jiang and Chen [30] recently developed a thermodynamic quantitative model to describe the phase transitions of nanocarbon as functions of its size and temperature through systematically considering the effects of surface stresses and surface energies. The fine nanosize amorphous structure of pure carbon nanostructures is thermodynamically unstable, owing to the high amount of free energy. Therefore, crystallization at a temperature regime might be expected.

The milled powders had an average crystallite size of about 5–10 nm as determined by the Williamson-Hall method as shown in Table 1 and Figure 3. Crystallite size values determined in this way may be low when the concentration of defects in the sample is higher compared to that in the reference large-particulate powder. The BET areas are strongly different for all samples and between 5.5 and 211.2 m^2/g as presented in Table 1. In the steady state, the BET surface area of the MAed powders was determined at about 211.2 m^2/g for several samples (C_{200} , C_{210} , C_{220} , etc.).

D is the average crystallite size, determined by the Williamson-Hall; SA is the specific surface area, determined by the BET-method.

Measuring the surface area of carbon nanostructures via nitrogen adsorption by Brunauer-Emmett-Teller (BET) method revealed a specific surface area of 211.2 m^2/g which seems relevant for surface area dependent applications such

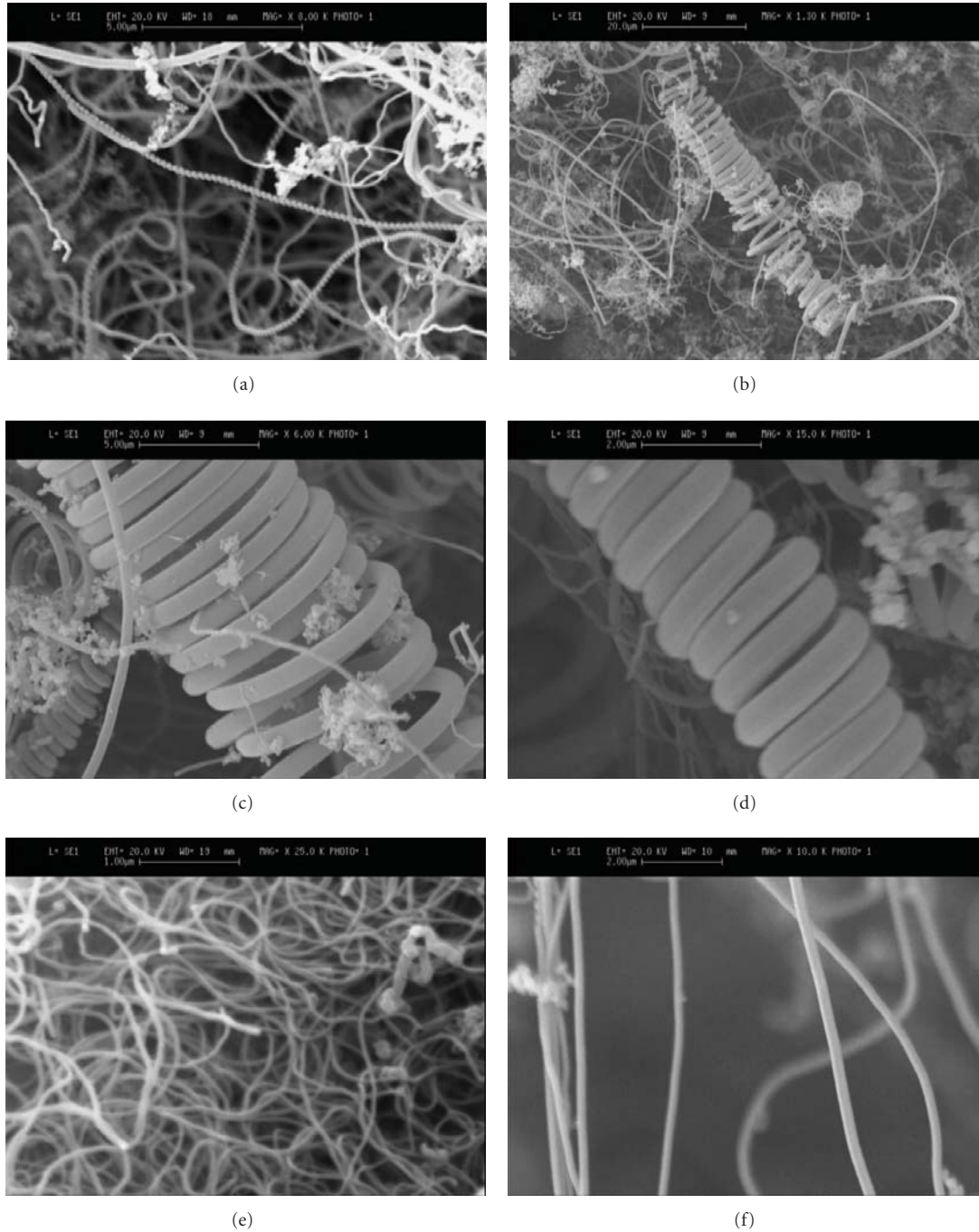


FIGURE 5: SEM images of MAed graphite powders for 150 h after one-step and two-step annealing with different morphologies: (a) high yield springlike MWCNFs (two-step), (b) individual MWCNFs with ultrahigh aspect ratio (two-step), (c) springlike MWCNFs encapsulated with carbon nanotubes (two-step), (d) S-MWCNF with an ultrahigh crystallinity structure (two-step), (e) high yield springlike MWCNTs (one-step), and (f) aligned arrays of MWCNTs (one-step).

as diffusion process. Assuming that all particles have spherical and theoretical density and form $d_{\text{BET}} = 6/S \cdot \rho$, where S is the surface area and ρ is the particle density (2.1 g/cm^3 for graphite), a BET particle diameter, d_{BET} , of about 20 nm is found for these nanoparticles. At the same time, these results are consistent with the HRTEM image

observations. Therefore, the obtained results of specific area (SA), crystallite size (D) for milled graphite indicate that graphite particles are highly chemically active.

According to TEM micrographs of the powders mechanically milled for 150 h in argon gas atmosphere shown in Figure 4, MAed powders are an ultrafine spherical particle

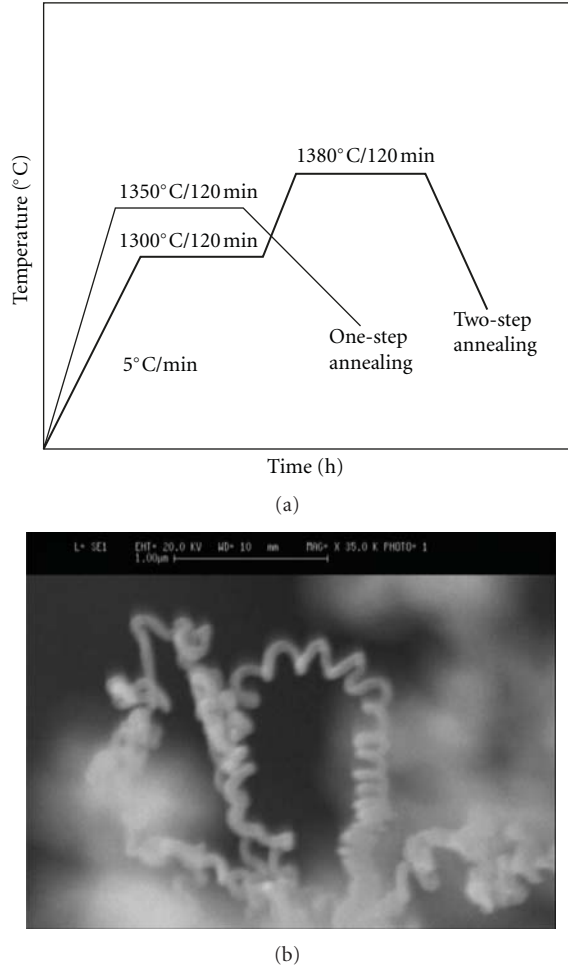


FIGURE 6: (a) Schematic diagram of annealing patterns to synthesize MWCNTs/S-MWCNFs by mechanochemical method and (b) S-MWCNTs with ultrahigh flexible and toughness.

powder with approximately 100 ± 20 nanometers in size. Because of highly chemically active carbon atoms, these are strongly agglomerated.

Interestingly, Figures 5(a)–5(f) show the SEM different images of MAed graphite powders (the sample of C_{150}) after one-step and two-step annealing. On the other hand, the heating program is indicated in Figure 6(a). A two-step annealing procedure was applied; that is, the samples were first heated to 1300°C at rate of 5°C/min and held there for 120 min, and they were then further heated to 1380°C at a rate of 5°C/min and held there for 120 h under Ar atmosphere. Furthermore, the usage of a two-step annealing condition and a suitable mechanical activation are the two crucial keys in ensuring the formation of S-MWCNFs under the mechanochemical method. However, until now the role of annealing for the formation of S-MWCNFs is not clear. SEM observations in a wide field show that the powders prepared with the heat-treated (C_{150}) contain much more nanotubes/nanofibers with peculiar structure namely, springlike multiwall carbon nanofibers (S-MWCNFs). The nanotubes

TABLE 1: Characteristic of different samples used to investigate during milling.

Milling time (h)	Sample (Id)	S. A. (m^2/g)	Crystallite size = D (nm)
0	C_0	5.5	31.1
5	C_5	21.2	30.1
10	C_{10}	25.8	29.8
30	C_{30}	35.1	27.4
50	C_{50}	45.6	25.4
60	C_{60}	50.1	24.6
80	C_{80}	62.5	22.1
90	C_{90}	70.2	20.1
100	C_{100}	78.9	18.5
120	C_{120}	115.2	13.9
130	C_{130}	145.2	11.2
140	C_{140}	175.5	8.5
150	C_{150}	200.5	5.2
160	C_{160}	205.5	4.9
170	C_{170}	207.4	4.8
180	C_{180}	209.1	4.7
190	C_{190}	209.5	4.8
200	C_{200}	211.2	4.8
210	C_{210}	211.2	4.8
220	C_{220}	211.2	4.8

are knotted and stretchy in appearance and are mainly S-MWCNFs (for two-step annealing in Figure 5(a)) which will be demonstrated later. In the SEM observation of C_{150} , a few multiwall carbon nanotubes (MWCNTs) were sporadically observed (for one-step annealing in Figure 5(e)). However, for the samples C_{70} , C_{90} , and C_{100} , no CNTs or CNFs were found in all observations after suitable annealing. A detailed study of the growth mechanism of the S-MWCNFs is underway. The interesting structure and physical properties (high aspect ratio ca. 1000 and low density) of the S-MWCNFs make it an obvious choice as obvious applications. In this way, Figure 6(b) shows that an individual MWCNF with a suitable aspect ratio was bent like a spring but still was not broken, indicating that the fiber is very flexible and tough for reinforcement in nanocomposite materials. Finally, in this investigation, an effective method was developed for the formation of ultracrystallinity S-MWCNTs and MWCNTs. As a matter of fact, the MT method guarantees production of CNT/CNF for different applications.

Meanwhile, TEM images of mechanically activated graphite powders after a one-step and two-step annealing are shown in Figures 7(a)–7(d). In Figures 5(a) and 5(b), many S-MWCNFs can be observed, which is consistent with the SEM observation. By TEM observation, we have found that most of nanofibers in the annealed powders are S-MWCNTs (for two-step annealing). Also, we confirmed that synthesized MWCNTs have fibrous structures with ultrahigh uniform grade (Figures 7(c) and 7(d)).

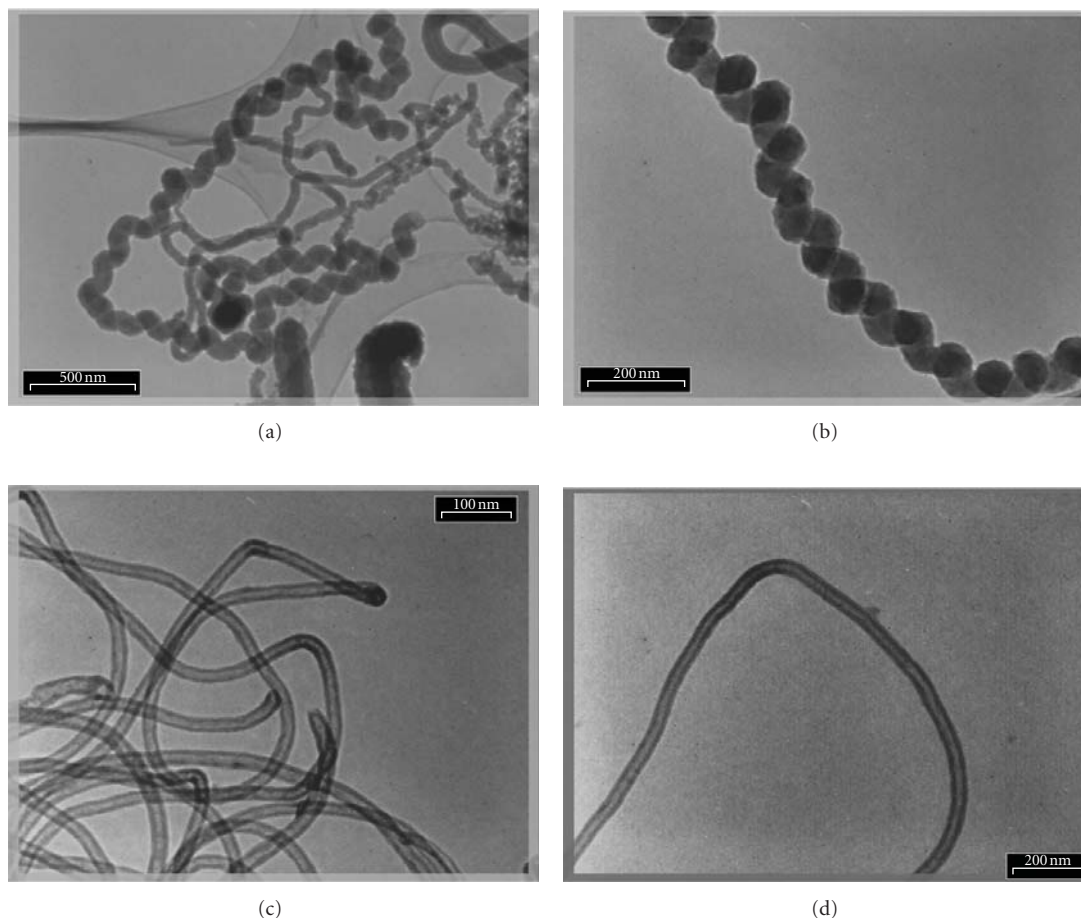


FIGURE 7: TEM images of MAed graphite powders for 150 h after one-step and two-step annealing with different morphologies: (a) springlike MWCNFs encapsulated with carbon nanotubes (two-step), (b) individual MWCNFs (two-step), (c) MWCNTs with an ultrahigh crystallinity structure (one-step), and (d) individual MWCNTs with narrow channels (one-step).

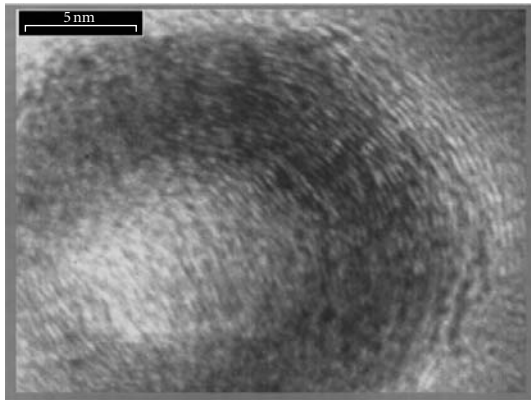
The selected area electron diffraction (SAED) pattern (Figure 8(a)) exhibits a pair of weak rings but strong spots for (002), together with a ring for (100) and a pair of weak arcs for (004) diffractions. The appearance of (002) diffractions as a pair of spots indicates some orientation of the (002) planes in the carbon tubes [31]. The yield of the prepared MWCNTs estimated by TEM observations is about 95% relative to the samples on copper grids, and the much less contents of the obtained product are nanoparticles. Thus, the high yield efficiency of this approach for the synthesis of MWCNT can be concluded, with an ultrahigh crystallinity and an excellent yield rather than previous works. In further investigation, the MWCNTs were analyzed by HRTEM in detail, and all nanostructures showed uniform lattice fringes, meaning that no amorphous product was formed. Figure 8(b) is the HRTEM image of a single CNT, which clearly indicates that the CNT structurally is a uniform structure with ultrahigh crystallinity. The interplanar spacing values are calculated from Bragg's diffraction equation using the diffraction ring diameter and the camera length of the transmission electron microscope. The calculated results indicate the interlayer

spacing in the walls, about 0.34 nm, corresponds to the 002 distance of graphitic carbon. The EDS spectrum of the carbon nanotube shows that these are fully elemental carbon except the elements of Ni, P, and Cu, which come from the supported grid for TEM measurement (Figure 8(c)).

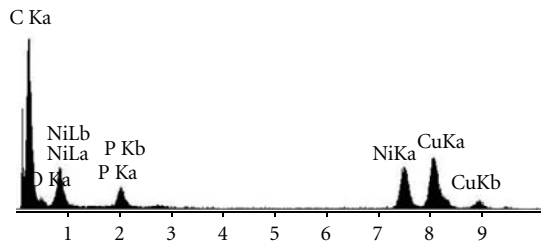
The most important feature of this specific structure is related to the formation of springlike MWCNF structure. It is difficult to distinguish individual walls and graphite sheets in TEM images and even HRTEM images. XRD was performed on the annealed powder. XRD investigation (Figure 9) provided a possible model for the structure of such springlike structure. According to the XRD pattern of the sample, it is obvious that the peak of (100) is as broadening as common peak of graphite in recrystallised carbon powder, that is, (002). This indicates that the nanotubes walls are not constructed from graphite sheets. This is not the ideal hexagonal graphite as it is also oriented in c-axis parallel to the diamond anvil cell axis and suggests polytype modifications of graphite in the springlike structure. This hypothesis provides a strong reason for the formation of such outstanding structure making the springlike carbon



(a)



(b)



(c)

FIGURE 8: Images of MAed graphite powders for 150 h after annealing at 1350°C for 2 h: (a) the SAED pattern of the obtained MWCNTs, (b) HRTEM, and (c) energy dispersive spectroscopy (EDS) of the purified carbon nanotubes.

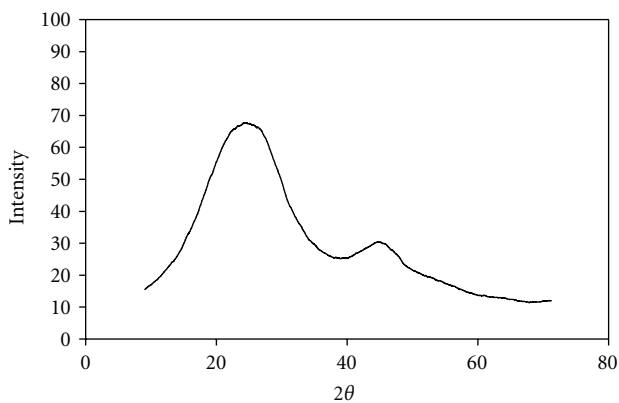


FIGURE 9: XRD Pattern of the springlike MWCNFs.

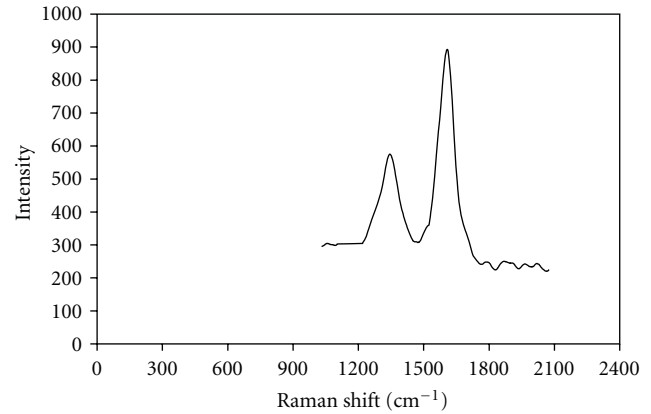


FIGURE 10: Raman spectra of the obtained MWCNTs.

nanofibers; however, the mechanism of such structure under specified mechanothermal condition is still unclear which is under investigation.

The Raman spectrum shows the D- and G-bands at 1350 and 1670 cm^{-1} , respectively. As shown before [31], the D-band is representative for the disordered carbon structures and defects, while the G-band shows the graphitization and the crystalline properties of the nanofibers/nanotubes. The graphite-related tangential G-band [32] at 1670 cm^{-1} was derived from Raman-allowed optical mode, which is related to vibration in all sp^2 carbon materials. The disorder-induced D-band [33] around 1350 cm^{-1} from the Raman spectra of sp^2 -bonded carbon materials is strongly dispersive as a function of laser excitation energy (E_{laser}). Generally, the ratio between the intensity of the G-band and D-band (I_G/I_D) can be used to show the structural defect and disordered carbon materials in a few micrometers scale. The I_G/I_D ratio obtained (see Figure 10) was relatively high compared with that of about 2.5. The I_G/I_D high ratio indicates the high purity of the present specimen.

4. Conclusion

In summary, we have successfully developed a controlled and specific method for synthesizing springlike MWCNFs and MWCNTs via a mechanothermal (MT) process. The versatility of this simple approach can be extended beyond nanotechnological purposes to many applications such as reinforcement in nanocomposite materials with desired properties and a suitable aspect ratio for improving mechanical properties. The purity and good quality of CNFs/CNTs obtained by mechanothermal method make suitable synthesis a promising method for the production of multiwall carbon nanotubes or other graphitic nanocarbons with different morphologies.

Acknowledgments

The authors would like to acknowledge Professor Anna Dash from the English Language Randwich community, Sydney, Australia, for helping in improvement of English of this paper and Mr. Jabbari for performing the experimental tests.

References

- [1] S. Iijima, "Helical microtubules of graphitic carbon," *Nature*, vol. 354, no. 6348, pp. 56–58, 1991.
- [2] M. Ouyang, J. L. Huang, and C. M. Lieber, "Fundamental electronic properties and applications of single-walled carbon nanotubes," *Accounts of Chemical Research*, vol. 35, no. 12, pp. 1018–1025, 2002.
- [3] M. M. J. Treacy, T. W. Ebbesen, and J. M. Gibson, "Exceptionally high Young's modulus observed for individual carbon nanotubes," *Nature*, vol. 381, no. 6584, pp. 678–680, 1996.
- [4] Y. F. Yin, T. Mays, and B. McEnaney, "Adsorption of nitrogen in carbon nanotube arrays," *Langmuir*, vol. 15, no. 25, pp. 8714–8718, 1999.
- [5] D. Li and Y. Xia, "Direct fabrication of composite and ceramic hollow nanofibers by electrospinning," *Nano Letters*, vol. 4, no. 5, pp. 933–938, 2004.
- [6] Y. H. Li, J. Ding, Z. Luan et al., "Competitive adsorption of Pb^{2+} , Cu^{2+} and Cd^{2+} ions from aqueous solutions by multi-walled carbon nanotubes," *Carbon*, vol. 41, no. 14, pp. 2787–2792, 2003.
- [7] D. S. Bethune, C. H. Kiang, M. S. De Vries et al., "Cobalt-catalysed growth of carbon nanotubes with single-atomic-layer walls," *Nature*, vol. 363, no. 6430, pp. 605–607, 1993.
- [8] T. Guo, P. Nikolaev, A. Thess, D. T. Colbert, and R. E. Smalley, "Catalytic growth of single-walled nanotubes by laser vaporization," *Chemical Physics Letters*, vol. 243, no. 1-2, pp. 49–54, 1995.
- [9] Y. M. Shyu and F. Chau-Nan Hong, "The effects of pretreatment and catalyst composition on growth of carbon nanofibers at low temperature," *Diamond and Related Materials*, vol. 10, no. 3–7, pp. 1241–1245, 2001.
- [10] J. M. Ting and N. Z. Huang, "Thickening of chemical vapor deposited carbon fiber," *Carbon*, vol. 39, no. 6, pp. 835–839, 2001.
- [11] M. Ritschel, M. Uhlemann, O. Gutfleisch et al., "Hydrogen storage in different carbon nanostructures," *Applied Physics Letters*, vol. 80, no. 16, pp. 2985–2987, 2002.
- [12] V. Ivanov, J. B. Nagy, P. Lambin et al., "The study of carbon nanotubules produced by catalytic method," *Chemical Physics Letters*, vol. 223, no. 4, pp. 329–335, 1994.
- [13] V. Vinciguerra, F. Buonocore, G. Panzera, and L. Occhipinti, "Growth mechanisms in chemical vapour deposited carbon nanotubes," *Nanotechnology*, vol. 14, no. 6, pp. 655–660, 2003.
- [14] E. Couteau, K. Hernadi, J. W. Seo et al., "CVD synthesis of high-purity multiwalled carbon nanotubes using $CaCO_3$ catalyst support for large-scale production," *Chemical Physics Letters*, vol. 378, no. 1-2, pp. 9–17, 2003.
- [15] D. Lupu, A. R. Biriş, A. Jianu et al., "Carbon nanostructures produced by CCVD with induction heating," *Carbon*, vol. 42, no. 3, pp. 503–507, 2004.
- [16] A. Okamoto and H. Shinohara, "Control of diameter distribution of single-walled carbon nanotubes using the zeolite-CCVD method at atmospheric pressure," *Carbon*, vol. 43, no. 2, pp. 431–436, 2005.
- [17] L. Piao, Y. Li, J. Chen, L. Chang, and J. Y. S. Lin, "Methane decomposition to carbon nanotubes and hydrogen on an alumina supported nickel aerogel catalyst," *Catalysis Today*, vol. 2, no. 74, pp. 145–155, 2002.
- [18] M. Yudasaka, R. Kikuchi, T. Matsui, Y. Ohki, S. Yoshimura, and E. Ota, "Specific conditions for Ni catalyzed carbon nanotube growth by chemical vapor deposition," *Applied Physics Letters*, vol. 67, pp. 2477–2479, 1995.
- [19] M. M. Shaijumon and S. Ramaprabhu, "Synthesis of carbon nanotubes by pyrolysis of acetylene using alloy hydride materials as catalysts and their hydrogen adsorption studies," *Chemical Physics Letters*, vol. 374, no. 5-6, pp. 513–520, 2003.
- [20] J. M. C. Moreno and M. Yoshimura, "Hydrothermal processing of high-quality multiwall nanotubes from amorphous carbon," *Journal of the American Chemical Society*, vol. 123, no. 4, pp. 741–742, 2001.
- [21] Y. Chen, M. J. Conway, and J. D. Fitzgerald, "Carbon nanotubes formed in graphite after mechanical grinding and thermal annealing," *Applied Physics A*, vol. 76, no. 4, pp. 633–636, 2003.
- [22] S. Manafi, H. Nadali, and H. R. Irani, "Low temperature synthesis of multi-walled carbon nanotubes via a sonochemical/hydrothermal method," *Materials Letters*, vol. 62, no. 26, pp. 4175–4176, 2008.
- [23] A. Eftekhari, S. Manafi, and F. Moztafzadeh, "Catalytic chemical vapor deposition preparation of multi-wall carbon nanotubes with cone-like heads," *Chemistry Letters*, vol. 35, no. 1, pp. 138–139, 2006.
- [24] V. Bajpai, L. Dai, and T. Ohashi, "Large-scale synthesis of perpendicularly aligned helical carbon nanotubes," *Journal of the American Chemical Society*, vol. 126, no. 16, pp. 5070–5071, 2004.
- [25] X. Chen, S. Yang, Y. Kato, and S. Motojima, "Influence of CVD conditions on the growth of carbon microcoils with circular cross-sections," *Materials Letters*, vol. 61, no. 14-15, pp. 2900–2903, 2007.
- [26] S. Yang, X. Chen, S. Motojima, and M. Ichihara, "Morphology and microstructure of spring-like carbon micro-coils/nanocoils prepared by catalytic pyrolysis of acetylene using Fe-containing alloy catalysts," *Carbon*, vol. 43, no. 4, pp. 827–834, 2005.
- [27] S. Yang, M. Hasegawa, X. Chen, and S. Motojima, "Synthesis and morphology of carbon microcoils produced using methane as a carbon source," *Carbon*, vol. 45, no. 7, pp. 1592–1595, 2007.
- [28] X. Chen, S. Yang, S. Motojima, and M. Ichihara, "Morphology and microstructure of twisting nano-ribbons prepared using sputter-coated Fe-base alloy catalysts on glass substrates," *Materials Letters*, vol. 59, no. 7, pp. 854–858, 2005.
- [29] G. K. Williamson and W. H. Hall, "X-ray line broadening from filed aluminium and wolfram," *Acta Metallurgica*, vol. 1, no. 1, pp. 22–31, 1953.
- [30] Q. Jiang and Z. P. Chen, "Thermodynamic phase stabilities of nanocarbon," *Carbon*, vol. 44, no. 1, pp. 79–83, 2006.
- [31] W. Wang, S. Kunwar, J. Y. Huang, D. Z. Wang, and Z. F. Ren, "Low temperature solvothermal synthesis of multiwall carbon nanotubes," *Nanotechnology*, vol. 16, no. 1, pp. 21–23, 2005.
- [32] C. J. Lee, J. Park, Y. Huh, and J. Yong Lee, "Temperature effect on the growth of carbon nanotubes using thermal chemical vapor deposition," *Chemical Physics Letters*, vol. 343, no. 1-2, pp. 33–38, 2001.
- [33] M. S. Dresselhaus, G. Dresselhaus, A. Jorio, A. G. Souza Filho, and R. Saito, "Raman spectroscopy on isolated single wall carbon nanotubes," *Carbon*, vol. 40, no. 12, pp. 2043–2061, 2002.

Research Article

Study on Carbon Nanocomposite Counterelectrode for Dye-Sensitized Solar Cells

Yiming Chen, Haiyan Zhang, Yuting Chen, and Jiapeng Lin

Faculty of Material and Energy, Guangdong University of Technology, Guangzhou 510006, China

Correspondence should be addressed to Yiming Chen, chenym@gdut.edu.cn

Received 22 October 2011; Accepted 23 March 2012

Academic Editor: Teng Li

Copyright © 2012 Yiming Chen et al. This is an open access article distributed under the Creative Commons Attribution License, which permits unrestricted use, distribution, and reproduction in any medium, provided the original work is properly cited.

Carbon nanocomposite electrodes were prepared by adding carbon nanotubes (CNTs) into carbon black as counterelectrodes of dye-sensitized solar cells (DSSCs). The morphology and structure of carbon nanocomposite electrodes were studied by scanning electron microscopy. The influence of CNTs on the electrochemical performance of carbon nanocomposite electrodes is investigated by cyclic voltammetry and electrochemical impedance spectroscopy. Carbon nanocomposite electrodes with CNTs exhibit a highly interconnected network structure with high electrical conductivity and good catalytic activity. The influence of different CNTs content in carbon nanocomposite electrodes on the open-circuit voltage, short-circuit current, and filling factor of DSSCs is also investigated. DSSCs with 10% CNTs content exhibit the best photovoltaic performance in our experiments.

1. Introduction

Since the technological breakthrough of dye-sensitive solar cells (DSSCs) in 1991, a great deal of progress has been made in various aspects ranged from main critical materials constituting DSSCs to the related manufacturing technologies, which covers both fundamental studies on DSSCs with small area and large-scaled industry researches.

The current studies on DSSCs are mainly focused on dye synthesis [1, 2], electron transfer kinetics [3], photoanode [4–7], solid (or quasi-solid) electrolyte [8–10], and so forth, while the specific researches on counterelectrodes (CEs) are relatively rare. As an important part of dye-sensitive solar cell, counterelectrode usually consists of conductive glass loaded with platinum or carbon as catalysts, which can enhance the charge transfer between the CE and electrolyte interface, decrease the recombination possibility of I_3^- and the electrons in the conduction band of TiO_2 , restrain the dark current, and consequently improve the open circuit voltage (V_{oc}) [11, 12]. So far, the platinum (or other precious metals) CEs have superior performance and thoroughly theoretical research, but they cannot be applied in large due to their high cost. Carbon, one low cost but high efficient catalyst [13, 14], can be used in CEs, and after high temperature treatment, the photoelectric properties of carbon CEs approach those

of platinum CEs. Carbon and its mixtures can contact well with the substrate at low temperature, which facilitates the manufacture of large-scaled electrodes, thus having a promising application prospect.

Ramasamy et al. [15] used spray-coated multiwall carbon nanotubes (CNTs) film on fluorine-doped tin oxide glass as CEs, and got a maximum energy conversion efficiency of 7.59% under one sun illumination (100 mW cm^{-2} , AM1.5G). Furthermore, electrochemical impedance spectroscopy analysis indicated a decrease in the charge transfer resistance of multiwall CNT CEs with increase of spraying time. Lee et al. [16, 17] made CEs for DSSCs by nanocarbon powder, which received a 7.56% photoelectric conversion efficiency, after 60 days of aging in dark room, the photoelectric conversion efficiency still remained 6.35% (i.e., 84% of its initial day efficiency (η)), with increases of open-circuit voltage (V_{oc}) and fill-factor (FF) but a decrease of short-circuit current density (J_{sc}). Murakami et al. [18] fabricated carbon CEs by using carbon black, under AM1.5 illumination simulation achieving a photoelectric conversion efficiency (η), short-circuit current density (J_{sc}), open-circuit voltage (V_{oc}), and fill-factor (FF) up to 9.1%, 16.8 mA/cm², 798 mV, and 68.5%, respectively. As is well known that the fill-factor (FF) depends on the thickness of the carbon layer,

when the thickness is less than 10 μm , the photoelectric conversion efficiency (η) improves as the thickness increases and the impedance decreases as the carbon layer thins. Huang et al. [19] manufactured CEs consisting of hard carbon spherules (HCSs), and the total photoelectric conversion efficiency (η) was 5.7%, while that of platinum CEs under the same circumstance was 6.5%. Trancik et al. [20] believe that CNTs can provide accreted locations for reagents due to their microdefects and offer excellent catalytic effect when serving as CEs for DSSCs.

Nevertheless, at present researches on carbon nanocomposite CEs for DSSCs and the corresponding synergistic effect are rarely reported. In this paper, multiwall carbon nanotubes (MWCNTs) were added into nanocarbon black, and the related influence on the catalytic activity of carbon CEs were investigated as well.

2. Experimental Procedure

2.1. Electrode Plate Fabrication

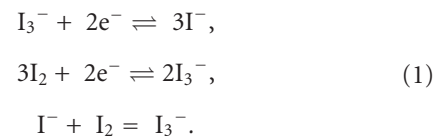
2.1.1. Counterelectrode Fabrication. Carbon nanotubes (99.9%, diameters: 40–60 nm, Shenzhen Nanotechnologies Co. Ltd, China) were added into nanocarbon black (99.9%) with the mass fraction 30%, 15%, 10%, 5%, 0%, and marked as sample A, B, C, D, and E, respectively. To enhance the dispersity of CNTs, a spot of emulsifying agent (Tianjin FuChen Chemistry Ltd., China) was added into above samples, and acetylacetone as pore-forming agent to enlarge the interface between electrode and electrolyte, with ethyl cellulose as adhesive. The mass ratio of CNTs, nanocarbon black, ethyl cellulose, emulsifying agent, and acetylacetone was $x: 1: 0.125: 0.1: 0.1$ (x altered from 0.3, 0.15, 0.1, 0.05 to 0), and appropriate amount of butanone was introduced as solvent. The mixture solutions were dispersed by ultrasonic cleaning to obtain homogeneous suspensions. Finally, a specific amount of the suspension was dropped onto the FTO glass, and then dried under room temperature for 1 h. The CEs plates for DSSCs were prepared with the dimension 8 mm \times 8 mm. Under the protection of nitrogen, the as-prepared electrode plates were heated at 450°C, 600°C, 800°C for 30 minutes, respectively.

2.1.2. Photoanode Plate Fabrication. The mixture comprising of 3 g nano-TiO₂ powder (Germany Degussa Ltd.), 10 mL ethanol together with 0.5 mL emulsifying agent and acetylacetone was ultrasonically dispersed to homogeneous TiO₂ suspension of proper viscosity. A specific amount of the suspension was dropped onto FTO glass, and then the FTO glass was dried under room temperature for 1 h and then heated at 450°C in atmosphere for 30 minutes. Once the as-obtained TiO₂ plate was cooled, the TiO₂ suspension was once again dropped onto it, and the same drying and heating as mentioned above were sequently conducted. After 3 or 4 time repetitions of the same procedure, TiO₂ multilayer membrane electrode plates were obtained with the dimension of 8 mm \times 8 mm, the same as that of the CE plate.

2.2. Electrochemical Performance Testing

2.2.1. Carbon Electrodes Catalytic Performance and Interface EIS Testing. The testing system consisted of nanocarbon electrode, platinum (PT) electrode, and electrolytic cell. The testing electrolyte was the mixture of KI and I₂ ($[\text{I}^-]: [\text{I}_2] = 10:1$), 0.1 M KCL as supporting electrolyte. The mixed solution of 25% anhydrous alcohol and 75% deionized water was used to improve iodine solubility. PT electrode served as the cathode.

The electrochemical reaction process of this electrolytic cell is shown in the following equations:



The reaction mechanism is as follows: I₃⁻ and I₂ are deoxidized near the cathode and oxidized near the anode. The reduction of I₃⁻ and I₂ dominates the whole electrochemical process. The more active the electrode material is, the stronger the reduction of I₃⁻ and I₂, and the better catalytic reduction performance for CEs is.

CHI660C electrochemical working station (Shanghai ChenHua instrument Ltd, China) was employed for C-V characteristic curve and EIS testing.

C-V characteristic curve: measuring the reduction performance of CEs for I₃⁻, I₂ (such as reduction potential, reduction current density). Testing conditions: initial potential 1.5 V, high potential 1.5 V, low potential 0 V, and scan rate 1–100 mV/s.

EIS testing: 0.6 V initial potential was applied to simulate illumination for DSSCs and then test the interface impedance between the electrolyte and the carbon electrode. Testing conditions: initial potential 0.6 V, high frequency 100000 Hz, low frequency 1 Hz, and amplitude 0.005 V. The test data were fitted by ZView2 software.

2.2.2. DSSCs Photoelectric Properties and EIS Testing. A solar simulator (xenon lamp, AM1.5, 100 mW/cm², calibrated by silicon standard solar cell, facular area 30 cm \times 30 cm, intensity unhomogeneity less than 3%), and Keithley 2400 Source Meter were performed, testing parameters of the cell, such as I-V characteristic curve, open-circuit voltage, short-circuit current density. Testing conditions: initial potential 0 V, high potential 0.8 V, the quantity of measuring points 150.

EIS testing was employed by using CHI660C electrochemical working station, testing the complex impedance to obtain the CT impedance of CEs and electrolyte. Testing conditions: initial potential 0.6 V, high frequency 100000 Hz, low frequency 1 Hz, amplitude 0.005 V. The test data was fitted by ZView2 software.

3. Results and Discussion

3.1. Surface Morphology Analysis of Electrodes. Scanning electron microscope (SEM, S-3400N) was employed to characterize the surface morphology of composite electrodes, and the SEM images of composite electrodes before and after thermal treatment were shown in Figures 1(a) and 1(b). It can be found in Figure 1(a) that, before thermal treatment, CNTs with the diameter 40–60 nm distributes near the carbon black, and the adhesive (ethyl cellulose) remains on the surface of carbon black, which decreases the contacting area between the carbon black and electrolyte, consequently affecting the corresponding catalytic performance. Figure 1(b) is the SEM image of composite electrode after 600°C thermal treatment under nitrogen atmosphere, indicating that the ethyl cellulose distributed between carbon black and CNTs surface decreases greatly. Furthermore, CNTs forms a network, to which carbon black evenly adheres, building a “grape cluster” structure and then getting a synergistic effect. After thermal treatment the outer diameters of CNTs decrease obviously. Due to high conductivity of CNT, electrons can conduct via the CNTs network distributed on the electrode film, which effectively enhances the conductivity of the electrodes. Moreover, the carbon black adhered to CNTs could enlarge the contacting area with the electrolyte, resulting in an increase of catalytic performance.

3.2. Electrochemical Performance Testing Results

3.2.1. Effects of CNTs Addition on the Reduction of I_3^-/I^- . At the scan rate 1–100 mV/s, the current density peak curves of PT CEs and CNTs-nanocarbon black composite CEs are shown in Figure 2. By the comparison of the reduction current peak of I_3^- and I_2 at different scan rates, it is revealed that current densities are all approximately in direct ratio with the square root of scan rates, which indicates that the total reaction rate depends on the ion diffusion in the electrolyte rather than the reduction rate of the ions absorbed onto the electrode surface. Among the reactions taken place on the electrode surface, the required potential of $I_3^- + 2e^- = 3I^-$ is higher than that of $3I_2 + 2e^- = 2I_3^-$, namely I_3^- is much more difficult to deoxidize than I_2 . However, the transmission (or diffusion) rate of electrons and ions within electrodes is less than the reduction rate of ions on the electrode surface, thus the diffusion of I_3^- is the determinant of CEs activity.

We can also find in Figure 2 that, at the same scan rate, composite carbon electrode with CNTs has a bigger reduction current density for I_3^- than that of PT electrode, on the other hand, the reduction current density for I_2 is smaller than that of PT electrode. The above results indicates that composite electrodes have stronger reduction for I_3^- than PT electrodes, but when it comes to the reduction for I_2 , the situation is totally opposite.

Figure 3 reveals the curves of the electrochemical catalytic performance of CEs versus the adding amount of CNTs. CEs with CNTs adding weight of 30%, 15%, 10%, 5%, and 0% enable I_2 with reduction potentials of -0.41 ,

-0.44 , -0.51 , -0.57 , and -0.59 V sequentially, as well as the reduction current density 4.98, 5.37, 4.68, 4.41, and 2.78 mA, respectively. Meanwhile, the corresponding parameters for I_3^- are similarly -0.77 , -0.83 , -0.92 , -0.96 and -0.92 V together with 5.82, 6.04, 5.31, 5.15, 3.44 mA.

It can be concluded that CEs with CNTs have obviously superior catalytic reduction ability to those without. And the catalytic reduction potentials of electrodes decrease after the addition of CNTs.

By adding specific amount of CNTs into counterelectrode, the catalytic performance of CEs is enhanced effectively; however, the enhancement is not direct ratio with the adding amount. We discover that the electrode performance of 15% CNTs adding is better than that of 5% and 10%, nevertheless, when the adding amount reaching 30%, its catalysis declines. Furthermore, once the mass fraction of CNTs in carbon black exceeds 30%, the catalytic reduction potential of electrodes increases and the current density decreases.

3.2.2. Effects of CNTs Addition on Carbon Electrode/Electrolyte Interface Impedance. The electrochemical impedance spectroscopy of nanocarbon electrode at 28°C is displayed in Figure 4, and the electrochemical impedance curves were fitted via the equivalent circuit in Figure 4. When conducting the fit, W , $R(E)$, $CPE(E)$, R_S were set as fixed value in the equivalent circuit model, where $R_{CT}(C)$, $R(E)$, W , R_S stand for the interface impedance between carbon electrode and electrolyte, PT electrode and electrolyte interface, Warburg impedance of electrolyte together with the contact impedance between C, TiO_2 , and FTO. R_{CT} indicates the resistance caused by charge transfer on the electrode surface.

CPE reveals the double-layer capacitance of the interface, with the expression $Z_{CPE} = T(j\omega)^{-P}$ ($0 \leq P \leq 1$). Z_{CPE} has two variables, that is, T and P , to be exactly, T revealing the solid-liquid interface capacitance, and P displaying the surface roughness of the electrode, namely, the deviation from plate condenser, thus indicating the capacitance characteristics of CPE. W characterizes the electrolyte impedance due to diffusion.

Table 1 shows that, the R_{CT} of carbon black-CNTs composite electrodes decreases obviously compared with nanocarbon black electrodes, that is, the resistance caused by charge transfer on the electrode surface decreases, due to the extraordinarily high conductivity and the netted CNTs being the bridges for electron transfer between carbon blacks. Moreover, there are some defects on the surface of CNTs, which can provide attachment position for reagent and accelerate the electron exchange between electrode and reagents. Nevertheless, the CPE-P of composite electrodes is less than that of carbon black, revealing the increase of surface roughness of electrodes after the adding of CNTs into carbon black, which may be caused by the diameter variance between CNTs and carbon black. The CPE-T of composite electrodes increases obviously, manifesting the increase of double-layer capacitance between the solid-liquid interface and the decrease of the interface

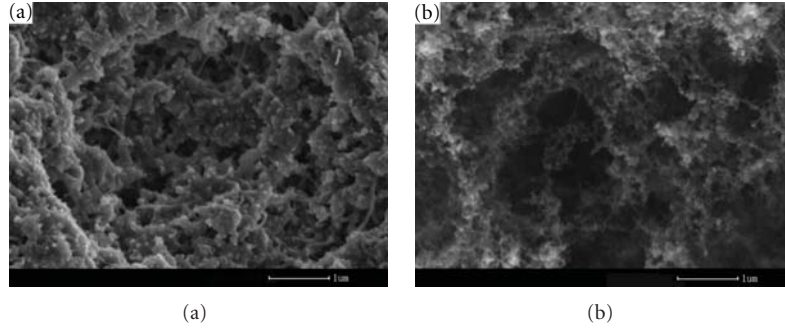


FIGURE 1: SEM image of the composite electrode: (a) untreated composite electrode—(b) composite electrode treated at 600°C in nitrogen.

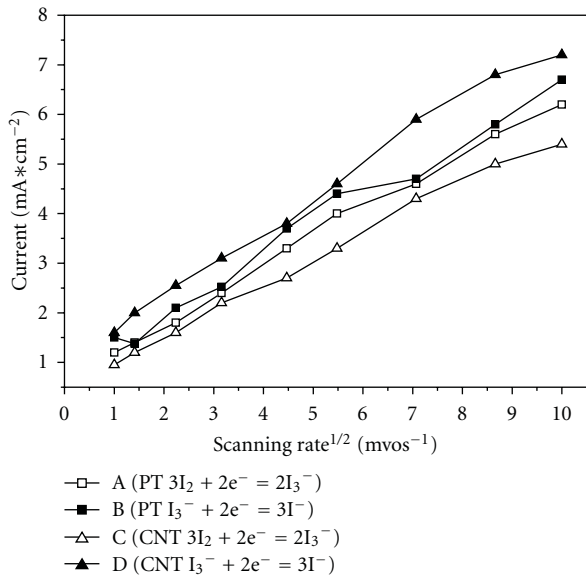


FIGURE 2: Peak current of cyclic voltammograms on composite electrode and Pt electrode.

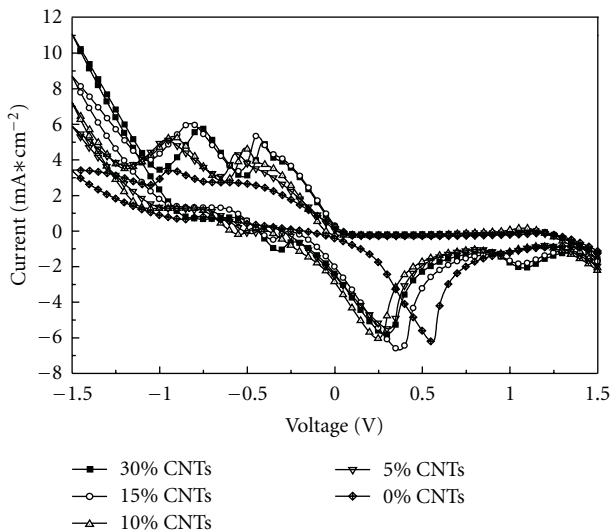


FIGURE 3: Cyclic voltammograms for composite electrode with different CNTs additions.

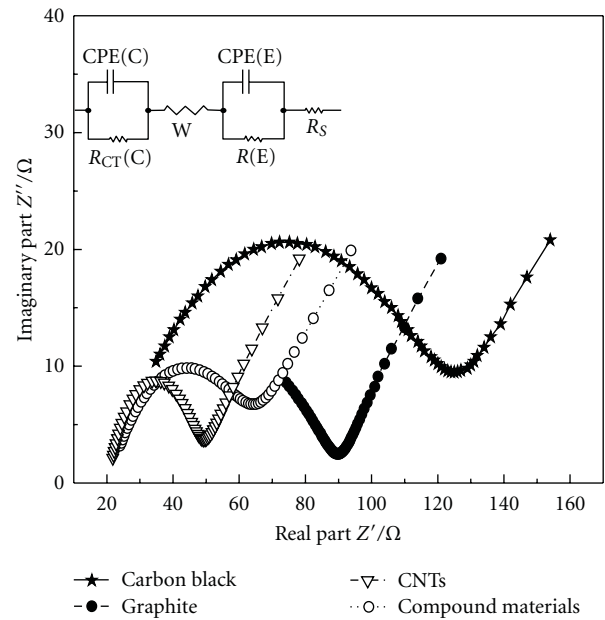


FIGURE 4: Electrochemical impedance spectroscopy and its equivalent circuit of nanocarbon electrode.

electric potential difference between the electrode and electrolyte.

3.2.3. Effects of CNTs Addition on the Impedance of DSSCs.

The electrochemical impedance spectroscopy for DSSCs with different CNTs additions at 30°C is shown in Figure 5, and was fitted by the equivalent circuit insetted in Figure 5, where R_{CT} (TiO_2) and CPE (TiO_2) represent the interface impedance between TiO_2 electrode and electrolyte. It is shown in Table 2 that, as the CNTs addition rises, the CPE-P decreases, leading to increases of both the surface roughness and the active catalytic points of the electrode surface; furthermore, the CPE-T decreases, resulting in the rise of the interface capacitance between the carbon electrode and electrolyte and the diminution of the electric potential difference of the two interfaces. Therefore, the catalytic performance of the CE is improved totally, which can be proved, in Figure 6, by all the increases of open-circuit voltage, short-circuit current, and the fill-factor for DCSs as

TABLE 1: Fitting results for electrochemical impedance spectroscopy of nanocarbon electrode.

Electrode material	$R_{CT}(C) / \Omega$	CPE-T	CPE-P
$\Phi 40-60$ nm CNT	26.70	$3.2462E-5$	0.708
Nanocarbon black	104.3	$9.6948E-5$	0.568
Graphite scale	69.53	$2.0033E-5$	0.411
Composite electrode	43.04	$2.1908E-4$	0.512

TABLE 2: Fitting results for electrochemical impedance spectroscopy for DSSCs with different CNTs addition.

CNTs content	$R_{CT}(C)/\Omega$	CPE-T	CPE-P	R^S
0%	356.4	$2.42E-5$	0.922	65.1
5%	1125.0	$9.09E-5$	0.718	121.4
10%	194.4	$3.39E-4$	0.624	152.3
30%	198.4	$4.78E-4$	0.573	242.3

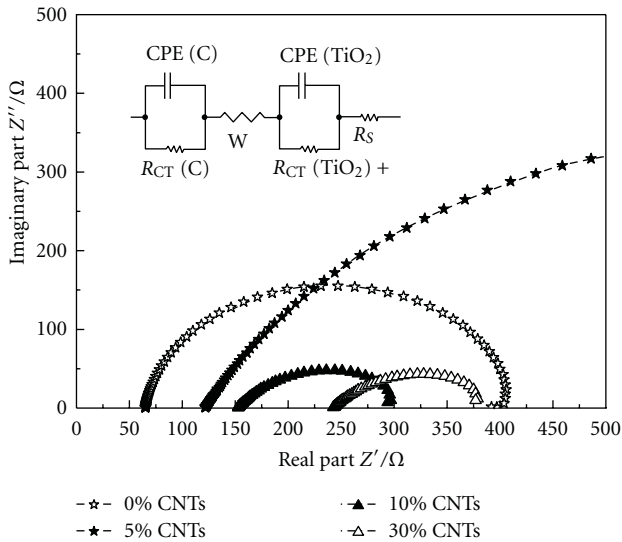


FIGURE 5: Electrochemical impedance spectroscopy for DSSCs and its equivalent circuit with different CNTs addition.

the rise of CNTs addition. However, as the increase of CNTs addition, R_s has a certain rise, indicating the increasing of the surface resistance between carbon film and FTO glass.

3.2.4. Effects of CNTs Addition on the Photovoltaic Performance of DSSCs. Photocurrent-photovoltage characteristics of DSSCs with different CNTs contents are shown in Figure 6. Combined with Table 2, it can be concluded that adding CNTs can improve the open-circuit voltage and short-circuit current of DSSCs. When the addition is less than 10%, the open-circuit voltage, short-circuit current, and fill-factor increase as the CNTs contents rises, nevertheless, when the adding amount reaches 30%, all the parameters mentioned above begin to reduce. The reason may be that with much CNTs addition, CNTs cannot be perfectly dispersed in carbon black and aggregate, resulting in the reduction of the

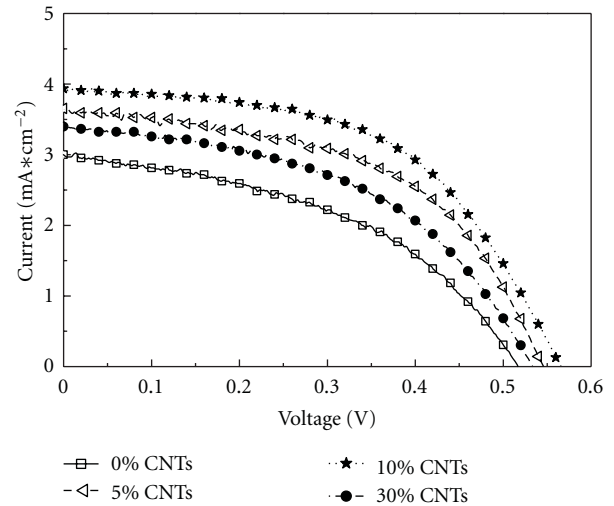


FIGURE 6: Photocurrent-photovoltage characteristics of DSSCs with different CNTs additions.

electrode surface area, and the increase of resistance caused by the charge transfer on the electrode surface.

4. Conclusion

CNTs with different content were added into nanocarbon counterelectrodes of DSSCs, and the effects of CNTs addition on the I^- and I_3^- oxidation reduction in the electrolyte as well as the carbon electrode/electrolyte interface were investigated by cyclic voltammetry and electrochemical impedance spectroscopy. DSSCs were assembled to test the parameters of photovoltaic performance. The results indicated that carbon nanocomposite electrodes with CNTs adding exhibit a highly interconnected network structure with high electrical conductivity and good catalytic activity. When the content of CNTs is 15%, the highest catalytic reduction ability of the electrode is obtained. With the CNTs

adding, the interface capacitance between carbon electrode and electrolyte improves but the electric potential difference of the interface decreases.

Acknowledgments

This work is supported by the National Natural Science Foundation of China (no. 20971027), by National Science and Technology Support Project of China (no. 2012BAK26B00), by the Specialized Research Fund for the Doctoral Program of Higher Education of China (no. 20094420110005), by the Guangdong Provincial Natural Science Foundation of China (no. 9251009001000006), and by the Science and Technology Program of Guangdong Province of China (no. 2009A030301008, no. 2009B090300017, no. 2010A090200063, no. 2010498E21, no. 2010A011300041, no. 2011B050300017, 2011A090200084).

References

- [1] C. Winder, G. Matt, J. C. Hummelen, R. A. J. Janssen, N. S. Sariciftci, and C. J. Brabec, "Sensitization of low bandgap polymer bulk heterojunction solar cells," *Thin Solid Films*, vol. 403–404, pp. 373–379, 2002.
- [2] G. Calogero and G. D. Marco, "Red Sicilian orange and purple eggplant fruits as natural sensitizers for dye-sensitized solar cells," *Solar Energy Materials and Solar Cells*, vol. 92, no. 11, pp. 1341–1346, 2008.
- [3] K. Tennakone, P. K. M. Bandaranayake, P. V. V. Jayaweera, A. Konno, and G. R. R. A. Kumara, "Dye-sensitized composite semiconductor nanostructures," *Physica E*, vol. 14, no. 1–2, pp. 190–196, 2002.
- [4] M. Gratzel, "Sol-Gel processed TiO₂ films for photovoltaic applications," *Journal of Sol-Gel Science and Technology*, vol. 22, no. 1–2, pp. 7–13, 2001.
- [5] A. F. Nogueira and M. A. De Paoli, "Dye sensitized TiO₂ photovoltaic cell constructed with an elastomeric electrolyte," *Solar Energy Materials and Solar Cells*, vol. 61, no. 2, pp. 135–141, 2000.
- [6] W. J. Lee, E. Ramasamy, D. Y. Lee, and J. S. Song, "Glass frit overcoated silver grid lines for nano-crystalline dye sensitized solar cells," *Journal of Photochemistry and Photobiology A*, vol. 183, no. 1–2, pp. 133–137, 2006.
- [7] S. Rani, P. Suri, P. K. Shishodia, and R. M. Mehra, "Synthesis of nanocrystalline ZnO powder via sol-gel route for dye-sensitized solar cells," *Solar Energy Materials and Solar Cells*, vol. 92, no. 12, pp. 1639–1645, 2008.
- [8] W. Geens, J. Poortmans, S. C. Jain et al., "Analytical study of PPV-oligomer- and C60-based devices for optimizing organic solar cells," *Solar Energy Materials and Solar Cells*, vol. 61, no. 1, pp. 43–51, 2000.
- [9] S. Ganesan, B. Muthuraaman, V. Mathew, J. Madhavan, P. Maruthamuthu, and S. Austin Suthanthiraraj, "Performance of a new polymer electrolyte incorporated with diphenylamine in nanocrystalline dye-sensitized solar cell," *Solar Energy Materials and Solar Cells*, vol. 92, no. 12, pp. 1718–1722, 2008.
- [10] C.-W. Shi, Q. Ge, B. Li, L. Tao, and Q. A. Liu, "Influence of additives on the performance of electrolytes in dye-sensitized solar cells," *Acta Physico, Chimica Sinica*, vol. 24, no. 12, pp. 2327–2330, 2008 (Chinese).
- [11] K. Takahashi, N. Kuraya, T. Yamaguchi, T. Komura, and K. Murata, "Three-layer organic solar cell with high-power conversion efficiency of 3.5%," *Solar Energy Materials and Solar Cells*, vol. 61, no. 4, pp. 403–416, 2000.
- [12] K. Imoto, K. Takahashi, T. Yamaguchi, T. Komura, J. I. Nakamura, and K. Murata, "High-performance carbon counter electrode for dye-sensitized solar cells," *Solar Energy Materials and Solar Cells*, vol. 79, no. 4, pp. 459–469, 2003.
- [13] T. Chen, Z. Sun, P. Guo, L. Wang, and S. Huang, "Deposition of carbon nanotubes film by LPCVD and related field emission property," *Acta Optica Sinica*, vol. 26, no. 5, pp. 777–782, 2006.
- [14] Q. Zhu, H. Zhang, Y. Chen, Y. Chen, L. Chen, and D. Yang, "Synthesis of aligned carbon nanotubes film by plasma-enhanced hot filament chemical vapor deposition," *Acta Optica Sinica*, vol. 28, no. 9, pp. 1824–1827, 2008.
- [15] E. Ramasamy, W. J. Lee, D. Y. Lee, and J. S. Song, "Spray coated multi-wall carbon nanotube counter electrode for tri-iodide (I₃⁻) reduction in dye-sensitized solar cells," *Electrochemistry Communications*, vol. 10, no. 7, pp. 1087–1089, 2008.
- [16] W. J. Lee, E. Ramasamy, D. Y. Lee, and J. S. Song, "Performance variation of carbon counter electrode based dye-sensitized solar cell," *Solar Energy Materials and Solar Cells*, vol. 92, no. 7, pp. 814–818, 2008.
- [17] W. J. Lee, E. Ramasamy, D. Y. Lee, and J. S. Song, "Grid type dye-sensitized solar cell module with carbon counter electrode," *Journal of Photochemistry and Photobiology A*, vol. 194, no. 1, pp. 27–30, 2008.
- [18] T. N. Murakami, S. Ito, Q. Wang et al., "Highly efficient dye-sensitized solar cells based on carbon black counter electrodes," *Journal of the Electrochemical Society*, vol. 153, no. 12, Article ID 047612JES, pp. A2255–A2261, 2006.
- [19] Z. Huang, X. Liu, K. Li et al., "Application of carbon materials as counter electrodes of dye-sensitized solar cells," *Electrochemistry Communications*, vol. 9, no. 4, pp. 596–598, 2007.
- [20] J. E. Trancik, S. C. Barton, and J. Hone, "Transparent and catalytic carbon nanotube films," *Nano Letters*, vol. 8, no. 4, pp. 982–987, 2008.

Research Article

Electric Double-Layer Capacitor Fabricated with Addition of Carbon Nanotube to Polarizable Electrode

Yoshiyuki Show

Department of Electrical and Electronic Engineering, Tokai University, 4-1-1 Kitakaname, Hiratsuka, Kanagawa, 259-1292, Japan

Correspondence should be addressed to Yoshiyuki Show, show@tokai-u.jp

Received 13 October 2011; Accepted 18 March 2012

Academic Editor: Sulin Zhang

Copyright © 2012 Yoshiyuki Show. This is an open access article distributed under the Creative Commons Attribution License, which permits unrestricted use, distribution, and reproduction in any medium, provided the original work is properly cited.

Electrical double-layer capacitor (EDLC) was fabricated with addition of carbon nanotube (CNT) to polarization electrodes as a conducting material. The CNT addition reduced the series resistance of the EDLC by one-twentieth, while the capacitance was not increased by the CNT addition. The low series resistance led to the high electrical energy stored in the EDLC. In this paper, the dependence of the series resistance, the specific capacitance, the energy, and the energy efficiencies on the CNT addition is discussed.

1. Introduction

Electric double-layer capacitors (EDLCs), supercapacitors, or ultracapacitors have the same type of electrical energy storage device, which is based on a double electric charge layer effect [1, 2]. Commercial EDLCs recently have capacitance value up to thousands F and the power density up to thousands W/kg, which is higher than that of conventional batteries (<1000 W/kg). Higher capacitance and power density allow higher energy to be stored and discharged at higher rate. Moreover, EDLCs have longer cycle lives exceeding 500000 times. These features have generated great interest in the application of EDLCs such as consumer electronics, hybrid electric vehicle [3], and industrial power managements. On the other hand, the energy density of EDLCs is below 10 Wh/kg, which is lower than that of batteries (35–40 Wh/kg of lead-acid batteries, ~150 Wh/kg of lithium ion batteries). The electrical energy (L_{stored}) stored in the EDLC is calculated according to the following equation:

$$L_{\text{stored}} = \frac{1}{2} CV^2, \quad (1)$$

where C is capacitance and V is voltage. This equation indicates that an increase in the capacitance leads the electrical energy stored in the EDLC to be high.

The capacitance of the EDLC is theoretically proportional to surface area (S) of polarizable electrodes, as based on the following equation:

$$C = \int \frac{\epsilon_0 \epsilon_r}{d} S, \quad (2)$$

where ϵ_0 and ϵ_r are permittivity in vacuum and relative permittivity of the double layer, respectively, and d is thickness of double layer. Therefore, activated carbon is widely used as a constituent of polarizable electrode in order to obtain large capacitance, because it has high surface area of over 1000 m²/g.

In addition to the surface area of the polarizable electrodes, the energy density is also gravened by the series resistance of the EDLC, because the charge and the discharge currents are followed in the series resistance. The energy loss (L_{loss}), which is caused by the current flowing in the serial resistance during the charge or the discharge, is estimated using the following equation:

$$L_{\text{loss}} = I^2 R_s \cdot t, \quad (3)$$

where I is the charge or the discharge current, R_s is the series resistance, and t is the charge or the discharge time. In the application of the EDLC to the second power system in an electric vehicle, the discharge for the acceleration and the charge by the deceleration take place over a short

period. Therefore, these charge and discharge currents are of a particularly high value when compared with those of other applications. Higher charge and discharge currents cause the energy loss to be increased. For these reasons, there is a strong requirement for the series resistance to be decreased in order to reduce the energy loss.

A decrease in series resistance (R_s) also allows the power density of EDLC to be increased, because maximum output power (P_{\max}) of EDLCs is theoretically calculated to the following equation:

$$P_{\max} = \frac{V^2}{4R_s}, \quad (4)$$

where V is the voltage. Therefore, the series resistance of EDLCs is also required to be reduced in order to increase the energy and the power densities.

Activated carbon is the base material widely used for the fabrication of polarizable electrodes [4, 5]. However, the activated carbon in itself does not have a high enough electrical conductance to act as a fully suitable material for the polarizable electrodes. An EDLC fabricated exclusively from activated carbon shows a high energy loss during the charge and the discharge processes, because it has high series resistance. Therefore, a conducting material such as acetylene black is generally added to the polarizable electrodes in order to decrease the series resistance.

Carbon nanotube (CNT) is one of the candidate materials for polarizable electrodes of the EDLC. The CNT is tube shaped with a diameter of a few nm, which is expected to be suitable for forming the double layer between the surface and the electrolyte. Moreover, CNTs have a high electrical conductivity [6] and chemical stability. It has been reported that the EDLC fabricated from multiwalled CNT showed high specific capacitance in high range of 4–135 F/g [7, 8]. For single-walled CNT, the specific capacitance of 180 F/g and the power density of 20 kW/kg at the energy density of 7 Wh/kg were reported [9]. Moreover, CNT-based electrodes fabricated by direct synthesis of CNT on the bulk Ni substrates have been reported to have the specific capacitance of 38.7 F/kg [10]. However, a comparative investigation of the specific capacitance, achieved with CNTs and activated carbon materials, revealed that activated carbon materials exhibited significantly higher capacitance [11]. On the other hand, the addition of CNT to activated carbon instead of acetylene black or graphite power for the polarizable electrodes also has been studied [12–15].

In this paper, CNTs are added to the polarizable electrode which is made of activated carbon. The CNT concentration in the polarizable electrode is from 0 to 100%. The dependence of the series resistance, the specific capacitance, the electrical energy, and the energy efficiency on the CNT addition is studied.

2. Experimental Conditions

CNT (Ohashi Kasga Tsusho Inc.) and activated carbon (Hohsen Corp.) were used as the base material for the

polarizable electrode. The ratio of the CNT to the activated carbon was varied from 0 (pure activated carbon) to 100% (pure CNT). These electrode materials were mixed in a mortar made of agate. Polytetrafluoroethylene (PTFE) was added to the mixture of CNT and activated carbon as binder at 17% in weight. Acetylene black (Kanto Chemical Co., Inc) was also mixed to some of the polarizable electrodes instead of the CNTs for reference/comparison purposes. The total mass of the polarizable electrode was varied from 30 mg to 120 mg.

The mixture was pressed at 20 MPa and formed into a disk shape with an area of 1 cm² (diameter of 11.5 mm) using a steel mold-type pressure apparatus. The thickness of the polarizable electrode hardly depends on the ratio of the constituents. In this experiment, it was varied from 0.5 to 2 mm by increasing its weight from 30 to 120 mg.

The constituents of the polarizable electrode were characterized by the scanning electron microscope (SEM) (Hitachi High-Technologies Corp., HF-2200TU and S-4800). The capacitance measurements were performed using a symmetrical cell configuration (a two-electrode system). The platinum plates were used as a collector electrode, because contact resistance between the polarizable electrode and the platinum plate is lower than any other metal such as stainless steel. A pair of polarizable electrodes was set up in a glass beaker or a can cell to provide both an anode and a cathode. An organic solvent (1.5 M SBP-BF₄/PC, Japan Carlit Co., Ltd.) was used as the electrolyte. This electrolyte has high electrical conductivity of 16 mS/cm.

The constant current charge-discharge measurement was carried out at 5 mA in the voltage range between 0.1 and 1.2 V using the source meter (Advantest Corp., R6243). The voltage change during the charge-discharge was measured. The series resistance and the capacitance of the EDLC were estimated from the voltage change by the mathematical fitting method described in Result and Discussion.

3. Result and Discussion

Figure 1 shows SEM images of (a) activated carbon (AC), (c) carbon nanotube (CNT), and (e) acetylene black (AB), which are constituents of the polarizable electrodes. The activated carbon was a particle with a size of 2–3 μm. A high-resolution SEM image shows that the activated carbon contains a great number of mesopores on its surface. The nitrogen adsorption measurements indicated that the activated carbon was 2000 m²/g in the specific surface area. The CNT was cylindrical-shaped material as shown in Figure 1(c). The diameter and the length were approximately 10 nm and 100 μm, respectively. No traces of the metal catalyst, which had been used for CNT growth, were found at the tips of the CNT in this SEM image. Furthermore, very little amorphous carbon, which is a byproduct of the CVD process, was found. This SEM investigation suggests that the CNT used is well purified by the post-acid washing process used after the CNT growth. The acetylene black used was a particle with a diameter of 50–60 nm, as shown in Figure 1(e).

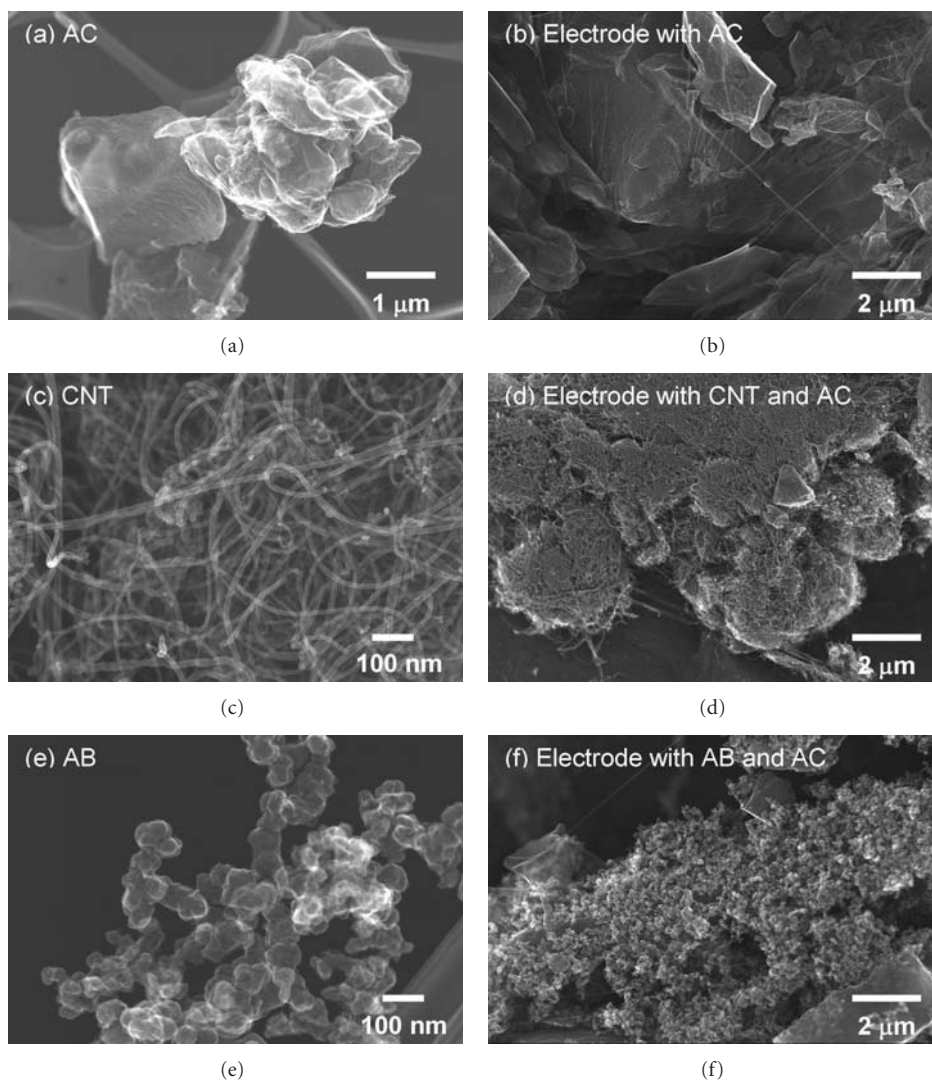


FIGURE 1: SEM images of (a) activated carbon (AB), (c) carbon nanotube (CNT), and (e) acetylene black (AB) as constituents of the polarizable electrodes. SEM images of polarizable electrodes fabricated from (b) exclusively activated carbon, (d) CNT and activated carbon, and (f) acetylene black and activated carbon.

Figure 1 also shows SEM images of polarizable electrodes fabricated from (b) exclusively activated carbon, (d) CNT and activated carbon, and (f) acetylene black and activated carbon. The concentration of CNT or acetylene black in polarizable electrode is 20%. Particles of activated carbon are stacked each other by the polytetrafluoroethylene (PTFE), which was added as binder as shown in Figure 1(b). Thin fiber-shaped PTFE was observed in this image. On the other hand, the activated carbon particles were covered with the CNT in the polarizable electrode containing CNT, as shown in Figure 1(d). The CNTs kept their long shape and were intertwined on many particles of the activated carbon in the polarizable electrode. The SEM image of the acetylene black in Figure 1(f) shows their particles are distributed on the activated carbon surface.

Figure 2 shows the charge-discharge curves of EDLCs fabricated with the following three types of polarizable electrodes: (a) those of exclusively activated carbon (no

CNT) and those containing (b) 10 and (c) 50% CNTs. Those polarizable electrodes were fixed at the weight of 60 mg. The charge-discharge measurements were carried out at a constant current of 5 mA. A rapid voltage change at the initial stage of the charge and the discharge, which is called the IR drop, was observed for all types of EDLCs. The IR drops of 0.45 V and 0.04 V were observed for (a) the EDLC without and (b) the EDLC with the 10% CNT addition, respectively. At 0.04 V the IR drop of the EDLC containing CNT at 10% was lower than that of the EDLC fabricated without using CNT.

The voltage gradually increased with an increase in the charging time after the initial stage of the charge. The inclination of the voltage changes for the EDLC without and EDLC with the 10% CNT was almost the same. This result suggests that these EDLCs have almost the same electric capacitance. However, the voltage of the EDLC without the CNT addition reached 1.2 V in a shorter time than that of

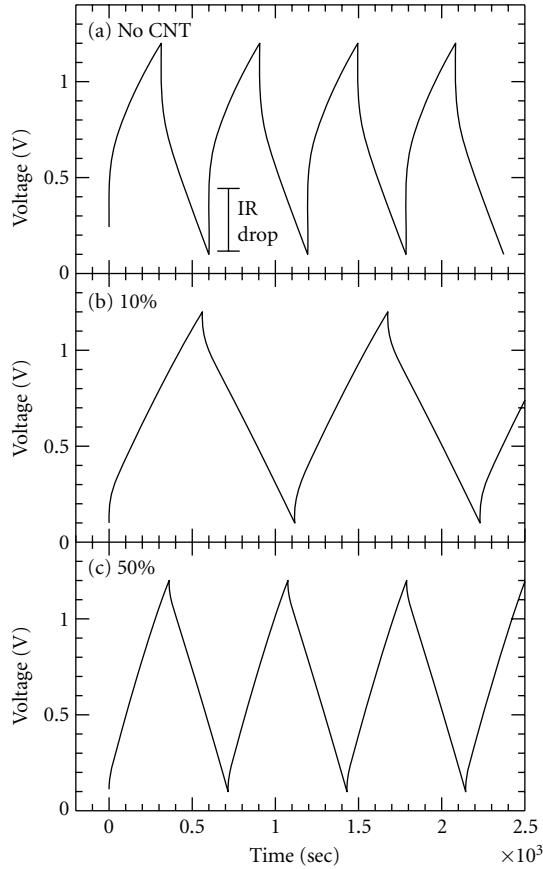


FIGURE 2: The charge-discharge curves of EDLCs fabricated with the following three types of polarizable electrodes: (a) those of exclusively activated carbon (no CNT) and those containing (b) 10 and (c) 50% CNTs.

the EDLC with the CNTs, because the IR drop is bigger. One cycle of the charge and the discharge on the EDLC without the CNT addition was 600 s. On the other hand, that of the EDLC with the CNT addition was 1200 s. A longer cycle time indicates that a higher amount of electric energy is stored in the EDLC, because this measurement is carried out using a constant current.

The EDLC containing CNT at 50% was 0.02 V in the IR drop, which was lower than that of 10%. However, one cycle of the charge and the discharge on this EDLC was as short as 700 s, because the inclination of the voltage changes was higher than that of 10%. Higher inclination suggests that the EDLC with the 50% CNT concentration is lower than that of 10% in the electrical capacitance.

An equivalent electric circuit model for the EDLCs, shown in Figure 3, was used to analyze the above charge-discharge curves. In this circuit, the equivalent capacitance (C) is originated from the formation of the electrical double layer at the interface between surface of the polarizable electrodes and the electrolyte. Larger surface area of the polarizable electrode generally generates larger capacitance. The parallel resistance (R_p) and the series resistance (R_s) are connected to the capacitance. The parallel resistance

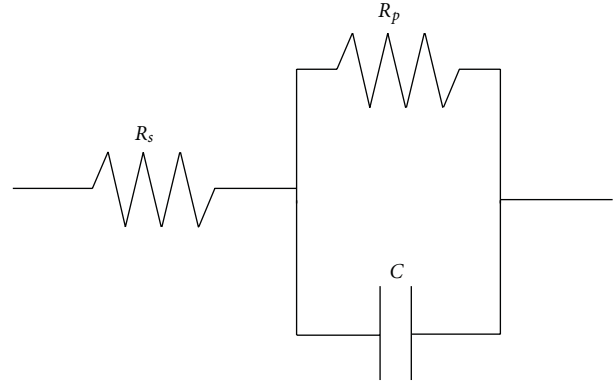


FIGURE 3: An equivalent electric circuit model for the EDLCs.

expresses the current leakage of the electrical double layer, which influences long-term energy storage. The series resistance consists of resistances of the polarizable electrodes and electrolyte, and contact resistance between the polarizable electrode and the collector electrode. The series resistance causes the IR drop and energy loss during the charge-discharge.

The equivalent series resistance (R_s) of the EDLC was estimated from the value of the IR drop according to the following equation:

$$R_s = \frac{V_{IR}}{(I_{charge} - I_{discharge})}, \quad (5)$$

where V_{IR} is the voltage change at the time that the flowing current changes from the discharge current $I_{discharge}$ (negative value) to the charge current I_{charge} (positive value). In this study, the value of $(I_{charge} - I_{discharge})$ is 10 mA. Therefore, the series resistance (R_s) was estimated to be 45, 4, and 2 Ω for the EDLCs without and those with CNT addition of 10% and 50%, respectively. No dependence of the series resistance on the charge-discharge current was observed in the range between 0.5 and 50 mA.

The inclination of the voltage change during the charge-discharge depends on the capacitance of the EDLC. Therefore, the capacitance (C) of the EDLC was estimated using the mathematical fitting technique according to the following equation explaining the relationship between the charging time and the voltage:

$$V(t) = R_p \cdot I_{charge} \left\{ 1 - \exp\left(-\frac{t}{C \cdot R_p}\right) \right\} + V_{IR}, \quad (6)$$

where $V(t)$ is the voltage as a function of the charging time (t), the capacitance (C), and the equivalent parallel resistance (R_p).

The capacitance was estimated to be 2.4 F for both EDLC without and that with CNT at concentration of 10% from the above method. On the other hand, the EDLC with 50% CNT was estimated to be as low as 1.2 F, because the inclination of the voltage change was high and the charge-discharge cycle was short. No dependence of the capacitance on the charge current was observed in the range from 0.5 to 50 mA.

Figure 4(a) shows the dependence of the series resistance on the ratio of CNT to activated carbon in the polarizable electrode. Moreover, those of the EDLC containing the acetylene black, instead of the CNT, are also shown. In this figure, the ratio of 0 means the EDLC is fabricated exclusively with the activated carbon without using the CNT and acetylene black. The series resistance of the EDLC fabricated with exclusively of the activated carbon showed as high as value 45Ω . When the CNTs were mixed with the activated carbon in the polarizable electrodes, the series resistance of the EDLC decreased with an increase in CNT concentration. The EDLC fabricated with a CNT concentration of 17% has a series resistance as low as 2Ω . This series resistance was approximately one quarter of an EDLC fabricated at the same concentration of acetylene black. No series resistance changed with an increase in CNT concentration above 20%. However, it increased to 2.5Ω in the face of the EDLC fabricated from 100% CNT, because clacks were formed in the polarizable electrodes by sinking them in the electrolyte.

The addition of the acetylene black to the polarizable electrode also decreased the series resistance of the EDLC. Both the EDLCs for concentration of the acetylene black at 50 and 100% are 4Ω . No clacks were formed in the polarizable electrodes formed from exclusively acetylene black. However, the series resistance was higher than EDLCs with addition of the CNT.

Figure 4(b) shows the dependence of the specific capacitance (F/g) on ratio of the CNT or the acetylene black to the activated carbon in the polarizable electrode. In this figure, the value was indicated as the capacitance par the weight of polarizable electrode. For example, the EDLC fabricated from exclusively the activated carbon showed the 2.4 F in the capacitance. This EDLC is fabricated with two pieces of polarizable electrode containing carbon materials, such as activated carbon, CNT, or acetylene black (120 mg in total weight). Therefore, the specific capacitance of this EDLC was calculated to be 24 F/g .

No significant change in the capacitance was observed with mixture of the CNT and the acetylene black up to 17%. The capacitance decreased with an increase in their ratio above 20%. The EDLC fabricated exclusively from the CNT showed the capacitance of 4 F/g . This value is higher than that of the EDLC fabricated exclusively from acetylene black. However, these values are extremely lower than that of the EDLC fabricated from exclusively activated carbon.

The specific capacitances for the CNT and the activated carbon in the polarizable electrode were estimated by the mathematical fitting technique according to the following equation:

$$C(x) = C_{\text{CNT}} \frac{x}{100} + C_{\text{AC}} \frac{(100-x)}{100}, \quad (7)$$

where $C(x)$ is specific capacitance for the fabricated polarizable electrode. C_{CNT} and C_{AC} are the specific capacitances for the CNT and the activated carbon, respectively. x is ratio of the CNT to activated carbon. The result of the mathematical fitting is also shown in Figure 4(b).

Table 1 shows the specific capacitance for the CNT, the acetylene black, and the activated carbon estimated by the

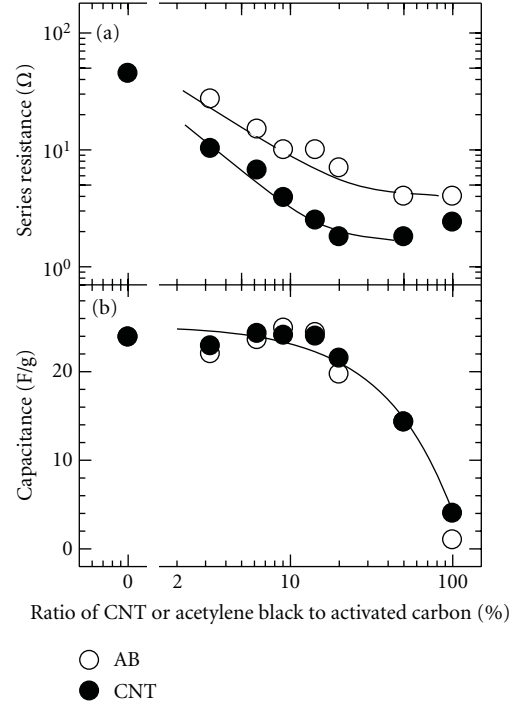


FIGURE 4: (a) The dependence of (a) the series resistance and (b) the specific capacitance on the ratio of the CNT or the acetylene black to the activated carbon in the polarizable electrode.

TABLE 1: Specific capacitance of various materials used for the fabrication of EDLCs.

Material	Specific capacitance (F/g)
Carbon Nanotube	4.5
Acetylene black	1.7
Activated carbon	24

above method. The CNT and the acetylene black were 4.5 and 1.7 F/g in specific capacitance, respectively. The CNT was higher than the acetylene black in the specific capacitance. However, they were lower than the activated carbon (24 F/g).

Figure 5 shows the dependence of (a) the electrical energy and (b) the energy efficiency on ratio of the CNT or the acetylene black to the activated carbon in the polarizable electrode, whose weight is fixed at 60 mg. The electric energy L stored in the EDLC was estimated by the discharge curve ranging between 1.2 V and 0.1 V with a constant current of 5 mA using the following equation:

$$L = \int V(t) \cdot i dt. \quad (8)$$

On the other hand, the energy efficiency η was defined by the ratio between the discharged and the charged electric power using the following equation:

$$\eta = \frac{L_{\text{discharge}}}{L_{\text{charge}}} \times 100, \quad (9)$$

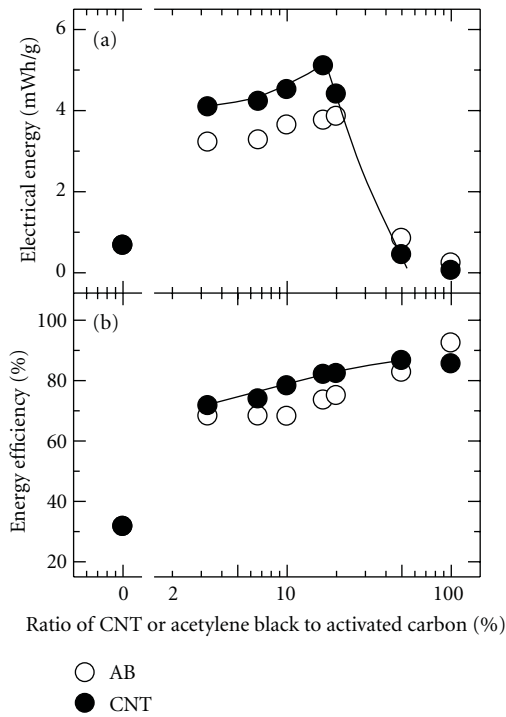


FIGURE 5: The dependence of (a) the electrical energy and (b) the energy efficiency on ratio of the CNT or the acetylene black to the activated carbon in the polarizable electrode.

where L_{charge} and $L_{\text{discharge}}$ are, respectively, the electric power charged and discharged between the voltage of 0.1 V and 1.2 V with a constant current of 5 mA.

The EDLC fabricated using exclusively activated carbon without the addition of any conducting materials showed a low electric energy of 0.7 mWh/g. When the CNTs were added to the polarizable electrodes up to 15%, the electric energy increased up to 5.1 mWh/g according to the increase in CNT concentration. The electric energy was on the contrary decreased by increasing the CNT concentration above 20%. The EDLCs with addition of the acetylene black also have the same trend in the electrical energy. However, the electric energy for EDLCs fabricated with CNTs was higher than that of those fabricated with acetylene black.

A low energy efficiency of 31% was observed for the EDLC fabricated exclusively from activated carbon as shown in Figure 5(b). The energy efficiency was improved by the addition of CNTs to the polarizable electrodes and linearly increased according to the increase in the CNT concentration. A high energy efficiency of 86% was observed for the EDLC with a 50% CNT concentration. The energy efficiency of the EDLCs with addition of the CNT was higher than that of the acetylene black.

Figure 6 shows the dependence of (a) the capacitance and (b) the series resistance on the weight and the thickness of the polarizable electrode in EDLC. The thickness of the polarizable electrode is increased by an increase in its weight, since the polarizable electrode is fixed at 11.5 mm in the diameter. The CNT or the acetylene black in the

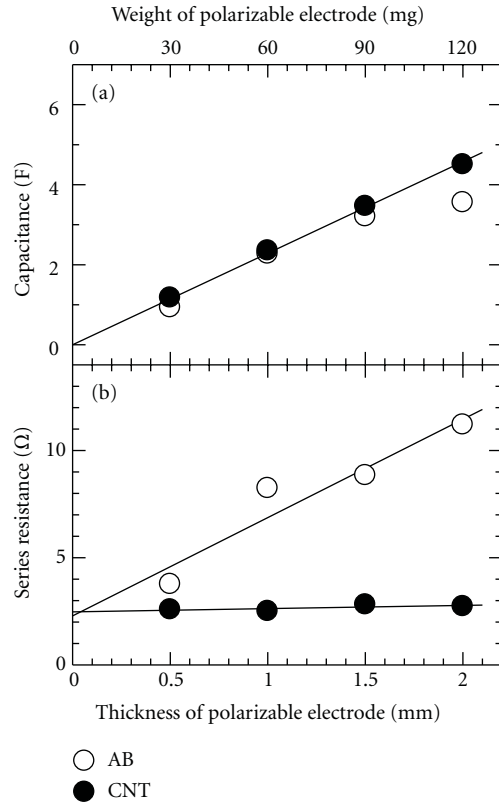


FIGURE 6: The dependence of (a) the capacitance and (b) the series resistance on the weight and the thickness of the polarizable electrode.

polarizable electrodes was fixed at 10% in the weight ratio. Both of the EDLCs fabricated with the CNT or the acetylene black linearly increased from 1.5 to 4.5 F in capacitance with an increase in the thickness of polarizable electrodes. The specific capacitances at various thicknesses were almost of the same value of 24 F/g. The series resistance of the EDLCs added with the acetylene black was increased from 3.7 to 11 Ω with increasing the thickness of polarizable electrode. On the other hand, the series resistance of the EDLCs fabricated with the CNT slightly increased from 2.5 Ω to 2.8 Ω with an increase in the thickness of polarizable electrode. The series resistance at the thickness of 0 mm was estimated to be 2.5 Ω by extrapolation method. The EDLC formed with the acetylene black also showed the same value. These series resistances represent the contact resistance between the polarizable electrode and the counter electrode, because the resistances of the polarizable electrode and the electrolyte are neglected at the thickness of 0 mm. Therefore, these results indicate that the series resistance of the EDLCs fabricated using the CNT are governed by the contact resistance, since the resistance of the polarizable electrode containing CNT is low enough.

Figure 7 shows the schematic model comparing the electrical conduction in the polarizable electrodes with addition of (a) the acetylene black or (b) the CNT. Acetylene black is particle with a diameter of 50–60 nm, which is smaller than activated carbon by a one-30th to a one-60th approximately.

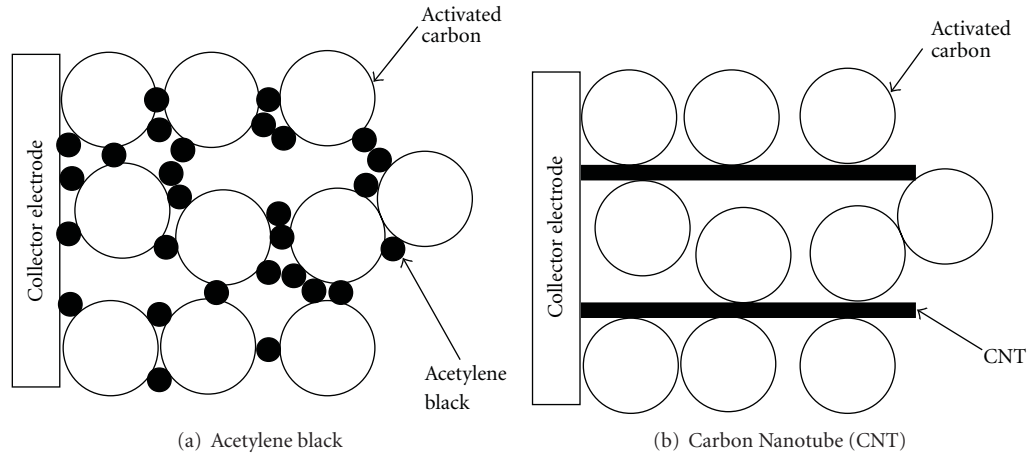


FIGURE 7: The schematic model comparing the electrical conduction in the polarizable electrodes with addition of (a) the acetylene black and (b) the CNT.

The particles of the acetylene black cover activated carbon particles in the polarizable electrode. The charge and the discharge currents flow through a large number of the acetylene black particles on the activated carbon. In this conduction mechanism, the acetylene black particles must connect to each other in order to effectively decrease the resistance of polarizable electrode. Although CNT has cylindrical shape with the diameter of 10 nm which is size a similar to that of acetylene black the length of CNT is as long as 100 μm . Therefore, one piece of CNT connects large number of activated carbon particles, because the length of CNT is longer than activated carbon by approximately 30–50 times. Therefore, CNT forms the electrical conduction mechanism in the polarizable electrode, which has higher conductivity comparing with acetylene black.

Activated carbon is a particle with the specific surface area of 2000 m^2/g . Therefore, it is widely used as a constitution of the EDLC. In this study, the specific capacitance for the activated carbon was 24 F/g. On the other hand, CNT also seems to have large surface area, because it has cylindrical shape with small diameter. The small diameter expects that CNT is more suitable constitution of the EDLC than activated carbon. However, the CNT showed 4.5 F/g in specific capacitance, which was smaller than the activated carbon. Small capacitance in this study suggests that only small surface area of CNT contributes to the double-layer capacitor. One possibility of this reason is the hydrophobic surface of CNT that causes its surface to be hardly wet with electrolyte.

EDLC fabricated from exclusively activated carbon shows high capacitance of 2.4 F. However, the electric energy stored in its EDLC is as low as 0.7 mWh/g, because its series resistance has value as high as 45 Ω . High series resistance loses electric energy during the charge and the discharge and also decreases the energy efficiency. The CNT addition into the polarizable electrode decreases the series resistance of the EDLC up to 2 Ω . Moreover, the EDLC with CNT addition increases to 5.1 mWh/g in the electric energy, because lower series resistance causes lower IR drop and longer charging

time. The small series resistance prevents losing electric energy during the charge and discharge. Therefore, the higher electric efficiency is observed from the EDLC with the addition of CNT. The addition of acetylene black also has the same trend in these characteristics. However, CNT is more effective than acetylene black as a conducting material.

The significant decrease in the capacitance of the EDLC with the addition of CNT was observed above 20%, because the specific capacitance of CNT is lower than that of activated carbon. The decrease of the capacitance leads to the lower stored electric energy. However, the efficiency increases with an increase in the CNT concentration, since the series resistance is decreased.

The CNT addition decreases the series resistance of EDLCs, because of its high aspect ratio. However, the CNT addition above 20% does not decrease the series resistance, because the series resistance becomes governed by the contact resistance between the polarizable electrode and the counter electrode. On the other hand, the capacitance decreases with an increase in the CNT concentration above 20%, because of low specific capacitance of CNT. These results suggest that the CNT is suitable material as the conducting material under the concentration of 20%.

4. Summary

The CNT addition into the polarizable electrodes up to 20% reduces the series resistance of the EDLC from 45 to 2 Ω . The reduction of the series resistance increases the electrical energy stored in the EDLC, and also prevents losing the energy loss during the charge and the discharge. However, the CNT addition does not increase the capacitance, because most of surface area of the CNT does not contribute to the electrical double layer capacitor. The EDLC with the 20% CNT addition shows the capacitance of 24 F/g, which is mainly contributed by activated carbon.

The EDLC with the CNT addition has lower than that of acetylene black in the series resistance. Since the series

resistance of the EDLC was decreased by the CNT addition, the EDLC achieves to increase the electric energy stored in it. Moreover, the energy efficiency for the charge and the discharge is also improved.

Acknowledgments

The author would like to thank Mr. Y. Miyamoto of the Technical Service Coordination Office, Tokai University, for the SEM investigations and Mrs. R. Kuwabara, H. Ino, M. Imano, H. Yoshida, Y. Totani, K. Koizumi, and K. Imaizumi for useful discussions.

References

- [1] H. I. Becker, "Low voltage electrolytic capacitor," U.S. Patent 2800616, 1957.
- [2] A. Nishino, "Capacitors: operating principles, current market and technical trends," *Journal of Power Sources*, vol. 60, no. 2, pp. 137–147, 1996.
- [3] K. Naoi and K. Machida, "Electrochemical Capacitors and Automobiles," *Kinzoku*, vol. 74, p. 1299, 2004.
- [4] M. Endo, T. Maeda, T. Takeda et al., "Capacitance and pore-size distribution in aqueous and nonaqueous electrolytes using various activated carbon electrodes," *Journal of The Electrochemical Society*, vol. 148, no. 8, pp. A910–A914, 2001.
- [5] T. Morimoto, K. Hiratsuka, Y. Sanada, and K. Kurihara, "Electric double-layer capacitor using organic electrolyte," *Journal of Power Sources*, vol. 60, no. 2, pp. 239–247, 1996.
- [6] T. W. Ebbesen, H. J. Lezec, H. Hiura, J. W. Bennett, H. F. Ghaemi, and T. Thio, "Electrical conductivity of individual carbon nanotubes," *Nature*, vol. 382, pp. 54–56, 1996.
- [7] E. Frackowiak, K. Metenier, V. Bertagna, and F. Beguin, "Supercapacitor electrodes from multiwalled carbon nanotube," *Applied Physics Letters*, vol. 77, no. 15, article 2421, 3 pages, 2000.
- [8] E. Frackowiak, K. Jurewicz, S. Delpeux, and F. Beguin, "Nanotubular materials for supercapacitors," *Journal of Power Sources*, vol. 97–98, pp. 822–825, 2001.
- [9] K. H. An, K. K. Jeon, W. S. Kim et al., "Characterization of supercapacitors using singlewalled carbon nanotube electrodes," *Journal of the Korean Physical Society*, vol. 39, pp. S511–S517, 2001.
- [10] B. J. Yoon, S. H. Jeong, K. H. Lee, H. S. Kim, C. G. Park, and J. H. Han, "Electrical properties of electrical double layer capacitors with integrated carbon nanotube electrodes," *Chemical Physics Letters*, vol. 388, pp. 170–174, 2004.
- [11] C. Emmenegger, P. Mauron, P. Sudan et al., "Investigation of electrochemical double-layer (ECDL) capacitors electrodes based on carbon nanotubes and activated carbon materials," *Journal of Power Sources*, vol. 124, no. 1, pp. 321–329, 2003.
- [12] C. Portet, P. L. Taberna, P. Simon, and E. Flahaut, "Influence of carbon nanotubes addition on carbon-carbon supercapacitor performances in organic electrolyte," *Journal of Power Sources*, vol. 139, no. 1–2, pp. 371–378, 2005.
- [13] C.-G. Liu, H.-T. Fang, D.-W. Wang, F. Li, M. Liu, and H.-M. Cheng, "Electrochemical Capacitance Characteristics of Activated Carbon Electrode Material with a Multi-Walled Carbon Nanotube Additive," *New Carbon Materials*, vol. 20, no. 3, pp. 205–210, 2005.
- [14] Y. Show and K. Imaizumi, "Decrease in equivalent series resistance of electric double-layer capacitor by addition of carbon

- nanotube into the activated carbon electrode," *Diamond and Related Materials*, vol. 15, no. 11–12, pp. 2086–2089, 2006.
- [15] Y. Show and K. Imaizumi, "Electric double layer capacitor with low series resistance fabricated by carbon nanotube addition," *Diamond and Related Materials*, vol. 16, no. 4–7, pp. 1154–1158, 2007.

Research Article

Estimating the Thermal Conductivities and Elastic Stiffness of Carbon Nanotubes as a Function of Tube Geometry

Z. H. Zhang, N. Yu, and W. H. Chao

Department of Mechanical Engineering, Yuan Ze University, Jhongli 32003, Taiwan

Correspondence should be addressed to N. Yu, nyu@saturn.yzu.edu.tw

Received 15 October 2011; Accepted 18 March 2012

Academic Editor: Sulin Zhang

Copyright © 2012 Z. H. Zhang et al. This is an open access article distributed under the Creative Commons Attribution License, which permits unrestricted use, distribution, and reproduction in any medium, provided the original work is properly cited.

The thermal conductivities and elastic properties of carbon nanotubes (CNTs) are estimated by using the double-inclusion model, which is based on rigorous elasticity approach. The model regards a CNT as one inclusion (the inner cylindrical void) embedded in the other (the outer coaxial single-crystal graphite shell). The concept of homogenization is employed, and vital microstructural parameters, such as CNT diameter, length, and aspect ratio, are included in the present model. The relationship between microstructure and thermal conductivities and elastic stiffness of CNTs is quantitatively characterized. Our analytical results, benchmarked by experimental data, show that the thermal conductivities and elastic stiffness of CNTs are strongly dependent on the diameter of CNT with little dependence on the length of CNT.

1. Introduction

The present work employs and modifies the double-inclusion model [1] to estimate, from a microstructural point of view, the thermal conductivities and elastic stiffness of carbon nanotubes (CNTs). Several models based on molecular dynamics simulation are developed for estimating the thermal conductive and elastic properties of CNTs [2–7] yet are not very computationally efficient. Some of the existing models are based on beam theories [8, 9] and can only estimate the Young moduli of CNTs. Robertson et al. [10] and Lu [11] employ energy methods to estimate the elastic properties of CNTs. Finite deformation is considered in Gao and Li [12] where the formulation is aimed at single-walled CNTs. A multiscale shear-lag-based approach later is developed for estimating Young's moduli of CNTs as well as stresses in CNT-based composites [13]. Chantrenne and Barrat [14] derive analytical expressions for the thermal conductivities of a single graphene and a CNT as a function of their characteristic lengths. Their analytical estimates show good agreement for single graphene but not for CNTs.

The reported experimental data of thermal conductivities and Young's and shear moduli of CNTs from literature are summarized in Tables 1 and 2, respectively. It is noted that the reported data are significantly different from each other

as the thermal and elastic properties of CNTs are functions of the microstructure of CNTs [15–18]. Qian et al. [19] also collect many experimental data on the Young modulus of CNTs, and they range from 320 GPa to 5.0 TPa. It is the objective of the present work to develop an analytical model to delineate the relationship between the microstructure and thermal conductive and elastic stiffness of CNTs.

2. The Model

2.1. Mori-Tanaka Theorem. Consider an infinite medium B , embodying a subregion V , which includes an inclusion Ω undergoing a heat flux-free transformation temperature gradient $\nabla T^{*\Omega}$. The matrix is denoted by M , and $V = M \cup \Omega$, see Figure 1. In view of the concept of Eshelby [20], Mori and Tanaka [21], and Hatta and Taya [22], one may find the disturbance temperature gradient $\{\nabla T^d\} = \{\nabla T_x^d, \nabla T_y^d, \nabla T_z^d\}^T$ at a typical location, x , in V due to a transformation temperature gradient $\{\nabla T^{*\Omega}\} = \{\nabla T_x^{*\Omega}, \nabla T_y^{*\Omega}, \nabla T_z^{*\Omega}\}^T$ in Ω as follows:

$$\{\nabla T^d(x)\} = [S^\Omega] \{\nabla T^{*\Omega}\}, \quad (1)$$

where the case of ellipsoidal V and Ω are considered. Eshelby's matrix $[S^\Omega]$ is a 3×3 matrix and is a function of

TABLE 1: The reported data of thermal conductivity of CNTs.

	CNT diameter (nm)	CNT length (nm)	CNT thickness (nm)	K (W/m-K)	SWCNT/MWCNT
Hone et al. [28]	1.4	100	NA	1750 ~ 5850	SWCNT
Berber et al. [4]	NA	NA	NA	6600	SWCNT
Osman and Srivastava [5]	NA	NA	NA	1000 ~ 2500	SWCNT
Kim et al. [29]	14	2.5 μm	NA	>3000	MWCNT
Maruyama [6]	NA	6 ~ 404	0.34	280 ~ 380	SWCNT
Bagchi and Nomura [30]	25	50 μm	10	3000	MWCNT
Bi et al. [7]	NA	2.5 ~ 25	NA	400 ~ 600	SWCNT

TABLE 2: The reported experimental data of Young's and shear moduli of CNTs.

	Length (nm)	Diameter (nm)	Thickness (nm)	SWCNT/MWCNT	Young's modulus (TPa)	Shear modulus (GPa)
Salvetat et al. [31]	180 ~ 370	4.5 ~ 20	0.34	SWCNT	0.067 ~ 0.5	0.7 ~ 6.5
Salvetat et al. [32]		26 ~ 76		MWCNT	1.28 \pm 0.59	
Krishnan et al. [33]	23.4 ~ 36.8	1.12 ~ 1.5		SWCNT	1.25 (average)	0.1
Yu et al. [34]		19 ~ 41	0.34	SWCNT	0.32 ~ 1.47	
Yu et al. [35]	1800 ~ 10990	13 ~ 36		MWCNT	0.27 ~ 0.95	

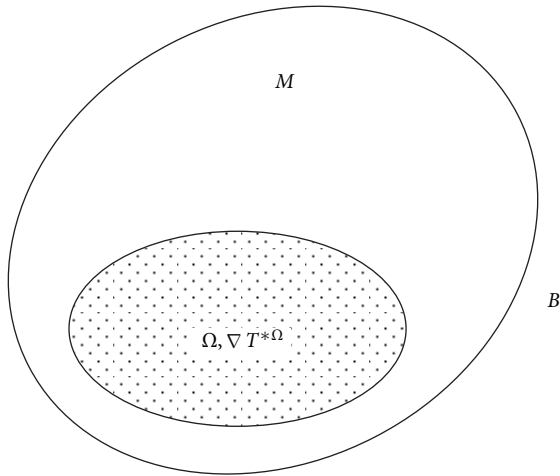


FIGURE 1: Mori-Tanaka model.

the geometry of inclusion Ω . In particular, the components of $[S^\Omega]$ for a circular cylindrical Ω are only functions of the aspect ratio of the cylinder [22]. It can be shown in a straightforward manner that the average temperature gradient of V , $\{\langle \nabla T^d \rangle_V\}$, is given by

$$\{\langle \nabla T^d \rangle_V\} = f \{\langle \nabla T^d \rangle_\Omega\} + (1-f) \{\langle \nabla T^d \rangle_M\}, \quad (2)$$

where the angle brackets $\langle \rangle$ represent an average quantity, $\{\langle \nabla T^d \rangle_\Omega\}$ is the average temperature gradient field of the inclusion, $\{\langle \nabla T^d \rangle_M\}$ is the average temperature gradient field of the matrix, and $f = \Omega/V$ is the inclusion volume

fraction. The average disturbance temperature gradient in region M due to $\nabla T^{*\Omega}$ is given by

$$\begin{aligned} \{\langle \nabla T^d \rangle_M\} &= \frac{1}{M} \int_M \{\nabla T^d(x)\} dV_x \\ &= \frac{1}{M} \left(\int_V \{\nabla T^d(x)\} dV_x - \int_\Omega \{\nabla T^d(x)\} dV_x \right) \\ &= \frac{1}{M} \left(\frac{\Omega}{V} \int_V [S^V] \{\nabla T^{*\Omega}\} dV \right) \\ &\quad - \frac{\Omega}{M} [S^\Omega] \{\nabla T^{*\Omega}\}, \end{aligned} \quad (3)$$

where S^V is Eshelby's matrix of inclusion V . Rearranging (3) gives

$$\{\langle \nabla T^d \rangle_M\} = \frac{\Omega}{M} ([S^V] - [S^\Omega]) \{\nabla T^{*\Omega}\}. \quad (4)$$

Substituting (1) and (4) into (2) gives the disturbance temperature gradient averaged over V due to a uniform transformation temperature gradient prescribed in Ω ,

$$\{\langle \nabla T^d \rangle_V\} = f [S^V] \{\nabla T^{*\Omega}\}. \quad (5)$$

Now consider a uniform transformation temperature gradient ∇T^{*M} in M . The heat flux and temperature gradient fields can be obtained by superposing two fields—one is due to $-\nabla T^{*M}$ and distributed over Ω , and the other is due to ∇T^{*M} and distributed over V . The average disturbance temperature gradient in Ω due to ∇T^{*M} in M is given by

$$\begin{aligned} \{\langle \nabla T^d \rangle_\Omega\} &= \frac{1}{\Omega} \int_\Omega [S(x; \Omega)] dV_x \{-\nabla T^{*M}\} \\ &\quad + \frac{1}{\Omega} \int_\Omega [S(x; V)] dV_x \{\nabla T^{*M}\} \\ &= ([S^V] - [S^\Omega]) \{\nabla T^{*M}\}. \end{aligned} \quad (6)$$

The average disturbance temperature gradient in M due to ∇T^{*M} prescribed in M is given by

$$\begin{aligned} \{\langle \nabla T^d \rangle_M\} &= \frac{1}{M} \int_M [S(x; \Omega)] dV_x \{\langle -\nabla T^{*M} \rangle\} \\ &+ \frac{1}{M} \int_M [S(x; V)] dV_x \{\langle \nabla T^{*M} \rangle\}. \end{aligned} \quad (7)$$

The first term on the right-hand side of (7) is in essence identical to (3) except ∇T^{*M} being replaced by $(-\nabla T^{*M})$. Thus, (4) can be used to give

$$\begin{aligned} \{\langle \nabla T^d \rangle_M\} &= \frac{\Omega}{M} ([S^V] - [S^\Omega]) \{\langle -\nabla T^{*M} \rangle\} \\ &+ [S^V] \{\langle \nabla T^{*M} \rangle\} \\ &= \frac{f}{1-f} [S^\Omega] \{\langle \nabla T^{*M} \rangle\} \\ &+ \frac{1-2f}{1-f} [S^V] \{\langle \nabla T^{*M} \rangle\}. \end{aligned} \quad (8)$$

Substituting (8) and (6) into (2), one obtains the disturbance temperature gradient averaged over V due to transformation temperature gradient ∇T^{*M} prescribed in M as follows:

$$\{\langle \nabla T^d \rangle_V\} = (1-f) [S^V] \{\langle \nabla T^{*M} \rangle\}. \quad (9)$$

2.2. Extended Mori-Tanaka Theorem. Consider an infinite homogeneous solid B with a thermal conductivity $\{K\} = \{K_x, K_y, K_z\}^T$. The solid B contains two ellipsoidal inclusions, V and Ω ($\Omega \subset V$). Let Ω and M ($= V - \Omega$) undergo distinct heat flux-free transformation. The uniform transformation temperature gradient in the absence of the surrounding medium is $\nabla T^{*\Omega}$ and ∇T^{*M} in Ω and M , respectively. The average of the disturbance temperature gradient resulting from $\nabla T^{*\Omega}$ is given by (1) and (5), and the volume average of the corresponding heat flux field is given by

$$\{\langle q^d \rangle_\Omega\} = [K] ([S^\Omega] - [I]) \{\langle \nabla T^{*\Omega} \rangle\}, \quad (10a)$$

$$\{\langle q^d \rangle_V\} = f [K] ([S^V] - [I]) \{\langle \nabla T^{*\Omega} \rangle\}, \quad (10b)$$

where I is the 3×3 identity matrix.

Similarly, the temperature gradient resulted from ∇T^{*M} is given by (6) and (9), and the corresponding heat flux fields are given by

$$\{\langle q^d \rangle_\Omega\} = [K] ([S^V] - [S^\Omega]) \{\langle \nabla T^{*M} \rangle\}, \quad (11a)$$

$$\{\langle q^d \rangle_V\} = (1-f) [K] ([S^V] - [I]) \{\langle \nabla T^{*M} \rangle\}. \quad (11b)$$

Combining (1), (6), (10a), and (11a) gives the average temperature gradient and heat flux in Ω due to $\nabla T^{*\Omega}$ and ∇T^{*M} ,

$$\{\langle \nabla T^d \rangle_\Omega\} = [S^\Omega] \{\langle \nabla T^{*\Omega} \rangle\} + ([S^V] - [S^\Omega]) \{\langle \nabla T^{*M} \rangle\}, \quad (12a)$$

$$\begin{aligned} \{\langle q^d \rangle_\Omega\} &= [K] ([S^\Omega] - [I]) \{\langle \nabla T^{*\Omega} \rangle\} \\ &+ [K] ([S^V] - [S^\Omega]) \{\langle \nabla T^{*M} \rangle\}. \end{aligned} \quad (12b)$$

The combination of (5), (9), (10b) and (11b) gives the average temperature gradient and heat flux in V due to $\nabla T^{*\Omega}$ and ∇T^{*M} ,

$$\begin{aligned} \{\langle \nabla T^d \rangle_V\} \\ = [S^V] \{f \{\langle \nabla T^{*\Omega} \rangle\} + (1-f) \{\langle \nabla T^{*M} \rangle\}\}, \end{aligned} \quad (13a)$$

$$\begin{aligned} \{\langle q^d \rangle_V\} \\ = [K] ([S^V] - [I]) \{f \{\langle \nabla T^{*\Omega} \rangle\} + (1-f) \{\langle \nabla T^{*M} \rangle\}\}. \end{aligned} \quad (13b)$$

The following relations can be derived in a straightforward manner:

$$\{\langle \nabla T^d \rangle_V\} = (1-f) \{\langle \nabla T^d \rangle_M\} + f \{\langle \nabla T^d \rangle_\Omega\}, \quad (14a)$$

$$\{\langle q^d \rangle_V\} = (1-f) \{\langle q^d \rangle_M\} + f \{\langle q^d \rangle_\Omega\}. \quad (14b)$$

Substituting (12a) and (12b), (13a) and (13b) into (14a) and (14b) gives

$$\begin{aligned} \{\langle \nabla T^d \rangle_M\} \\ = [S^V] \{\langle \nabla T^{*M} \rangle\} \\ + \frac{f}{1-f} \{([S^V] - [S^\Omega]) (\{\langle \nabla T^{*\Omega} \rangle\} - \{\langle \nabla T^{*M} \rangle\})\}, \end{aligned} \quad (15a)$$

$$\begin{aligned} \{\langle q^d \rangle_M\} \\ = [K] ([S^V] - [I]) \{\langle \nabla T^{*M} \rangle\} \\ + \frac{f}{1-f} [K] \{([S^V] - [S^\Omega]) (\{\langle \nabla T^{*\Omega} \rangle\} - \{\langle \nabla T^{*M} \rangle\})\}. \end{aligned} \quad (15b)$$

2.3. Thermal Conductivities and Elastic Constants of Double Inclusion. Consider an ellipsoidal matrix M , containing an ellipsoidal inhomogeneity Ω . The matrix M is embedded in

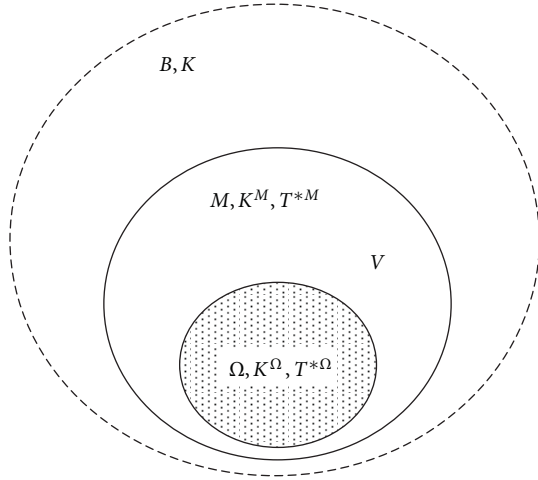


FIGURE 2: Double-inclusion model.

an infinite medium B . The thermal conductivity of Ω , M , and B is given by

$$K = K(x) = \begin{cases} K^\Omega & \text{if } x \text{ in } \Omega, \\ K^M & \text{if } x \text{ in } M, \\ K & \text{otherwise,} \end{cases} \quad (16)$$

respectively; see Figure 2. To solve the double-inhomogeneity problem, one may replace the inhomogeneity, Ω , and the matrix, M , by a reference material with thermal conductivity $\{K\}$, which is the thermal conductivity of B . Then one could prescribe transformation temperature gradient $\nabla T^{*\Omega}$ and ∇T^{*M} in Ω and M , respectively, to compensate the material mismatch, which is essentially Eshelby's concept of equivalent inclusion [20]. When the infinity domain B is subjected to far-field temperature gradient $\{\nabla T^\infty\}$, the heat flux and temperature gradient fields of the double inclusion $V (= M \cup \Omega)$ are in general not uniform, and their averages are, with the help of (12a), (12b), and (15a) and (15b), given by

$$\begin{aligned} \{\langle \nabla T^d \rangle_\Omega\} &= \{\nabla T^\infty\} + [S^\Omega] \{\nabla T^{*\Omega}\} \\ &+ ([S^V] - [S^\Omega]) \{\nabla T^{*M}\}, \end{aligned} \quad (17a)$$

$$\begin{aligned} \{\langle q^d \rangle_\Omega\} &= [K] \{\{\nabla T^\infty\} + ([S^\Omega] - [I]) \{\nabla T^{*\Omega}\}\} \\ &+ ([S^V] - [S^\Omega]) \{\nabla T^{*M}\}, \end{aligned} \quad (17b)$$

$$\begin{aligned} \{\langle \nabla T^d \rangle_M\} &= \{\nabla T^\infty\} + [S^V] \{\nabla T^{*M}\} + \frac{f}{1-f} \\ &([S^V] - [S^\Omega]) (\{\nabla T^{*\Omega}\} - \{\nabla T^{*M}\}), \end{aligned} \quad (18a)$$

$$\begin{aligned} \{\langle q^d \rangle_M\} &= [K] \{\{\nabla T^\infty\} + ([S^V] - [I]) \{\nabla T^{*M}\}\} \\ &+ \frac{f}{1-f} ([S^V] - [S^\Omega]) \\ &(\{\nabla T^{*\Omega}\} - \{\nabla T^{*M}\}). \end{aligned} \quad (18b)$$

Since the temperature gradient and the heat flux fields must be preserved after homogenization, the following constraint conditions must be satisfied:

$$\begin{aligned} [K^\Omega] \{\{\nabla T^\infty\} + [S^\Omega] \{\nabla T^{*\Omega}\} + ([S^V] - [S^\Omega]) \{\nabla T^{*M}\}\} \\ = [K] \{\{\nabla T^\infty\} + ([S^\Omega] - [I]) \{\nabla T^{*\Omega}\} \\ + ([S^V] - [S^\Omega]) \{\nabla T^{*M}\}\}, \end{aligned} \quad (19a)$$

$$\begin{aligned} [K^M] \{\{\nabla T^\infty\} + [S^V] \{\nabla T^{*M}\} \\ + \frac{f}{1-f} ([S^V] - [S^\Omega]) (\{\nabla T^{*\Omega}\} - \{\nabla T^{*M}\})\} \\ = [K] \{\{\nabla T^\infty\} + ([S^V] - [I]) \{\nabla T^{*M}\} + \frac{f}{1-f} \\ ([S^V] - [S^\Omega]) (\{\nabla T^{*\Omega}\} - \{\nabla T^{*M}\})\}. \end{aligned} \quad (19b)$$

Solving (19a) and (19b) simultaneously, one finds

$$\{\langle \nabla T^{*M} \rangle_M\} = [A] \{\nabla T^\infty\}, \quad (20a)$$

$$\{\langle \nabla T^{*\Omega} \rangle_\Omega\} = [B] \{\nabla T^\infty\}, \quad (20b)$$

where

$$\begin{aligned} [A] &= \left[\frac{f}{1-f} ([K^M][S^V] - [K^M][S^\Omega] \right. \\ &\quad \left. - [K][S^V] + [K][S^\Omega]) \right. \\ &\quad \left. + ([K][S^V] - [K] - [K^M][S^V]) \right. \\ &\quad \left. + \frac{f}{1-f} \right. \\ &\quad \left. ([K^M][S^V] - [K^M][S^\Omega] \right. \\ &\quad \left. - [K][S^V] + [K][S^\Omega]) \right. \\ &\quad \left. [[K^\Omega][S^\Omega] - [K]([S^\Omega] - [I])]^{-1} \right. \\ &\quad \left. ([K][S^V] - [K][S^\Omega]) \right. \\ &\quad \left. - [K^\Omega][S^V] + [K^\Omega][S^\Omega] \right]^{-1} \end{aligned}$$

$$\begin{aligned} & \left[\frac{f}{1-f} ([K^M][S^V] - [K^M][S^\Omega]) \right. \\ & \quad \left. - [K][S^V] + [K][S^\Omega] \right) \\ & \quad \left[[K^\Omega][S^\Omega] - [K]([S^V] - [I]) \right]^{-1} \\ & \quad \left. ([K] - [K^\Omega]) - ([K] - [K^M]) \right], \end{aligned} \quad (21)$$

$$\begin{aligned} [B] = & \left[[K^\Omega][S^\Omega] - [K]([S^\Omega] - [I]) \right]^{-1} \left[([K] - [K^\Omega]) \right] \\ & + \left[[K^\Omega][S^\Omega] - [K]([S^\Omega] - [I]) \right]^{-1} \\ & \left[[K]([S^V] - [S^\Omega]) - [K^\Omega]([S^V] - [S^\Omega]) \right] [A]. \end{aligned} \quad (22)$$

Substituting (17a) and (17b) and (18a) and (18b) into (14a) and (14b), one finds

$$\begin{aligned} \{ \langle \nabla T^d \rangle_V \} = & \{ \nabla T^\infty \} \\ & + [S^V] \{ f \{ \nabla T^{*\Omega} \} + (1-f) \{ \nabla T^{*M} \} \}, \end{aligned} \quad (23a)$$

$$\begin{aligned} \{ \langle q^d \rangle_V \} = & [K] \{ \nabla T^\infty \} \\ & + ([S^V] - [I]) \\ & \left[f \{ \nabla T^{*\Omega} \} + (1-f) \{ \nabla T^{*M} \} \right]. \end{aligned} \quad (23b)$$

The thermal conductivities \bar{K} of the double inclusion V are defined by

$$\{ \langle q^d \rangle_V \} = [\bar{K}] \{ \langle \nabla T^d \rangle_V \}. \quad (24)$$

The combination of (20a) and (20b), (23a) and (23b), and (24) gives

$$\begin{aligned} [\bar{K}] = & [K] \left[\{ [I] + ([S^V] - [I]) [f[B] + (1-f)[A]] \} \right] \\ & \left[\{ [I] + [S^V] [f[B] + (1-f)[A]] \} \right]^{-1}. \end{aligned} \quad (25)$$

A reasonable choice for the reference material for homogenization is the matrix material. Thus, $\nabla T^{*M} = 0$. Letting $[A] = 0$ in (25) gives

$$\begin{aligned} [\bar{K}] = & [K^M] \left[\{ [I] + f([S^V] - [I]) \} \right. \\ & \left. \left[([K^M] - [K^\Omega])[S^\Omega] - [K^M] \right]^{-1} \right. \\ & \left. \left[([K^\Omega] - [K^M]) \right] \right] \\ & \left[\{ [I] + f[S^V] \} \right. \\ & \left. \left[([K^M] - [K^\Omega])[S^\Omega] - [K^M] \right]^{-1} \right. \\ & \left. \left[([K^\Omega] - [K^M]) \right] \right]^{-1}. \end{aligned} \quad (26)$$

In the case of CNT, the inner inclusion Ω is a void, and the outer M is a graphene. Therefore, the $[K^\Omega]$ in (26) may be neglected as the thermal conductivity of air is much less than that of the graphene, or $[K^\Omega] = 0$ in the case of a vacuum. Therefore, the thermal conductivities of a CNT can be estimated by

$$\begin{aligned} [\bar{K}] = & [K^M] \left(([S^\Omega] - [I] - f([S^V] - [I])) \right. \\ & \left. ([S^\Omega] - [I] - f[S^V])^{-1} \right). \end{aligned} \quad (27)$$

Specifically,

$$\bar{K}_{ii} = K_{ii}^M \left(1 - \frac{f}{1 - S_{ii}^\Omega + f S_{ii}^V} \right) \quad i = 1 \sim 3; \text{ no sum on } i. \quad (28)$$

In view of the analogy between heat conduction and linear elasticity, the elastic constants $[\bar{C}]$, which is a 6×6 matrix, of a CNT can be estimated by

$$\begin{aligned} [\bar{C}] = & [C^M] \left(([C^\Omega] - [I] - f([C^V] - [I])) \right. \\ & \left. ([C^\Omega] - [I] - f[C^V])^{-1} \right), \end{aligned} \quad (29)$$

where $[C^M]$ is the stiffness matrix of a single-crystal graphite, $[I]$ is the 6×6 identity matrix, and the components of Eshelby's matrix for anisotropic elastic inclusions are given by Mura [23]. In particular, the shear moduli of a CNT can be estimated by

$$\bar{C}_{ii} = C_{ii}^M \left(1 - \frac{f}{1 - S_{ii}^\Omega + f S_{ii}^V} \right) \quad i = 4 \sim 6; \text{ no sum on } i. \quad (30)$$

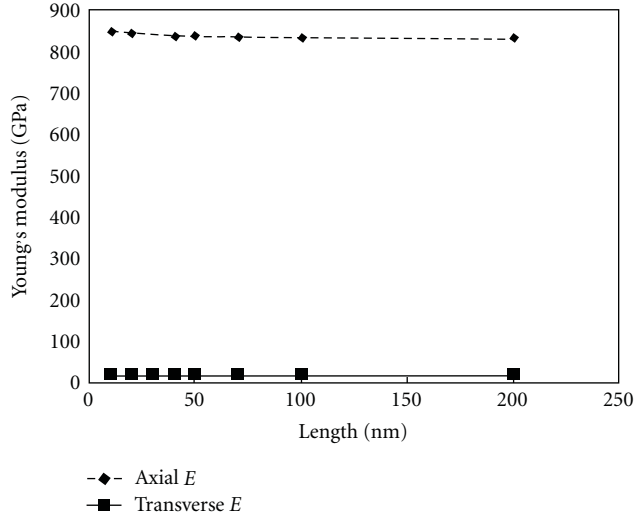


FIGURE 3: Young's modulus as a function of CNT length for $t = 0.34$ nm and $D = 1.2$ nm.

3. Results

The following elastic properties of a single-crystal graphite are used in our calculations [24]:

$$[C^M] = \begin{bmatrix} 1060 & 15 & 180 & 0 & 0 & 0 \\ 15 & 36.5 & 15 & 0 & 0 & 0 \\ 180 & 15 & 1060 & 0 & 0 & 0 \\ 0 & 0 & 0 & 4.5 & 0 & 0 \\ 0 & 0 & 0 & 0 & 440 & 0 \\ 0 & 0 & 0 & 0 & 0 & 4.5 \end{bmatrix} \text{ GPa.} \quad (31)$$

As it is indicated in Figure 3, where the diameter and thickness of CNT are assumed to be 1.2 nm and 0.34 nm, respectively, the length of CNT does not affect its axial and transverse Young's moduli significantly. The relationship between axial Young's modulus and the diameter of CNT is shown in Figure 4, where the length and thickness of CNT are assumed to be 1 μm and 0.34 nm, respectively. The predicted axial Young's modulus increases with a decrease in CNT diameter, which is consistent with the available experimental data, yet is in contrast with what is predicted by Li and Chou [18]. It is noted that axial Young's modulus drops significantly when the CNT diameter is greater than 1.2 nm. The transverse Young modulus of CNT exhibits a similar relation with CNT diameter. The relationship between CNT diameter and thickness, for a fixed axial Young's modulus of 1 TPa, is shown in Figure 5, which agrees with Thostenson et al. [25].

The in-plane and out-of-plane thermal conductivities of graphene are assumed to be equal to 2,000 and 10 W/m-K, respectively [26] in the present calculations. The thermal conductivity of air varies from 0.02 to 0.08 W/m-K as the temperature varies from -55°C to $1,000^\circ\text{C}$ and is negligible. As it is indicated in Figure 6, where the diameter of CNT is assumed to be 1.2 nm and 1.4 nm and the CNT thickness is

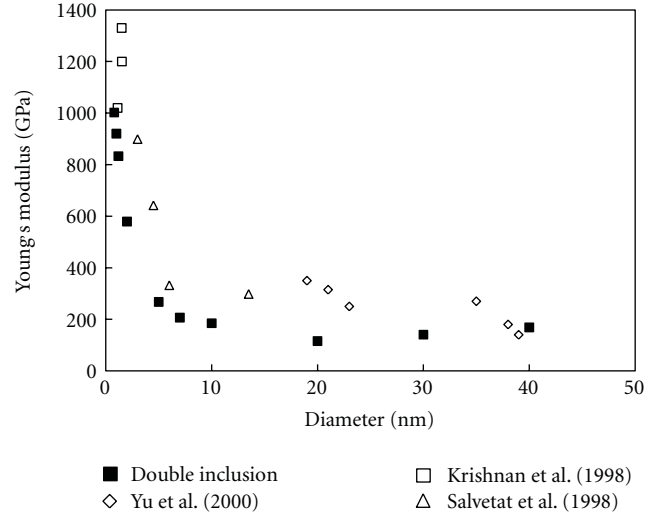


FIGURE 4: Young's modulus versus CNT diameter for $t = 0.34$ nm and $L = 1000$ nm.

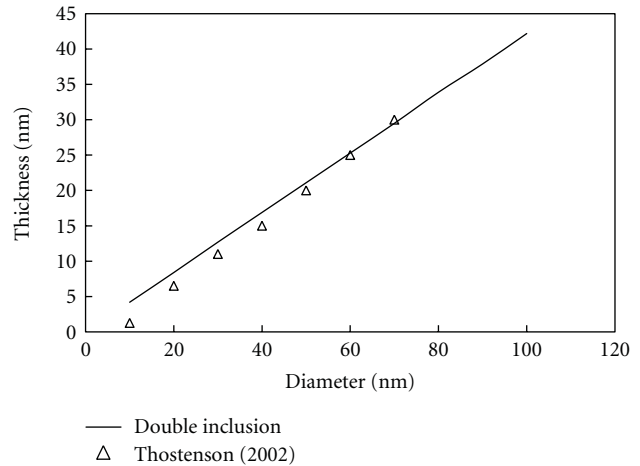


FIGURE 5: The relationship between CNT diameter and CNT thickness for $\bar{E} = 1$ TPa.

assumed to be 0.34 nm, the length of CNT does not affect its axial thermal conductivity significantly, which is consistent to the findings of Yang et al. [27] and Hone et al. [28]. The relationship between CNT diameter and its thermal conductivity for a fixed length of 100 nm is shown in Figure 7, where the thickness of CNT is assumed to be 0.34 nm, and the axial thermal conductivity of CNT decreases dramatically with an increase in CNT diameter when the CNT diameter is less than 10 nm. When the CNT diameter is greater than 10 nm, the decrease in axial thermal conductivity of CNT becomes gradual. Figure 8 shows the relationship between CNT aspect ratio and its axial thermal conductivity. The axial thermal conductivity increases with an increase in the aspect ratio of CNT [17]. The relationship between the axial thermal conductivity of MWCNT and its number of layers is shown in Figure 9, where the MWCNT outer diameter, length, and thickness of each layer are assumed to be 14 nm, 100 nm, and 0.34 nm, respectively.

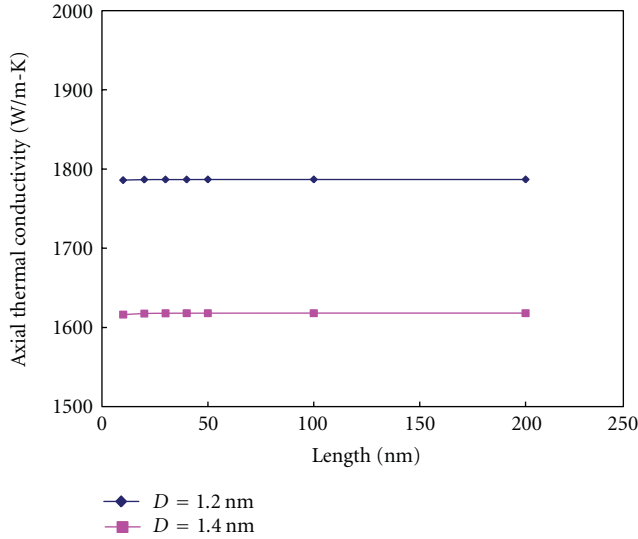


FIGURE 6: Axial thermal conductivity of CNT as a function of CNT length for $t = 0.34$ nm, $D = 1.2$ nm, and $D = 1.4$ nm.

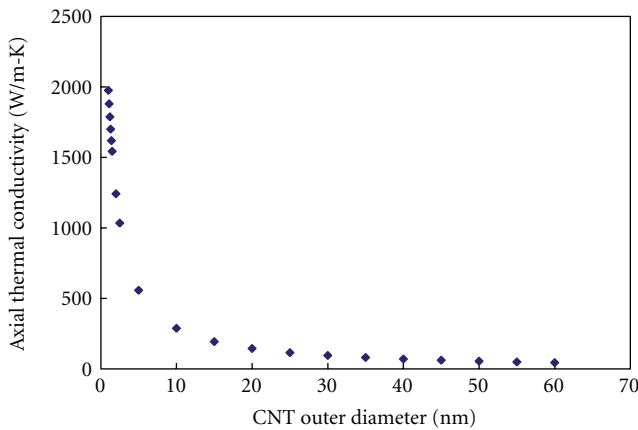


FIGURE 7: Axial thermal conductivity as a function of CNT outer diameter for $t = 0.34$ nm and $L = 100$ nm.

4. Conclusion

In the present work, the double-inclusion model [1], which is based on elasticity solutions [20, 21] and is originally presented in the context of linear elasticity, is employed and extended to predict the thermal conductivities and elastic constants of CNTs. Though the theorem proposed by Mori and Tanaka [21] is not restricted to ellipsoidal inclusions, the present work regards a CNT as a circular cylindrical shell containing a concentric circular cylindrical void, that is, two coaxial circular cylindrical inclusions—one is embedded in the other. The outer shell is composed of a single-crystal graphite sheet.

Our results indicate that (1) the length of CNT does not significantly affect its thermal conductivities, axial and transverse Young's and shear moduli; (2) with an increase in CNT diameter, axial and transverse Young's moduli and thermal conductivities as well as shear moduli decrease. This may

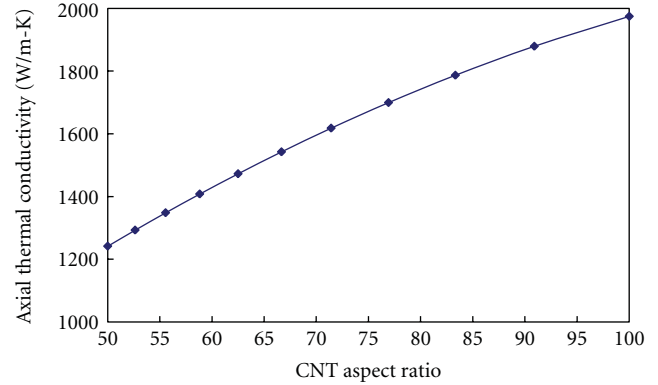


FIGURE 8: Relationship between axial thermal conductivity and CNT aspect ratio.

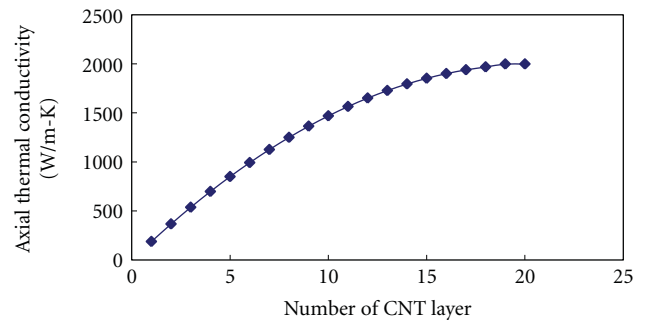


FIGURE 9: Relationship between axial thermal conductivity of MWCNT and its number of layers.

explain why the reported experimental data in the literature (see Tables 1 and 2) are scattered when the thermal conductivity and elastic properties of a CNT are considered as functions of its microstructure, in particular, its diameter. The results derived from the present model agree quite well with the available experimental measurement and observation.

Acknowledgment

This work is supported by the National Science Council in Taiwan under Grant no. NSC95-2221-E-155-016 to Yuan Ze University, Taiwan.

References

- [1] M. Hori and S. Nemat-Nasser, "Double-inclusion model and overall moduli of multi-phase composites," *Mechanics of Materials*, vol. 14, no. 3, pp. 189–206, 1993.
- [2] B. I. Yakobson, C. J. Brabec, and J. Bernholc, "Nanomechanics of carbon tubes: instabilities beyond linear response," *Physical Review Letters*, vol. 76, no. 14, pp. 2511–2514, 1995.
- [3] G. Gao, T. Çağın, and W. A. Goddard, "Energetics, structure, mechanical and vibrational properties of single-walled carbon nanotubes," *Nanotechnology*, vol. 9, no. 3, pp. 184–191, 1998.
- [4] S. Berber, Y. K. Kwon, and D. Tománek, "Unusually high thermal conductivity of carbon nanotubes," *Physical Review Letters*, vol. 84, no. 20, pp. 4613–4616, 2000.

- [5] M. A. Osman and D. Srivastava, "Temperature dependence of the thermal conductivity of single-wall carbon nanotubes," *Nanotechnology*, vol. 12, no. 1, pp. 21–24, 2001.
- [6] S. Maruyama, "A molecular dynamics simulation of heat conduction in finite length SWNTs," *Physica B*, vol. 323, no. 1–4, pp. 193–195, 2002.
- [7] K. Bi, Y. Chen, J. Yang, Y. Wang, and M. Chen, "Molecular dynamics simulation of thermal conductivity of single-wall carbon nanotubes," *Physics Letters A*, vol. 350, no. 1–2, pp. 150–153, 2006.
- [8] S. Govindjee and J. L. Sackman, "On the use of continuum mechanics to estimate the properties of nanotubes," *Solid State Communications*, vol. 110, no. 4, pp. 227–230, 1999.
- [9] V. M. Harik, "Ranges of applicability for the continuum beam model in the mechanics of carbon nanotubes and nanorods," *Solid State Communications*, vol. 120, no. 7–8, pp. 331–335, 2001.
- [10] D. H. Robertson, D. W. Brenner, and J. W. Mintmire, "Energetics of nanoscale graphitic tubules," *Physical Review B*, vol. 45, no. 21, pp. 12592–12595, 1992.
- [11] J. P. Lu, "Elastic properties of carbon nanotubes and nanoropes," *Physical Review Letters*, vol. 79, no. 7, pp. 1297–1300, 1997.
- [12] X.-L. Gao and K. Li, "Finite deformation continuum model for single-walled carbon nanotubes," *International Journal of Solids and Structures*, vol. 40, no. 26, pp. 7329–7337, 2003.
- [13] X. L. Gao and K. Li, "A shear-lag model for carbon nanotube-reinforced polymer composites," *International Journal of Solids and Structures*, vol. 42, no. 5–6, pp. 1649–1667, 2005.
- [14] P. Chantrenne and J.-L. Barrat, "Analytical model for the thermal conductivity of nanostructures," *Superlattices and Microstructures*, vol. 35, no. 3–6, pp. 173–186, 2004.
- [15] P. Poncharal, Z. L. Wang, D. Ugarte, and W. A. De Heer, "Electrostatic deflections and electromechanical resonances of carbon nanotubes," *Science*, vol. 283, no. 5407, pp. 1513–1516, 1999.
- [16] M. C. Llaguno, J. Hone, A. T. Johnson, and J. E. Fischer, "Thermal conductivity of single wall carbon nanotubes: diameter and annealing dependence," in *Proceedings of the AIP Conference*, vol. 591, pp. 384–387, 2001.
- [17] P. Grassberger and L. Yang, "Heat conduction in low dimensions: from fermi-pasta-ulam chains to single-walled nanotubes," 2002, <http://arxiv.org/abs/cond-mat/0204247v1>.
- [18] C. Li and T. W. Chou, "A structural mechanics approach for the analysis of carbon nanotubes," *International Journal of Solids and Structures*, vol. 40, no. 10, pp. 2487–2499, 2003.
- [19] D. Qian, G. J. Wagner, W. K. Liu, M. F. Yu, and R. S. Ruoff, "Mechanics of carbon nanotubes," *Applied Mechanics Reviews*, vol. 55, no. 6, pp. 495–533, 2002.
- [20] J. D. Eshelby, "The determination of elastic field of an ellipsoidal inclusion and related problems," *Proceedings of the Royal Society of London A*, vol. 241, no. 1226, pp. 376–396, 1957.
- [21] T. Mori and K. Tanaka, "Average stress in matrix and average elastic energy of materials with misfitting inclusions," *Acta Metallurgica*, vol. 21, no. 5, pp. 571–574, 1973.
- [22] H. Hatta and M. Taya, "Equivalent inclusion method for steady state heat conduction in composites," *International Journal of Engineering Science*, vol. 24, no. 7, pp. 1159–1172, 1986.
- [23] T. Mura, *Micromechanics of Defects in Solids*, Martinus Nijhoff, Boston, Mass, USA, 1982.
- [24] J. Z. Liu, Q. Zheng, and Q. Jiang, "Effect of a rippling mode on resonances of carbon nanotubes," *Physical Review Letters*, vol. 86, no. 21, pp. 4843–4846, 2001.
- [25] E. T. Thostenson, W. Z. Li, D. Z. Wang, Z. F. Ren, and T. W. Chou, "Carbon nanotube/carbon fiber hybrid multiscale composites," *Journal of Applied Physics*, vol. 91, no. 9, pp. 6034–6037, 2002.
- [26] Electronics Cooling 2007, http://www.electronics-cooling.com/articles/2001/2001_august_techbrief.php.
- [27] D. J. Yang, S. G. Wang, Q. Zhang, P. J. Sellin, and G. Chen, "Thermal and electrical transport in multi-walled carbon nanotubes," *Physics Letters, Section A*, vol. 329, no. 3, pp. 207–213, 2004.
- [28] J. Hone, A. Zettl, and M. Whitney, "Thermal conductivity of single-walled carbon nanotubes," *Synthetic Metals*, vol. 103, no. 1–3, pp. 2498–2499, 1999.
- [29] P. Kim, L. Shi, A. Majumdar, and P. L. McEuen, "Mesoscopic thermal transport and energy dissipation in carbon nanotubes," *Physica B*, vol. 323, no. 1–4, pp. 67–70, 2002.
- [30] A. Bagchi and S. Nomura, "On the effective thermal conductivity of carbon nanotube reinforced polymer composites," *Composites Science and Technology*, vol. 66, no. 11–12, pp. 1703–1712, 2006.
- [31] J. P. Salvetat, G. A. D. Briggs, J. M. Bonard et al., "Elastic and shear moduli of single-walled carbon nanotube ropes," *Physical Review Letters*, vol. 82, no. 5, pp. 944–947, 1998.
- [32] J. P. Salvetat, J. M. Bonard, N. B. Thomson et al., "Mechanical properties of carbon nanotubes," *Applied Physics A*, vol. 69, no. 3, pp. 255–260, 1999.
- [33] A. Krishnan, E. Dujardin, P. N. Yianilos, and M. M. J. Treacy, "Young's modulus of single-walled nanotubes," *Physical Review B*, vol. 58, no. 20, pp. 14013–14019, 1998.
- [34] M. F. Yu, B. S. Files, S. Arepalli, and R. S. Ruoff, "Tensile loading of ropes of single wall carbon nanotubes and their mechanical properties," *Physical Review Letters*, vol. 84, no. 24, pp. 5552–5555, 2000.
- [35] M. F. Yu, T. Kowalewski, and R. S. Ruoff, "Investigation of the radial deformability of individual carbon nanotubes under controlled indentation force," *Physical Review Letters*, vol. 85, no. 7, pp. 1456–1459, 2000.

Review Article

Large-Scale Integrated Carbon Nanotube Gas Sensors

Joondong Kim

Nano-Mechanical Systems Research Center, Korea Institute of Machinery and Materials (KIMM), Daejeon 305343, Republic of Korea

Correspondence should be addressed to Joondong Kim, joonkim@kimm.re.kr

Received 16 October 2011; Revised 7 March 2012; Accepted 20 March 2012

Academic Editor: Teng Li

Copyright © 2012 Joondong Kim. This is an open access article distributed under the Creative Commons Attribution License, which permits unrestricted use, distribution, and reproduction in any medium, provided the original work is properly cited.

Carbon nanotube (CNT) is a promising one-dimensional nanostructure for various nanoscale electronics. Additionally, nanostructures would provide a significant large surface area at a fixed volume, which is an advantage for high-responsive gas sensors. However, the difficulty in fabrication processes limits the CNT gas sensors for the large-scale production. We review the viable scheme for large-area application including the CNT gas sensor fabrication and reaction mechanism with a practical demonstration.

1. Introduction

Due to the excellent and well-known properties of nanoscale materials, intensive research has been performed in various areas. The one-dimensional nanoscale structure of a nanowire or a nanotube is attractive for use in effective cold cathodes [1], field emitters [2], and vacuum microelectronics [3, 4]. Recently, silicide nanowire has shown the possibility of nanoscale interconnection with low resistance [5, 6]. Additionally, carbon nanotubes have been applied in various applications such as energy storage devices, sensors [7, 8], and actuators. The electrical conductivity of carbon nanotubes (CNTs) is prominent (10^6 S m^{-2}), and thus CNT films also possess a low sheet resistance while holding an excellent optical transmittance in the visible spectrum comparable to that of commercial indium-tin-oxide (ITO); a transparent CNT film heater has been realized [9].

The one-dimensional nanoscale structure of CNT has a large surface area to volume ratio, which is an advantage for maximizing the surface response. Moreover, the radii, which are comparable to the Debye length, offer greater potential in sensing performance, compared to bulk, by showing sensitive changes upon exposure to gas molecules.

CNTs have been intensively investigated for use in gas sensing devices due to their unique physical and chemical properties [10–18]. It has been proven that CNTs present the p-type semiconducting property due to their unique chirality. The absorbing gas molecules can significantly

change the conductivity of CNTs by withdrawing and donating electrons [7, 10, 19]. Moreover, the high surface-to-volume ratio of CNTs provides an advantage in sub-ppm level gas detection. The theoretical concept of using metal-nanoparticle functionalized CNTs has been reported and it has been shown that metal nanoparticles act as reactive sites to target gas molecules. A significant change in electrical conductivity is driven by absorbing target molecules [15–20].

This paper reviews the previous reports on CNT-based gas sensors. It discusses the deployment method of CNTs for large-scale applications with a working mechanism.

2. Fabrication Methods

2.1. Fabrication of CNTs. Generally, three types of method are used to growth CNTs [14]. The first method is the arc-discharge method, which grows single and multi-walled CNTs in a vacuum system under an inert gas atmospheric condition. In laser ablation, a carbon target ablated by intense laser pulses in a furnace and the formed CNTs are collected on a cold substrate. The chemical vapor deposition method is the most popular technique; it uses a gaseous carbon source resulting in vertical grown CNTs. Moreover, quality CNTs can be produced at a reduced growth temperature under 1000°C , which compares favorably to the temperature above 3000°C of the arc-discharge or the laser ablation processes. Recently, the hydrothermal method has been developed for the formation of crystalline particles or films;

this method provides more opportunity for the modification of the CNT configuration [15]. Hetero-structured CNT entities, such as CNT-ZnO film [21] and Fe₃O₄ nanoscale crystal-treated CNTs [22], have demonstrated the quality heterojunction between CNTs [15].

2.2. Dielectrophoresis. It is an essential process to assign nanostructures at a designated spot for device applications [5, 6]. Dielectrophoresis (DEP) is a promising approach to align nanostructures at a designated position with high reliability and accessibility. A motion is induced by the polarization effect exerting a force on a dielectric particle under a nonuniform electric field condition. The DEP method was performed to align CNTs by dropping the CNT-containing solution between the electric field applied to metal electrodes.

2.3. Inkjet Printing. Although the benefit of nanomaterials has been clarified in various applications, the assignment of manipulating the nanoscale materials with certainty in practical applications still remained. It is an essential and inevitable process to control the nanomaterials at designated positions. Inkjet printing is the demand-oriented technology by dropping ink droplets when required. The drop-on-demand scheme is realistic and large area available approach of locating functional materials [8]. The inkjet printing method provides the schemes of high sensitive CNT-embedded gas sensor units on a wafer-scale by inkjetting carbon-nanotube-contained solution following the conventional lithographical metal lift-off processes.

3. Results and Discussion

3.1. CNT Mats. In the sensor fabrication, a Ti adhesion layer of 5 nm thick was deposited before a 50 nm thick Pt coating on an SiO₂-coated wafer. Firstly, a CNTs dispersed solution was prepared by ultrasonic vibrating from the CNTs grown substrate, and then the CNT solution was dropped between Pt electrodes under an ac electric field of 10 V at 10 kHz. The CNTs-connected electrodes were observed by field emission scanning electron microscopy (FESEM, FEI Sirion), as shown in Figure 1. No post contact treatment has been performed to reinforce the contact formation between CNTs to Pt electrodes.

The electrical measurement from the as-placed CNTs on Pt electrodes gave a resistance of 64.5 kΩ swept by Keithley 2400, as shown in Figure 2. There was no significant contact noisy resistance reported as much as Megohm unit [23], which was supposed to be very small [6].

Figure 3 is the CNT sensor response to 100 ppb NO₂ gas. The CNT sensor response [R] was defined as the ratio $R = (R_i - R_r)/R_i$, where R_i and R_r represent the initial resistance and the reacted resistance to NO₂ gas, respectively. Two different magnitude voltages of 0.5 and 2.0 V were applied and four various processing steps were taken to investigate the CNT sensor performance. The first process (I) was the sensor response to NO₂ for 50 min showing different responses by changing the applied voltage. A higher input voltage of 2.0 V enhanced the sensing response compared to that of 0.5 V

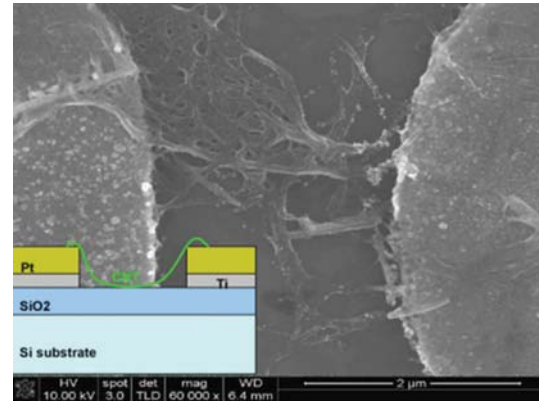


FIGURE 1: A SEM image of the as-deposited CNTs on Pt electrodes by a DEP method. Inset shows a schematic cross-sectional view [7].

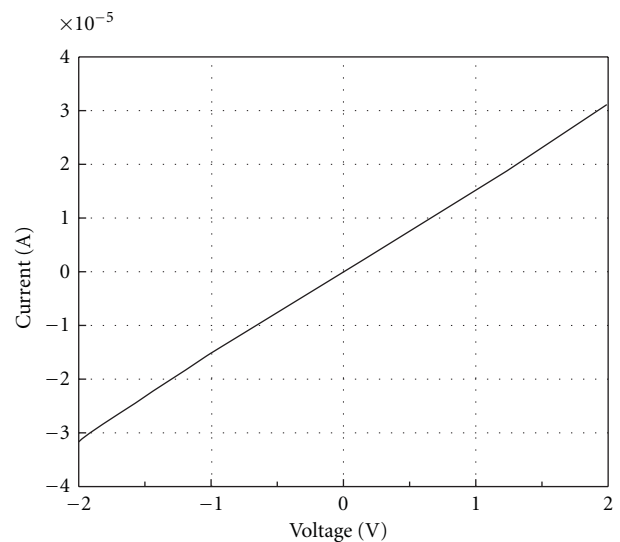


FIGURE 2: Electrical measurement of the as-deposited CNTs on Pt electrodes [7].

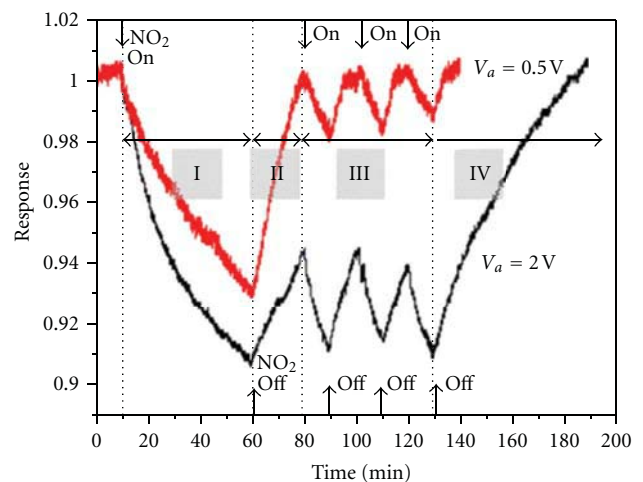


FIGURE 3: The time-dependent sensing response to 100 ppb NO₂ of the CNT sensor at room temperature [7].

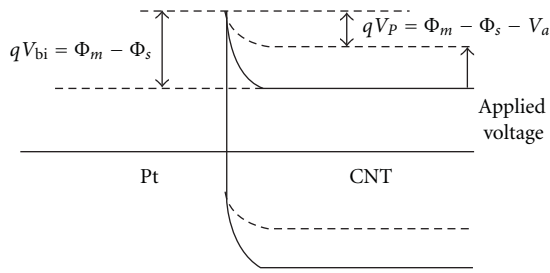


FIGURE 4: The band diagram of the Pt and CNT junction [7].

applied case. The second process (II) was to recover the initial resistance by UV illumination for a limited time span of 20 min. The third process (III) was performed to investigate the transient NO_2 responses and UV light recovery steps for 10 min time spans. The last step (IV) was performed for fully recovering the initial resistance by longer time duration of 60 min, especially for the 2.0 V case.

The UV-illuminated recovery seems to be very effective; otherwise, it takes more than 15 h. The UV illumination decreases the desorption-energy barrier to facilitate NO_2 desorption from the CNTs. As clearly shown in the figure, the larger voltage input provided higher response in the first region (I). More details will be discussed in the later part. In the second step (II), the case of a lower voltage of 0.5 V was fully recovered for 20 min, while the higher voltage of 2.0 V was partially recovered. For the transient responses (III), the NO_2 sensing and recovery were repeatedly achieved in a 10 min time span. A long recovery time of 60 min was needed to recover the initial resistance for the 2.0 V input case denoted as region IV. It is remarkable that the applied voltage controls the sensor responses. The gas sensing response was improved by increasing the applied voltage. However, the higher applied voltage case required a longer recovery time of 60 min, resulting from the increased transferring carriers from CNTs to electrodes. This can be explained by changes in the Schottky junction formation between CNTs and Pt electrodes, where the work function is 4.5 and 5.65 eV, respectively. A corresponding schematic of the Schottky formation of Pt and CNT contacts is shown in Figure 4.

There exists a potential barrier for the electron transferring from CNTs to the metal. The band bending or built-in potential (V_{bi}) of the Pt and CNT connection is given by

$$V_{bi} = \Phi_m - \Phi_s. \quad (1)$$

The initial built-in potential is equal to 1.15 eV from the equation. Under the bias (V_a), the carrier transferring from CNTs to Pt is enhanced due to the reduced potential barrier as given by

$$V_p = \Phi_m - \Phi_s - V_a. \quad (2)$$

The easier electron transferring by the forward bias-induced barrier lowering may enhance the gas reacting response, which also explains the longer recovery time for the higher applied voltage case. By increasing the number of transferring electrons from CNTs to the Pt electrode by increasing

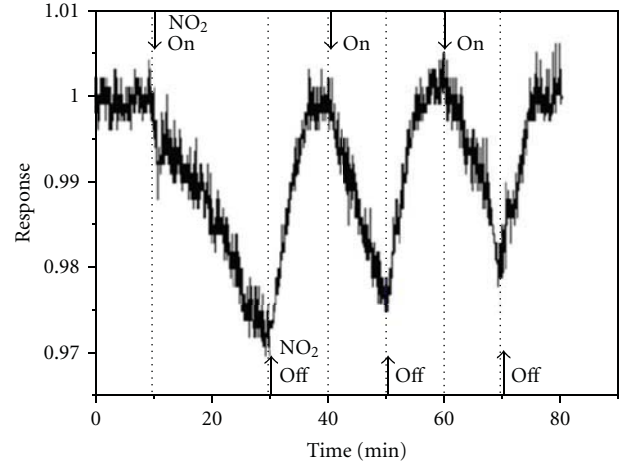


FIGURE 5: The time-dependent sensing response to 50 ppb NO_2 of the CNT sensor at room temperature [7].

the input voltage, more electrons might be captured by NO_2 molecules resulting in the need of a longer recovery time.

Figure 5 shows the sensor response at an NO_2 concentration of 50 ppb. The bias voltage of 2 V was applied, and the experimental conditions and processes were given similar to the case of 100 ppb NO_2 . The CNT sensor detected the 50 ppb level of NO_2 successfully and repeatedly. Due to the low NO_2 concentration, the first gas reaction was performed in 20 min, and then the time was spanned as 10 min. This CNT sensor operating at room temperature and atmospheric pressure showed highly sensitive and reliable performances. It is an advantage in fabrication to reduce the processing steps and cost.

3.2. Pd-Decorated CNTs. In preparation of the CNT containing solution, commercial arc discharge synthesized single-wall CNTs (Iljin nanotech, ASP-100) were dispersed in a dimethylformamide (DMF) solution for hydrophilic condition to debundle and stabilize the CNT dispersion in solution followed by centrifugation for 30 min to remove residuals. The supernatant was decanted after the sonication process. The concentration of the CNT solution was approximately $20 \mu\text{g mL}^{-1}$. To produce the Pd nanoparticle decoration on CNTs, a palladium(II) chloride (Sigma Aldrich) solution was mixed with the bare CNT solution at a volume ratio of 3 : 10. The CNT-containing solution of $0.2 \mu\text{L}$ was dropped between the Pt electrodes under an ac electric field of $10 V_{p-p}$ (peak-to-peak) at 1 kHz.

Figure 6 showed the Pd-decorated CNTs on the Pt metal electrodes. The interdigitated Pt electrodes having 10 fingers with a $2 \mu\text{m}$ gap were presented in Figure 6(a). The image of a single finger was presented in Figure 6(b). The enlarged images were shown in Figures 6(c) and 6(d). The Pt nanoparticle-decorated CNTs were clearly observed. Thermal treatment was performed by a rapid thermal process (RTP 2000, SNTK), which stabilized the contact between the CNTs and Pt metal electrodes by lowering the contact resistance. Raman spectroscopy was used to investigate the

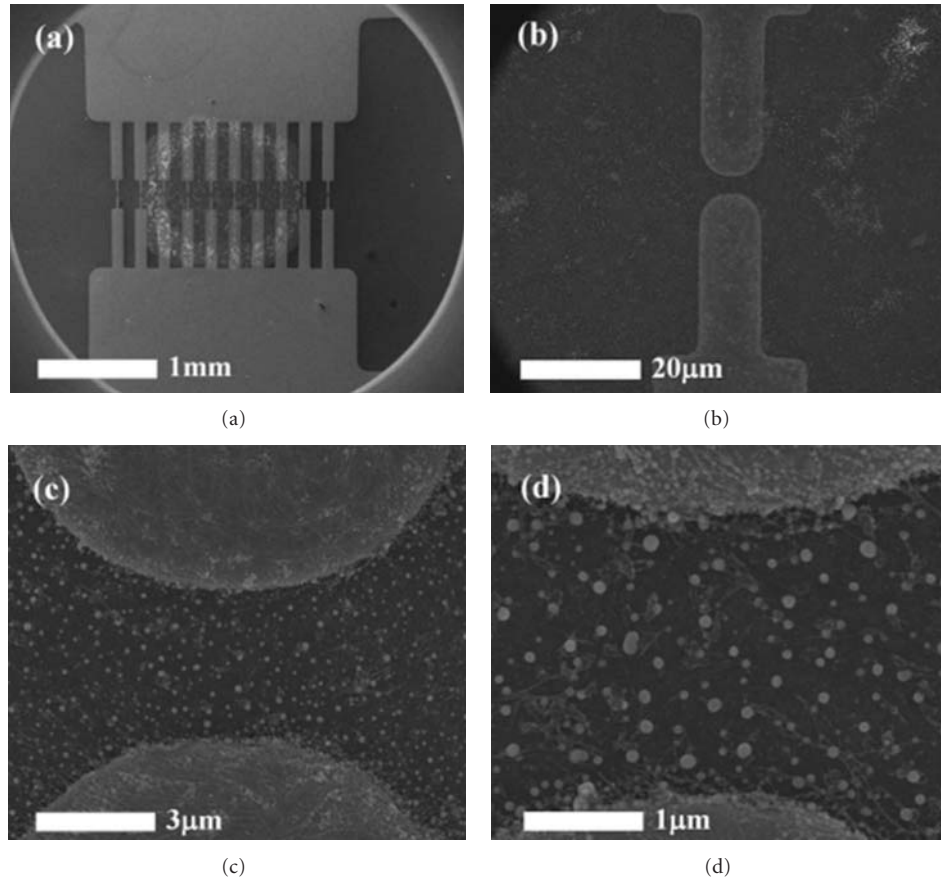


FIGURE 6: SEM images of Pd-CNTs between Pt electrodes assembled by the DEP method. (a) Ten finger Pt electrodes, (b) a single finger, (c) Pd-CNTs aligned Pt electrodes, and (d) an enlarged image of (c) [24].

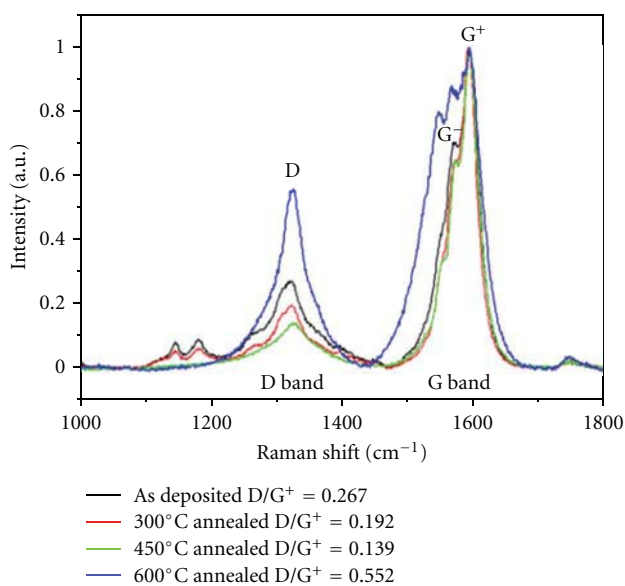


FIGURE 7: Raman signals of D and G spectra at 632.8 nm excitation showing the defect ratios from the Pd-CNTs treated at different temperatures [24].

defect level of Pd-CNT samples. The Raman spectra were observed at 632.8 nm excitation (1.96 eV) on the dropped and dried CNT solution on a silicon substrate. Three different types of samples were thermally treated at 300, 450, and 600°C for 1 min in an N₂ environment. The as-deposited sample was also investigated.

Figure 7 depicts the G band Raman peaks obtained at 1592 cm⁻¹ (G⁺) and 1572 cm⁻¹ (G⁻). The ratio of G⁻/G⁺ indicates the portion of metallic CNTs. The high peak value of D to G⁻ suggests a band resonance condition or heavy defect. Each peak of D was normalized by the G⁻ peak as the Pd-deposited CNTs showed 0.267 of the D/G⁻ value. By increasing the temperature, the D/G⁻ signal was remarkably reduced to 0.192 and 0.139 at 300°C and 450°C, respectively. It is worth noting that the increased defect ratio of 0.552 at a high annealing temperature of 600°C implies the oxidation of CNTs or damage on the CNT surface. It was found that there exists an optimum heat treating temperature to cure Pd-decorated CNTs, reducing the defect ratio. According to the Raman investigation, the CNT samples were thermally treated at 450°C after the DEP process for sensor fabrication, which also significantly reduced the initial sensor resistance of 225 MΩ to 220 Ω.

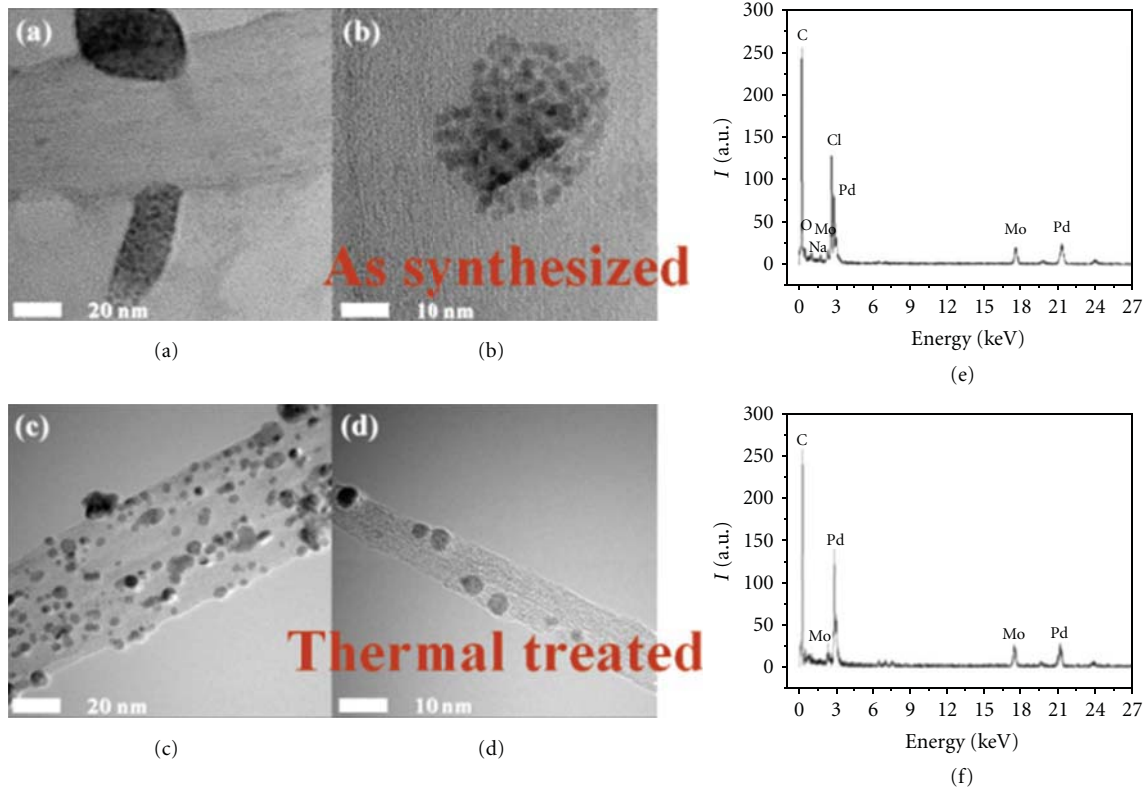


FIGURE 8: TEM images of Pd-decorated CNT. (a) and (b) are the as-synthesized case and (c) and (d) are thermally treated case, respectively. EDS analyses of (e) and (f) present the transition of chemical composition by a thermal treatment [24].

TEM images of Pd-CNTs are presented in Figure 8 before and after the thermal annealing. The aggregation of Pd nanoparticles was observed from the as-synthesized Pd-CNT sample as shown in Figures 8(a) and 8(b). Otherwise, the thermally treated Pd-CNTs at 450°C provided the uniformly dispersed Pd nanoparticles ranging from 3 to 5 nm in diameter, as shown in Figures 8(c) and 8(d). The EDS analysis was performed to investigate the compositional changes of the Pd-CNTs by thermal treatment. Figure 8(e) depicts the chemical signals of Pd, carbon (C), molybdenum (Mo), and chloride (Cl) as well. The Mo peak and Cl peak mainly originated from the TEM grid and Pd solution of palladium(II) chloride, respectively. After thermal treating at 450°C, the Cl peak was significantly removed, as shown in Figure 8(f), which contributed to reducing the sensor contact resistance.

The two types of fabricated bare CNTs and Pd-CNT gas sensors were loaded in a chamber for NO₂ gas detection with varying concentration levels of 100 ppb, 500 ppb, and 1 ppm. The response time and recovery time were limited to 5 min and 10 min, respectively. The target gas level was modulated by mixing the filtered clean air with pure NO₂ gas (99.999%) in a calibrator with an accuracy resolution of 0.1%. The measurement was performed in an atmospheric pressure condition without vacuum system assistance [25] or a gate control [26], which is an important feature in realizing the practical sensor application. The clean air was used as a base gas and purged for 5 min, which stabilized the base

measurement condition. During the purging process, there was little change in resistance values, showing the balanced electron-hole transportation in the steady state.

The sensor response (SR) was defined as the ratio of resistance change $SR = \Delta R/R_{ini}$, where ΔR and R_{ini} represent the resistance change by reacting to NO₂ gas and an initial resistance, respectively. The sensor responses were measured at different operating temperatures of room temperature (RT), 88, 145, and 321°C controlled by a ceramic heater with a digital power controller. The temperature was read by a k-type thermocouple. The gas responses from a Pd-CNT sensor and a bare CNT sensor were presented in Figures 9(a) and 9(b), respectively. During the limited response time of 5 min, the maximum response was found at 88°C from the Pd-CNT. For 100 ppb NO₂ detection, the sensor gave 0.25% response at RT without heating but the enhanced response was achieved at 88°C to be 3.67% and 2.79% from the Pd-CNT sensor and the bare CNT sensor, respectively. By increasing the gas concentration, the responses were proportionally increased. At a fixed heating temperature of 88°C, the Pd-CNT sensor response was found to be 8.54% at 500 ppb and 9.91% at 1 ppm, respectively. The enhanced response is attributed to the increase of gas absorption by the heating operation. To investigate the effect of heating temperature, the sensor response was scanned by varying the operating temperature.

At a fixed concentration of 100 ppb, the Pd-CNT sensor was more sensitive at 88°C, giving 3.67% compared to 3.45%

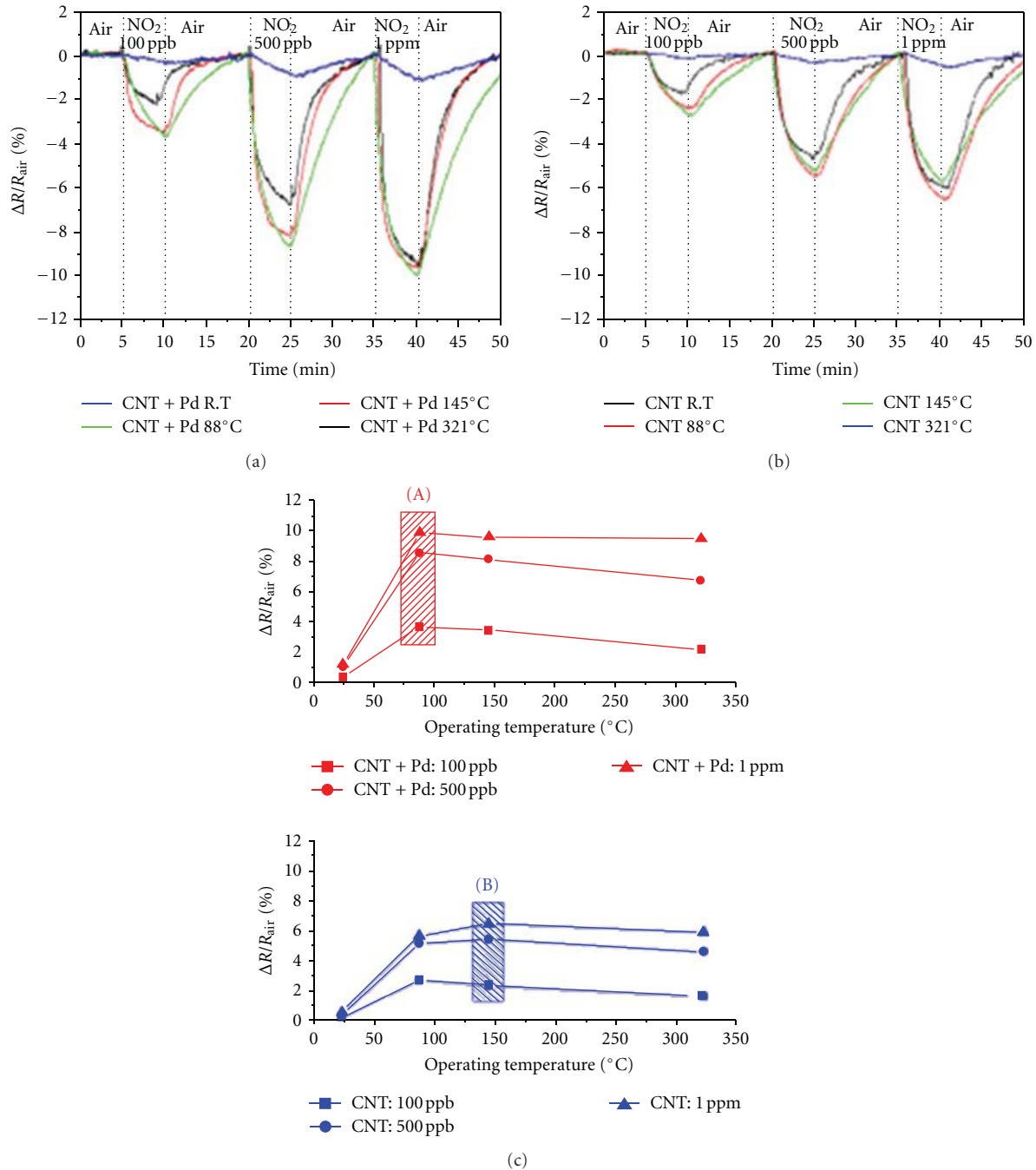


FIGURE 9: Sensor responses of (a) Pd-CNTs and (b) bare CNTs. The enhanced responses were achieved from the Pd-CNTs sensor. (c) The heating operation improved the sensor responses. The optimum operating temperatures were reduced by Pd decoration [24].

at 145°C or 2.17% at 321°C, as presented in Figure 9(c). It clearly indicates that there exists an optimum operating temperature. Above the critical temperature, the thermal conductivity of CNTs is decreased due to phonon scattering [28] and accelerates the desorption of gas molecules from the CNTs by lowering the energy barrier, resulting in a decrease of the response [25, 29]. Otherwise, the bare CNT sensor has a higher optimum operating temperature of 145°C with lower sensor response compared to the performance of the

Pd-CNTs. It is considered that the contribution of the Pd nanoparticle decoration on CNTs is quite significant in response to NO_2 gas.

Figure 10 presents the sensing mechanism of the Pd-CNTs sensor. A schematic of the Pd-CNT sensor is illustrated in Figure 10(a). The reaction of Pd decoration spots on CNTs was presented in Figure 10(b). Ideally, each Pd nanoparticle on a CNT forms a Schottky contact localizing the depletion region, which hinders the hole carrier mobility. Moreover,

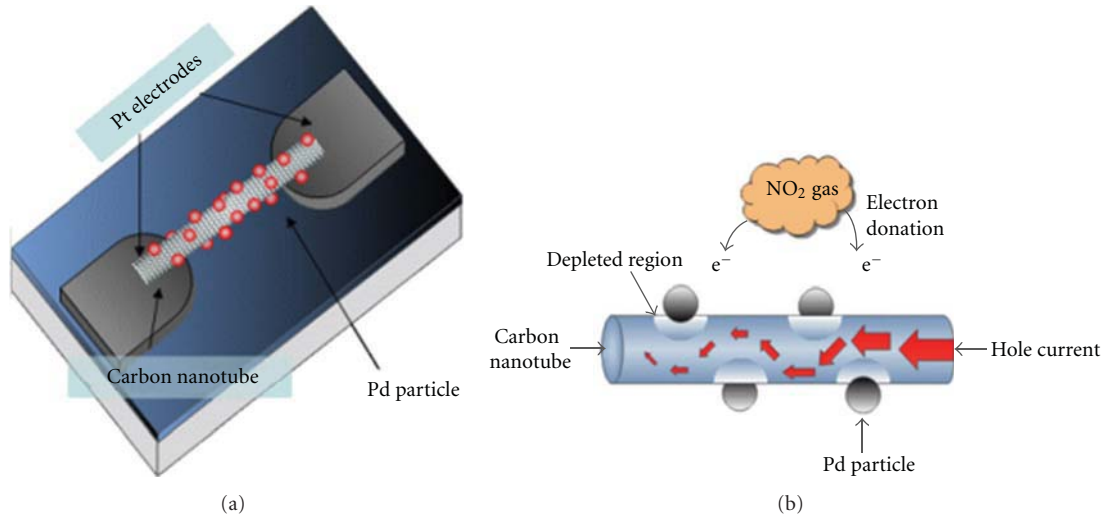


FIGURE 10: (a) A schematic of the sensor structure of the Pd-decorated CNTs. (b) The enhanced sensing mechanism of Pd-CNTs forming the depletion region by Pd nanoparticles [24].

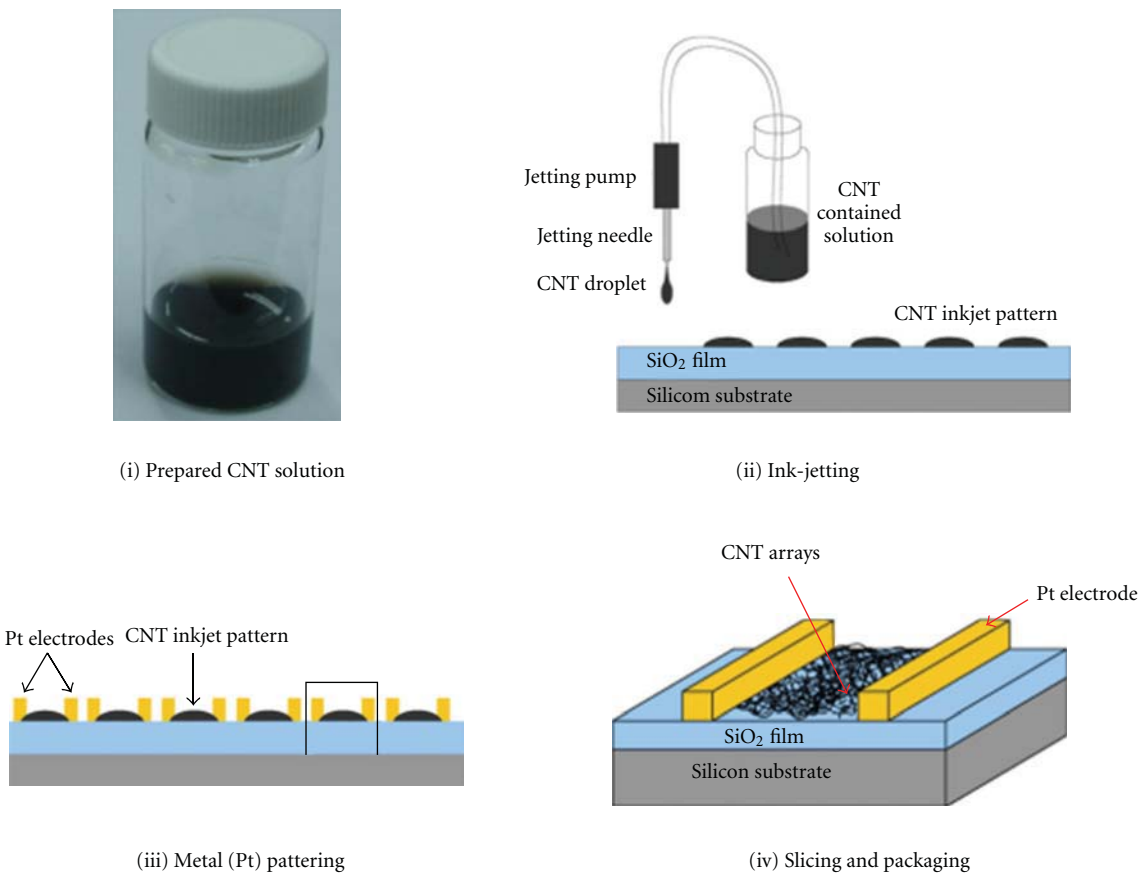


FIGURE 11: Gas sensor units fabrication steps [27].

the supply of electron carriers by reacting to the oxidizing gas of NO₂ causes an increase in electron-hole recombination, causing the lower hole carrier density in a CNT, which raises the effect of localizing depletion regions. This reaction conclusively reduces the hole carrier concentration,

which increases the sensor resistance, resulting in enhancing the response of the Pd-CNT sensor. It presents the scheme of a highly sensitive Pd-CNT gas sensor working in an atmospheric pressure condition, which is freed from the assistance of a vacuum system or a gate control, which may

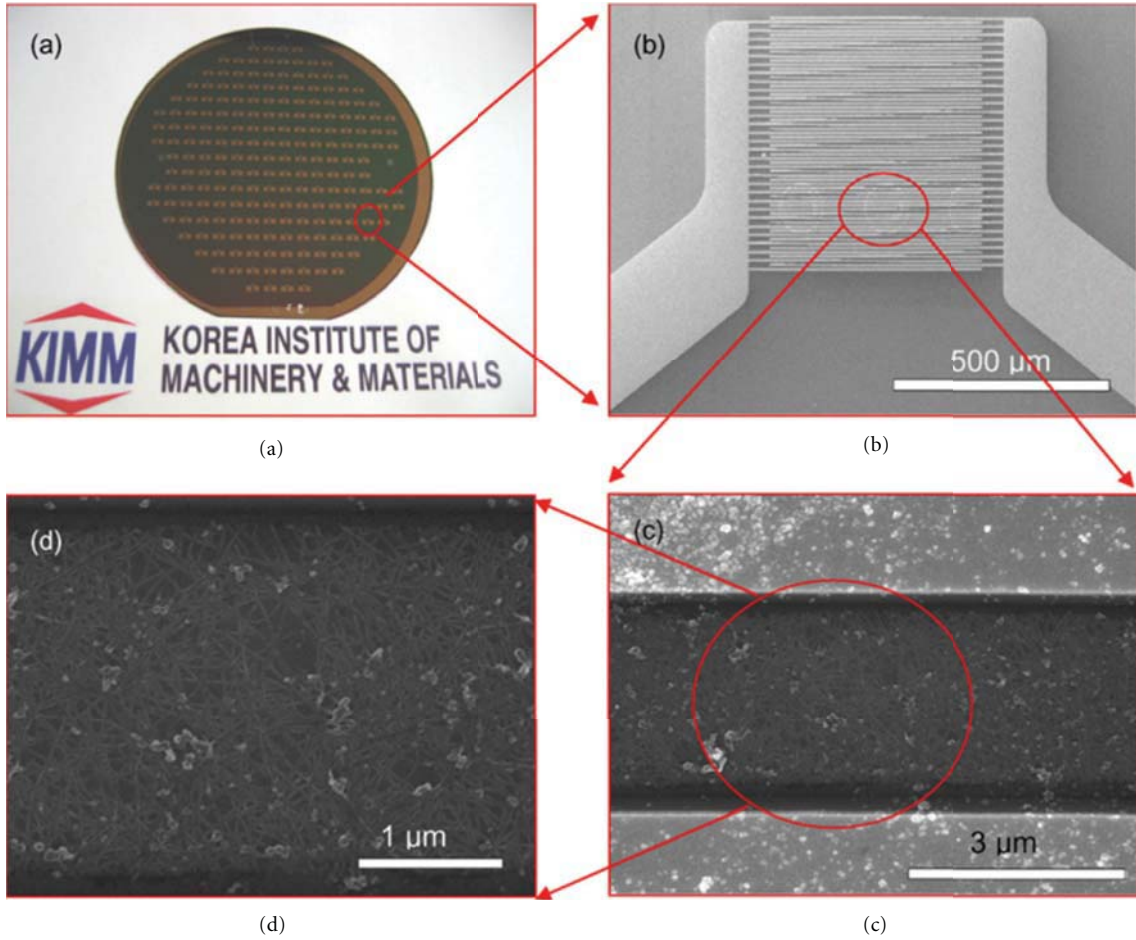


FIGURE 12: (a) A photograph image of 200 gas sensor units fabricated on a 4 in. wafer. (b) Interdigitated electrode fingers from a unit device. Enlarged SEM images of circle spots from (b) to (c) and from (c) to (d). CNT arrays clearly underlaid the Pt electrode fingers [27].

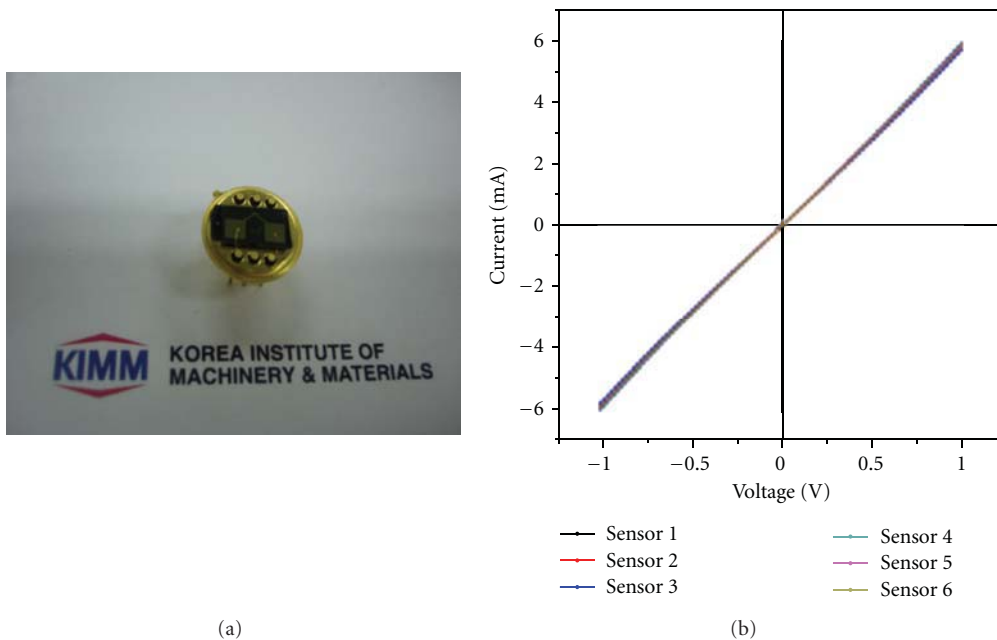


FIGURE 13: (a) A packed sensor unit. (b) I-V characteristics of the unit sensors [27].

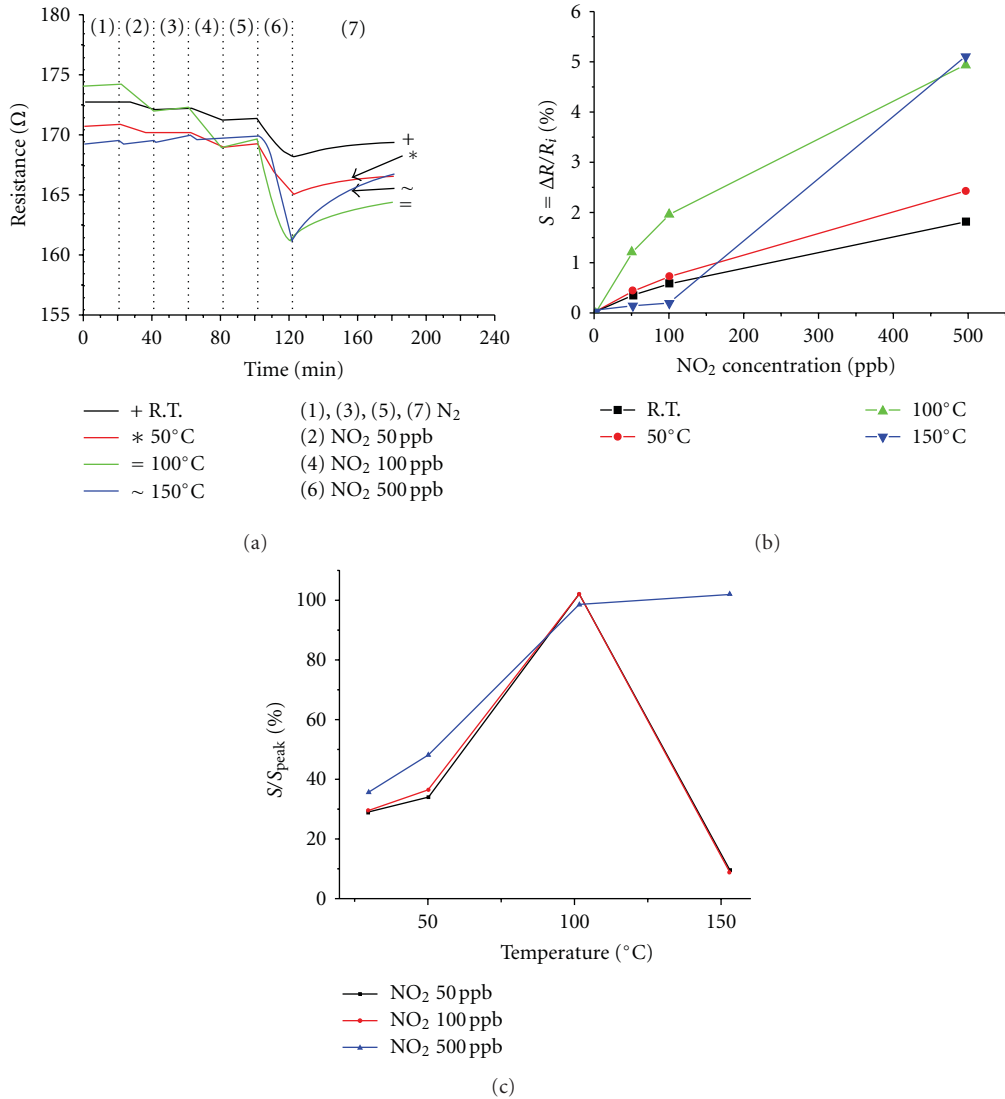


FIGURE 14: (a) The initial resistance values of unit sensors ranged from 172.7 to 169.2 Ω . NO₂ concentration was varied from 50 to 500 ppb with scanning temperatures. (b) A chart of sensitivity changes by varying temperatures and gas concentrations. (c) A chart of temperature effects on sensitivity by fixing NO₂ concentration. The sensitivity values were normalized by the peak sensitivity for different concentrations [27].

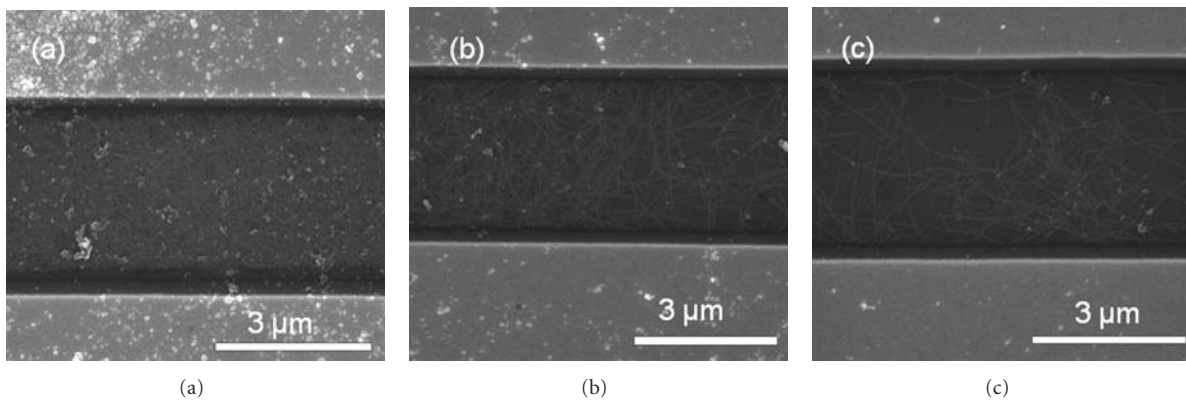


FIGURE 15: CNT array density was modulated by inkjet printing times. The resistance values were measured to be (a) 170 Ω , (b) 315 Ω , and (c) 575 Ω , respectively [27].

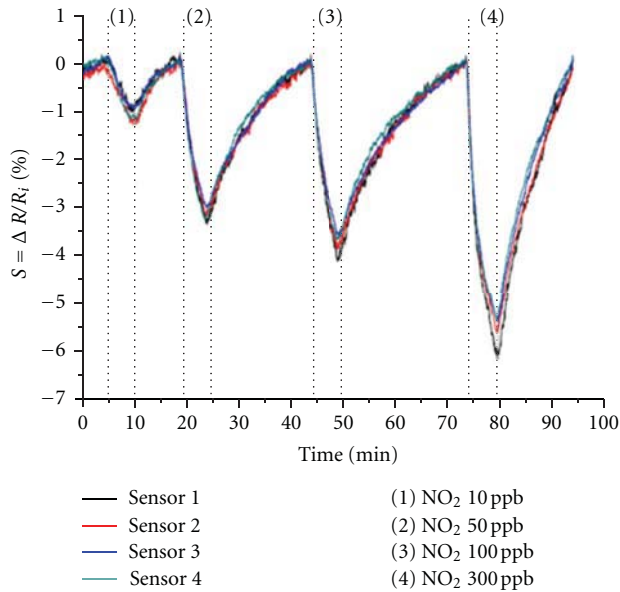


FIGURE 16: The thinner CNT array density response to NO_2 gas, which has resistances of 570–590 Ω . The enhanced active area of CNT arrays improved the sensitivity and detected 10 ppb level of NO_2 [27].

provide advantages in sensor fabrication steps and practical applications.

3.3. Inkjet Method

3.3.1. Gas Sensor Fabrication Steps. The location of nanomaterial at designated positions is an essential process to fabricate nanoscale-structure-embedded systems. Inkjet method was applied to deposit the CNT arrays on a 4 in. wafer. The gas sensor unit fabrication was prepared by following steps: (i) preparing the CNT-contained solution, (ii) inkjetting the CNT-contained solution on an Si wafer, (iii) metal (Pt) patterning on the deposited CNT arrays, and (iv) slicing and packaging a sensor unit. The steps are illustrated in Figure 11. In preparation of CNT-contained solution, commercial CNTs (Iljin nanotech, ASP-100) were dispersed in DMF (dimethylformamide) dispersant to debundle and stabilize the CNT dispersion in solution and then centrifuged for 30 min to remove residuals. The solution concentration of 20 $\mu\text{g}/\text{mL}$ was deposited on a 4 in. Si wafer according to the align references. Metal contacts (Pt) were interdigitally formed on the deposited CNT arrays by conventional metal lift-off processes, which provide the spontaneous metal-sitting structure above CNT arrays.

The 200-gas sensor units fabricated on a 4 in. wafer are shown in Figure 12(a). The scanning electron microscopy (SEM) images of a single sensor unit and interdigitated electrodes were shown 12(b) and 12(c), respectively. Figure 12(d) presents the uniformly distributed CNT arrays under electrodes. Interdigitated electrode has a gap of 3 μm , where is the CNT active region to response to gas species. As shown clearly, CNT arrays are underlaid the Pt electrode fingers, which ensure the response is derived from the CNTs instead of metal contacts. The electrode metal of Pt has a

higher work function (5.65 eV) than that of CNT (4.9 eV), which derives the Ohmic contact formation [30].

3.3.2. Packed Units. Figure 13(a) is an image of the packed unit sensor. Figure 13(b) shows that the electrical measurements of unit devices randomly picked from slicing a wafer. The resistance values are uniformly low (169.3–176 Ω) due to the structural benefit of metal-sitting on CNT arrays. An attractive contact architecture of metal-sitting structure provides physically and electrically solid contacts without the posttreatment, such as focused-ion-beam (FIB) assisted metal deposition, which may cause noisy contact resistances [31].

3.3.3. Responses to NO_2 Gas. Figure 14(a) shows the sensor responses to NO_2 gas. For gas sensing, the sensor was loaded in a chamber and then N_2 purged for 10 min to stabilize a base measurement line. The gas responses were performed at different temperature settings by room temperature (RT), 50, 100, and 150 $^\circ\text{C}$. The sensing measurements were performed for 10 min exposure to gas followed by a 10 min recovery period for three times. It showed that the gas sensor is sensitive to NO_2 gas exposure and revealed the changes of sensitivity by temperature modulation. 50 ppb level of NO_2 were detected at RT, 50, and 100 $^\circ\text{C}$. Interestingly, however, no significant change was found from 150 $^\circ\text{C}$ case. The sensitivity ($S = \Delta R/R_i$) is defined as the ratio of resistance changes (ΔR) by reacting to NO_2 versus the initial resistance value (R_i) and was shown in Figure 14(b). Figure 14(c) shows the sensitivity chart by varying temperature at a fixed gas concentration. It clearly presents the tendency of sensitivity changes by heating temperatures. By increasing temperature, the reaction between gas molecules to CNTs is facilitated. However, beyond a critical temperature, the thermal conductivity of CNT is decreased due to the phonon scattering [31] and accelerates the desorption of gas molecules from the CNT with lowering energy barrier resulting in decreasing of sensitivity [32]. The metal-sitting architecture has an advantage to prevent the modification of Schottky barrier modulation by adsorbed gas molecules [33] and ensures the responses to gas molecules come from the active entity of CNT arrays.

3.3.4. CNT Density Modification. Due to the benefit of inkjet printing method, the density of CNT arrays would be modulated resulting in control of resistances as shown in Figure 15. The sensors having a thinner dense CNT arrays were fabricated, which have resistance of 570–590 Ω . Figure 16 showed that the detection level of sensors was reached to 10 ppb NO_2 with uniform performances at room temperature and atmospheric pressure not at vacuum condition [34, 35]. The sensitivity was obtained to be 5.73% for 100 ppb NO_2 , which showed the higher response than that of 0.58% from the sensor having a resistance of 170 Ω at room temperature as presented in Figure 14. The improved detecting performance of thinner density case is attributed to the enhanced active area of CNT array by being effectively exposed to gas molecules with less inactive CNT entities resulting from overlapping one to others. Detecting a target

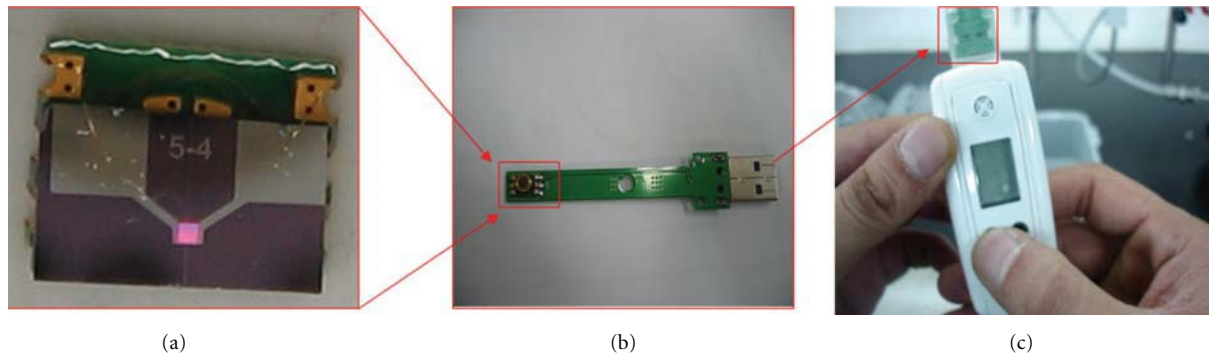


FIGURE 17: (a) A single sensor unit, (b) A sensor unit equipped USB, (c) A sensor kit.

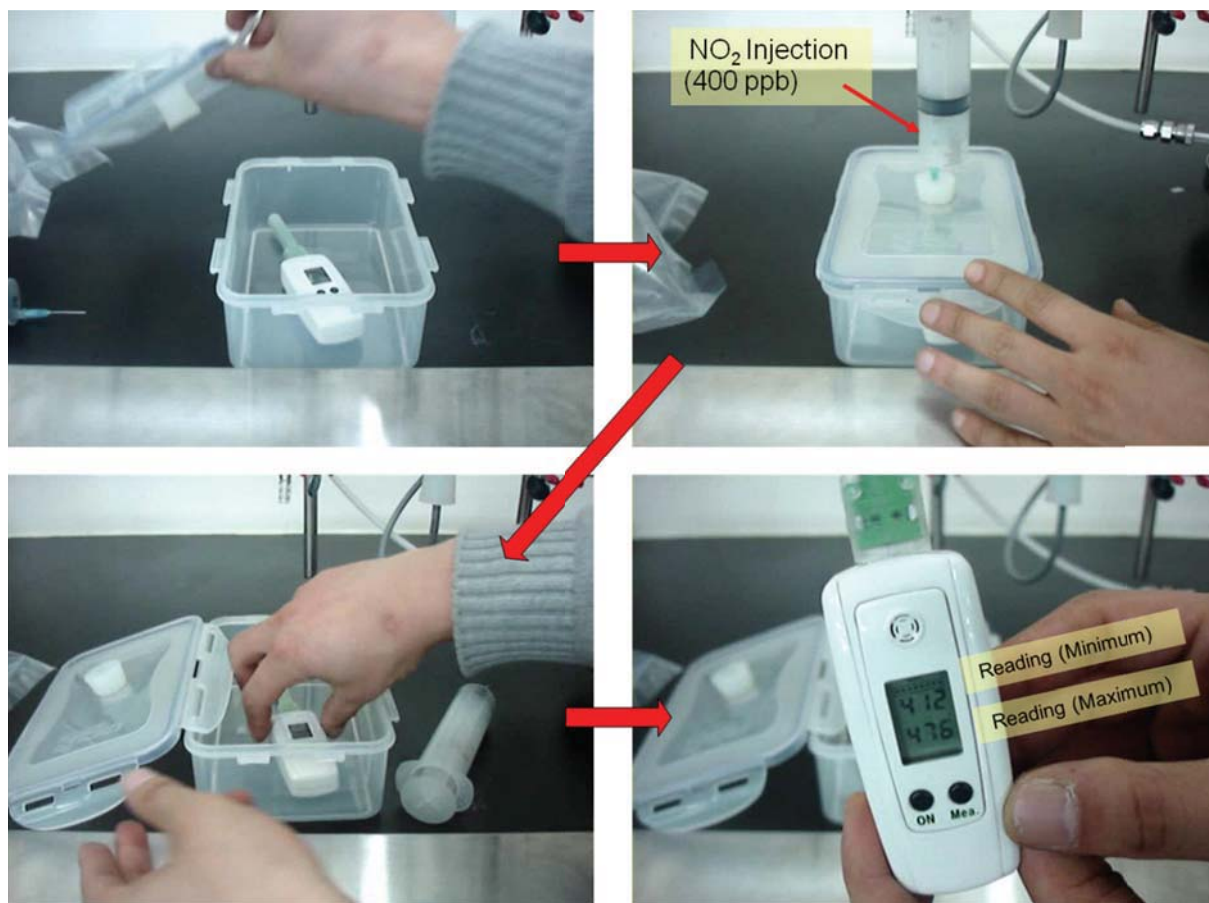


FIGURE 18: Demonstration of the CNT gas sensor kit. The CNT sensor indicates an NO₂ reading of 412 ppb.

gas at the atmospheric condition is a merit in sensor operation and fabrication as well by simplifying the structures. It implies that the controlling exposing surface area of CNT arrays may enhance the reaction to gas molecules to improve sensitivity without a heating or a vacuum equipment. All the samples responded similarly at each gas concentration, which is a strong proof of the uniform fabrication of sensor by inkjet printing method.

3.3.5. CNT Sensor Kit. Inkjet-printed CNT sensor units were fabricated as a portable sensor kit. A single sensor unit was

Au-wired on a printed circuit board (PCB) as shown in Figures 17(a) and 17(b). A sensor module has a universal serial bus (USB) port to show its reading value on the display, as shown in Figure 17(c). The sensor module has a rechargeable Li-ion battery. The wafer-scale fabricated CNT unit cells were tested for uniformity to NO₂ gas response. The resistance change according to the NO₂ gas concentration was previously programmed according to the NO₂ gas concentration. Figure 18 shows the setup of the demonstration test. A CNT gas sensor kit was placed in a test box and then a 400 ppb quantity of NO₂ was injected into the

box. After the gas response, the sensor kit indicated 412 ppb (minimum) value.

3.3.6. Development Prospects. A two terminal device detects the change of resistance due to exposure to the target gas. This structure has the advantage of easy fabrication. As previously discussed, the sensing performance can be substantially enhanced by modulating the operating voltage, heating condition, and functional decoration in the CNT entities. Having a three-device for a transistor would improve the CNT sensor performance, especially in terms of producing a significant reduction in recovery time [36] by means of a gate signal. The CNT has advantages for use as a high sensitive gas sensor that will be available to implantation in a compact package. However, pristine CNTs have certain limits due to their lack of selectivity and long recovery time [16]. To resolve these problems, functionalized CNTs have been proposed and intensively investigated. These functionalized CNTs can be tuned to the binding energy [37] in order to modulate the dynamic response of CNT sensors, leading to a high potential for use in selective gas detection with a quick response.

4. Conclusions

Two types of CNT sensors were fabricated with bare CNTs and Pd-decorated CNTs. The dielectrophoresis method was applied to align the CNTs between the Pt electrodes. Raman spectroscopy revealed that postheat treatment at 450°C was effective in reducing the chemical residuals, giving a low defect ratio of D/G⁻ in the Pd-CNT composition. It has been proved that the localized depletion region formed by Pd nanoparticles on the CNTs significantly improves the sensor reaction at atmospheric pressure conditions by control of the carrier transportation.

Inkjet printing method was used to demonstrate the reliable mass production of highly sensitive CNT-based gas sensors by producing 200 sensor units on a 4-inch wafer. Inkjet method was adopted to control the deposition of carbon nanotubes at designated positions via the modulation of density of CNT arrays. Direct metal patterning above the CNT arrays provide simple and stable contact formation between metal and CNT arrays. The performances of the sensors were uniform and highly sensitive; they were sufficiently sensitive to detect a 10 ppb level of NO₂.

Although CNTs are potential materials for use in high sensitive gas sensor applications, their promise has not yet been fulfilled in terms of commercialization, mainly due to the lack of selectivity and repeatability. Commercial success may be attained in the near future by developing high functioning CNTs and an effectively combined sensing mechanism.

Acknowledgment

The author acknowledges the financial support of the Korea Institute of Energy Technology Evaluation and Planning (KETEP-20113030010110). Some parts of this paper were reported from the author's previous reports.

References

- [1] M. I. Shakir, M. Nadeem, S. A. Shahi, and N. M. Mohamed, "Carbon nanotube electric field emitters and applications," *Nanotechnology*, vol. 17, pp. R41–R56, 2006.
- [2] J. Kim, E. S. Lee, C. S. Han, Y. Kang, D. Kim, and W. A. Anderson, "Observation of Ni silicide formations and field emission properties of Ni silicide nanowires," *Microelectronic Engineering*, vol. 85, no. 8, pp. 1709–1712, 2008.
- [3] B. Zeng, G. Xiong, S. Chen, W. Wang, D. Z. Wang, and Z. F. Ren, "Field emission of silicon nanowires grown on carbon cloth," *Applied Physics Letters*, vol. 90, no. 3, Article ID 033112, 3 pages, 2007.
- [4] G. N. Fursey, "Field emission in vacuum micro-electronics," *Applied Surface Science*, vol. 215, no. 1–4, pp. 113–134, 2003.
- [5] J. Kim, D. H. Kim, E.-S. Lee, C.-S. Han, and Y. C. Park, "Electrical characteristics of single and doubly connected Ni silicide nanowire grown by plasma-enhanced chemical vapor deposition," *Applied Physics Letters*, vol. 90, no. 25, Article ID 253103, 3 pages, 2007.
- [6] J. Kim and W. A. Anderson, "Direct electrical measurement of the self-assembled nickel suicide nanowire," *Nano Letters*, vol. 6, no. 7, pp. 1356–1359, 2006.
- [7] J. H. Lee, J. Kim, H. W. Seo et al., "Bias modulated highly sensitive NO₂ gas detection using carbon nanotubes," *Sensors and Actuators B*, vol. 129, no. 2, pp. 628–631, 2008.
- [8] J.-W. Song, J. Kim, Y.-H. Yoon, B.-S. Choi, J.-H. Kim, and C.-S. Han, "Inkjet printing of single-walled carbon nanotubes and electrical characterization of the line pattern," *Nanotechnology*, vol. 19, no. 9, Article ID 095702, 2008.
- [9] A. S. Shamaev and V. A. Samarin, "On propagation of acoustic waves in the medium consisting of a fluid and an elastic material," *Journal of Mathematical Sciences*, vol. 144, no. 4, pp. 4284–4291, 2007.
- [10] C. Cantalini, L. Valentini, I. Armentano, J. M. Kenny, L. Lozzi, and S. Santucci, "Carbon nanotubes as new materials for gas sensing applications," *Journal of the European Ceramic Society*, vol. 24, no. 6, pp. 1405–1408, 2004.
- [11] J. Kong, N. R. Franklin, C. Zhou et al., "Nanotube molecular wires as chemical sensors," *Science*, vol. 287, no. 5453, pp. 622–625, 2000.
- [12] A. Fujiwara, K. Ishii, H. Suematsu et al., "Gas adsorption in the inside and outside of single-walled carbon nanotubes," *Chemical Physics Letters*, vol. 336, no. 3–4, pp. 205–211, 2001.
- [13] C. Marliere, P. Poncharal, L. Vaccarini, and A. Zhab, "Effect of gas adsorption on the electrical properties of single walled carbon nanotubes mats," *Materials Research Society Symposium Proceedings*, vol. 593, pp. 173–177, 2000.
- [14] Y. Wang and T. W. Yeow, "A review of carbon nanotubes-based gas sensors," *Journal of Sensors*, vol. 2009, Article ID 493904, 24 pages, 2009.
- [15] Y. Hu and C. Guo, *Carbon Nanotubes—Growth and Applications*, InTech, Vienna, Austria, 2011.
- [16] T. Zhang, S. Mubeen, N. V. Myung, and M. A. Deshusses, "Recent progress in carbon nanotube-based gas sensors," *Nanotechnology*, vol. 19, no. 33, Article ID 332001, 2008.
- [17] Z. Zanolli, R. Leghrib, A. Felten, J. J. Pireaux, E. Llobet, and J. C. Charlier, "Gas sensing with au-decorated carbon nanotubes," *ACS Nano*, vol. 5, no. 6, pp. 4592–4599, 2011.
- [18] C. E. Cava, R. V. Salvatierra, D. C. B. Alves, A. S. Ferlauto, A. J. G. Zarbin, and L. S. Roman, "Self-assembled films of multi-wall carbon nanotubes used in gas sensors to increase the sensitivity limit for oxygen detection," *Carbon*, vol. 50, no. 5, pp. 1953–1958, 2012.

- [19] J. Li, Y. Lu, Q. Ye, M. Cinke, J. Han, and M. Meyyappan, "Carbon nanotube sensors for gas and organic vapor detection," *Nano Letters*, vol. 3, no. 7, pp. 929–933, 2003.
- [20] H. Y. Jung, S. M. Jung, J. R. Kim, and J. S. Suh, "Chemical sensors for sensing gas adsorbed on the inner surface of carbon nanotube channels," *Applied Physics Letters*, vol. 90, no. 15, Article ID 153114, 3 pages, 2007.
- [21] W. D. Zhang, "Growth of ZnO nanowires on modified well-aligned carbon nanotube arrays," *Nanotechnology*, vol. 17, no. 4, pp. 1036–1040, 2006.
- [22] B. Jia, L. Gao, and J. Sun, "Self-assembly of magnetite beads along multiwalled carbon nanotubes via a simple hydrothermal process," *Carbon*, vol. 45, no. 7, pp. 1476–1481, 2007.
- [23] L. Dong, J. Bush, V. Chirayos et al., "Dielectrophoretically controlled fabrication of single-crystal nickel silicide nanowire interconnects," *Nano Letters*, vol. 5, no. 10, pp. 2112–2115, 2005.
- [24] J.-H. Yun, J. Kim, Y. C. Park, J.-W. Song, D.-H. Shin, and C.-S. Han, "Highly sensitive carbon nanotube-embedding gas sensors operating at atmospheric pressure," *Nanotechnology*, vol. 20, no. 5, Article ID 055503, 2009.
- [25] Y. D. Lee, W.-S. Cho, S.-I. Moon et al., "Gas sensing properties of printed multiwalled carbon nanotubes using the field emission effect," *Chemical Physics Letters*, vol. 433, no. 1–3, pp. 105–109, 2006.
- [26] O. Kuzmich, B. L. Allen, and A. Star, "Carbon nanotube sensors for exhaled breath components," *Nanotechnology*, vol. 18, no. 37, Article ID 375502, 2007.
- [27] J. Kim, J. H. Yun, J. W. Song, and C. S. Han, "The spontaneous metal-sitting structure on carbon nanotube arrays positioned by inkjet printing for wafer-scale production of high sensitive gas sensor units," *Sensors and Actuators B*, vol. 135, no. 2, pp. 587–591, 2009.
- [28] M. Fujii, X. Zhang, H. Xie et al., "Measuring the thermal conductivity of a single carbon nanotube," *Physical Review Letters*, vol. 95, no. 6, Article ID 065502, 4 pages, 2005.
- [29] W. Wongwiriyan, S. Honda, H. Konishi et al., "Single-walled carbon nanotube thin-film sensor for ultrasensitive gas detection," *Japanese Journal of Applied Physics*, vol. 44, pp. L482–L484, 2005.
- [30] H. M. Manohara, E. W. Wong, E. Schlecht, B. D. Hunt, and P. H. Siegel, "Carbon nanotube schottky diodes using Ti-Schottky and Pt-Ohmic contacts for high frequency applications," *Nano Letters*, vol. 5, no. 7, pp. 1469–1474, 2005.
- [31] F. Hernández-Ramírez, A. Tarancón, O. Casals, J. Arbiol, A. Romano-Rodríguez, and J. R. Morante, "High response and stability in CO and humidity measures using a single SnO₂ nanowire," *Sensors and Actuators B*, vol. 121, no. 1, pp. 3–17, 2007.
- [32] M. Fujii, X. Zhang, H. Xie et al., "Measuring the thermal conductivity of a single carbon nanotube," *Physical Review Letters*, vol. 95, no. 6, Article ID 065502, pp. 1–4, 2005.
- [33] K. Bradley, J.-C. P. Gabriel, A. Star, and G. Gruner, "Short-channel effects in contact-passivated nanotube chemical sensors," *Applied Physics Letters*, vol. 83, no. 18, pp. 3821–3823, 2003.
- [34] Y. W. Chang, J. S. Oh, S. H. Yoo, H. H. Choi, and K.-H. Yoo, "Electrically refreshable carbon-nanotube-based gas sensors," *Nanotechnology*, vol. 18, no. 43, Article ID 435504, 2007.
- [35] J. Chung, K. H. Lee, J. Lee, D. Troya, and G. C. Schatz, "Multiwalled carbon nanotubes experiencing electrical breakdown as gas sensors," *Nanotechnology*, vol. 15, no. 11, pp. 1596–1602, 2004.
- [36] T. Someya, J. Small, P. Kim, C. Nuckolls, and J. T. Yardley, "Alcohol vapor sensors based on single-walled carbon nanotube field effect transistors," *Nano Letters*, vol. 3, no. 7, pp. 877–881, 2003.
- [37] P. C. P. Watts, N. Mureau, Z. Tang, Y. Miyajima, J. David Carey, and S. R. P. Silva, "The importance of oxygen-containing defects on carbon nanotubes for the detection of polar and non-polar vapours through hydrogen bond formation," *Nanotechnology*, vol. 18, no. 17, Article ID 175701, 2007.

Research Article

Properties of Reaction Intermediates from Unzipping Nanotubes via the Diketone Formation: A Computational Study

Takashi Yumura and Toshiyuki Kanemitsu

Department of Chemistry and Materials Technology, Kyoto Institute of Technology, Matsugasaki, Sakyo-ku, Kyoto 606-8585, Japan

Correspondence should be addressed to Takashi Yumura, yumura@chem.kit.ac.jp

Received 13 October 2011; Accepted 18 March 2012

Academic Editor: Sulin Zhang

Copyright © 2012 T. Yumura and T. Kanemitsu. This is an open access article distributed under the Creative Commons Attribution License, which permits unrestricted use, distribution, and reproduction in any medium, provided the original work is properly cited.

We investigated properties of an armchair nanotube attached by specific numbers of diketone groups along the tube axis using density functional theory (DFT) calculations. The results from DFT calculations show that multiple diketone attachments into an armchair nanotube cleave the CC bonds along the tube axis, forming a large hole. Then, the six-membered rings surrounding the hole are planarized, and zigzag edges appear. Due to these geometrical changes, the functionalized armchair nanotubes exhibit properties similar to those in corresponding graphene ribbons with zigzag edges. For example, diketone-attached nanotubes have a spin-polarized ground state with frontier orbitals whose amplitudes are localized at diketone O atoms. As a consequence of the existence of the localized orbitals, unpaired electrons appear only on the diketone O atoms in an armchair nanotube.

1. Introduction

Honeycomb carbon sheets [1, 2] are contained in both single-walled carbon nanotubes [3, 4] and single-layer graphite, also called graphene [5]. The two carbon allotropes, which use the same building blocks, exhibit similar and unique electronic properties resulting from small band gaps [1, 2]. Although the unique properties primarily come from π orbitals in the frontier orbital region, there are some differences in their electronic properties. The differences originate from the dimensionality of the nanocarbon materials. In fact, one-dimensional nanotubes exhibit metallic or semi-conducting character, depending on how the honeycomb sheet rolls up [6–9]. The properties of thin strips of graphene (graphene-ribbons) are strongly influenced by their width and edge structures (armchair- and zigzag-edges) [10–23]. In particular, zigzag nanoribbons have radical character, which is localized at their edges.

To demonstrate the ability to connect nanotubes and graphene [24–30], Kosynkin et al. successfully converted a nanotube into a nanoribbon via a chemical treatment [26]. In this intriguing experiment [26], KMnO_4 oxidizes a nanotube and unzips the nanotube longitudinally to form a nanoribbon,

as shown in Figure 1. In the proposed reaction mechanism, KMnO_4 binds initially to a CC bond in the nanotube. After the binding, one diketone group is formed by cleaving the attached CC bond. Because the first diketone formation distorts the neighboring CC bonds, the distorted CC bonds become a suitable site for the second KMnO_4 addition. After a sequence of oxidation reactions, the CC bonds of the tube are successfully cleaved along the tube axis. Although their proposal appears plausible and is consistent with the experimental findings, atomic-scale views of the reaction intermediates, which include a nanotube attached by multiple diketone groups, are still required.

For this purpose, computer simulations based on density functional theory (DFT) [31–38] can provide insights into the reaction mechanism. Although several computational studies have focused on unzipping nanotubes with and without H-atom termination [31–35], there are a few reports discussing those created by the addition of oxygen pairs [36, 37]. For example, Rangel et al. used DFT calculations to investigate the sequential addition of oxygen pairs to a model with a finite-length (5, 5) tube. The model, which included 100 atoms, has a tube length of $\sim 10 \text{ \AA}$. Based on the tube length, the maximum number of oxygen pairs attached to

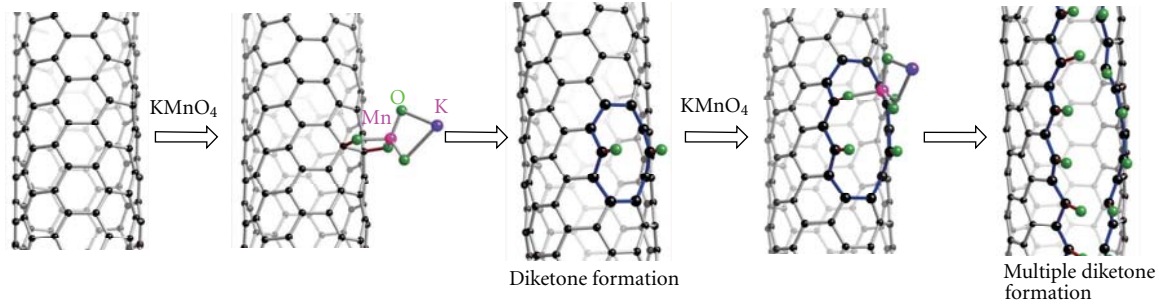


FIGURE 1: Reaction mechanism for unzipping a nanotube by KMnO_4 , proposed in [26]. The optimized structures for a nanotube ((5,5) nanotube) attached by KMnO_4 , and a one-diketone-attached nanotube bound by second KMnO_4 were obtained in the PW91 calculation.

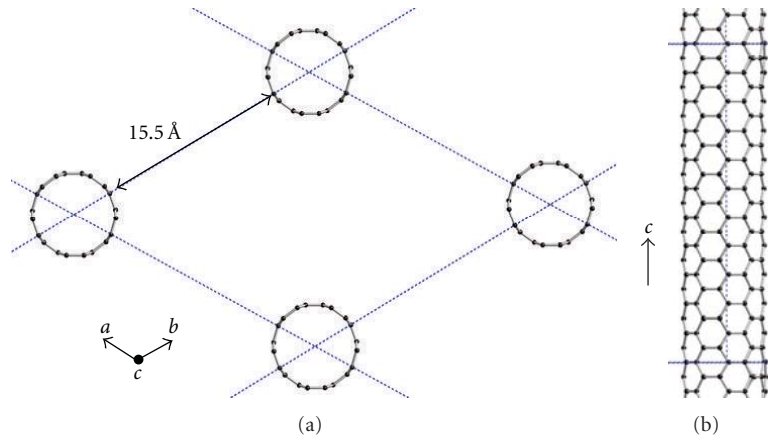


FIGURE 2: (a) Cross-section of the hexagonal unit cell for the (5,5) nanotube in periodic boundary condition (PBC) calculations, given by blue hashed lines. (b) Side-view of the nanotube along the tube axis (the c vector). Its supercell was given by blue-hashed lines.

the tube (N_{op}) can be as many as 5. According to the DFT calculations, cleaving the tube CC bonds by diketone formation was found for N_{op} larger than 3. Although their DFT findings can partially explain the experimental results, the structural features of the oxygen-pair attached nanotubes are artificially affected by the model size. In fact, the separation between the carbon atoms attached by oxygen pairs is influenced by the tube edges. Furthermore, attached oxygen atoms cannot line up along the tube axis at regular intervals. Because these structural features have a strong impact on the electronic properties, detailed insight into the properties of diketone-attached nanotubes is still required.

To improve our understanding of the conversion of nanotubes into nanoribbons by multiple diketone attachments, we employed DFT calculations for a sufficiently long tube model and an infinite-length model using a periodic boundary condition (PBC). In the current study, we focused on how the properties of diketone-attached nanotubes change as a function of the degree of oxidation (i.e., the number of diketones formed on a nanotube surface (N_{op})). It is expected that the diketone-attached nanotubes have properties in between a pristine nanotube and the resultant graphene-nanoribbon. Thus, we focused on how a nanotube becomes planar via a sequence of diketone formation and how the planarization affects the electronic properties.

2. Method of Calculation

The DFT calculations used in the current study are based on the Perdew-Wang (PW91) functional [39]. When some numbers of diketones are formed on a CC bond perpendicular to the axis of a (5,5) armchair nanotube, the CC bonds at the binding sites are proposed to be cleaved [26]. After cleaving the attached CC bonds along the axis, zigzag edges appeared at the binding sites. Previous theoretical studies indicate that a spin-polarized solution for the zigzag nanoribbons with attached ketone groups is energetically stable relative to its spin-unpolarized solution [18–20]. We performed both spin-polarized and spin-unpolarized calculations to obtain local minima of the diketone-attached nanotubes.

In the PBC calculations implemented in the Vienna ab initio Simulation Package (VASP v.4.6) [40], we employed a hexagonal supercell in Figure 2. The supercell contains 200 C atoms in the (5,5) nanotube and some number of oxygen pairs. In the current study the number of attached oxygen pairs (N_{op}) ranges from 1 to 7. The kinetic energy cutoff of the plane-wave basis set is 349.5 eV with ultrasoft Vanderbilt-type pseudopotentials [41]. We allowed full geometry relaxation in the axial direction, but separations between adjacent tubes are fixed at 15.5 Å (Figure 2)

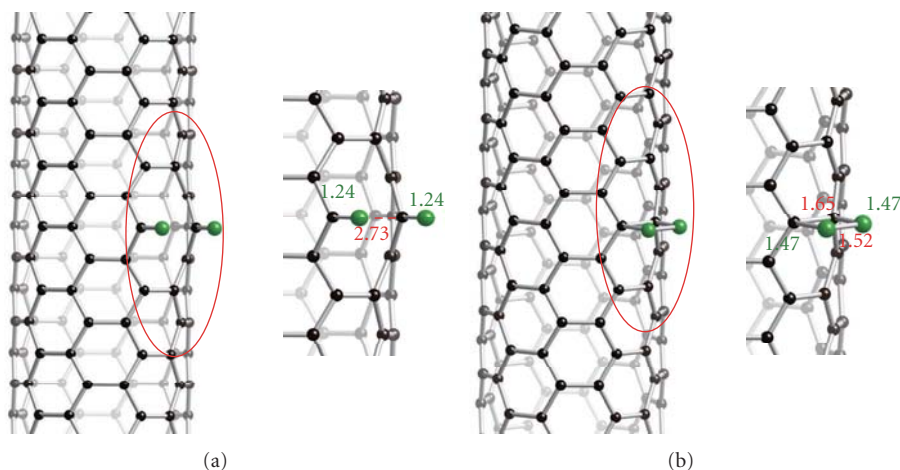


FIGURE 3: (a) Optimized structure for the (5,5) nanotube attached by one diketone group, where the CC bond at the binding site opens. (b) The other type of the nanotube attached by one oxygen pair, where the OO bond as well as the CC bond at the binding site retain.

(In the PBC calculations (Figure 2), we relaxed cell parameter in c vector as well as position of included atoms. However two cell parameters in a and b vectors were fixed, and eventually intertube separations are fixed). The intertube separations were large enough to avoid significant intertube interactions [42–44]. The cell size is also large enough to avoid interactions between the guests located on the neighboring unit cells. We employed a $1 \times 1 \times 5$ k -point mesh for geometry optimization of the nanotube systems. In PBC calculations of metallic systems with no band gap, we sometimes faced a difficulty in converging their total energy. To avoid the difficulty, the convergence was enhanced in the VASP program using fractional occupancy generated by Gaussian broadening ($\sigma_{\text{GB}} = 0.03$ eV) of the one-electron energy levels. As a result, the energy levels close to the Fermi level have fractional occupations. Based on the PW91 calculations, the CC bond length in graphene was determined to be 1.421 Å, which is consistent with the experimental value [1, 2] suggesting that the method of our choice is appropriate for the present study.

In the finite-length model calculation performed with the Gaussian 03 program [45], we fully optimized a (5,5) nanotube terminated by H atoms ($\text{C}_{230}\text{H}_{20}$) plus N_{op} oxygen pairs. The length of the tube model was approximately 27 Å, which was large enough to model the corresponding infinite-length tube [46–49]. We used the 6–31G* basis set [50] for the attached oxygen pairs as well as the neighboring 58 C atoms, and the 3–21 G basis set for all of the other atoms [51]. Similar to previous theoretical studies [18–20], single and triplet spin states of the diketone-attached nanotubes were obtained for the finite-length calculations.

3. Results and Discussion

3.1. Formation of One Diketone Group on a (5,5) Nanotube. As proposed by Kosynkin et al. [26], the diketone formation would be an indispensable reaction to cleave the tube CC bonds at the binding sites. In this section, we describe how DFT calculations were used to investigate relationships

between the diketone formation and the CC bond cleavage. For this purpose, we constructed two types of initial geometries for the addition of two oxygen atoms into the (5,5) nanotube, which can be distinguished by whether the attached C–O bonds are longer or shorter. As a result of PW91 optimization, we obtained two local minima, as shown in Figure 3. Figure 3(a) displays the optimized structure for the formation of one diketone group on the (5,5) nanotube. As shown in Figure 3(a), the optimized CO bond length is 1.24 Å, which indicated the presence of two CO double bonds (The optimized geometry was obtained by using the initial geometry of the nanotube attached by one oxygen-atom pair with shorter C–O bonds). Then, the CC bond at the binding site is broken (CC separation, 2.73 Å). Another type of optimized structure was also obtained, and it is shown in Figure 3(b) (The optimized geometry was obtained by using the initial geometry of the nanotube attached by one oxygen-atom pair with longer C–O bonds). The optimized structure is 31.3 kcal/mol more unstable compared to the structure in Figure 3(a). A similar value was obtained in [37]. In the oxygen-pair addition shown in Figure 3(b), two single CO bonds (1.47 Å) are formed. Then, the OO bond (1.52 Å) stretches, but it does not completely break. The optimized structure retains the tube CC bond at the binding site.

A comparison between the two optimized structures elucidated the roles of the oxygen-pair addition in the CC bond cleavage. To understand the different chemical bonds between the two C_2O_2 networks, the valence concept was utilized. Conceptually, the two C_2O_2 networks are connected by an electron transfer, which is indicated by the arrows in Figure 4. The green arrow in Figure 4 indicates a single-electron transfer from the OO bond to the CO bond, while a blue arrow indicates a single-electron transfer from the attached CC bond to the CO bond. As a result of the electron transfer, the CC and OO bonds are cleaved, and two double CO bonds are formed (Figure 4). This process can be rationalized with the Mulliken charge populations, and the calculated values are also presented in Figure 4. Thus,

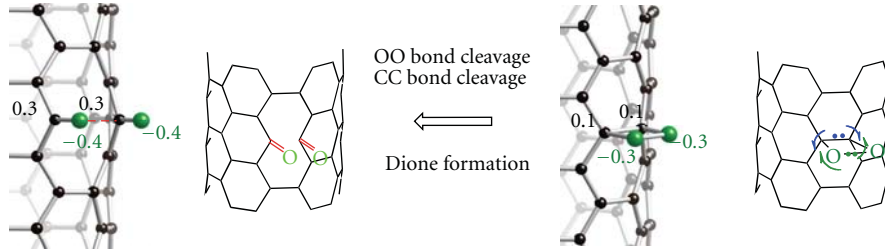


FIGURE 4: A view of oxygen pair-attached tubes from valence concept, and Mulliken charge population.

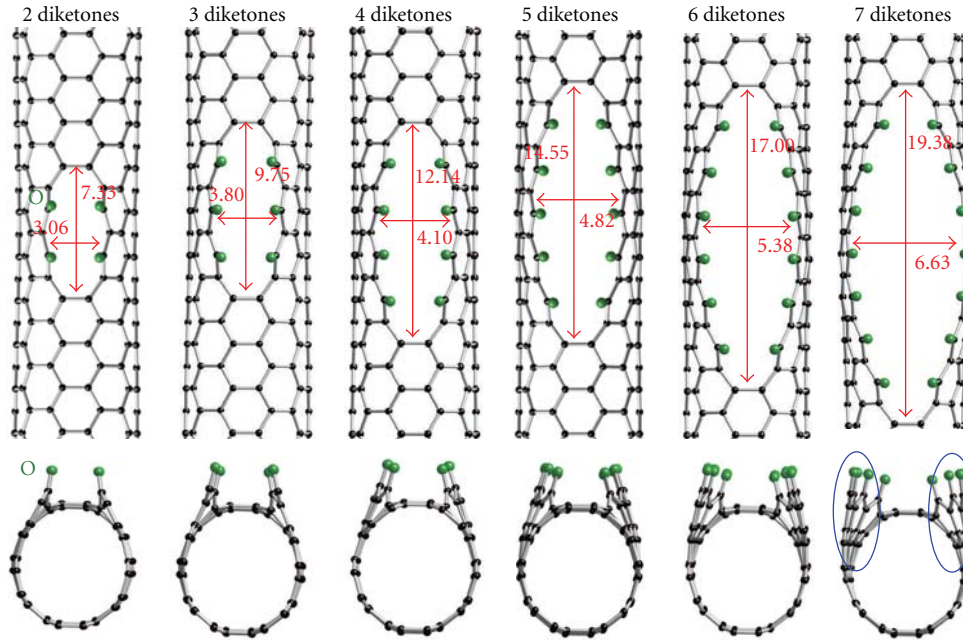


FIGURE 5: Overview of a series of optimized structures for diketone-attached nanotubes. The number of diketone groups (N_{op}) ranges from 2 to 7.

the DFT results support the experimental prediction posited in [26].

3.2. A Series of Diketone-Attached Infinite-Length (5,5) Nanotube. In this section, we discuss a series of diketone-attached infinite-length (5,5) nanotube where the number of attached diketone groups (N_{op}) ranges from 2 to 7. Their local minima were obtained from spin-polarized and spin-unpolarized DFT calculations. Table 1 shows the relative energy between the spin-polarized and spin-unpolarized solutions of each diketone-attached nanotube ($\Delta E_{state} = E_{polarized} - E_{unpolarized}$). The negative ΔE_{state} values in Table 1 suggest that a spin-polarized solution is energetically preferable relative to a spin-unpolarized solution. In particular, 3- and 4-diketone-attached nanotubes have substantial ΔE_{state} values (-4.2 and -6.2 kcal/mol, resp.).

Figure 5 provides an overview of the structures for the optimized N_{op} -diketone-attached nanotubes in the spin-polarized ground state. For comparison, the optimized structures for the corresponding H-attached nanotubes are also displayed in Figure 6. In Figure 5, the attached oxygen (green) atoms are aligned along the tube axis irrespective

TABLE 1: Relative energy between spin-polarized and spin-unpolarized solutions of N_{op} diketone-attached nanotubes.

	N_{op}^a					
ΔE_{state}^b	2	3	4	5	6	7
	0.0	-4.2	-6.2	-1.8	-3.0	-2.7

^a N_{op} : the number of diketone groups binding to the (5,5) nanotube.

^b ΔE_{state} (kcal/mol): energy differences between spin-polarized and spin-unpolarized states of an N_{op} -diketone-attached nanotube ($E_{polarized} - E_{unpolarized}$). Negative values indicate that a spin-polarized state is stable relative to a spin-unpolarized state.

of the number of attached oxygen atoms. It is important to note that the OO separations along the tube axis are nearly constant (~ 2.5 Å) for larger N_{op} values. Such geometrical features cannot be found by Rangel et al. [36]. As in the case of the 1-diketone-attached nanotube, the CC bonds break as the multiple diketone groups are formed on the nanotube. With an increase in N_{op} , larger CC separations are found. Accordingly, a larger hole is generated in the N_{op} -diketone-attached nanotube with a larger N_{op} value, as shown in Figure 5. For

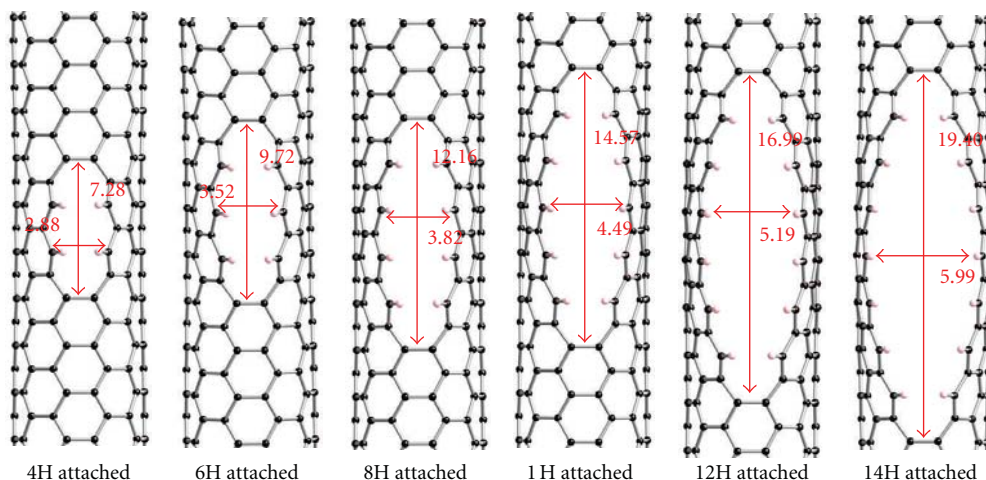


FIGURE 6: Overview of a series of optimized structures for hydrogen-attached nanotubes. The number of attached H atoms ranges from 4 to 14.

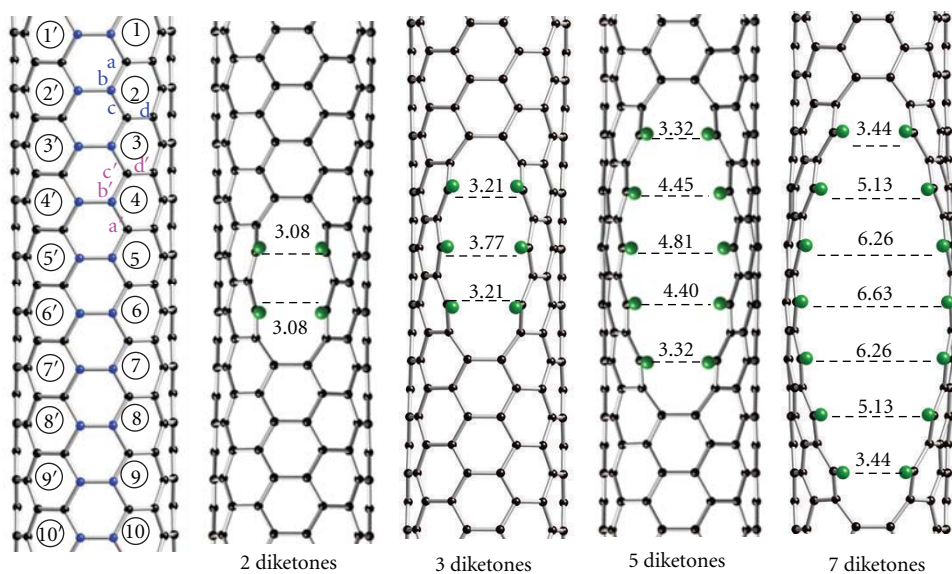


FIGURE 7: Detailed optimized structures for 2-, 3-, 5-, and 7-diketone-attached nanotubes. We labeled six-membered rings that will be attached by oxygen pairs. Values in Å indicate the optimized CC separations, created by diketone formation. Dihedral angles of the a, b, c, and d carbon atoms are defined. Note that the carbon atoms labeled by “b” are the binding site for ketone formation.

example, the 7-diketone-attached nanotube has a hole of 19.4×6.6 Å. Interestingly, the hole width (6.6 Å) is comparable to the diameter of the pristine (5,5) nanotube (6.9 Å). In terms of the hole formation, similarities were found in the H-attached nanotubes in Figure 6. However, the H-attached nanotube has a slightly smaller hole than the corresponding diketone-attached nanotube case. The different hole sizes can be reproduced in the finite-length calculations. According to Mulliken population analyses in the finite-length calculations, the attached oxygen atoms have substantial negative charges ($-0.38e \sim -0.29e$) (nanotubes attached by smaller number of oxygen pairs have more significant charges with negative signs). Between the paired oxygen atoms attached to the nanotubes, repulsive forces exert, forming the larger holes in the diketone-attached nanotubes

than those in the corresponding H-atom-attached nanotubes where such negative charges do not appear on the attached H-atoms.

Because of the large-hole formation, the 7-diketone-attached nanotube cannot retain a tubular structure. However, some of the six-membered rings seem to be planarized and are shown as circles in Figure 5. To determine how the hole formation results in planarizing of the six-membered rings, we investigate in detail the structural features of the 2-, 3-, 5-, and 7-diketone-attached nanotubes, as shown in Figure 7. The six-membered rings attached by a ketone group are labeled to identify the binding sites. For example, the binding sites in the 7-diketone-attached nanotube have blue carbon atoms in the six-membered rings with labels ranging from “3” to “9.” The dependence of the CC bond cleavage on

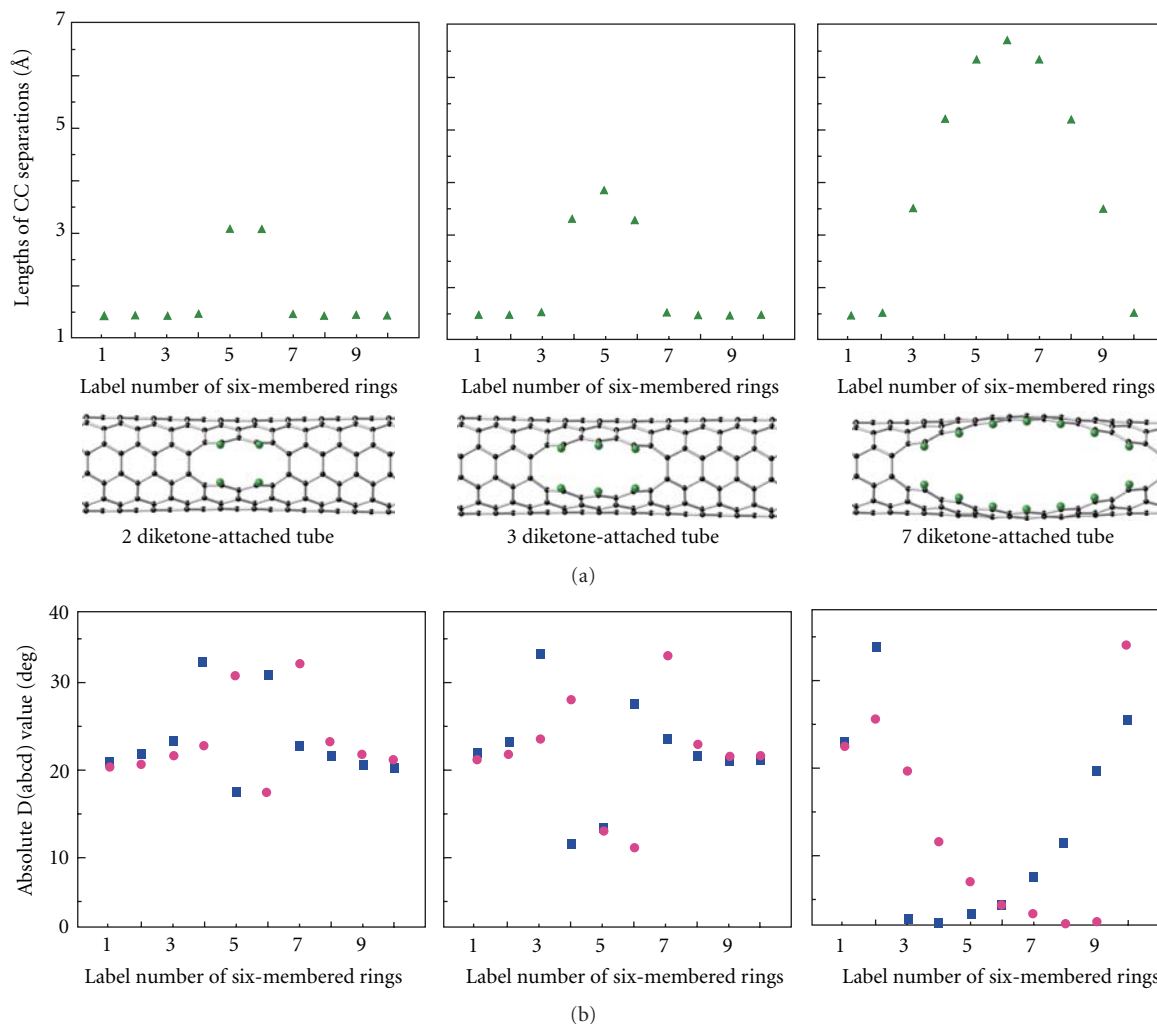


FIGURE 8: (a) Variations of CC bonds separated by diketone formation, depending on the binding sites. (b) Site dependences of the dihedral angles (D) defined by a , b , c , and d in Figure 7. The absolute D values (in degree) are plotted. The number in the abscissa axis of (a) and (b) corresponds to the label number of six-membered rings in Figure 7.

the location of the attached six-membered rings is displayed in Figures 7 and 8(a). In Figures 7 and 8(a), the two carbon atoms are significantly separated in the nanotubes with larger numbers of attached diketone groups. In particular, the longest CC separation was found in the middle of the hole in the 7-diketone-attached nanotube and is labeled “6” in Figure 7. On the other hand, smaller CC separations were found in the nanotubes attached by a smaller number of diketone groups ($N_{op} = 2$ or 3).

Planarization of the six-membered rings surrounding the hole is quantified in Figure 8(b) using the dihedral angles (D) of the four C atoms (a , b , c , and d (a' , b' , c' , and d') in Figure 7) neighboring the attached site. It is important to note that the pristine (5,5) tube and the planer graphene have absolute D values of 19.8 (Dihedral angles of a , b , c , and d atoms have positive D values, whereas those of a' , b' , c' , and d' have negative values.) and 0, respectively, as shown in Figure 9. Thus, the dihedral angles are useful parameters for determining if a six-membered ring is planar in the

diketone-attached tube. In fact, their D values would approach 19.8 degrees, when the diketone-attached nanotube exhibits a tubular structure. In contrast, the planarized six-membered rings appear in the diketone-attached nanotube with D values close to 0.

As shown in Figure 8(b), we observe an increase in the D values near the binding sites of the 2-diketone-attached nanotube. In addition to the D values larger than 19.8 degrees, two six-membered rings have a smaller D value. Much smaller D values are observed for the 3-diketone-attached nanotube where two diketone-attached rings, labeled 4 and 6, have D values of approximately 10 degrees. Decreasing D values indicate that the curvature of the ring is substantially reduced. When larger numbers of diketone groups are attached on a tube, nearly planar six-membered rings are present. For example, some six-membered rings have D values ranging from 0 to 10 degrees in the 7-diketone-attached nanotube. More importantly, Figures 8(a) and 8(b)

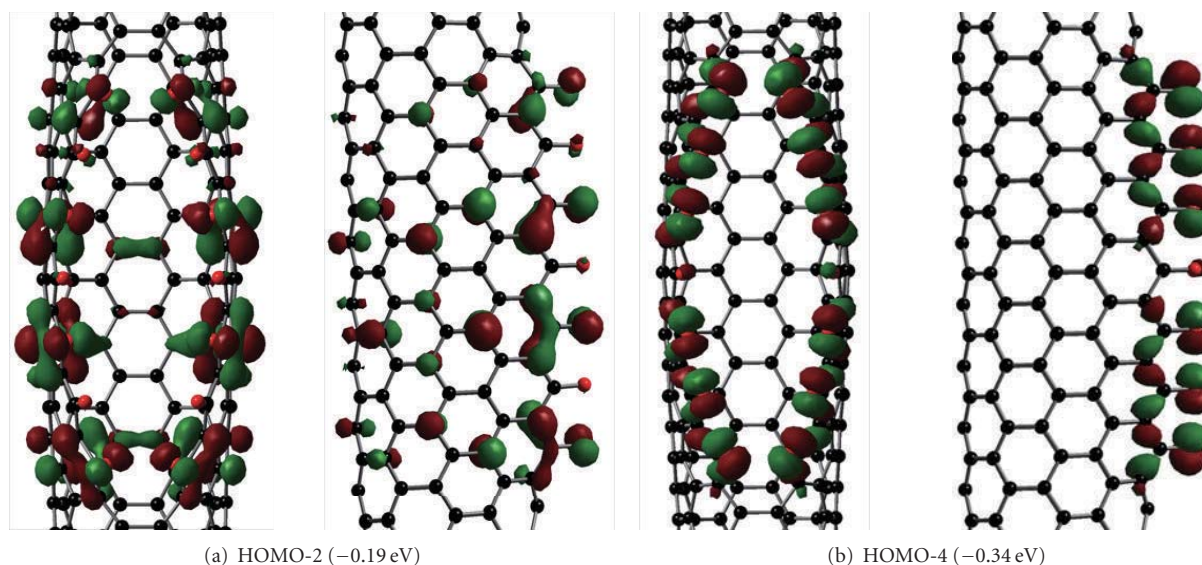


FIGURE 11: Representative α -spin orbitals of the 7-diketone-attached nanotube in the frontier orbital region. An energy value in parentheses indicates the energy difference between the α -spin HOMO and a certain orbital.

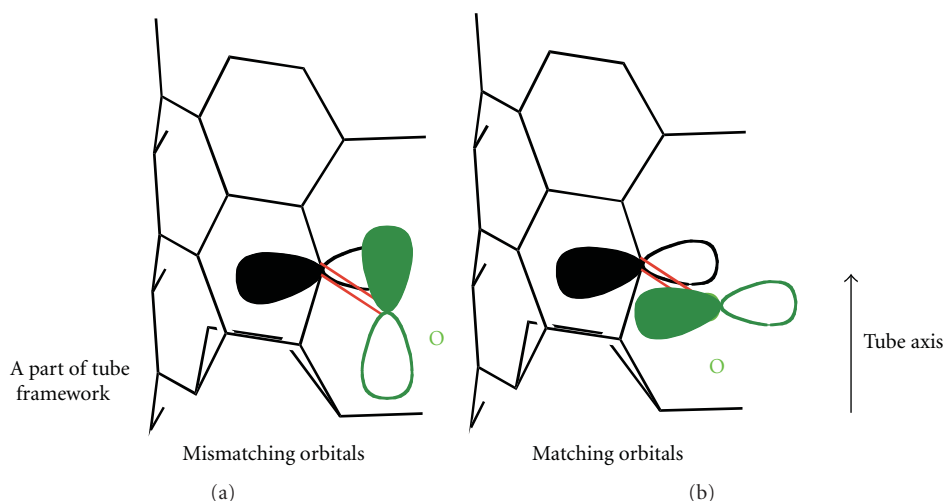


FIGURE 12: Couplings between an oxygen p orbital and a tube p orbital.

is interesting to note that the localized orbitals have nodes resulting from the sine terms in (1). For example, the HOMO-2 has three nodes along an oxygen-chain, and the HOMO-4 has one node.

Based on the p(O) orbital orientation in the localized orbitals, the two types of orbitals have different distributions of π orbitals in the tube moiety. In fact, the HOMO-2 has carbon p orbitals slightly distributed into the tube. On the other hand, the HOMO-4 does not have p orbitals on the tube C atoms, except for carbon atoms that are next-nearest neighbor to a diketone oxygen atom. The different behaviors can be understood from Figure 12 [52]. When parallel p(O) orbitals are perpendicular to the tube π orbitals, they cannot mix with the tube π orbitals. As a result, localized orbitals containing parallel p(O) orbitals do not exhibit amplitudes on the tube moiety. In contrast, perpendicular p(O) orbitals

can interact with the tube π orbitals. Because of the interactions, some amplitudes appear in the tube moiety in the frontier orbital containing perpendicular p(O) orbitals. Consequently, the planarization of the six-membered rings with multiple diketone attachments plays a significant role in determining the orbital features in the frontier orbital region.

Detailed analyses of the frontier orbitals revealed that HOMO-4 is occupied by an α electron, but it is not occupied by a β electron. Therefore, the α HOMO-4 is one of the key orbitals that determines the spin density distribution in the 7-diketone-attached nanotube. However, there are many frontier orbitals with amplitudes that exist only on the diketone groups. In fact, nine α -orbitals lie less than 0.5 eV below the HOMO. These orbitals can be distinguished by the number of nodes as well as the orientation of the p(O) orbitals involved (e.g., perpendicular or parallel orientation).

Because many magnetic orbitals exist in the frontier orbital region, we cannot identify all of the orbitals that determine the spin density distributions in the diketone-attached nanotube. However, localized orbitals resulting from p oxygen atoms, such as the HOMO-4, can contribute to the localized radical character.

4. Conclusions

Density functional theory (DFT) PW91 calculations were employed to investigate the properties of a (5,5) nanotube attached to some number of diketone groups. According to the DFT calculations, the formation of two double CO bonds on the nanotube cleaves one CC bond at the attachment site. For the high degree of diketone formation on the armchair nanotube, the CC bonds at the binding sites lengthen significantly, and, eventually, a large hole is formed. Then, the six-membered rings surrounding the large hole are substantially planarized. Because the planarized six-membered rings have zigzag edges attached to diketone groups, the functionalized armchair nanotubes exhibit electronic properties similar to those in nanographene ribbons with zigzag edges. In fact, orbitals with amplitudes primarily localized at diketone groups appear in the frontier orbital region. Based on the orbital features, diketone-attached nanotubes have a spin-polarized ground state, with the unpaired electrons localized on the oxygen atoms

Acknowledgments

The project is partially supported by a Grant-in-Aid for Young Scientists (B) from the Japan Society for the Promotion of Science (JSPS) (T. Yumura at the Kyoto Institute of Technology) (no. 22710088) and a Grant-in-Aid for Scientific Research (C) from JSPS (T. Yumura at the Kyoto Institute of Technology) (no. 23560934).

References

- [1] M. S. Dresselhaus, G. Dresselhaus, and P. C. Eklund, *Science of Fullerenes and Carbon Nanotubes*, Academic Press, San Diego, Calif, USA, 1996.
- [2] R. Saito, G. Dresselhaus, and M. S. Dresselhaus, *Physical Properties of Carbon Nanotubes*, Imperial College Press, London, UK, 1998.
- [3] S. Iijima, "Helical microtubules of graphitic carbon," *Nature*, vol. 354, no. 6348, pp. 56–58, 1991.
- [4] S. Iijima and T. Ichihashi, "Single-shell carbon nanotubes of 1-nm diameter," *Nature*, vol. 363, no. 6430, pp. 603–605, 1993.
- [5] K. S. Novoselov, A. K. Geim, S. V. Morozov et al., "Electric field in atomically thin carbon films," *Science*, vol. 306, no. 5696, pp. 666–669, 2004.
- [6] J. W. Mintmire, B. I. Dunlap, and C. T. White, "Are fullerene tubules metallic?" *Physical Review Letters*, vol. 68, no. 5, pp. 631–634, 1992.
- [7] R. Saito, M. Fujita, G. Dresselhaus, and M. S. Dresselhaus, "Electronic structure of chiral graphene tubules," *Applied Physics Letters*, vol. 60, no. 18, pp. 2204–2206, 1992.
- [8] K. Tanaka, K. Okahara, M. Okada, and T. Yamabe, "Electronic properties of bucky-tube model," *Chemical Physics Letters*, vol. 191, no. 5, pp. 469–472, 1992.
- [9] N. Hamada, S. I. Sawada, and A. Oshiyama, "New one-dimensional conductors: graphitic microtubules," *Physical Review Letters*, vol. 68, no. 10, pp. 1579–1581, 1992.
- [10] M.-H. Whangbo, R. Hoffmann, and R. B. Woodward, "Conjugated one and two dimensional polymers," *Proceedings of the Royal Society of London A*, vol. 366, no. 1724, pp. 23–46, 1979.
- [11] T. Yamabe, K. Tanaka, K. Ohzeki, and S. Yata, "Electronic structure of polyacene. A one-dimensional graphite," *Solid State Communications*, vol. 44, no. 6, pp. 823–825, 1982.
- [12] M. Kertesz and R. Hoffmann, "Higher order Peierls distortion of one-dimensional carbon skeletons," *Solid State Communications*, vol. 47, no. 2, pp. 97–102, 1983.
- [13] K. Yoshizawa, K. Yahara, K. Tanaka, and T. Yamabe, "Bandgap oscillation in polyphenanthrenes," *Journal of Physical Chemistry B*, vol. 102, no. 3, pp. 498–506, 1998.
- [14] K. Nakada, M. Fujita, G. Dresselhaus, and M. S. Dresselhaus, "Edge state in graphene ribbons: nanometer size effect and edge shape dependence," *Physical Review B*, vol. 54, no. 24, pp. 17954–17961, 1996.
- [15] K. Kusakabe and M. Maruyama, "Magnetic nanographite," *Physical Review B*, vol. 67, no. 9, Article ID 092406, 2003.
- [16] M. Fujita, K. Wakabayashi, K. Nakada, and K. Kusakabe, "Peculiar localized state at zigzag graphite edge," *Journal of the Physical Society of Japan*, vol. 65, no. 7, pp. 1920–1923, 1996.
- [17] K. Wakabayashi, M. Sigrist, and M. Fujita, "Spin wave mode of edge-localized magnetic states in nanographite zigzag ribbons," *Journal of the Physical Society of Japan*, vol. 67, no. 6, pp. 2089–2093, 1998.
- [18] O. Hod, V. Barone, J. E. Peralta, and G. E. Scuseria, "Enhanced half-metallicity in edge-oxidized zigzag graphene nanoribbons," *Nano Letters*, vol. 7, no. 8, pp. 2295–2299, 2007.
- [19] H. Zheng and W. Duley, "First-principles study of edge chemical modifications in graphene nanodots," *Physical Review B*, vol. 78, no. 4, Article ID 045421, 2008.
- [20] G. Lee and K. Cho, "Electronic structures of zigzag graphene nanoribbons with edge hydrogenation and oxidation," *Physical Review B*, vol. 79, no. 16, Article ID 165440, 2009.
- [21] T. Yumura, K. Kimura, H. Kobayashi, R. Tanaka, N. Okumura, and T. Yamabe, "The use of nanometer-sized hydrographene species for support material for fuel cell electrode catalysts: a theoretical proposal," *Physical Chemistry Chemical Physics*, vol. 11, no. 37, pp. 8275–8284, 2009.
- [22] X. Y. Hu, H. W. Tian, W. T. Zheng et al., "Metallic-semiconducting phase transition of the edge-oxygenated armchair graphene nanoribbons," *Chemical Physics Letters*, vol. 501, no. 1–3, pp. 64–67, 2010.
- [23] T. Yumura, H. Kobayashi, and T. Yamabe, "Roles of radical characters of pristine and nitrogen-substituted hydrographene in dioxygen bindings," *Journal of Chemical Physics*, vol. 133, no. 17, Article ID 174703, 2010.
- [24] A. L. Higginbotham, D. V. Kosynkin, A. Sinitskii, Z. Sun, and J. M. Tour, "Lower-defect graphene oxide nanoribbons from multiwalled carbon nanotubes," *ACS Nano*, vol. 4, no. 4, pp. 2059–2069, 2010.
- [25] D. V. Kosynkin, W. Lu, A. Sinitskii, G. Pera, Z. Sun, and J. M. Tour, "Highly conductive graphene nanoribbons by longitudinal splitting of carbon nanotubes using potassium vapor," *ACS Nano*, vol. 5, no. 2, pp. 968–974, 2011.
- [26] D. V. Kosynkin, A. L. Higginbotham, A. Sinitskii et al., "Longitudinal unzipping of carbon nanotubes to form graphene nanoribbons," *Nature*, vol. 458, no. 7240, pp. 872–876, 2009.
- [27] A. Sinitskii, A. A. Fursina, D. V. Kosynkin, A. L. Higginbotham, D. Natelson, and J. M. Tour, "Electronic transport in monolayer graphene nanoribbons produced by chemical unzipping

- of carbon nanotubes," *Applied Physics Letters*, vol. 95, no. 25, Article ID 253108, 2009.
- [28] L. Jiao, L. Zhang, X. Wang, G. Diankov, and H. Dai, "Narrow graphene nanoribbons from carbon nanotubes," *Nature*, vol. 458, no. 7240, pp. 877–880, 2009.
- [29] A. L. Elias, A. R. Botello-Mendez, D. Meneses-Rodríguez et al., "Longitudinal cutting of pure and doped carbon nanotubes to form graphitic nanoribbons using metal clusters as nanoscalpels," *Nano Letters*, vol. 10, no. 2, pp. 366–372, 2010.
- [30] A. G. Cano-Márquez, F. J. Rodríguez-Macas, J. Campos-Delgado et al., "Ex-MWNTs: graphene sheets and ribbons produced by lithium intercalation and exfoliation of carbon nanotubes," *Nano Letters*, vol. 9, no. 4, pp. 1527–1533, 2009.
- [31] X. Wang, "Deformation guided unzipping of nanotubes: a first-principles study," *Physics Letters A*, vol. 374, no. 48, pp. 4894–4898, 2010.
- [32] B. Huang, Y.-W. Son, G. Kim, W. Duan, and J. Ihm, "Electronic and magnetic properties of partially open carbon nanotubes," *Journal of the American Chemical Society*, vol. 131, no. 49, pp. 17919–17925, 2009.
- [33] B. Wang and J. Wang, "First-principles investigation of transport properties through longitudinal unzipped carbon nanotubes," *Physical Review B*, vol. 81, no. 4, Article ID 045425, 2010.
- [34] H. Santos, L. Chico, and L. Brey, "Carbon nanoelectronics: unzipping tubes into graphene ribbons," *Physical Review Letters*, vol. 103, no. 8, Article ID 086801, 2009.
- [35] B. Huang, Z. Li, Y.-W. Son, G. Kim, W. Duan, and J. Ihm, "Multiple localized states and magnetic orderings in partially open zigzag carbon nanotube superlattices: an ab initio study," *Journal of Chemical Physics*, vol. 133, no. 8, Article ID 084702, 2010.
- [36] N. L. Rangel, J. C. Sotelo, and J. M. Seminario, "Mechanism of carbon nanotubes unzipping into graphene ribbons," *Journal of Chemical Physics*, vol. 131, no. 3, Article ID 031105, 2009.
- [37] H. Zhang, M. Zhao, T. He et al., "Orientation-selective unzipping of carbon nanotubes," *Physical Chemistry Chemical Physics*, vol. 12, no. 41, pp. 13674–13680, 2010.
- [38] J. Wang, L. Ma, Q. Yuan, L. Zhu, and F. Ding, "Transition-metal-catalyzed unzipping of single-walled carbon nanotubes into narrow graphene nanoribbons at low temperature," *Angewandte Chemie*, vol. 50, no. 35, pp. 8041–8045, 2011.
- [39] J. P. Perdew and Y. Wang, "Accurate and simple analytic representation of the electron-gas correlation energy," *Physical Review B*, vol. 45, no. 23, pp. 13244–13249, 1992.
- [40] G. Kresse and J. Furthmüller, "Efficient iterative schemes for ab initio total-energy calculations using a plane-wave basis set," *Physical Review B*, vol. 54, no. 16, pp. 11169–11186, 1996.
- [41] D. Vanderbilt, "Soft self-consistent pseudopotentials in a generalized eigenvalue formalism," *Physical Review B*, vol. 41, no. 11, pp. 7892–7895, 1990.
- [42] T. Yumura, M. Kertesz, and S. Iijima, "Confinement effects on site-preferences for cycloadditions into carbon nanotubes," *Chemical Physics Letters*, vol. 444, no. 1–3, pp. 155–160, 2007.
- [43] T. Yumura and M. Kertesz, "Cooperative behaviors in carbene additions through local modifications of nanotube surfaces," *Chemistry of Materials*, vol. 19, no. 5, pp. 1028–1034, 2007.
- [44] T. Yumura and M. Kertesz, "Roles of conformational restrictions of a bismalonate in the interactions with a carbon nanotube," *Journal of Physical Chemistry C*, vol. 113, no. 32, pp. 14184–14194, 2009.
- [45] M. J. Frisch et al., *Gaussian 03*, Gaussian, Pittsburgh, Pa, USA, 2003.
- [46] T. Yumura, K. Hirahara, S. Bandow, K. Yoshizawa, and S. Iijima, "A theoretical study on the geometrical features of finite-length carbon nanotubes capped with fullerene hemisphere," *Chemical Physics Letters*, vol. 384, no. 4–6, pp. 320–325, 2004.
- [47] T. Yumura, S. Bandow, K. Yoshizawa, and S. Iijima, "The role of fullerene hemispheres in determining structural features of finite-length carbon nanotubes," *Journal of Physical Chemistry B*, vol. 108, no. 31, pp. 11426–11434, 2004.
- [48] T. Yumura, D. Nozaki, S. Bandow, K. Yoshizawa, and S. Iijima, "End-cap effects on vibrational structures of finite-length carbon nanotubes," *Journal of the American Chemical Society*, vol. 127, no. 33, pp. 11769–11776, 2005.
- [49] T. Yumura, M. Kertesz, and S. Iijima, "Local modifications of single-wall carbon nanotubes induced by bond formation with encapsulated fullerenes," *Journal of Physical Chemistry B*, vol. 111, no. 5, pp. 1099–1109, 2007.
- [50] W. J. Hehre, K. Ditchfield, and J. A. Pople, "Self-consistent molecular orbital methods. XII. Further extensions of gaussian-type basis sets for use in molecular orbital studies of organic molecules," *The Journal of Chemical Physics*, vol. 56, no. 5, pp. 2257–2261, 1972.
- [51] J. S. Binkley, J. A. Pople, and W. J. Hehre, "Self-consistent molecular orbital methods. 21. Small split-valence basis sets for first-row elements," *Journal of the American Chemical Society*, vol. 102, no. 3, pp. 939–947, 1980.
- [52] T. A. Albright, J. K. Burdett, and M.-H. Whangbo, *Orbital Interactions in Chemistry*, A Wiley-Interscience, New York, NY, USA, 1984.

Research Article

Nanopore-Based DNA Analysis via Graphene Electrodes

Qing Zhao,¹ Yang Wang,¹ Jianjin Dong,¹ Lina Zhao,² X. F. Rui,³ and Dapeng Yu²

¹ State Key Laboratory for Mesoscopic Physics, School of Physics, Peking University, Beijing 100871, China

² CAS Key Lab for Biomedical Effects of Nanomaterials and Nanosafety, Institute of High Energy Physics, Chinese Academy of Sciences, Beijing 100049, China

³ Link A Media Devices Corporation, Santa Clara, CA 95051, USA

Correspondence should be addressed to Qing Zhao, zhaqing@pku.edu.cn and Dapeng Yu, yudp@pku.edu.cn

Received 21 September 2011; Accepted 22 February 2012

Academic Editor: Sulin Zhang

Copyright © 2012 Qing Zhao et al. This is an open access article distributed under the Creative Commons Attribution License, which permits unrestricted use, distribution, and reproduction in any medium, provided the original work is properly cited.

We propose an improvement for nanopore-based DNA analysis via transverse transport using graphene as transverse electrodes. Our simulation results show conspicuous distinction of tunneling current during translocation of different nucleotides through nanopore. Applying the single-atom thickness property of graphene, our findings demonstrate the feasibility of using graphene as transverse electrodes in future rapid and low-cost genome sequencing.

1. Introduction

Nanopore-based DNA analysis is a fast rising star as a single-molecule technique, and most apt to be the next generation of DNA sequencing [1]. With longitudinal electric field, DNA molecule is forced to pass through the pore with nanometer scale, presenting obvious current blockage signal by blocking the ion flux through the pore. Pioneer works have been done with biological pores and channels, such as α -hemolysin [2], which provides a predefined, repeatable, and precise pore structure atomically and a series of limitations, like short lifetime and sensitivity to environment conditions, as well. To overcome these disadvantages, solid-state nanopore [3] was introduced with the developing technology of nanofabrication [4], which shows great durability, possibility for geometry controlling, and compatibility with semiconductor industries [5]. Real-time DNA sequencing is still a big challenge nowadays because the method of longitudinal current detection only focused on the distinctive geometry and structure of four kinds of nucleotides, and great challenge remains such that the nanopore is too thick to realize single-base resolution and translocation of single base is too fast for recording (microseconds per base) [6]. An alternative approach in measuring the transverse current to get single-base resolution was put forward by Zwolak and Ventra in 2005 [7]. The basic idea is when

the bases are passing one by one through a voltage-biased tunnel gap inside a solid-state nanopore, they will alternately change the tunneling current based on how the localized base states contribute to the tunneling current since different bases have different local electronic densities of states with different spatial extent owing to their different chemical composition [8]. Intensive calculation work had been reported based on transverse current of different electrode-nucleotide couplings, spreading from the influence of noise [9] and environment [10] to the modification of electrodes [11]. However, most of them encountered the problem of interference of adjacent nucleotides when they are in the nanopore simultaneously. Since the length of DNA molecule is 0.32 nm per nucleotide, much smaller than the thickness of most available materials for transverse electrodes, it is hard to distinguish the neighboring nucleotides, even using the electrodes comprised of 3×3 gold atoms arranged as a (111) surface [8, 12].

Graphene is a two-dimensional hexagonal carbon lattice that was recently discovered [13] and has attracted intensive research attention due to its unique mechanical and electric properties [14]. Its single-atom thickness, ability to survive large transmembrane pressures, and intrinsic conducting properties [15] make it particularly attractive in DNA sequencing field since it holds hope for enabling transverse conductance measurements with single-base resolution.

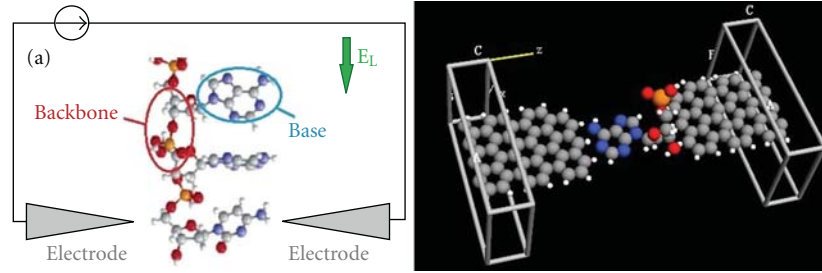


FIGURE 1: Principal diagram of nanopore-based DNA analysis: ssDNA is driven through a nanopore with two graphene electrodes by a longitudinal electric field; the transverse graphene electrodes are applied on defined voltage and used to measure the transverse current. The graphene electrodes are 8.6 Å wide and 12.1 Å apart. The SiN membrane and insulating cover layer are hidden in the graph.

DNA translocation experiment through graphene nanopores has been reported recently by three independent groups [16–18], while, in their study, graphene only acts as supporting membrane for nanopores, instead of the transverse electrode to measure tunnelling current. Making graphene as transverse electrode to resolve DNA conductance with single-base resolution experimentally is still very challenging nowadays. A numerical simulation was presented for achieving DNA transverse conductance via graphene nanogap [19], making graphene-based transverse conductance a promising candidate for robust DNA sequencing. However, nanogap may allow several DNA sequences to pass the gap simultaneously, which may lead to interference problems.

Herein, we propose and theoretically demonstrate a quantum transport simulation using graphene to comprise the transverse electrodes embedded in an SiN nanopore, which can avoid the problem of simultaneous DNA sequence translocation from the nanogap since nanopore has less dimension size compared with nanogap. SiN is used here to act as supporting membrane for graphene. From the simulation results, there exists a perfect exponential relation between the transport current and transverse voltage applied to the electrodes within an appropriate range, and, fortunately, significant distinction between different nucleotides has been demonstrated, implying the feasibility of this method in rapid genome sequencing.

2. Model and Method

Figure 1(a) presents the working principle of a nanopore-based DNA analysis: ssDNA is forced to translocate a nanopore by a longitudinal electric field (E_L), and the transverse current is measured via graphene transverse electrodes which are applied on defined voltage. Figure 1(b) shows the cross-section view of our simulation system: single-layer graphene electrodes are embedded in a 6 nm SiN layer and covered with a 1~2 nm insulating layer, which are hidden in the graph. The graphene electrodes are 7.4 Å wide and 12.1 Å apart, which is also the diameter of the nanopore in the SiN membrane. SiN membrane is used because it is most commonly used in DNA translocation experiment in solid-state nanopore field. The diameter is wide enough for a ssDNA to pass through and narrow enough to hamper two ssDNAs to translocate simultaneously and achieve a

measurable tunneling current. Figure 1(b) only shows part of the graphene electrodes and one nucleotide of a DNA sequence, since the rest parts of the nanopore device do not affect the tunneling effect and the thickness of electrodes is much smaller than the scale of the nucleotide molecule.

The simulation process is implemented as follows. First, the position of the nucleotides were set by manual control, in order to get an appropriate coupling of the maximum tunneling current with the electrodes' atoms. The relative positions of four kinds of nucleotides to the graphene electrodes were set up the same, located by the same part, the deoxyribose, of the nucleotides. Then the system of this time section, in which the base is in the flat location of the graphene electrodes, providing the strongest and most characteristic signals of tunneling current in the entire translocation process, was calculated by Atomistix ToolKit (ATK), a quantum transport simulation software, within the extended Hückel method, a semiempirical quantum chemistry method, developed by Hofmann in 1963 considering both pi and sigma orbitals [20]. Using this method, we can get the electronic distribution of the system and deduce the corresponding electric properties, such as the transmission spectra and so on. Finally, transverse currents from the transmission spectra were calculated via nonequilibrium Green's function method [21] and the current curves were contrasted to make our final conclusion. Regarding the issue of strand orientation as it passes through the nanopore, previous calculations showed that the proposed graphene nanopore device is essentially insensitive to strand orientation [22]. Therefore, we did not pay special attention to strand orientation issue during simulation.

Figures 2(a)–2(d) show the transmission spectra of adenosine, thymidine, cytidine, and guanosine under the same bias voltage of 2.4 V (± 1.2 V on each graphene transverse electrode), respectively. Because the transmission coefficient of each nucleotide, as well as the tunneling current, is quite different from each other, nearly one or two orders, to hold the maximums of four diagrams the same, we use different scale in each figure. In Figure 2, we could easily pick out the unique and characteristic resonance levels for each kind of nucleotide. We see clearly the characteristic resonance levels for each kind of nucleotide, which results from their unique base types. This could be the foundation of real sequencing in the future. Here, the “windows” of the

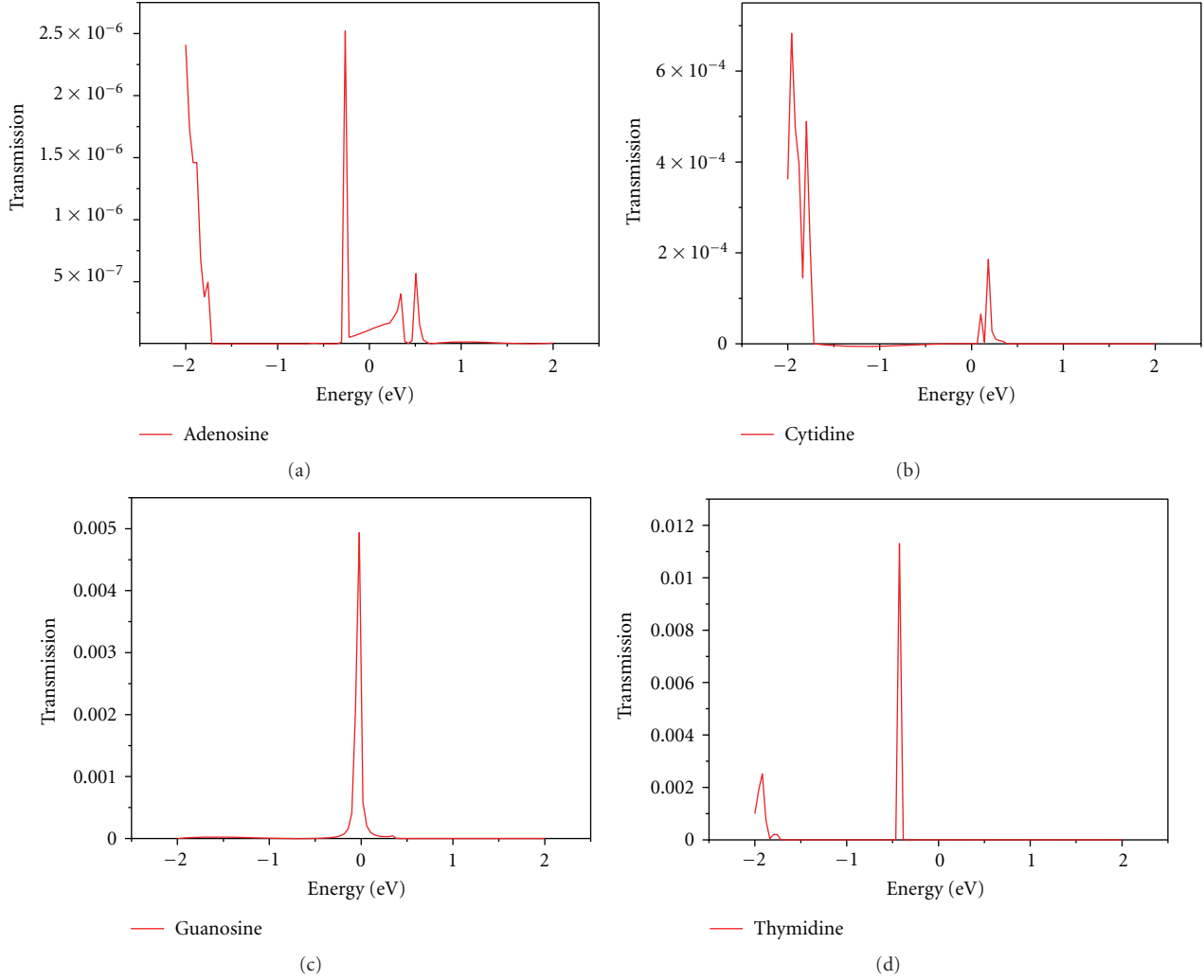


FIGURE 2: ((a)–(d)) The transmission spectra of adenosine, cytidine, guanosine, and thymidine under the same bias voltage of 2.4 V (± 1.2 V on each electrodes, which determine the “window” of the transmission), respectively. Because the transmission coefficient of each nucleotide, as well as the tunneling current, is quite different from each other, nearly one or two orders; to hold the maximums of four diagrams the same, we use different scale in each figure.

spectra are determined by ε_R and ε_L , the bias voltages applied on the graphene electrodes.

Consider the well-known formula for the transverse current, as follows [23]:

$$I_{LR}(V) = \frac{2e}{h} \int_{-\infty}^{\infty} d\varepsilon T_{LR}(\varepsilon) [f(\varepsilon - \varepsilon_L) - f(\varepsilon - \varepsilon_R)], \quad (1)$$

in which, L, R imply the left and right graphene electrode of our system, $V = \varepsilon_L - \varepsilon_R$ is the bias voltage, T_{LR} is the transmission coefficient, shown in Figure 2, which is calculated from the Hamiltonian matrices of the system, and $f(\varepsilon - \varepsilon_{(L/R)})$ is the Fermi distribution function. The equation shows that the transverse electrical current is proportional to the sum of the transmission peaks inside the bias voltage range, which is called the “window.” By this method, the tunneling current could be calculated easily with a Python script of ATK, using the extended Hückel method.

3. Simulation Results and Discussion

Figure 3(a) is V - $\ln I$ curve of adenosine base pair with bias from 0.0 V to 3.0 V with a step of 0.2 V. Here, when voltage is below 1.0 V, the tunneling current is very small, almost hard to detect, as demonstrated in $\ln I$ value. $\ln I$ from -45 to -42 means a null current, which is verified by a simulation carried out on non-load electrode system, where no DNA molecule was used. The current curve of non-load electrodes, shown in Figure 3(a), gave all points below 10^{-19} A. The V - $\ln I$ curve of adenosine clearly shows that, under 1.0 V, the current approximates zero, suggesting the close of the tunneling. The current quickly rises from 1.0 V to 1.4 V, and, when the voltage is above 1.4 V, the current behaves a perfect exponential relation with the bias voltage. This reveals a great deal of useful information: first, there exists a threshold voltage at about 1.2 V, above which the tunneling effect starts to show; second, only within an appropriate range of bias,

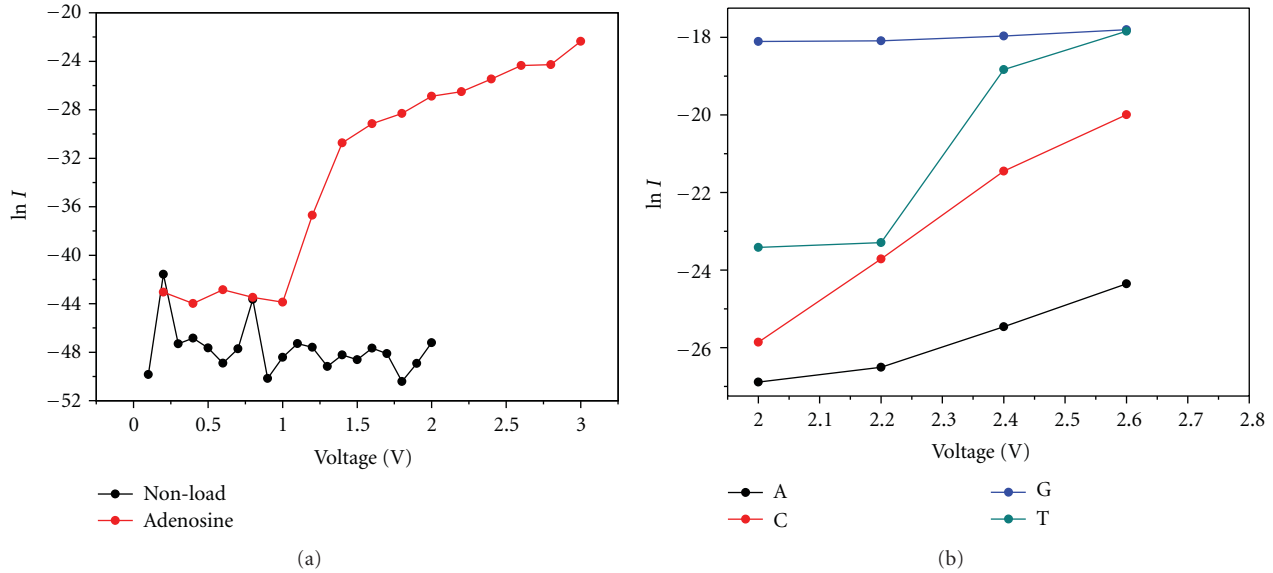


FIGURE 3: (a) The V - $\ln I$ curve of adenosine from 0 V to 3.0 V with a step of 0.2 V, and the current curve of non-load electrodes system from 0.0 V to 2.0 V with a step of 0.1 V. (b) Four distinguishable V - $\ln I$ curves of four nucleotides, A, C, G, T, respectively. All of which express linear relationship from 2.0 V to 2.6 V with the same step of 0.2 V. At most voltages, they keep a difference of one or two orders to each other.

which is from 1.4 V to 3.0 V in our case, the conclusion before could be held. Our next simulation with four different nucleotides was carried out in this voltage range.

Figure 3(b) represents the transverse current $\ln I$ - V curves of four nucleotides, ranging from 2.0 V to 2.6 V with the same step of 0.2 V.

All four curves express linear relationship within this voltage range and show conspicuous distinction between different nucleotides, nearly one or two orders to each other, which agrees with the results by Zwolak and ventra [7], although in a different arrangement of the current intensities. This may result from the different coupling of nucleotides with graphene and nucleotides with Au, which Zwolak used as transverse electrodes in his simulation. The distinct difference in $\ln I$ at the same bias voltage for each nucleotide indicates a potential sequencing approach by using graphene transverse-electrode-based nanopore: we can utilize transverse current to characterize electronic signatures of each nucleotide.

Such transverse current distinction between different nucleotides may result from the geometry dimensions of the different base types. We could see clearly that the current has a same arrangement as the sizes of the four base types (i.e., G, T, C, A). Because the nanopore is just a little bigger than the nucleotides, the tunneling effect is very sensitive to the distance between transverse electrodes. So the small difference in base size will lead to great discrepancy in transverse current. The second reason may be the different interaction between graphene electrodes and base atoms. For instance, the guanosine and cytidine with three hydrogen bonds in the bases have much higher currents than the thymidine and adenosine with two ones. The tunneling current may come from the hydrogen bond on the base, which has been discussed before [24]. Because the thickness

of graphene is only single atom, the distance between the electrode and the translocating nucleotide (less than 1 Å) is much less than that of the neighboring ones (more than 3 Å), as well as the interaction between them. Thus we need not to consider the interference from the neighboring nucleotides in our calculations.

At last, we could conceive the experimental realization of the proposed method. First, transfer and locate a graphene ribbon, narrow enough to compare with the diameter of the nanopore we expect, on the SiN membrane. Then use transmission electron microscope to fabricate a nanopore on the membrane [25], where the graphene ribbon is located. When the pore is fabricated, the graphene ribbon is cut off into two segments, just on the two sides of the nanopore, and can act as transverse electrodes. After being covered with an insulating layer, the nanopore device with graphene transverse electrodes is fabricated. Here, the most challenge maybe the graphene ribbon is very difficult to manipulate at such narrow scale.

4. Summary

In summary, quantum transport simulation using graphene as transverse electrodes was carried out in nanopore-based-DNA analysis, and the obtained $\ln I$ - V curves show exponential relation between the current and the voltage. Moreover, distinguishable distinctions in $\ln I$ under same bias voltage between different nucleotides were demonstrated, indicating the feasibility of the nanopore-based DNA analysis via graphene electrodes. Such findings are fundamentally useful toward the ultimate goal of inexpensive and fast DNA sequencing.

Acknowledgments

This project is financially supported by the National Natural Science Foundation of China (Project no. 50902004, 11023003), National 973 Projects (no. 2007CB936202, 2009CB623703, MOST) from China's Ministry of Science and Technology, and the Research Fund for the Doctoral Program of Higher Education.

References

- [1] K. Healy, "Nanopore-based single-molecule DNA analysis," *Nanomedicine*, vol. 2, no. 4, pp. 459–481, 2007.
- [2] J. J. Kasianowicz, E. Brandin, D. Branton, and D. W. Deamer, "Characterization of individual polynucleotide molecules using a membrane channel," *Proceedings of the National Academy of Sciences of the United States of America*, vol. 93, no. 24, pp. 13770–13773, 1996.
- [3] C. Dekker, "Solid-state nanopores," *Nature Nanotechnology*, vol. 2, no. 4, pp. 209–215, 2007.
- [4] K. Healy, B. Schiedt, and I. P. Morrison, "Solid-state nanopore technologies for nanopore-based dna analysis," *Nanomedicine*, vol. 2, no. 6, pp. 875–897, 2007.
- [5] S. Liu, Q. Zhao, Q. Li et al., "Controlled deformation of Si₃N₄ nanopores using focused electron beam in a transmission electron microscope," *Nanotechnology*, vol. 22, no. 11, Article ID 115302, 2011.
- [6] D. Branton, D. W. Deamer, A. Marziali et al., "The potential and challenges of nanopore sequencing," *Nature Biotechnology*, vol. 26, no. 10, pp. 1146–1153, 2008.
- [7] M. Zwolak and M. Di Ventra, "Electronic signature of dna nucleotides via transverse transport," *Nano Letters*, vol. 5, no. 3, pp. 421–424, 2005.
- [8] J. Lagerqvist, M. Zwolak, and M. Di Ventra, "Fast dna sequencing via transverse electronic transport," *Nano Letters*, vol. 6, no. 4, pp. 779–782, 2006.
- [9] M. Krems, M. Zwolak, Y. V. Pershin, and M. Di Ventra, "Effect of noise on dna sequencing via transverse electronic transport," *Biophysical Journal*, vol. 97, no. 7, pp. 1990–1996, 2009.
- [10] J. Lagerqvist, M. Zwolak, and M. Di Ventra, "Influence of the environment and probes on rapid DNA sequencing via transverse electronic transport," *Biophysical Journal*, vol. 93, no. 7, pp. 2384–2390, 2007.
- [11] V. Meunier and P. S. Krstić, "Enhancement of the transverse conductance in DNA nucleotides," *Journal of Chemical Physics*, vol. 128, no. 4, Article ID 041103, 2008.
- [12] Y. He, L. Shao, R. H. Scheicher et al., "Differential conductance as a promising approach for rapid DNA sequencing with nanopore-embedded electrodes," *Applied Physics Letters*, vol. 97, no. 4, Article ID 043701, 2010.
- [13] K. S. Novoselov, A. K. Geim, S. V. Morozov et al., "Electric field in atomically thin carbon films," *Science*, vol. 306, no. 5696, pp. 666–669, 2004.
- [14] A. K. Geim, "Graphene: status and prospects," *Science*, vol. 324, no. 5934, pp. 1530–1534, 2009.
- [15] A. K. Geim and K. S. Novoselov, "The rise of graphene," *Nature Materials*, vol. 6, no. 3, pp. 183–191, 2007.
- [16] G. F. Schneider, S. W. Kowalczyk, V. E. Calado et al., "DNA translocation through graphene nanopores," *Nano Letters*, vol. 10, no. 8, pp. 3163–3167, 2010.
- [17] C. A. Merchant, K. Healy, M. Wanunu et al., "DNA translocation through graphene nanopores," *Nano Letters*, vol. 10, no. 8, pp. 2915–2921, 2010.
- [18] S. Garaj, W. Hubbard, A. Reina, J. Kong, D. Branton, and J. A. Golovchenko, "Graphene as a subnanometre trans-electrode membrane," *Nature*, vol. 467, no. 7312, pp. 190–193, 2010.
- [19] H. W. Postma, "Rapid sequencing of individual DNA molecules in graphene nanogaps," *Nano Letters*, vol. 10, no. 2, pp. 420–425, 2010.
- [20] R. Hoffmann, "An extended Hückel theory. I. Hydrocarbons," *The Journal of Chemical Physics*, vol. 39, no. 6, pp. 1397–1412, 1963.
- [21] M. D. Ventra, *Electrical Transport in Nanoscale Systems*, Cambridge University Press, Cambridge, UK, 2008.
- [22] T. Nelson, B. Zhang, and O. V. Prezhdo, "Detection of nucleic acids with graphene nanopores: Ab initio characterization of a novel sequencing device," *Nano Letters*, vol. 10, no. 9, pp. 3237–3242, 2010.
- [23] S. Datta, *Electrical Transport in Mesoscopic Systems*, Cambridge University Press, Cambridge, UK, 1995.
- [24] M. H. Lee and O. F. Sankey, "Theory of tunneling across hydrogen-bonded base pairs for DNA recognition and sequencing," *Physical Review E*, vol. 79, no. 5, Article ID 051911, 10 pages, 2009.
- [25] J. Zhang, L. You, H. Ye, and D. Yu, "Fabrication of ultrafine nanostructures with single-nanometre precision in a high-resolution transmission electron microscope," *Nanotechnology*, vol. 18, no. 15, Article ID 155303, 2007.

Research Article

Dry-Transfer of Aligned Multiwalled Carbon Nanotubes for Flexible Transparent Thin Films

Matthew Cole,¹ Pritesh Hiralal,^{1,2} Kai Ying,¹ Chi Li,^{1,3} Yan Zhang,¹ Kenneth Teo,⁴ Andrea Ferrari,¹ and William Milne^{1,5}

¹Electrical Engineering Division, Department of Engineering, University of Cambridge, 9 JJ Thomson Avenue, Cambridge CB3 0FA, UK

²Nokia Research Centre, Broers Building, 21 JJ Thomson Avenue, Cambridge CB3 0FA, UK

³Display Research Centre, School of Electronic Science and Engineering, Southeast University, Nanjing 210096, China

⁴AIXTRON Ltd., Anderson Road, Swavesey CB24 4FQ, UK

⁵Department of Information Display, Kyung Hee University, Seoul 130-701, Republic of Korea

Correspondence should be addressed to Matthew Cole, mtc35@cam.ac.uk

Received 14 October 2011; Accepted 26 December 2011

Academic Editor: Teng Li

Copyright © 2012 Matthew Cole et al. This is an open access article distributed under the Creative Commons Attribution License, which permits unrestricted use, distribution, and reproduction in any medium, provided the original work is properly cited.

Herein we present an inexpensive facile wet-chemistry-free approach to the transfer of chemical vapour-deposited multiwalled carbon nanotubes to flexible transparent polymer substrates in a single-step process. By controlling the nanotube length, we demonstrate accurate control over the electrical conductivity and optical transparency of the transferred thin films. Uniaxial strains of up to 140% induced only minor reductions in sample conductivity, opening up a number of applications in stretchable electronics. Nanotube alignment offers enhanced functionality for applications such as polarisation selective electrodes and flexible supercapacitor substrates. A capacitance of 17 F/g was determined for supercapacitors fabricated from the reported dry-transferred MWCNTs with the corresponding cyclic voltograms showing a clear dependence on nanotube length.

1. Introduction

Carbon nanotubes, one-dimensional high aspect ratio carbon allotropes, have received significant interest in the past two decades as a viable candidate material to replace the industry pervading, and increasingly expensive, transparent conductor, indium tin oxide (ITO). Although highly transparent and highly conductive, ITO exhibits poor flexing performance due to microcrack formation. Carbon nanotube networks are extremely flexible [1–3], highly conductive [4–6] and offer impressive optical transparency [4, 7–9]. Nevertheless, in order to fully exploit these features, films must be free-standing or supported on substrates of similar opacity and flexibility, namely, polymers and elastomers. Little work on the direct deposition of aligned nanotubes onto polymers has been reported [10], and as a result few applications exploit the properties of pristine nanotubes. Direct nanotube deposition on polymers necessitates substantial reductions in growth temperatures. This most often results in the

deposition of inflexible pyramidal carbon nanofibres [11] rather than highly graphitic and conductive nanotubes.

A variety of solution processes have been explored to produce nanotube thin films [5, 12–14]. Nevertheless, such detrimental *chemi douche* processing, employing aggressive sonication and costly acid treatments, ultimately degrades the nanotubes electronic properties. Nanotube alignment has been demonstrated in a number of ways [15–17] though solution processing produces isotropic networks lacking the advantageous structural anisotropy associated with the initial as-grown one-dimensional nanostructures. Consequently, a wet-chemistry-free, inexpensive, and facile transfer technique, that retains the nanotubes alignment, is necessary for applications such as flexible optoelectronic polarisers and supercapacitors for next-generation energy storage [18–21] and display technologies.

Carbon nanotube-based thin films offer extremely high surface areas which make them functionally desirable for high-density energy storage, though binderless processes

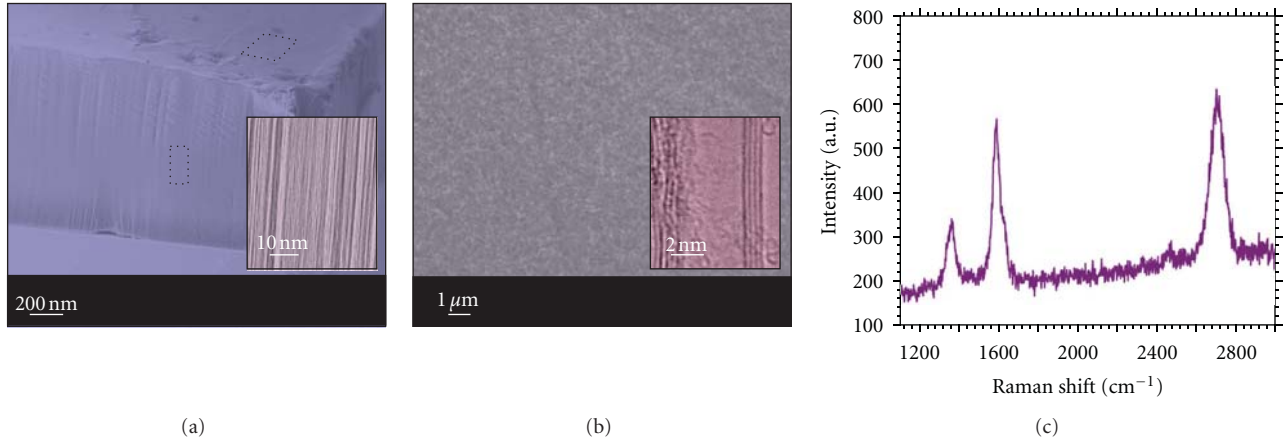


FIGURE 1: (a) Side profile SEM micrograph of the source MWCNTs. *Inset*: high-resolution SEM micrograph of the lower highlighted area demonstrating the extremely linear growth. (b) Areal SEM micrograph of the upper highlighted area in (a) illustrating the spaghetti-like morphology of the forest surface. *Inset*: HR-TEM micrograph showing four graphitic side walls. (c) Raman spectra (3 mW, 633 nm) of the as-grown MWCNTs. No distinguishable RBM peaks were observed ($100\text{--}500\text{ cm}^{-1}$ wave numbers not shown), relative to the spectrometers noise floor, suggesting a largely multiwall population.

that offer strong surface and intertube adhesion combined with excellent conductivities and nanotube alignment are advantageous traits. We herein report on the dry-transfer of multiwalled carbon nanotubes to polymer substrates and demonstrate control over the sheet resistance and optical transparency of the transferred thin films. Simple supercapacitor structures have also been demonstrated as one viable application of the proposed technique.

2. Experiment

Multiwalled carbon nanotubes (MWCNTs) were synthesised by thermal chemical vapour deposition (CVD) in a commercially available cold-walled reactor (AIXTRON, Black Magic). Bilayer catalysts were prepared by RF sputtering 10 nm Al_2O_x onto 200 nm thermally oxidised Si substrates which were subsequently exposed to ambient atmosphere and coated with 1 nm thermally evaporated Fe (0.2 \AA/s). The chamber was prepressurised to 26 mbar with 8 sccm C_2H_2 diluted in 192 sccm H_2 . An ohmically heated graphite stage was ramped at 5°C/s to 700°C . Growth was repeatedly observed to initiate at $\sim 520^\circ\text{C}$. Figures 1(a) and 1(b) show typical profile and areal scanning electron micrographs (SEMs) of an as-grown MWCNT forest. A high-resolution transmission electron micrograph (HR-TEM) of an individual MWCNT is given in the inset of Figure 1(b). The MWCNTs are formed from 2–5 graphitic walls, were 25 ± 13 (S.D) nm in diameter, and had an initial growth rate of $\sim 0.8\text{ }\mu\text{m/s}$ that monotonically decreased over time. Figure 1(c) is the Raman spectra of the as-grown forest (Renishaw InVia, He-Ne source operating at 633 nm/3 mW). The spectra are characteristic of MWCNTs [22, 23] and were highly uniform across samples, highlighting process reproducibility.

Figure 2 illustrates the dry-transfer process. A polycarbonate (PC) destination substrate is angled toward the sources MWCNTs and is compressed using a quartz cylinder,

rotated and sheared at $\sim 1\text{ cm/s}$. The MWCNTs readily debond from the source substrate and adhere to the PC. The dry-transfer process does not degrade the crystallographic order of the MWCNTs, as evidenced *via* Raman spectroscopy. A variety of destination substrates were considered, including poly(ethylene terephthalate), polycarbonate, and Al foil. In the latter case, when transferring extremely short nanotubes ($<1\text{ }\mu\text{m}$), self-assembled monolayer (SAM) adhesion promoters were necessary, such as poly(lysine) and aminopropyltriethoxy silane (APTES). Prior to SAM treatment MWCNTs did not adhere to the Al foil, whereas after treatment nearly 100% (by area) were successfully transferred.

Figure 3(c) shows a $900\text{ nm} \times 900\text{ nm}$ AFM micrograph (Agilent) of a dry-transferred MWCNT film on a PC substrate demonstrating the high degree of alignment. An optical micrograph of poly(lysine)-treated Al foil with a dry-transferred MWCNT film is given in Figure 3(d). The inset depicts a schematic of the substrates cross-section.

MWCNT thin films were patterned by standard photolithography and O_2 reactive ion etching (RIE: 0.2 mbar, 100 W, 120 s) (Figures 3(b) and 3(e)). Transparency control was demonstrated using RIE. The transparency between the polymer-protected 5, 20, and $50\text{ }\mu\text{m}$ dots was controlled, as illustrated in Figure 3(f). Transparency control was also demonstrated by adjusting the length of the MWCNTs prior to the dry-transfer, (by varying the CVD growth duration). In this instance, films were defined by patterning the bilayer catalyst prior to growth. A Mo catalyst-passivation process was used to prevent nanotube growth from particular areas. No nanotubes grew from those areas coated with Mo (20 nm). An inexpensive laser-jet patterning technique was employed to achieve this. Patterned MWCNT forests were then transferred, as afore mentioned. Repeatedly rolled films became sufficiently compacted such that they formed free-standing, pristine MWCNT “paper” that maintained structural integrity even under rigorous mechanical strain.

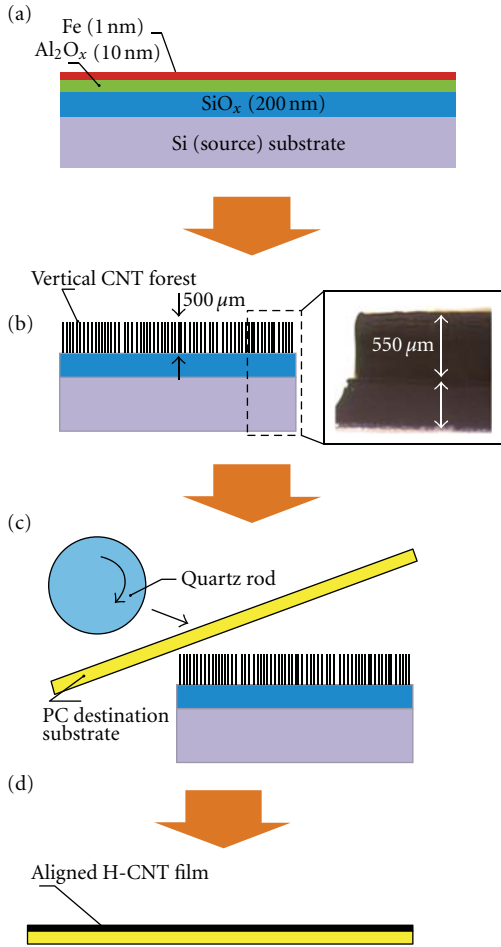


FIGURE 2: The dry-transfer process. (a) Cross-sectional illustration of the Si/SiO₂ (200 nm) growth substrate magnetron sputtered with 10 nm Al₂O_x/1 nm Fe thermally evaporated (Lesker PVD). (b) MWCNT synthesis by thermal CVD: 700°C, 26 mbar, 192 sccm H₂ : 8 sccm C₂H₂, 10 min. *Inset*: Optical micrograph of an as-grown 550 μm tall MWCNT forest. (c) PET destination substrate angled towards the source nanotube forest. PET and source nanotube substrate are compressed by a rolled quartz cylinder, moving at a rate of ~1 cm/s. (d) Aligned MWCNT thin film.

Uniaxial strain and bend radii measurements were performed using computer-controlled custom-built systems connected to a Keithley 6430 source-measure unit. Experiments were performed at room temperature and pressure.

3. Results and Discussions

Figure 4 shows optical micrographs of three prepatterned transferred samples of differing MWCNT length. The sheet resistance (R_s) and optical transmittance (T) were found to be strongly dependent on the MWCNT length. Figure 5(a) shows the UV-Vis-NIR transmittance of films fabricated from MWCNTs < 1 μm to 500 μm in length. For the most opaque and highly conductive films, $R_s \sim 1.2 \Omega/\text{sq.}$ with ~9% transparency (550 nm). For nominally equivalent samples, two- and four-probe conductivity measurements yielded

$R_s \sim 10.2 \Omega/\text{sq.}$ and $\sim 2.6 \Omega/\text{sq.}$, respectively, evidencing a low contact resistance (7.6 Ω/sq). The most transparent films (85% for <1 μm long MWCNTs) had sheet resistances as low as 550–1000 Ω/sq. Reducing the nanotube length substantially increased the optical transmission whilst only increasing the sheet resistance by approximately one order of magnitude (Figure 5(b)). This observation can be explained in terms of the increased number of inter-nanotube junctions for films comprised of shorter nanotubes. Furthermore, one would expect longer nanotubes to increase the films conductivity as the rolling process produces substantially thicker films which offer lower bulk resistance. The DC conductivity in such films is primarily dependent on tunnelling between individual nanotubes. As a result, the conductivity is critically dependent on the number of conduction pathways, junctions, and the general network morphology—all of which can be varied by adjusting the nanotube length and degree of alignment. The films demonstrated optoelectronic characteristics nearing the ITO benchmark and superior characteristics to competing organic technologies such as TDA and PEG-enhanced PEDOT:PSS [24, 25].

The sheet resistance (R_s) and optical transparency at 550 nm (T) are related by [26–28];

$$T = \left[1 + \left(\frac{tZ_0}{2} \right) \sigma_{\text{opt}} \right]^{-2} = \left[1 + 188.5 \frac{1}{R_s} \left(\frac{\sigma_{\text{opt}}}{\sigma_{\text{dc}}} \right) \right]^{-2} \quad (1)$$

where Z_0 is the impedance of free space (377 Ω), σ_{opt} is the optical conductivity, and σ_{dc} is the direct current electrical conductivity. A viable transparent electrode must demonstrate low- R_s and high- T throughout the optical window (300–900 nm). For an ideal transparent conductor, $(\sigma_{\text{opt}}/\sigma_{\text{dc}}) \rightarrow 0$. Fitting (1) gives $(\sigma_{\text{opt}}/\sigma_{\text{dc}}) = 1.7 \times 10^{-1}$. Graphite has a conductivity ratio of 9.1×10^{-2} , whereas current driven applications require 4.5×10^{-3} . The minimum industry standard for (brittle) transparent conductors, typical for display applications, is 2.9×10^{-2} (>90% for <100 Ω/sq.) [26, 29]. The reported conductance ratio is somewhat off the industry standard but is nevertheless close to the state-of-the-art for thin films prepared from chemically modified graphene [26]. Though the pristine thin films offer only modest performance, it is important to stress that these films are chemically *untreated*. The films have not been doped in anyway. Suitable doping will lead to conductivity enhancements, for a given transparency, thus allowing the films to compete with more traditional vacuum and spray processing, which intrinsically employ *en route* doping procedures.

The AC sheet resistance of the dry-transferred films was investigated at microwave frequencies using a technique described in detail in [30]. The transmissive sheet resistances, in the 120–175 THz range, were found to be 0.3 and 640 Ω/sq., for nanotubes 500 μm and 1 μm long, and were broadly consistent with the DC measurements for films of similar optical characteristics discussed previously.

The uniaxial strain response of the dry-transferred MWCNTs and the primary competing technologies, namely CVD grown (2–4 layer) hot press laminated graphene (HPLG) [31] and commercially available PET-supported

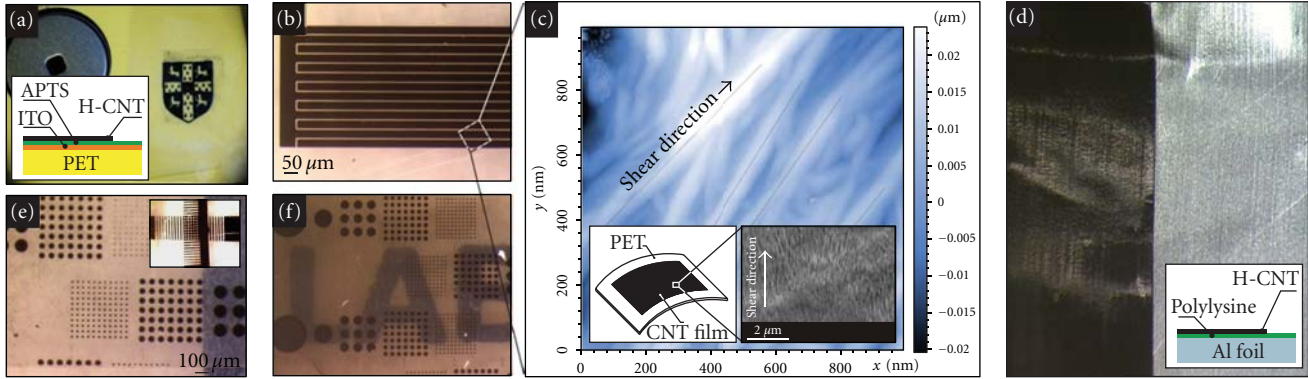


FIGURE 3: Patterned dry-transferred MWCNT thin films. (a) Patterning by Mo catalyst passivation. $\text{Al}_2\text{O}_3/\text{Fe}$ bilayer catalyst patterned using laser-jet/paper transfer and Mo deposition. Patterned MWCNT films were transferred to the destination PC (as described in Figure 2). A self-assembled monolayer, APTES was employed for PET/ITO substrates prior to transfer. (b, e) An aligned MWCNT film patterned into 5 μm interdigitated electrodes by standard photolithography and O_2 RIE (0.2 mbar, 100 W, 120 s). *Inset*: optical micrograph of a Mo-passivated prepatterned CNT film shear transferred to a PET substrate and a second perpendicularly aligned prepatterned forest shear transferred. (c) AFM micrograph (900 nm \times 900 nm) of a dry-transferred MWCNT film on a PC substrate. *Inset*: SEM micrograph of a transferred film showing the high level of macroscopic alignment. (d) Optical micrograph of poly(lysine)-treated (right) with a dry-transferred MWCNT film (left). Prior to treatment MWCNTs did not adhere. *Inset*: schematic of the substrate cross-section. (f) Transparency control by O_2 RIE with 5, 20, and 50 μm dots defined by conventional photolithography.

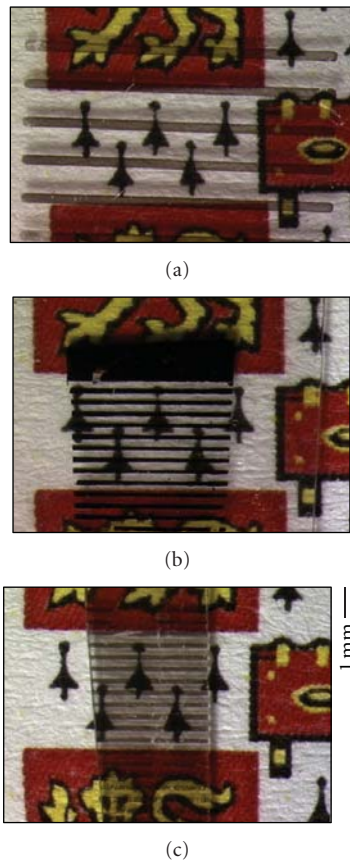
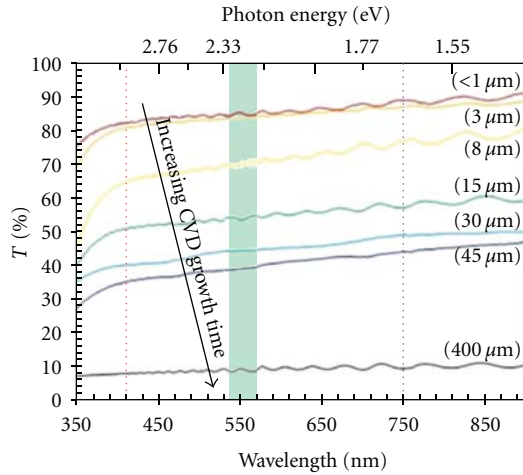


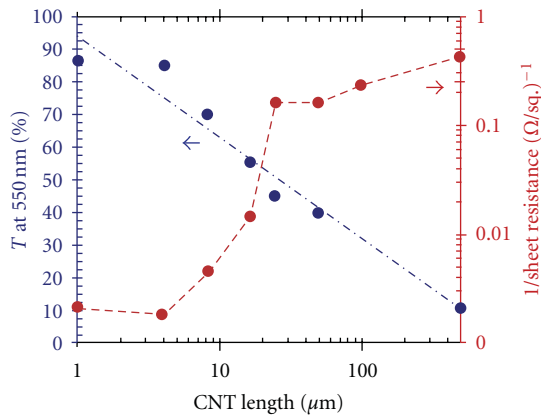
FIGURE 4: (a-c) Optical micrographs of Mo-passivated patterned MWCNT thin films transferred to PET showing controllable transparency by adjusting the length of the source nanotubes. The presented micrographs are for nanotubes that are (a, c) 30 μm and (b) 500 μm in length.

ITO, is shown in Figure 6(a). Samples were electrically contacted using mechanical clamps and conductive epoxy (inset Figure 6(a)). The maximum uniaxial tensile strain (ϵ), defined as the strain for which $\partial(\Delta R/R)/\partial\epsilon \rightarrow \infty$, of commercially available ITO was $\sim 1.2\%$. HPLG samples failed at $\sim 15\%$ and showed excellent correspondence with the theoretical values for single graphene flake failure [32, 33]. The dry-transferred MWCNT thin films withstood strains of up to 140% (the limit of the apparatus) whilst showing only a minor reduction in conductivity ($\Delta R/R_0 \sim 5$, where R_0 denotes the initial/relaxed sheet resistance). Similar performance has been reported elsewhere, though predominately only in the case of solution-processed single-walled carbon nanotube thin films [34]. As the films become increasingly strained, the MWCNTs align. The individual MWCNTs observe negligible strain during this aligning stage. It is not until the film has maximised its degree of alignment that the MWCNTs undergo nanoscopic straining and eventually fail catastrophically. As a result, exceptionally high failure strains are possible owing to the networks porosity and anisotropy.

The cyclic strain performance is plotted in Figure 6(b). Under equivalent conditions, ITO/PET was strained to 1% and then relaxed. The resistivity of the ITO/PET was around 44% larger than the initial unstrained film. Straining irreversibly increased the sheet resistance of the ITO through microcrack formation. In contrast, dry-transferred films were strained (50%), then relaxed, and the process repeated. The initial strain (cycle 1) increased the sample resistance by approximately 42%; however each cycle thereafter the relaxed resistance repeatedly returned to this value. The long-term flexing stability of the dry-transferred thin films was considered by straining samples by 22%, over 100 cycles. The dry-transferred films showed a negligible increase in



(a)

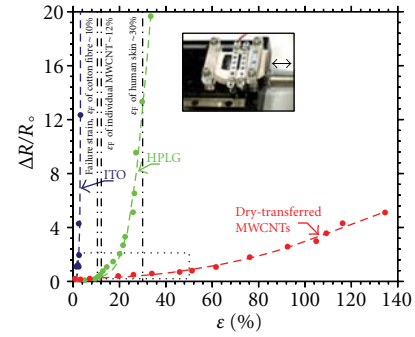


(b)

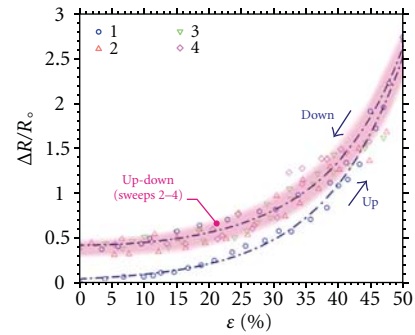
FIGURE 5: Opto-electronic performance. (a) UV-Vis-NIR. Variation in the optical transmission of dry-transfer MWCNT films consisting of MWCNTs of increasing source length. (b) Sheet resistance and optical transparency as a function of nanotube length.

resistance over time. Figure 6(c) depicts a dependence on the electrode separation. Increasing the electrode separation (L) tended to increase the maximum attainable strain as this increased the amount of available material over which the strain was distributed. Figure 6(d) shows the variation in the normalised change in resistance ($\Delta R/R_0$) as a function of the radius of curvature. The inset(s) depict the apparatus during a typical measurement. $\Delta R/R_0 = 0.09$ and was largely independent of the radius of curvature over the range considered. $\Delta R/R_0$ of the ITO samples increased by over three orders of magnitude for curvatures < 9.5 mm. Similarly, HPLG samples showed a linear increase in $\Delta R/R_0$ for radius < 5 mm.

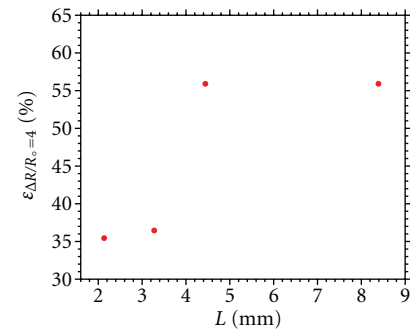
A key feature of the reported technique is the ability to align the nanotubes during the inexpensive and rapid dry-transfer process. The degree of nanotube alignment is illustrated in Figure 7, which plots the Steridian 37 (Str37) function for a transferred sample, calculated using the SPIP image analysis software. Str37 is defined as the ratio of the in-plane distance between the real autocorrelation centre



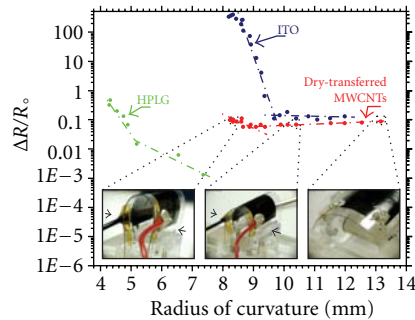
(a)



(b)



(c)



(d)

FIGURE 6: (a) Normalised resistance ($\Delta R/R_0$) for ITO, hot press laminated grapheme (HPLG), and dry-transferred MWCNTs ($\sim 220 \mu\text{m}$ in length) as a function of uniaxial strain. Failure strains of human skin, cotton fibre, and individual MWCNTs are included for comparison. (b) cyclic performance of a dry-transferred MWCNT thin film (for a fixed nanotube length of $130 \mu\text{m}$). (c) Strain (at $\Delta R/R_0 = 4$) as a function of electrode separation. (d) Variation in sample resistance as a function of the radius of curvature. *Insets*: optical micrographs taken during a typical measurement. Note the lack of film de-binding, even under high curvature.

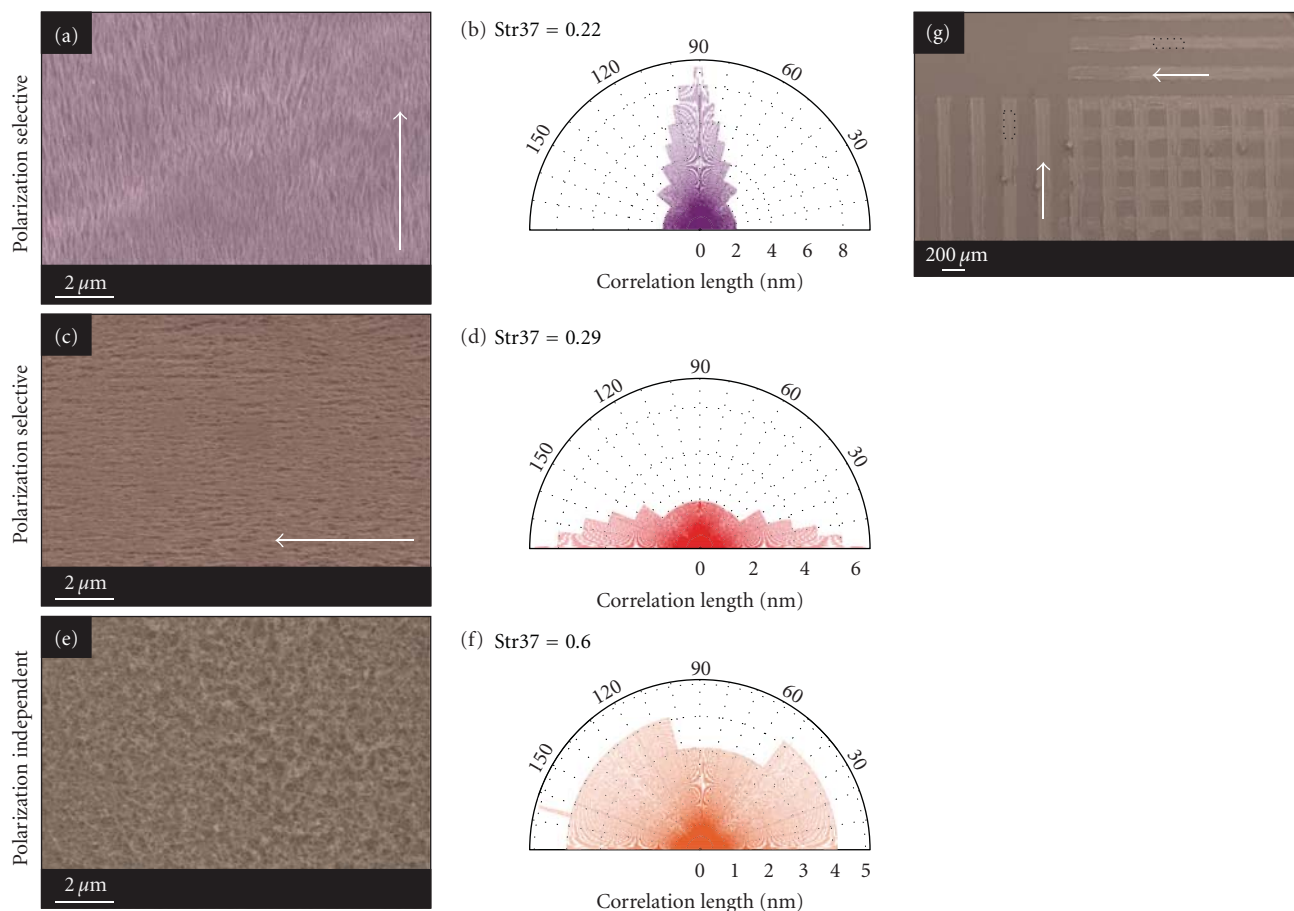


FIGURE 7: (a, c) SEM micrographs of the polarisation selective, partially transparent electrodes. (b, d) Str37 quantifying the alignment of the vertical (0.22) and horizontal (0.29) transfers, compared to (e, f) an unaligned compressed film (0.60). (g) SEM micrograph of crossed-transfers on a single untreated PET substrate. Arrows denote the transfer direction.

and the boundary at which the height of the image has decayed to 37% of the depth-range at this autocorrelation centre. An autocorrelation is applied to the images depth-range to infer the position. The decay in the depth-range in all directions is evaluated and the Str37 value is calculated [35, 36]. For perfectly aligned arrays $\text{Str37} = 0$, whilst for disordered networks which exhibit no directional preference, $\text{Str37} = 1$. Depending on the roll technique both well-aligned (Figures 7(a)–7(d)) and highly isotropic networks could be transferred (Figures 7(e) and 7(f)). $\text{Str37} = 0.26$ for the aligned transfers and 0.60 for the compressed/isotropic transfers.

Aligned nanotube electrodes may find application as tunable optical polarisers and advanced electrode materials in next generation flexible display technologies. Figure 7(g) shows a fabricated bilayer structure. Here crossed and aligned structures, of controlled controlled pitch, were transferred to a PET substrate by successive rolls of pre-patterned forests to from optical polarisers that exploit the nanoscopic spacing of the nanotubes, and also the microscopic spacing of the patterned films.

To demonstrate one potential application of the dry-transferred thin films, two-electrode electric double-layer

(EDLC) cells were constructed. Due to the films' high conductivity, the MWCNTs functioned as both the active material and charge collector, reducing the overall material requirements therefore increasing the weight fraction of the active material in the device. The final EDLC was $10 \text{ mm} \times 10 \text{ mm}$ (Figure 8(a)). An insulating porous separator (Celgard 2500) was sandwiched between two MWCNT electrodes soaked in electrolyte (1M Tetraethylammonium tetrafluoroborate (Et_4NBF_4) in propylene carbonate, Sigma-Aldrich). Al tape was used to externally electrically contact the cell. Three different films, comprised of different MWCNT lengths, were considered. The nanotube lengths and active weights were $28.5 \mu\text{m}/0.6 \text{ mg} \cdot \text{cm}^{-2}$ (1 min growth), $96 \mu\text{m}/1.1 \text{ mg} \cdot \text{cm}^{-2}$ (5 min), and $235 \mu\text{m}/2.3 \text{ mg} \cdot \text{cm}^{-2}$ (10 min). Cells were characterised by galvanostatic charge/discharge ($1 \text{ mA}/\text{cm}^2$) and cyclic voltammetry ($50 \text{ mV}/\text{s}$) measured using an Autolab PGSTAT302N potentiostat (Figure 8(b)).

Thicker films offered higher conductivities and longer nanotubes showed a higher capacitance per unit area as well as a lower equivalent series resistance (ESR), both of which are essential for high-power delivery. The capacitance of the two-electrode MWCNT EDLCs was estimated to be between

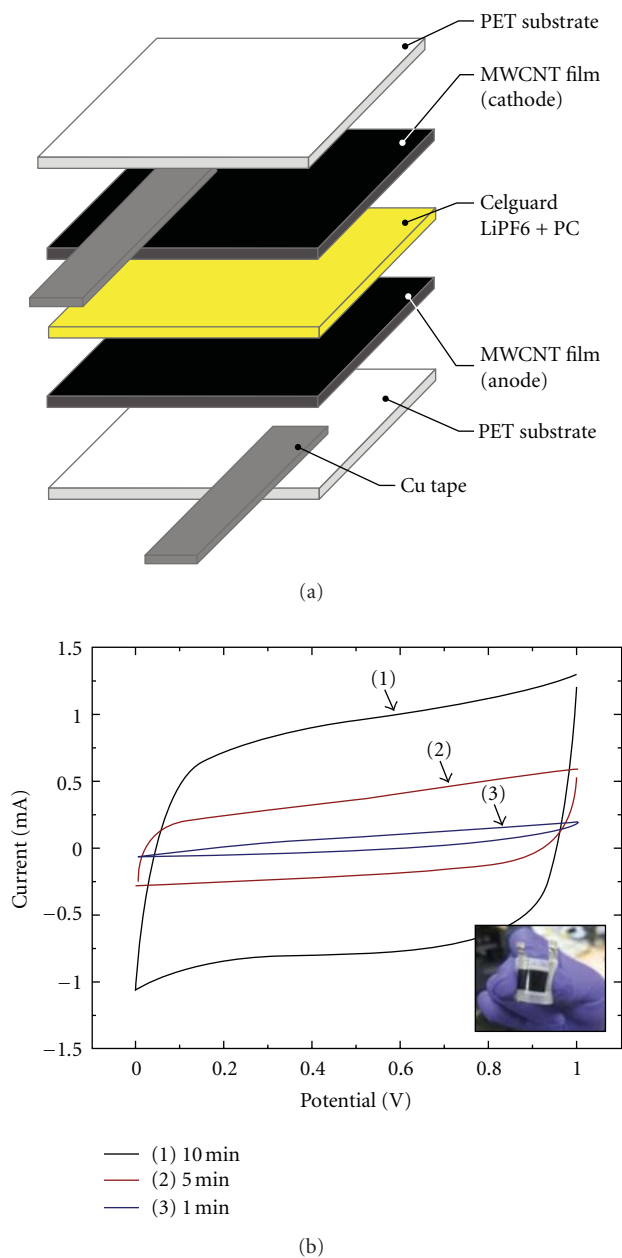


FIGURE 8: Dry-transferred MWCNT supercapacitor. (a) Schematic of the supercapacitor structure using a Celguard 2500 porous separator soaked in Et_4NBF_4 . (b) Cyclic voltammetry for aligned MWCNT electrodes synthesised for (1) 10 min, (2) 5 min and (3) 1 min. The *inset* shows a fabricated device under flexing.

6 and 17 F/g, for cells biased to 1 V. This is roughly twice the capacitance reported for sprayed, solution-processed single-walled carbon nanotube devices under similar experimental conditions [37]. The ESR decreases with increasing film conductivity and ranged from $1000\ \Omega$ ($28.5\ \mu\text{m}$) to $44\ \Omega$ ($235\ \mu\text{m}$) corroborating the sheet resistance estimates made previously. Nevertheless, the overall ESR is still somewhat higher than expected. This is most likely attributed to the relatively resistive Schottky barrier at the Al-MWCNT interface, the intrinsic resistivity of the electrolyte, as well

as contributions from the multiple electrolyte/MWCNT interfaces. Thicker electrodes increase the energy density allowing the active material to occupy a greater volume ratio. However, this is offset by higher ion diffusion barriers in the inner regions of the electrode, resulting in substantial internal resistance and consequently reducing high-power performance. This limits the practical thickness of any nanostructured electrode. Thus, ideally thick electrodes that possess both high capacitance and that are operable at high power are desired. Up to the thicknesses studied, approximately constant power densities were observed ($2.48\ \text{W/g}$), indicating that high permeability is maintained even for thicker electrodes.

4. Conclusions

We have reported the development of an MWCNT dry-transfer technique capable of transferring CVD-synthesised aligned MWCNTs to a variety of flexible substrates without chemically pre-treating the MWCNTs to enhance their adhesion. Accurate control over both the optical transparency and sheet resistance was shown to depend critically on the length of the as-grown MWCNTs. The dry-transferred MWCNT thin films showed a change in resistance as low as 5 for strains in excess of 140%, outperforming PET-supported ITO by two orders of magnitude and hot press laminated graphene by one order of magnitude. The alignment of the constituent MWCNTs was shown to be controllable and was demonstrated to offer a viable approach to the fabrication of flexible transparent polarisation selective electrodes for advanced display technologies. Double-layer supercapacitor cells were fabricated and showed a modest capacitance of up to 17 F/g. The results demonstrated that the dry-transferred MWCNT electrodes are excellent candidates for inexpensive, compact, high-energy-density storage and offer industry compatibility *via* a facile active material transfer approach.

Acknowledgments

This work was supported by the Schiff Studentship, Cambridge University. M. Cole acknowledges the support of St. John's College Cambridge and St. Edmund's College Cambridge. C. Li thanks the Scientific Research Foundation of Graduate School of Southeast University, China (Grant no. YBJJ0926). K. Teo acknowledges the support of the EC Grant TECHNOtube.

References

- [1] D. Zhang, K. Ryu, X. Liu et al., "Transparent, conductive, and flexible carbon nanotube films and their application in organic light-emitting diodes," *Nano Letters*, vol. 6, no. 9, pp. 1880–1886, 2006.
- [2] K. Bradley, J. C. P. Gabriel, and G. Grüner, "Flexible nanotube electronics," *Nano Letters*, vol. 3, no. 10, pp. 1353–1355, 2003.
- [3] C. Qing, K. Hoon-sik, N. Pimparkar et al., "Medium-scale carbon nanotube thin-film integrated circuits on flexible plastic substrates," *Nature*, vol. 454, no. 7203, pp. 495–500, 2008.

- [4] W. Zhuangchun, C. Zhihong, X. Du et al., "Transparent, conductive carbon nanotube films," *Science*, vol. 305, no. 5688, pp. 1273–1276, 2004.
- [5] Y. Zhou, L. Hu, and G. Grüner, "A method of printing carbon nanotube thin films," *Applied Physics Letters*, vol. 88, no. 12, Article ID 123109, 2006.
- [6] L. Hu, D. S. Hecht, and G. Gruner, "Percolation in transparent and conducting carbon nanotube networks," *Nano Letters*, vol. 4, no. 12, pp. 2513–2517, 2004.
- [7] E. Artukovic, M. Kaempgen, D. S. Hecht, S. Roth, and G. Grüner, "Transparent and flexible carbon nanotube transistors," *Nano Letters*, vol. 5, no. 4, pp. 757–760, 2005.
- [8] H. E. Unalan, G. Fanchini, A. Kanwal, A. D. Pasquier, and M. Chhowalla, "Design criteria for transparent single-wall carbon nanotube thin-film transistors," *Nano Letters*, vol. 6, no. 4, pp. 677–682, 2006.
- [9] B. B. Parekh, G. Fanchini, G. Eda, and M. Chhowalla, "Improved conductivity of transparent single-wall carbon nanotube thin films via stable postdeposition functionalization," *Applied Physics Letters*, vol. 90, no. 12, Article ID 121913, 2007.
- [10] S. Hofmann, C. Ducati, B. Kleinsorge, and J. Robertson, "Direct growth of aligned carbon nanotube field emitter arrays onto plastic substrates," *Applied Physics Letters*, vol. 83, no. 22, pp. 4661–4663, 2003.
- [11] S. Hofmann, C. Ducati, J. Robertson, and B. Kleinsorge, "Low-temperature growth of carbon nanotubes by plasma-enhanced chemical vapor deposition," *Applied Physics Letters*, vol. 83, no. 1, pp. 135–137, 2003.
- [12] P. Beecher, P. Servati, A. Rozhin et al., "Ink-jet printing of carbon nanotube thin film transistors," *Journal of Applied Physics*, vol. 102, no. 4, Article ID 043710, 2007.
- [13] N. P. Armitage, J. C. P. Gabriel, and G. Grüner, "Quasi-Langmuir-Blodgett thin film deposition of carbon nanotubes," *Journal of Applied Physics*, vol. 95, no. 6, pp. 3228–3230, 2004.
- [14] M. A. Meitl, Y. Zhou, A. Gaur et al., "Solution casting and transfer printing single-walled carbon nanotube films," *Nano Letters*, vol. 4, no. 9, pp. 1643–1647, 2004.
- [15] M. Chhowalla, K. B. K. Teo, C. Ducati et al., "Growth process conditions of vertically aligned carbon nanotubes using plasma enhanced chemical vapor deposition," *Journal of Applied Physics*, vol. 90, no. 10, pp. 5308–5317, 2001.
- [16] Z. F. Ren and Z. P. Huang, "Synthesis of large arrays of well-aligned carbon nanotubes on glass," *Science*, vol. 282, no. 5391, pp. 1105–1107, 1998.
- [17] C. J. Strobl, C. Schäfle, U. Beierlein, J. Ebbecke, and A. Wixforth, "Carbon nanotube alignment by surface acoustic waves," *Applied Physics Letters*, vol. 85, no. 8, pp. 1427–1429, 2004.
- [18] S. Bhattacharyya, E. Kymakis, and G. A. J. Amaratunga, "Photovoltaic properties of dye functionalized single-wall carbon nanotube/conjugated polymer devices," *Chemistry of Materials*, vol. 16, no. 23, pp. 4819–4823, 2004.
- [19] W. X. Chen, J. Y. Lee, and Z. Liu, "The nanocomposites of carbon nanotube with Sb and SnSb_{0.5} as Li-ion battery anodes," *Carbon*, vol. 41, no. 5, pp. 959–966, 2003.
- [20] C. Du, J. Yeh, and N. Pan, "High power density supercapacitors using locally aligned carbon nanotube electrodes," *Nanotechnology*, vol. 16, no. 4, pp. 350–353, 2005.
- [21] V. Gupta and N. Miura, "Polyaniline/single-wall carbon nanotube (PANI/SWCNT) composites for high performance supercapacitors," *Electrochimica Acta*, vol. 52, no. 4, pp. 1721–1726, 2006.
- [22] A. M. Rao, A. Jorio, M. A. Pimenta et al., "Polarized Raman study of aligned multiwalled carbon nanotubes," *Physical Review Letters*, vol. 84, no. 8, pp. 1820–1823, 2000.
- [23] E. F. Antunes, A. O. Lobo, E. J. Corat, and V. J. Trava-Airoldi, "Influence of diameter in the Raman spectra of aligned multiwalled carbon nanotubes," *Carbon*, vol. 45, no. 5, pp. 913–921, 2007.
- [24] B. D. Martin, N. Nikolov, S. K. Pollack et al., "Hydroxylated secondary dopants for surface resistance enhancement in transparent poly(3,4-ethylenedioxythiophene)-poly(styrenesulfonate) thin films," *Synthetic Metals*, vol. 142, no. 1–3, pp. 187–193, 2004.
- [25] F. C. Krebs and B. Winther-Jensen, "High-conductivity large-area semi-transparent electrodes for polymer photovoltaics by silk screen printing and vapour-phase deposition," *Solar Energy Materials and Solar Cells*, vol. 90, no. 2, pp. 123–132, 2006.
- [26] S. De, P. J. King, M. Lotya et al., "Flexible, transparent, conducting films of randomly stacked graphene from surfactant-stabilized, oxide-free graphene dispersions," *Small*, vol. 6, no. 3, pp. 458–464, 2010.
- [27] S. De, T. M. Higgins, P. E. Lyons et al., "Silver nanowire networks as flexible, transparent, conducting films: extremely high DC to optical conductivity ratios," *ACS Nano*, vol. 3, no. 7, pp. 1767–1774, 2009.
- [28] E. M. Doherty, S. De, P. E. Lyons et al., "The spatial uniformity and electromechanical stability of transparent, conductive films of single walled nanotubes," *Carbon*, vol. 47, no. 10, pp. 2466–2473, 2009.
- [29] L. Gao, W. Ren, J. Zhao, L. P. Ma, Z. Chen, and H. M. Cheng, "Efficient growth of high-quality graphene films on Cu foils by ambient pressure chemical vapor deposition," *Applied Physics Letters*, vol. 97, no. 18, Article ID 183109, 3 pages, 2010.
- [30] R. J. Collier and D. G. Hasko, "Measurement of the sheet resistance of resistive films on thin substrates from 120 to 175 GHz using dielectric waveguides," *Journal of Applied Physics*, vol. 91, no. 4, p. 2547, 2002.
- [31] S. Bae, H. Kim, Y. Lee et al., "Roll-to-roll production of 30-inch graphene films for transparent electrodes," *Nature Nanotechnology*, vol. 5, no. 8, pp. 574–578, 2010.
- [32] C. Lee, X. Wei, J. W. Kysar, and J. Hone, "Measurement of the elastic properties and intrinsic strength of monolayer graphene," *Science*, vol. 321, no. 5887, pp. 385–388, 2008.
- [33] V. M. Pereira, A. H. Castro Neto, and N. M. R. Peres, "Tight-binding approach to uniaxial strain in graphene," *Physical Review B*, vol. 80, no. 4, Article ID 045401, 8 pages, 2009.
- [34] L. Hu, W. Yuan, P. Brochu, G. Gruner, and Q. Pei, "Highly stretchable, conductive, and transparent nanotube thin films," *Applied Physics Letters*, vol. 94, no. 16, Article ID 161108, 3 pages, 2009.
- [35] Q. Zhang, P. Vichchulada, and M. D. Lay, "Effect of deposition conditions on percolation in single-walled carbon nanotube networks," *Physica Status Solidi A*, vol. 207, no. 3, pp. 734–738, 2010.
- [36] P. Vichchulada, Q. H. Zhang et al., "Macroscopic electrical properties of ordered single-walled carbon nanotube networks," *Applied Materials Interfaces*, vol. 2, pp. 467–473, 2010.
- [37] M. Kaempgen, C. K. Chan, J. Ma, Y. Cui, and G. Gruner, "Printable thin film supercapacitors using single-walled carbon nanotubes," *Nano Letters*, vol. 9, no. 5, pp. 1872–1876, 2009.

Research Article

Improving the RF Performance of Carbon Nanotube Field Effect Transistor

S. Hamieh

Faculty of Sciences I, Lebanese University, Beirut, Lebanon

Correspondence should be addressed to S. Hamieh, hamiehs@yahoo.fr

Received 27 September 2011; Accepted 9 February 2012

Academic Editor: Teng Li

Copyright © 2012 S. Hamieh. This is an open access article distributed under the Creative Commons Attribution License, which permits unrestricted use, distribution, and reproduction in any medium, provided the original work is properly cited.

Compact model of single-walled semiconducting carbon nanotube field-effect transistors (CNTFETs) implementing the calculation of energy conduction subband minima under VHDLAMS simulator is used to explore the high-frequency performance potential of CNTFET. The cutoff frequency expected for a MOSFET-like CNTFET is well below the performance limit, due to the large parasitic capacitance between electrodes. We show that using an array of parallel nanotubes as the transistor channel combined in a finger geometry to produce a single transistor significantly reduces the parasitic capacitance per tube and, thereby, improves high-frequency performance.

1. Introduction

Carbon nanotubes belong to the fullerenes family and are sheets of graphite rolled in the shape of a tube. Depending on the direction in which the nanotubes are rolled (chirality), they can be either metallic or semiconducting [1]. Semiconducting nanotubes have been used in high-performance transistors where the channel is the nanotube itself. Since the first demonstration of carbon nanotube field-effect transistors (CNTFETs) in 1998 [2, 3], there has been an immense research concerning the electrical properties and the physical understanding of CNTFET [1, 4, 5]. The manufacturing of CNTFET processes progress continually: one of the most advanced is the chemical vapor deposition technique (CVD). The CNTFET can be characterized by high carrier mobility, low leakage current, important on state current relatively to the applied voltages, and low inverse sub-threshold slope. These properties allow us to consider the design of high-speed and high-performance electronic circuits. High-performance CNTFET operating close to the ballistic limit has been reported in [6–8]. However, due to the large size of the probe pads relative to the CNT device, the parasitic capacitance of the pads can dominate the measured frequency response and inhibit measurement of the intrinsic response of CNT transistors. Moreover, the low current drive and high-input/output impedance of single CNTFET make

it difficult to perform direct measurements of high-frequency electrical properties using instrumentation based on a reference impedance of $50\ \Omega$. In order to make a direct measurement of a recognized high-frequency figure of merit, such as f_T small signal S -parameter measurements were achieved by a newly developed multiple-channel CNTFET structure whose output impedance is much lower than the usual single-channel CNTFET and a deembedding scheme that removes existing errors in measured S -parameters [9]. The authors of [9] measure $f_T = 10.3\ \text{GHz}$ after de-embedding. More recently, using one individual $100\ \mu\text{m}$ long single-walled carbon nanotube, 100 individual nanotube top-gated field effect transistors are combined in a finger geometry to produce a single transistor with a cutoff frequency (after deembedding parasitic capacitance of the finger structure) of $7.6\ \text{GHz}$; before deembedding the cutoff frequency is $0.2\ \text{GHz}$ [10].

In this work, we use compact model, in a quasi-static approach simulations to examine the high-frequency performance potential for a state-of-the-art CNTFET. Using an array of parallel nanotubes as the transistor channel combined in a finger geometry to produce a single transistor significantly reduces the parasitic capacitance per tube and, thereby, improves high-frequency performance. The results presented here should prove useful for understanding and

optimizing high-frequency characteristics of CNTFET and assessing the potential of CNTFET for nanoelectronic RF applications.

This paper is organized as follows. In Section 2, the compact model is presented. In Section 3, the results of our model using VHDL-AMS simulator in the quasistatic approach are shown and discussed. In Section 4 a new architecture is proposed and the results of the proposed architecture are presented. The conclusions are summarized in Section 5.

2. Approach

A simple model for ballistic nanotransistors is described in [11, 12]. For details about this model, we refer the reader to [13–15]. In this model, the gate voltage V_{gs} induces charge in the CNTFET channel Q_{cnt} . It also modulates the top of the energy band between the source and the drain by an amount V_{cnt} . As the source-drain barrier is lowered, current flows between the source and the drain. The electrons coming from the source fill $+k$ states and the electrons coming from the drain fill up the $-k$ states. The control potential V_{cnt} is computed self consistently using

$$V_{\text{cnt}} = \frac{LC_I V_{\text{gi}} + C_{\text{SE}} V_{\text{si}} + C_{\text{DE}} V_{\text{di}} - Q_{\text{cnt}}}{LC_I + C_{\text{DE}} + C_{\text{SE}}}, \quad (1)$$

where V_{gi} , V_{si} , and V_{di} are the intrinsic gate, source, and drain potential respectively. C_{SE} , and C_{DE} are the contact capacitance of the source and drain, C_I is the gate oxide capacitance (see Table 1), Q_{cnt} depends on the number of carriers in the channel n_{cnt} which is the sum of the energy subband contributions, and L is the nanotube length. The drain current equation is derived from the Landauer formula which describes ballistic transport with ideal contacts:

$$I = \frac{4ek_B T}{h} \sum_p \left[\ln \left(1 + \exp \frac{-V_{\text{si}} - \Delta_p + V_{\text{cnt}}}{k_B T} \right) - \ln \left(1 + \exp \frac{-V_{\text{di}} - \Delta_p + V_{\text{cnt}}}{k_B T} \right) \right], \quad (2)$$

where Δ_p is the minima of the p th energy subband. The subbands minima can be calculated using zone folding method of the graphene electron dispersion:

$$\epsilon_v(\mathbf{k}) = \epsilon_{\text{graphene}} \left(|\mathbf{k}| \frac{\mathbf{K}_2}{|\mathbf{K}_2|} + \nu \mathbf{K}_1 \right) \quad (3)$$

with

$$\nu = -\left(\frac{N}{2} + 1 \right), \dots, \frac{N}{2}, \quad (4)$$

$$-\frac{\pi}{|\mathbf{T}|} < |\mathbf{k}| < \frac{\pi}{|\mathbf{T}|},$$

where $|\mathbf{T}|$ is the unit vector for the carbon nanotube (CNT), N is the number of hexagons in CNT unit cell, and \mathbf{K}_1 and \mathbf{K}_2 define the CNT reciprocal unit cell [16].

TABLE 1: CNTFET parameters (see text for discussion about the used values of the parameters).

Parameter	Name	Value	Unit
n	Helicity parameter	19	
m	Helicity parameter	0	
d	Diameter	1.49×10^{-9}	m
T	Temperature	300	K
R_d	Drain contact resistance	17×10^3	Ω
R_s	Source contact resistance	23×10^3	Ω
R_g	Gate contact resistance	10	Ω
L	Nanotube length	100×10^{-9}	m
V_{FB}	Flat band potential	-40×10^{-3}	V
C_I	Gate oxide capacitance	100×10^{-12}	F/m
C_{DE}	Drain capacitance	0.1×10^{-18}	F
C_{SE}	Source capacitance	0.1×10^{-18}	F

3. Quasistatic Approach and Results of Simulation

In the quasistatic approach to transistor modeling, dynamic behavior is predicted by employing static equations for charge (or carrier density) and transport current, but with static voltages replaced by their time-dependent counterparts:

$$Q(V_G, V_D, V_S) \rightarrow Q(V_G(t), V_D(t), V_S(t)), \quad (5)$$

$$I(V_G, V_D, V_S) \rightarrow I(V_G(t), V_D(t), V_S(t)),$$

where Q is charge, I is current, t is time, and V_G , V_D , and V_S are the gate, drain, and source voltages, respectively. Employing the model presented in the last section with the quasistatic assumption, one can determine the ac behavior of CNTFET. The standard procedure is to assume sinusoidal excitation, write each time-dependent quantity in (5) in terms of static (dc or bias) and dynamic (ac, or small-signal) parts, for example, $V(t) = V_c + V_a \exp(j\omega t)$ where V_c refers to the dc value and V_a refers to the complex ac amplitude, and then make simulation to solve the equations for the ac terminal currents in terms of the ac terminal voltages.

3.1. VHDL-AMS Implementation. The MOSFET-like CNTFET compact model introduced in last section using the quasistatic approach is implemented with VHDL-AMS simulation tool. The main quantities used in the model are the control potential V_{cnt} , the subbands energy level Δ_p , and the source (drain) Fermi level $\mu_{S(D)}$. A maximum of 12 intrinsic parameters are necessary as input of this model: the chirality vector (n, m), the diameter, the flatband voltage V_{FB} , the contact resistances (R_s, R_d, R_g), the contact drain (source) capacitance C_{DE} (C_{SE}), and the gate oxide capacitance per unit length C_I . (The values of the parameters shown in Table 1 are estimated under the assumption that the compact model results for I - V characteristics should be compatible with the results of the model based on Boltzmann transport equation.) The value of C_I can be calculated from, $C_I = 2\pi\epsilon_0\epsilon_{\text{ox}}/((2h + d)/d)$, for a nanotube surrounded by

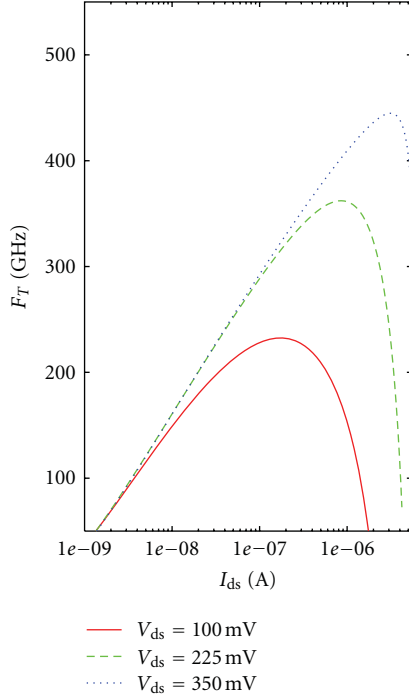


FIGURE 1: Intrinsic f_T as function of I_{ds} for $V_{ds} = 100$ mV (solid line), $V_{ds} = 225$ mV (dotted line), and $V_{ds} = 350$ mV (dashed line).

a coaxial gate, both separated by an oxide of thickness h with permittivity ϵ_{ox} . The device parameters used in the simulation for the I - V characteristics are summarized in Table 1. In Figure 1, we show the results of simulation based on our model for the intrinsic f_T as function of I_{ds} for $V_{ds} = 100$ mV (solid line), $V_{ds} = 225$ mV (dotted line), and $V_{ds} = 350$ mV (dashed line). The variation of f_T with I_{ds} , which is apparent in Figure 1, can be divided into three regions. region *I* is the low current region where f_T decreases as I_{ds} decreases, region *II* is midcurrent region where f_T is approximately constant, and region *III* is the high-current region where f_T decreases as I_{ds} increases. The reasons for this behavior of f_T with I_{ds} can be appreciated by plotting I_{ds} as function of V_{gs} at constant V_{ds} where $g_m = \partial I_{ds} / \partial V_{gs} |_{V_{ds}}$ is zero in the high-current region. The results of the simulation are very promising: the maximum obtained value of $f_T \sim 450$ GHz. However, if the extrinsic parasitic capacitance was included the RF performance of the carbon nanotube transistor will be reduced significantly. This will be our goal in the next section where we propose a new architecture to improve the performance of the CNTFET in the RF regime.

4. Multifinger Multitube Field-Effect Transistors

In this section, a new architecture “multifinger multitube field-effect transistor” (MMFET) is proposed that expected to increase the performance of the nanotube in high-frequency applications [10]. In the proposed architecture, using an array of parallel nanotubes as the transistor channel

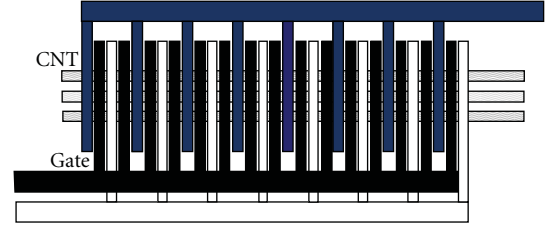


FIGURE 2: Schematic indication of MMFET device geometry (not to scale). In total, there are 16 tubes and 25 fingers (gates) in our design.

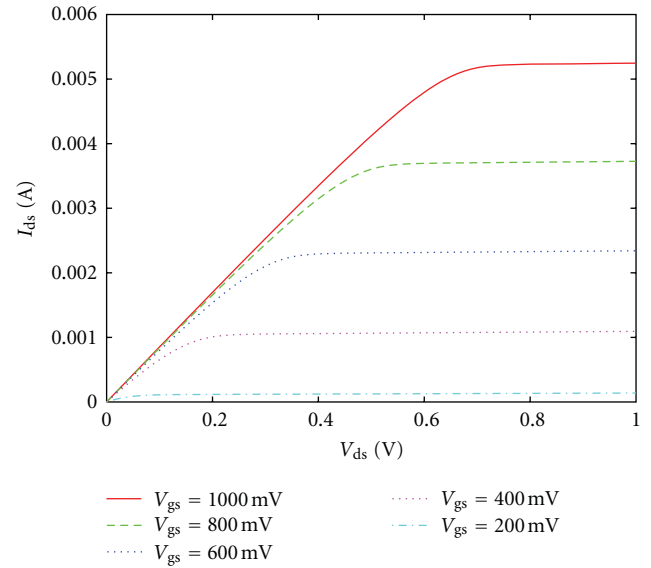


FIGURE 3: I_{ds} - V_{ds} for the (19,0) CNTFET (color online).

combined in a finger geometry to produce a single transistor significantly reduces the parasitic capacitance per tube and, thereby, improves high-frequency performance. Shown in Figure 2 a schematic indication of the MMFET geometry (not to scale). In total, there are 16 tubes and 25 fingers (gate) in our design. The distance between two nanotubes is taken to be $2d$ [17]. In the next two subsection we will study the DC performance and dispersion of this new architecture, and in the last two subsections, we will study the RF performance and applications of such architecture in RF circuits like ring oscillator.

4.1. DC Performance of MMFET. Figure 3 shows the simulated I_{ds} - V_{ds} characteristic for constant V_{gs} (see figure) at room temperature of our device. The device parameters used in the simulation are summarized in Table 1. The simulation has taken into account the series resistances. As one can expect, the current found for MMFET is $400\times$ the single CNTFET current for the same characteristics.

4.2. Dispersion. Many physical parameters values vary in a wide range when nanotubes are manufactured. The most important impact is due to diameter dispersion. Here we will study the impact of the dispersion on the obtained diameters

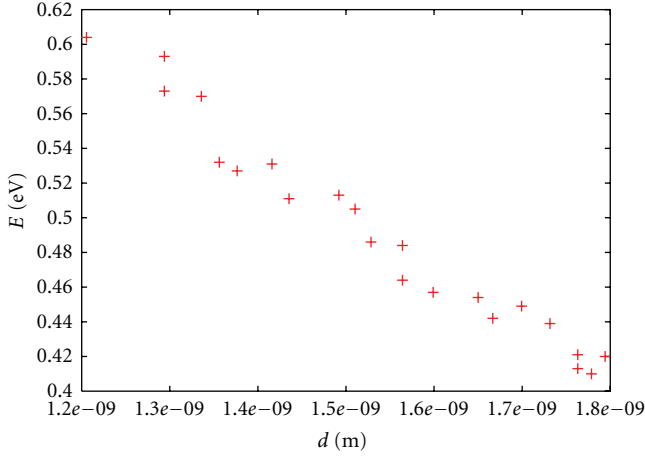


FIGURE 4: Minimum of the nanotube energy subband versus tube diameter.

based on chirality vectors. The simulation is done using the following steps.

- (1) Find all chirality vectors (m, n) which produce a diameter between 1.2 nm and 1.8 nm.
- (2) Eliminate those vectors that give a metallic nanotube. 22 chirality vectors are found after elimination.
- (3) Generate a uniform random number to pick up 16 chirality vectors out of the 22 chirality vectors. (Note that, the 16 chirality vectors correspond to the 16 nanotubes used in our simulation in the new architecture.)
- (4) Generate another uniform random numbers for each trial.

In Figure 4, we show the minimum sub-band energy of the nanotube versus tube diameter for each chirality vector. The impact of the diameter dispersion on the I_{ds} - V_{gs} characteristic at $V_{ds} = 800$ mV is shown in Figure 5. According to the results shown in Figure 5, we can conclude that the I_{on}/I_{off} ratio is very sensitive to diameter spreading. To see the distribution of I_{ds} for fixed $V_{ds} = 0.8$ V, we show the current versus number of events that fall within I_{ds} and $I_{ds} \pm \Delta I_{ds}$ with $\Delta I_{ds} = 0.2$ mA. This distribution, as one can expect, can be compared to gaussian distribution with, in this case, a mean value $I_{ds}^{mean} \sim 3.4$ mA and $\sigma \sim 0.21$ mA. Figure 6 shows the number of trial versus the current at $V_{ds} = 800$ mV.

4.3. RF Response with Parasitic Capacitance of MMFET. From Section 3 we conclude that intrinsic device delay metric of CNTFET has high performance. However, from a circuit/system perspective, a realistic scenario should incorporate all the necessary parasitics. For the sake of comparison, we have studied the MMFET device with same characteristics as Si MOSFETs of the 65 nm technology. The parasitic capacitance per nanotube C_{tube} (C_{tube} is the capacitance added when a one nanotube is added to our device) between the gate and the source (drain) electrode is computed using Fastcap [18]. The thickness of the Pd source (drain) film is

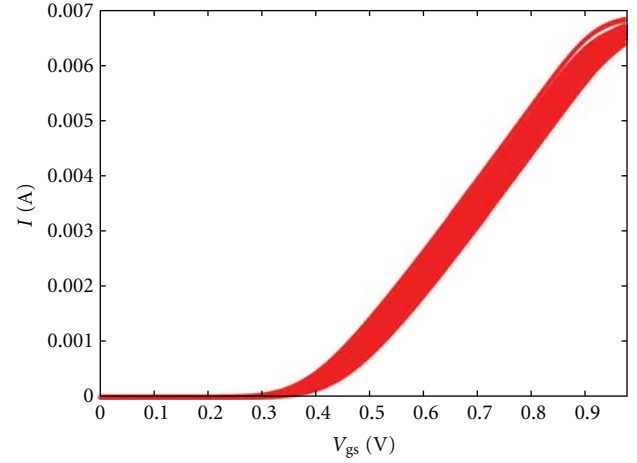


FIGURE 5: Impact of the diameter dispersion on the I_{ds} - V_{gs} characteristic at $V_{ds} = 800$ mV.

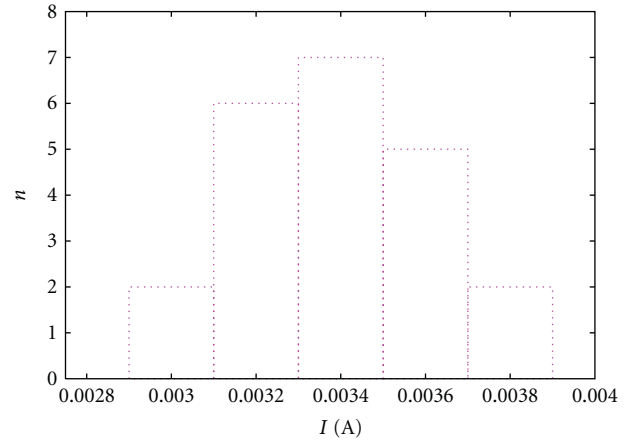


FIGURE 6: The number of trial versus the current at $V_{ds} = 800$ mV.

100 nm thick and 60 nm of length, the gate insulator Al_2O_3 thickness is 65 nm with dielectric constant ~ 9 , and the Al gate is 150 nm thick and 140 nm length. It is assumed that each nanotube introduces a 4 nm width. Using Fastcap, with the geometries shown in Figure 7, we obtain $C_{tube} \sim 0.1$ fF. In Figure 10 we show the discretization used in Fastcap for the geometries that we proposed. (For the sake of clearness we give details on the simulation of the capacitor by Fastcap:

- (i) we generate two cuboid with cubegen;
- (ii) the generated objects are combined in a list where we define their position with respect to each other and the dielectric material;
- (iii) we run Fastcap on the *lst* file with the option *l*. To produce a picture of the capacitor the *m* option should be used.)

In this simulation, we have used the measured parasitic capacitance for the multifinger device found in [10] as our

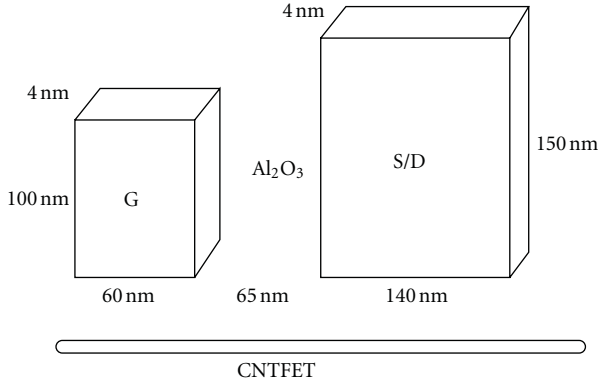


FIGURE 7: The used geometries for calculating the parasitic capacitance per nanotube C_{tube} in the MMFET.

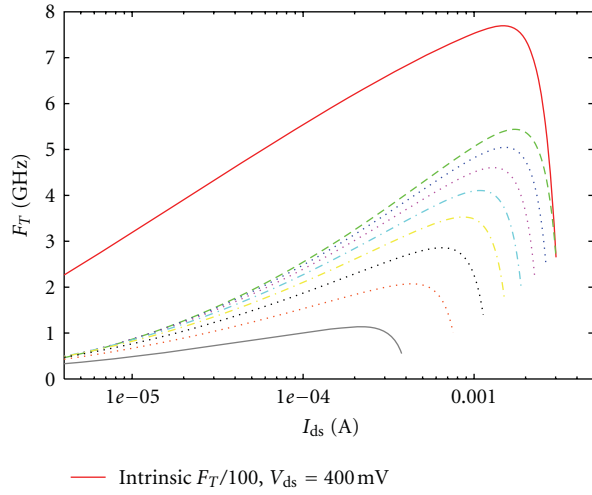


FIGURE 8: RF response with parasitic capacitance of MMFET at $V_{\text{ds}} = 400 \text{ mV}$: from top down the number of nanotube changes from 16 to 2 by step of 2. Intrinsic $F_T/100$ solid line. Same parameters as CMOS 65 nm technology are used (see text).

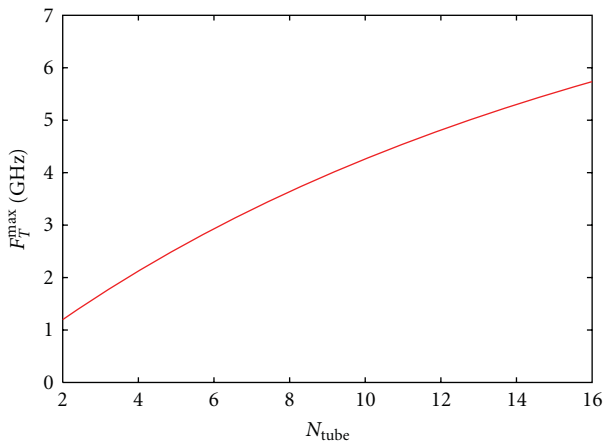


FIGURE 9: The maximum value of extrinsic F_T of the MMFET at $V_{\text{ds}} = 400 \text{ mV}$ versus number of nanotubes, n_{tube} .

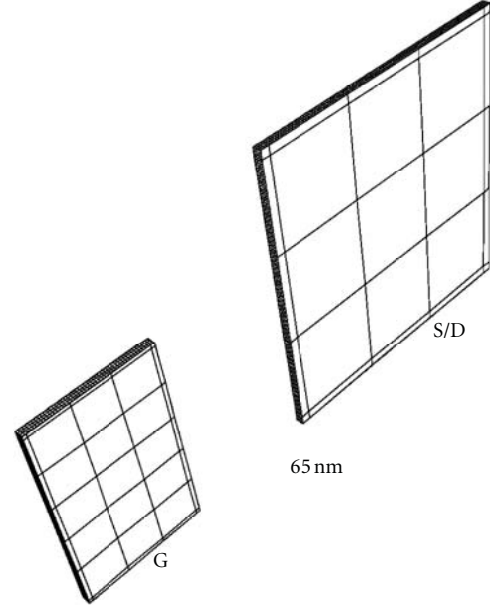


FIGURE 10: Discretization used in Fastcap.

initial value $C_{\text{exp}} \sim 50 \text{ fF}$, and for each nanotube we have introduced C_{tube} in such way:

$$C_{\text{total}} = C_{\text{exp}} + (N_{\text{tube}} - 1)N_{\text{finger}}C_{\text{tube}}, \quad (6)$$

where N_{tube} and N_{finger} are the number of tubes and fingers in the device, respectively. (With a new technology this value can be reduced significantly.)

In Figure 8, we show the results of simulation based on our model for the F_T as function of I_{ds} for $V_{\text{ds}} = 400 \text{ mV}$: the intrinsic $F_T/100$ (solid line), and from top down extrinsic MMFET where the number of nanotube change from 16 to 2 by step of 2. The device parameters used in this simulation are summarized in Table 2. As expected, the MMFET device that we propose improves the performance of the carbon nanotube in the RF regime where we found the maximum extrinsic $F_T^{\text{ex}} \sim 6 \text{ GHz}$ (see Figure 9) and the maximum intrinsic $F_T^{\text{in}} \sim 800 \text{ GHz}$ value that has to be compared to the maximal measured value $F_T^{\text{in}} \sim 10.2 \text{ GHz}$ [9].

4.4. Ring Oscillator with Carbon Nanotube. The parasitic capacitors play important role in the delay characteristics of a MMFET-based circuit. Simulations have been done with a three-stage ring oscillator (see Figures 11 and 12) and the effect of these parasitics has been studied. Figure 13 shows the effect on the natural oscillation frequency of parasitic capacitors with the parameters summarized in Table 2. (Of course the parasitic capacitance is not taken from Table 2.) It can be concluded from Figure 13 that in the range studied here, the parasitics dominate the performance. It should be noted, however, that the accurate estimation of the parasitics would be possible only when the layout geometry and a fabrication process of the MMFETs will be known. Further, it is worthwhile to mention that, for long channel MMFET under high bias, the effects of scattering with phonon are important and have to be considered.

TABLE 2: CNTFET parameters.

Parameter	Name	Value	Unit
n	Helicity parameter	19	
m	Helicity parameter	0	
d	Diameter	1.49×10^{-9}	m
T	Temperature	300	K
R_d	Drain contact resistance	17×10^3	Ω
R_s	Source contact resistance	23×10^3	Ω
R_g	Gate contact resistance	10	Ω
L	Nanotube length	8250×10^{-9}	m
V_{FB}	Flat band potential	-40×10^{-3}	V
C_f	Gate oxide capacitance	100×10^{-12}	F/m
C_{DE}	Drain capacitance	0.1×10^{-18}	F
C_{SE}	Source capacitance	0.1×10^{-18}	F
C_{GS}	Gate-source capacitance	87.5×10^{-15}	F
C_{GD}	Gate-drain capacitance	87.5×10^{-15}	F
n_{tube}	Number of tubes	16	—
n_{finger}	Number of finger	25	—

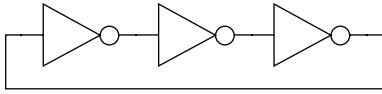
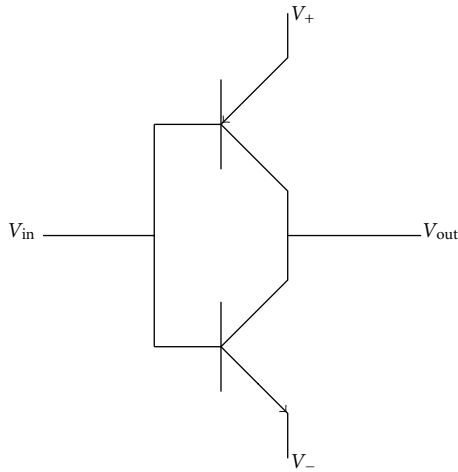
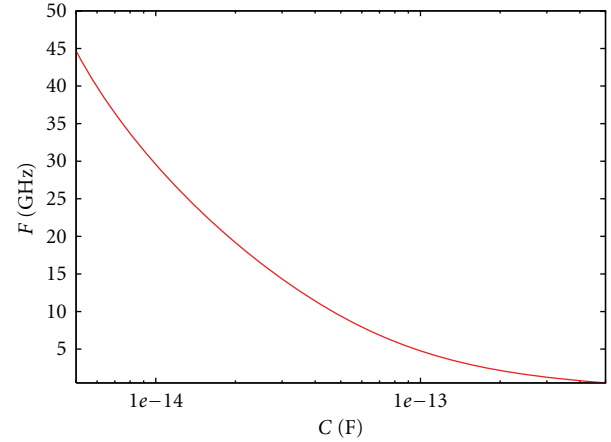


FIGURE 11: Three-stage ring oscillator.

FIGURE 12: Schematic representation of a single inverter with $V_+ = 0.4$ V and $V_- = 0.4$ V.

5. Conclusions

This paper use circuit-compatible modeling technique for the ballistic CNTFET for applications to radio frequency circuits. Results of simulation for radio frequency circuits using VHDL-AMS simulator in the intrinsic case are presented. A new architecture was proposed to improve the performance of the CNTFET. We found that the extrinsic F_T and the natural oscillation frequency of a three-stage ring oscillator are ~ 10 Ghz in the cases considered here. An experimental

FIGURE 13: Natural oscillation frequency as function of C_{para} under ballistic transport.

validation for the obtained results is necessary. From our analysis on the high-frequency performance of CNTFET, we conclude the following.

- (i) Classical lithography reproduces the same problem as CMOS. To overcome this problem we propose a metallic nanotube contacts.
- (ii) Effect of phonon scattering can be important and have to be considered in the RF regime.
- (iii) Non-quasistatic effects may not be very important.

We hope to address some of these issues in the near future.

Acknowledgment

The authors would like to thank the support of this work by the Institut TELECOM under NanoRF project.

References

- [1] P. L. McEuen, M. S. Fuhrer, and H. Park, "Single-walled carbon nanotube electronics," *IEEE Transactions on Nanotechnology*, vol. 1, no. 1, pp. 78–85, 2002.
- [2] S. J. Tans, A. R. M. Verschueren, and C. Dekker, "Room-temperature transistor based on a single carbon nanotube," *Nature*, vol. 393, no. 6680, pp. 49–52, 1998.
- [3] R. Martel, T. Schmidt, H. R. Shea, T. Hertel, and P. Avouris, "Single- and multi-wall carbon nanotube field-effect transistors," *Applied Physics Letters*, vol. 73, no. 17, pp. 2447–2449, 1998.
- [4] M. P. Anantram and F. Léonard, "Physics of carbon nanotube electronic devices," *Reports on Progress in Physics*, vol. 69, no. 3, pp. 507–561, 2006.
- [5] S. J. Wind, J. Appenzeller, and P. Avouris, "Vertical scaling of carbon nanotube field-effect transistors using top gate electrodes," *Applied Physics Letters*, vol. 80, no. 20, p. 3817, 2002.
- [6] A. Javey, J. Guo, Q. Wang, M. Lundstrom, and H. Dai, "Ballistic carbon nanotube field-effect transistors," *Nature*, vol. 424, no. 6949, pp. 654–657, 2003.

- [7] A. Javey, J. Guo, D. B. Farmer et al., "Self-aligned ballistic molecular transistors and electrically parallel nanotube arrays," *Nano Letters*, vol. 4, no. 7, pp. 1319–1322, 2004.
- [8] Y.-M. Lin, J. Appenzeller, Z. Chen, Z.-G. Chen, H.-M. Cheng, and P. Avouris, "High-performance dual-gate carbon nanotube FETs with 40-nm gate length," *IEEE Electron Device Letters*, vol. 26, no. 11, pp. 823–825, 2005.
- [9] K. Narita, H. Hongo, M. Ishida, and F. Nihey, "RF performance of multiple-channel carbon nanotube transistors," in *Proceedings of the Trends in NanoTechnology Conference (TNT '06)*, Grenoble, France, September 2006.
- [10] D. Wang, Z. Yu, S. McKernan, and P. J. Burke, "Ultrahigh frequency carbon nanotube transistor based on a single nanotube," *IEEE Transactions on Nanotechnology*, vol. 6, no. 4, pp. 400–403, 2007.
- [11] J. Guo, S. Datta, and M. Lundstrom, "A numerical study of scaling issues for schottky barrier carbon nanotube transistors," *Condensed Matter*, vol. 1, 26 pages, 2003.
- [12] J. Guo, M. Lundstrom, and S. Datta, "Performance projections for ballistic carbon nanotube field-effect transistors," *Applied Physics Letters*, vol. 80, no. 17, pp. 3192–3194, 2002.
- [13] A. Raychowdhury, S. Mukhopadhyay, and K. Roy, "A circuit-compatible model of ballistic carbon nanotube field-effect transistors," *IEEE Transactions on Computer*, vol. 23, no. 10, pp. 1411–1420, 2004.
- [14] C. Maneux, J. Goguet, S. Fregonese, T. Zimmer, H. Cazin d'Honincthun, and S. Galdin-Retailleau, "Analysis of CNTFET physical compact model," in *Proceedings of the IEEE International Conference on Design and Test of Integrated Systems in Nanoscale Technology (DTIS '06)*, pp. 40–45, La Marsa, Tunisia, September 2006.
- [15] P. Desgreys, J. G. da Silva, and D. Robert, "Dispersion Impact on Ballistic CNTFET n+-i-n+ Performances," in *Proceedings of the European Nano Systems Workshop (ENS '06)*, Paris, France, December 2006.
- [16] R. Saito, G. Dresselhaus, and M. S. Dresselhaus, *Physical Properties of Carbon Nanotubes*, Imperial College Press, London, UK, 1998.
- [17] A. Keshavarzi, A. Raychowdhury, J. Kurtin, K. Roy, and V. De, "Carbon nanotube field-effect transistors for high-performance digital circuits—Transient analysis, parasitics, and scalability," *IEEE Transactions on Electron Devices*, vol. 53, no. 11, pp. 2718–2726, 2006.
- [18] K. Nabors and J. White, "FastCap: a multipole accelerated 3-D capacitance extraction program," *IEEE Transactions on Computer*, vol. 10, no. 11, pp. 1447–1459, 1991.

Research Article

An Investigation on the Formation of Carbon Nanotubes by Two-Stage Chemical Vapor Deposition

M. S. Shamsudin,^{1,2} M. F. Achoi,^{1,2} M. N. Asiah,^{1,2} L. N. Ismail,^{1,3} A. B. Suriani,^{1,2}
S. Abdullah,^{1,2} S. Y. S. Yahya,^{1,2} and M. Rusop^{1,3}

¹Centre of Nanoscience and Nanotechnology (NANO-SciTech Centre), Institute of Science, Universiti Teknologi MARA (UiTM),
40450 Shah Alam, Malaysia

²School of Physics and Material Studies, Faculty of Applied Sciences, Universiti Teknologi MARA (UiTM),
40450 Shah Alam, Malaysia

³NANO-ElecTronic Centre, Faculty of Electrical Engineering, Universiti Teknologi MARA (UiTM),
40450 Shah Alam, Malaysia

Correspondence should be addressed to M. S. Shamsudin, nanopizza@rocketmail.com

Received 21 August 2011; Accepted 12 January 2012

Academic Editor: Teng Li

Copyright © 2012 M. S. Shamsudin et al. This is an open access article distributed under the Creative Commons Attribution License, which permits unrestricted use, distribution, and reproduction in any medium, provided the original work is properly cited.

High density of carbon nanotubes (CNTs) has been synthesized from agricultural hydrocarbon: camphor oil using a one-hour synthesis time and a titanium dioxide sol gel catalyst. The pyrolysis temperature is studied in the range of 700–900°C at increments of 50°C. The synthesis process is done using a custom-made two-stage catalytic chemical vapor deposition apparatus. The CNT characteristics are investigated by field emission scanning electron microscopy and micro-Raman spectroscopy. The experimental results showed that structural properties of CNT are highly dependent on pyrolysis temperature changes.

1. Introduction

In 1993, Iijima's group reported the synthesis of carbon nanotubes (CNTs) by a simple technique [1]. They had been selected as excellent candidates, which were largely derived from their unique structural, mechanical, and chemical properties [2]. The CNT can be divided into three types: single-walled, double-walled, and multiwalled nanotubes [3]. From the application and industrial point of view it is highly desirable to synthesize well-ordered and dense arrays of purified CNT at low processing temperature and cost and high mass production approach, and mostly it should follow a safe and high-quality specification. Several pyrolysis techniques have been introduced, including the most prevailing method: thermal [4] or plasma [5] chemical vapor deposition (CVD). In our approach, our group appraise the potential custom-made two-stage catalytic CVD [6] natural hydrocarbon camphor oil as a carbon source and titanium dioxide (TiO₂) solution as a catalyst to synthesize CNT.

TiO₂ is extensively used for wide-range applications such as energy storage and conversion, starting photocatalyst material, corrosive and bacterial protection and is also to remove of organic contaminants from wastewater [7–10]. TiO₂ powder and solution are commercially available in the market but it is more recommended to use self-prepared TiO₂ solution for desired properties and to ease compositional modification. This is due to its lower vaporization temperature and molarity compared to the commercialize samples.

2. Experimental

A standard ethanol (EtOH) solution with $M = 46.07$ g/mol, purity $\approx 99.8\%$ from Fluka chemical was used as a solvent, and titanium (IV) isopropoxide (TTiP) ($M = 340.33$ g/mol, purity $\approx 99.995\%$) from Sigma Aldrich was used as a precursor. Glacial acetic acid (GAA) ($M = 60.05$ g/mol, purity $\approx 99.98\%$) and triton-x ($M = 646.8$ g/mol, purity

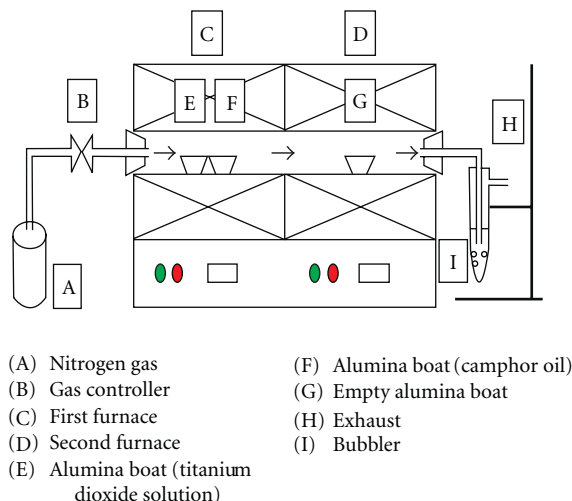


FIGURE 1: Schematic diagram of custom-made two-stage catalytic CVD.

≈ 98.0%) were purchased from Baker. For this work, TiO_2 solution was synthesized using the sol gel method [11, 12]. In present work, the simple synthesis procedure for TiO_2 solution is as follows: the hydrolyzation process of 18.91 mL of TTiP using 2.50 mL of GAA under room temperature, 0.20 mL of distilled water together with 0.02 mL of triton-x as the stabilizer and 78.40 mL of EtOH as the solvent are mixed under continuously mechanical stirring at 4 rpm and 60°C for 1 hour. After the period, the solution was stirred continuously at 3 rpm. The solution was left for 24 hours of ageing time. The custom-made two-stage catalytic CVD is a part of lab-scale equipment and compatible for feasibility studies. The desired quantity of 10 mL purified 0.5 M TiO_2 solution and 10 mL of camphor oil were placed in a separate alumina boat without further treatment. Those alumina boats were located side by side inside quartz tube at the centre of the first furnace in the custom-made two-stage catalytic CVD as in Figure 1. A slower 15-bubble-per-minute nitrogen gas flow was used to remove atmospheric air from the reaction tube for 5 minutes. The flow rate of nitrogen gas was reduced to 10 bubbles per minutes simultaneously activating the set vaporization temperature switch at the first furnace. When the first furnace achieved this set vaporization temperature, the set pyrolysis temperature at reaction zone was activated to pyrolyze the carbon and catalyst content for 1 hour. The operation was then followed by thermal annealing at the same pyrolysis temperature for 30 minutes, and then both furnaces were let to cool down naturally to the ambient temperature under a flowing nitrogen gas condition. Black powder was observed on the inner wall of quartz tube at the second furnace zone [13]. The dimension, arrangement, and surface morphology of the production CNT were characterized using field emission scanning electron microscopy (FESEM) (ZEISS 77 Supra 40VP) and micro-Raman spectroscopy with a laser of 514 nm (Horiba Jobin Yvon 79DU420A-OE-325).

3. Results and Discussion

In this work, our group successfully synthesized at various pyrolysis temperatures from 700 to 900°C at increments of 50°C. The hydrocarbon source derived from camphor oil was selected due to its low vaporization temperature, lower dependence on crude oil, and safer handling material. To the best of our knowledge, due to depletion of fossil-based carbon precursor that leads to high prices, we were taking proactive steps in strategizing to utilize camphor-oil-based natural hydrocarbon to produce CNT. Based on our humble knowledge, there was no documented experimental study on the initial stage of the formation of CNT by custom-made two-stage catalytic CVD. A hydrocarbon feedstock camphor oil contains 10 carbon atoms, 16 hydrogen atoms, and 1 oxygen atom flowed to the reaction chamber. The pyrolysis temperature range in the second furnace was sufficient enough to break the chemical bonding between carbon atoms, hydrogen atoms, and oxygen atom in the camphor oil molecules. There were no attachments between carbon, hydrogen, and oxygen atoms resulting in those free carbon atoms to attach to the catalyst clusters due to perfect catalytic effect and bind together with other carbon atoms to form CNT. The Ti clusters were trapped inside the CNT structure during deposition process. The major parameter used in this process was pyrolysis temperature. The pyrolysis of CNT was increased with the increasing of pyrolysis temperature. This was supported by FESEM micrograph analysis that shows the top view micrograph of CNT at various pyrolysis temperatures as in Figure 2 where the numbers of CNT were increasing directly with the pyrolysis temperature. In Figures 2(a), 2(b), and 2(c), the samples still contain traces of the carbonaceous byproduct which in this case is the amorphous carbon that caused the irregular structure. In Figures 2(d) and 2(e), regular structure of CNT was formed. These results show fairly good agreement with previous studies where the shape of carbon-based materials gradually changes from spherical-like structure to a perfect tubular structure with the increase in pyrolysis temperature [14].

Figure 3 illustrates the micro-Raman measurements on the samples synthesized at various pyrolysis temperatures confirming the disappearance of the single-walled CNT synthesized at 700 until up to 900°C. The peaks in the micro-Raman spectra, which laid in the Raman shift from 100 to 400 cm^{-1} , can be attributed to the appearance of single-walled type of CNT [15]. This pattern was known as radial breath mode. Generally the carbon content has two major peaks: a D band peak at 1325–1372 cm^{-1} and G band peak at 1609–1630 cm^{-1} for samples synthesized at 700 to 900°C. The D band peak represents a finite crystal size and lattice defect inside the graphene atomic layer known as disordered structure, on the other hand, the G band peak represents a perfect hexagonal of graphite structure. The intensity of micro-Raman patterns increases slightly with the increasing of pyrolysis temperatures. This result confirms that the graphite structure of the CNT is highly dependent on the pyrolysis temperatures at the second furnace. The main reason is that the catalytic activity of TiO_2 solution is becoming more excellent at higher temperature. This is

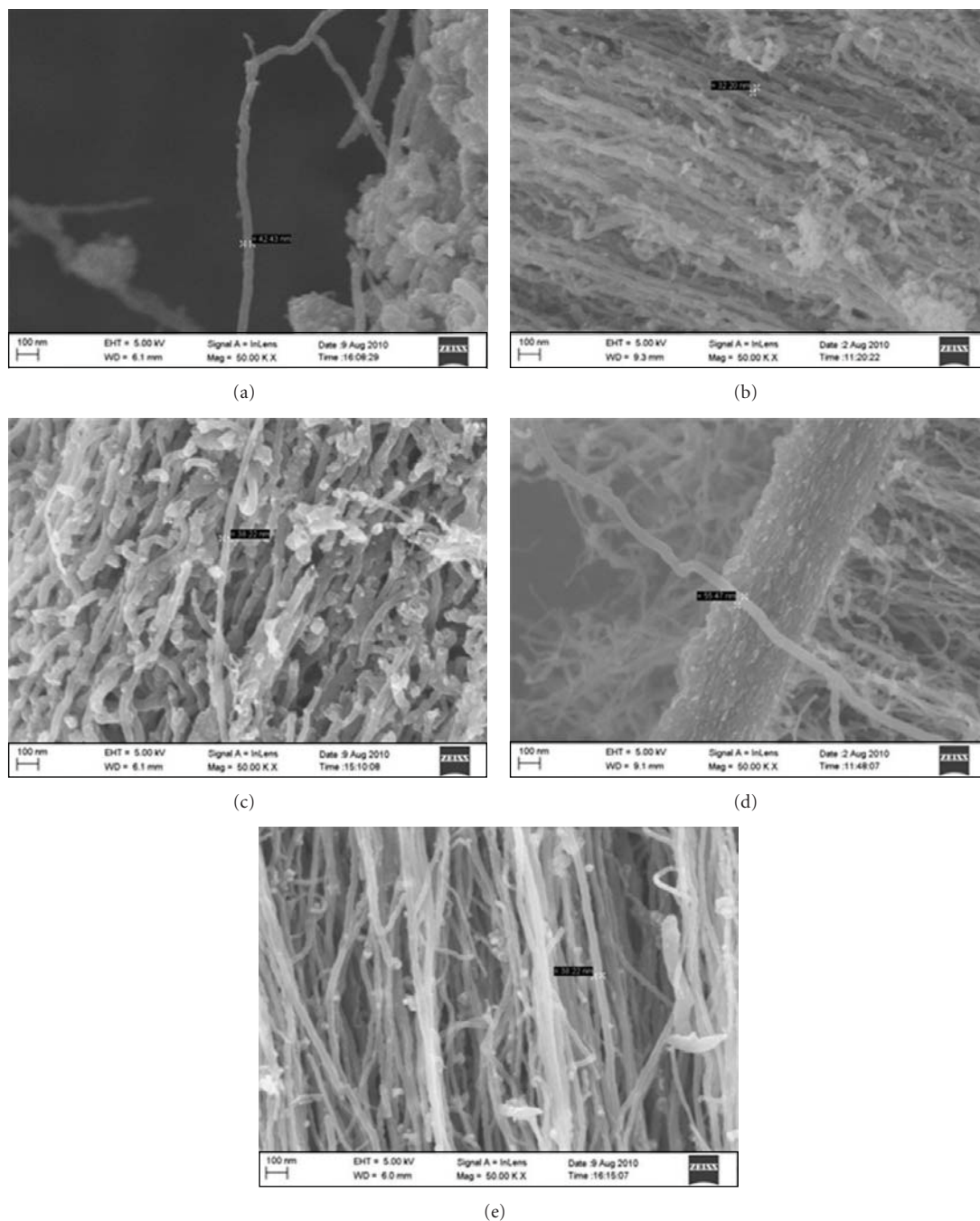


FIGURE 2: FESEM top view of micrographs of the CNT at different pyrolysis temperatures: (a) 700, (b) 750, (c) 800, (d) 850, and (e) 900°C.

due to the TiO_2 solution total decomposition, which results in the production of small Ti clusters with higher catalytic effect that induces the pyrolysis of CNT at high reaction temperature. It was slightly different when we measured the intensity of micro-Raman spectra at lower temperature. The Ti/C clusters produced cannot be fully decomposed in the second furnace due to TiO_2 and carbon feedstock solution cannot be fully pyrolyzed. Subsequently, it has low catalytic effect for the formation of CNT. The ratio of D and G band (I_D/I_G) features intensity provides information on

the quality of production of CNT. The information on the quality of the CNT is shown in Figure 4. The I_D/I_G ratio decreases with an increase in pyrolysis temperature. The lowest magnitude ratio gives the best well-ordered structure of CNT. The smallest value of I_D/I_G ratio was registered at 900°C and was about 0.76, the temperature that was highly selective for synthesis of CNT. As discussed before, at higher pyrolysis temperature Ti cluster is fully decomposed for the formations of CNT and has higher catalytic activity effect. Moreover, these observations show that the CNT synthesized

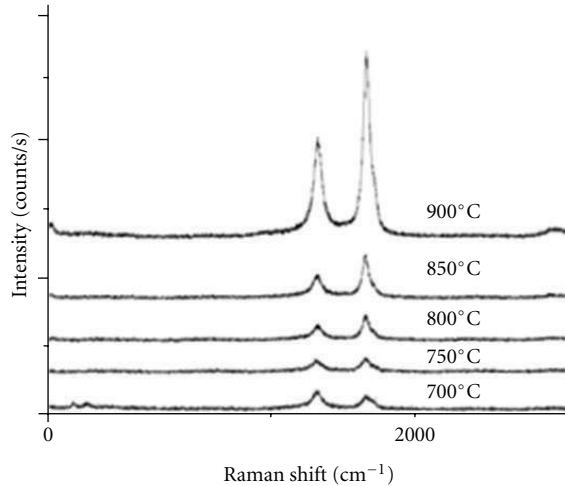


FIGURE 3: Micro-Raman patterns of CNT at different pyrolysis temperatures.

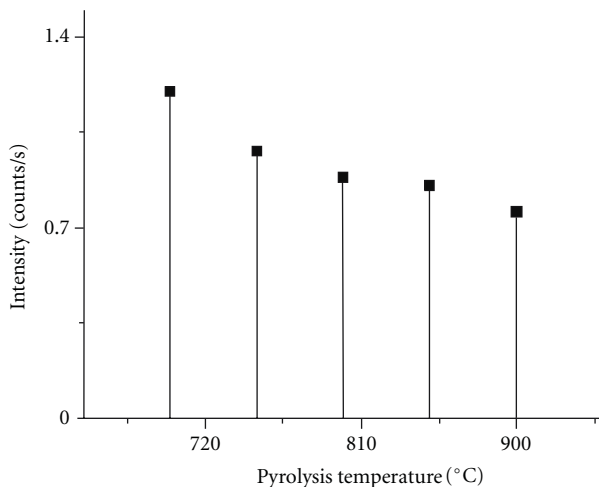


FIGURE 4: I_D/I_G ratio patterns of CNT at different pyrolysis temperatures.

at 700°C has higher disorder compared to CNT synthesized at higher temperature: 900°C. This was due to the poor catalytic activity of the Ti cluster over the CNT pyrolysis at this lower temperature. The peak position and I_D/I_G ratio for those samples are summarized in Table 1. It was noted that micro-Raman results were consistent with FESEM analysis.

4. Conclusions

The analysis of pyrolysis temperatures to synthesis camphor-oil-based CNT using TiO_2 solution as a catalyst was studied. The results show that the higher pyrolysis temperatures favor the pyrolysis of CNT. The form of CNT was found to grow at higher temperature ($\sim 900^\circ\text{C}$), with good dimension which showed unique lateral alignment, uniform nanotubes diameter within 10 to 40 nm, and distribution within the bundle when compared to other samples at lower pyrolysis temperature. In the same context, the production of TiO_2

TABLE 1: The D and G peak position and ratio of I_D/I_G growth of CNT at different pyrolysis temperatures.

Pyrolysis temperature ($^\circ\text{C}$)	D peak (cm^{-1})	G peak (cm^{-1})	Ratio I_D/I_G
700	1352	1610	1.20
750	1350	1605	0.98
800	1351	1611	0.88
850	1353	1604	0.86
900	1352	1609	0.76

solution plays an important role as a catalyst to be used in a custom-made two-stage catalytic CVD. Hence, it is a good idea to grow CNT for laboratory commercialization.

Acknowledgments

This work was supported by Sime Darby Research Sdn Bhd, Malaysian Ministry of Higher Education (MOHE), Malaysian Ministry of Science, Technology and Innovation (MOSTI), and Universiti Teknologi MARA through Excellence Fund under Contact no. 600-RMI/ST/DANA 5/3/Dst 435/2011).

References

- [1] S. Iijima and T. Ichihashi, "Single-shell carbon nanotubes of 1-nm diameter," *Nature*, vol. 363, no. 6430, pp. 603–605, 1993.
- [2] A. B. Suriani, R. Md Nor, and M. Rusop, "Vertically aligned carbon nanotubes synthesized from waste cooking palm oil," *Journal of the Ceramic Society of Japan*, vol. 118, no. 1382, pp. 963–968, 2010.
- [3] A. B. Suriani, A. A. Azira, S. F. Nik, R. Md Nor, and M. Rusop, "Synthesis of vertically aligned carbon nanotubes using natural palm oil as carbon precursor," *Materials Letters*, vol. 63, no. 30, pp. 2704–2706, 2009.
- [4] A. Mathur, S. Wadhwa, and M. Tweedie, "Low-dimensional systems and nanostructures," *Physica E*, vol. 44, no. 1, p. 29, 2011.
- [5] Y. Yabe, Y. Ohtake, T. Ishitobi, Y. Show, T. Izumi, and H. Yamauchi, "Synthesis of well-aligned carbon nanotubes by radio frequency plasma enhanced CVD method," *Diamond and Related Materials*, vol. 13, no. 4–8, pp. 1292–1295, 2004.
- [6] M. S. Shamsudin, S. Abdullah, and M. Rusop, *Advanced Materials Research*, vol. 364, p. 191, 2012.
- [7] A. L. Linsebigler, G. Lu, and J. T. Yates Jr., "Photocatalysis on TiO_2 surfaces: principles, mechanisms, and selected results," *Chemical Reviews*, vol. 95, no. 3, pp. 735–758, 1995.
- [8] A. V. Murugan, V. Samuel, and V. Ravi, "Synthesis of nanocrystalline anatase TiO_2 by microwave hydrothermal method," *Materials Letters*, vol. 60, no. 4, pp. 479–480, 2006.
- [9] R. J. Matyi, L. H. Schwartz, and J. B. Butt, "Particle Size, Particle Size Distribution, and Related Measurements of Supported Metal Catalysts," *Catalysis Reviews*, vol. 29, no. 1, pp. 41–99, 1987.
- [10] H. Choi, E. Stathatos, and D. D. Dionysiou, "Photocatalytic TiO_2 films and membranes for the development of efficient

- wastewater treatment and reuse systems,” *Desalination*, vol. 202, no. 1–3, pp. 199–206, 2007.
- [11] M. F. Achoi, A. M. Nor, S. Abdullah, and M. Rusop, *AIP Conference Proceedings*, vol. 1328, p. 295, 2011.
- [12] M. N. Asiah, M. Z. Basri, and M. Rusop, *Defect and Diffusion Forum*, vol. 312–315, p. 1027, 2011.
- [13] H. Li, C. Shi, X. Du, C. He, J. Li, and N. Zhao, “The influences of synthesis temperature and Ni catalyst on the growth of carbon nanotubes by chemical vapor deposition,” *Materials Letters*, vol. 62, no. 10–11, pp. 1472–1475, 2008.
- [14] R. B. Little, “Mechanistic aspects of carbon nanotube nucleation and growth,” *Journal of Cluster Science*, vol. 14, no. 2, pp. 135–185, 2003.
- [15] C. P. Deck and K. Vecchio, “Growth mechanism of vapor phase CVD-grown multi-walled carbon nanotubes,” *Carbon*, vol. 43, no. 12, pp. 2608–2617, 2005.

Research Article

The Effects of Radial Compression on Thermal Conductivity of Carbon and Boron Nitride Nanotubes

Haijun Shen

School of Aerospace and Mechanics, Tongji University, Shanghai 200092, China

Correspondence should be addressed to Haijun Shen, shj@tongji.edu.cn

Received 20 September 2011; Accepted 30 January 2012

Academic Editor: Teng Li

Copyright © 2012 Haijun Shen. This is an open access article distributed under the Creative Commons Attribution License, which permits unrestricted use, distribution, and reproduction in any medium, provided the original work is properly cited.

By using molecular dynamics method, thermal conductivity of (10, 10) carbon and boron nitride (BN) nanotubes under radial compression was investigated, and the λ - T (thermal conductivity versus temperature) curves of the two nanotubes were obtained. It is found that with the increase of temperature the thermal conductivity of two nanotubes decreases; the nanotubes, under both the local compression and whole compression, have lower thermal conductivity, and the larger the compressive deformation is, the lower the thermal conductivity is; the whole compression has more remarkable effect on thermal conductivity than the local compression.

1. Introduction

As the feature sizes of MEMSs (microelectro mechanical systems) continue to be scaled down, the problem of thermal dissipation becomes even more important. It has been found that very few materials are known to exhibit high thermal conductivity at reduced dimensions, and traditional semiconductors like Si have a dramatic suppression of thermal conductivity at the nanoscale [1].

Just like carbon nanotubes can be viewed as rolling a graphite sheet into a cylinder, boron nitride (BN) tubes can also be regarded as geometrically derived by rolling a hexagonal BN sheet into a cylinder. Due to low-dimensional effects, carbon and BN nanotubes have been predicted to have unusual thermal properties [2, 3]. The thermal conductivity of an isolated carbon nanotube has been predicted to reach 1800–6000 W/mK at room temperature [4]. Similarly, the thermal conductivity (290 K) of isolated BN nanotube has been reported to be 1620 W/mK [5].

Recent Xu and Buehler [6] carried out a systematic investigation of the effects of axial tensile, compressive and torsional strain on the thermal conductivity of single-walled carbon nanotubes using MD simulation, and found that the thermal conductivity drops when the different strain is applied to carbon nanotube, respectively. However, up to now the work about the effects of radial compression on

carbon nanotube as well as BN nanotube is not found. Here we perform nonequilibrium MD simulation to investigate the thermal conductivity of the (10, 10) carbon and BN nanotubes under radial compression and discuss the effects of the local and whole compressive deformation on thermal conductivity of the carbon and BN nanotubes.

2. The Investigated Objects and Method

2.1. The Investigated Objects. Figure 1 shows the investigated objects, (10, 10) zigzag carbon and BN nanotubes. Considering that within the length range of 1 nm to 25 nm nanotubes have little change in thermal conductivity [7], the present tube length is taken to be 8.85 nm to 9.81 nm. The (10, 10) carbon tube is generated by the nanotube generator [8], a program module developed by us. The (10, 10) BN tube is constructed by alternately replacing the carbon atoms of (10, 10) carbon tube with boron or nitrogen atoms. After geometrically optimizing the carbon and BN nanotubes through MD simulation at 270 K, the initial configurations are obtained. The initial diameter D of the carbon and BN nanotubes is 1.36 nm and 1.52 nm, respectively.

2.2. Method. In classical MD, atoms are regarded as basic particles, and the temperature of the simulated system is given through the equipartition theorem of energy. When the

practical temperature is lower than the Debye temperature of material, the thermal capacity will be highly correlative with the temperature of system, the equipartition theorem of energy will become invalidated [9], and the quantum correction to temperature must be performed. In the present MD calculations of thermal conductivity, the temperature of both the nanotube systems is taken above their Debye temperature so that quantum effects can be ignored. The Debye temperature of the carbon and BN nanotubes takes 420 K [10] and 400 K [11], respectively.

In this study the EMD (equilibrium molecular dynamics) method with the time step of 0.5 fs is applied to geometrically optimize the carbon and BN nanotubes, as well as to calculate the thermal conductivity of the carbon and BN nanotubes locally or wholly compressed in radial direction (see Figure 1). The process to calculate the thermal conductivity can be described as the following: firstly relaxing the tubes in the NTV ensemble for 3×10^5 time-steps, then locally or wholly compressing the carbon and BN nanotubes in the radial direction through two parallel rigid plates, where the loading rate takes 0.03 nm per 1000 time steps, and the temperature is controlled at 270 K through Nose method; fixing the two rigid plates when the carbon and BN tubes reach certain deformation, calculating the heat flux of each time step for the subsequent 4×10^6 time-steps, and obtaining the thermal conductivity of the compressed tubes through integrating the autocorrelation function of heat flux [12].

In the present MD simulations, the Velocity-Verlet algorithm is taken. Tersoff potential, one three-body potential based on the concept of bond order, is used to describe the interaction between atoms. The Tersoff potential explicitly includes an angular contribution of the force and has been widely used in various applications for III–V elements. The Tersoff potential and its parameters for the carbon, BN atomic systems see [13, 14]. In the simulations of the local compression the width of two rigid-plates takes 0.74 nm. The interaction between atoms and the rigid plates is described using the L-J potential:

$$U(r) = 4\epsilon \left[\left(\frac{\sigma}{r} \right)^{12} - \left(\frac{\sigma}{r} \right)^6 \right], \quad (1)$$

where r is the distance between atoms and rigid-plate; the constants ϵ and σ take 0.440 kJ and 0.385 nm [15], respectively.

In our EMD simulations, based on the Green-Kubo linear response theory, the thermal conductivity has the following formula [16]

$$\lambda = \frac{1}{K_B T^2 V} \int_0^{+\infty} \langle q(t) \cdot q(0) \rangle dt, \quad (2)$$

where K_B is the Boltzmann constant, T the simulative temperature, V the volume of simulated system, that is, the cross-section area ($= \pi D^2/4$) multiplying the tube length, t time, and q the effective heat flux.

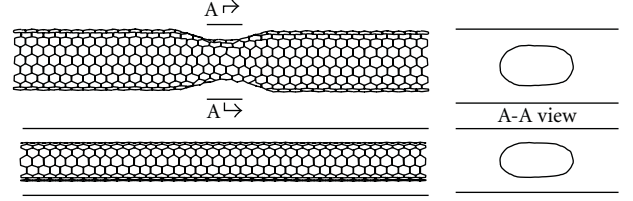


FIGURE 1: The carbon and BN nanotubes under local and whole radial compression.

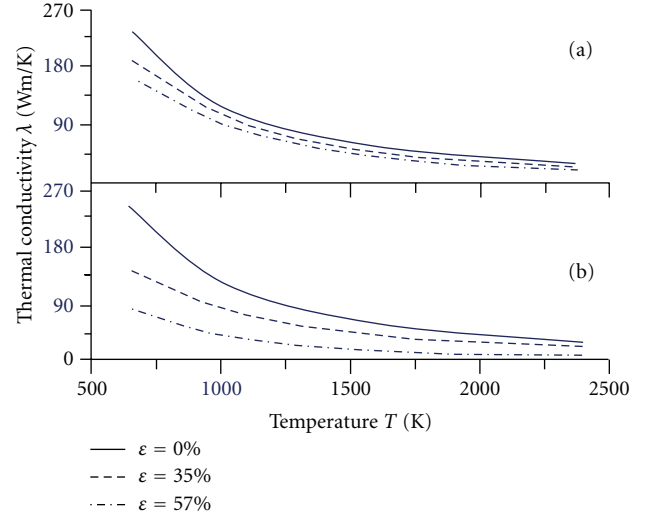


FIGURE 2: The λ - T curves of carbon tube under (a) local and (b) whole compression.

The effective heat flux q has the following expression [11] of:

$$q(t) = \frac{d}{dt} \sum_i \vec{r}_i(t) e_i(t), \quad \text{that is, } q(t) = \sum_i \vec{v}_i e_i + \sum_i \vec{r}_i \frac{de_i}{dt}, \quad (3)$$

where v_i is the velocity of the i th atom, e_i the total energy of the i th atom, and \vec{r}_i the coordinate.

3. Results and Discussion

It is proved that the contribution to thermal conductivity of nanotube mainly comes from two parts, that is, (1) the interaction between electrons and phonons, that is dependent on electronic structures (molecular configuration) and phonon scattering, and (2) the interaction between phonons, that is, correlative to atomic vibration.

Figure 2 gives the λ - T (thermal conductivity versus temperature) curves of the carbon nanotube under different local compressive strain and whole compressive strain ϵ , and Figure 3 gives those of the BN nanotube. For convenience to discuss, Figure 4 presents the λ - T curves of the carbon nanotube under different compression modes, that is, the local compression and whole compression, and Figure 5 presents those of the BN nanotube. In these figures the compressive

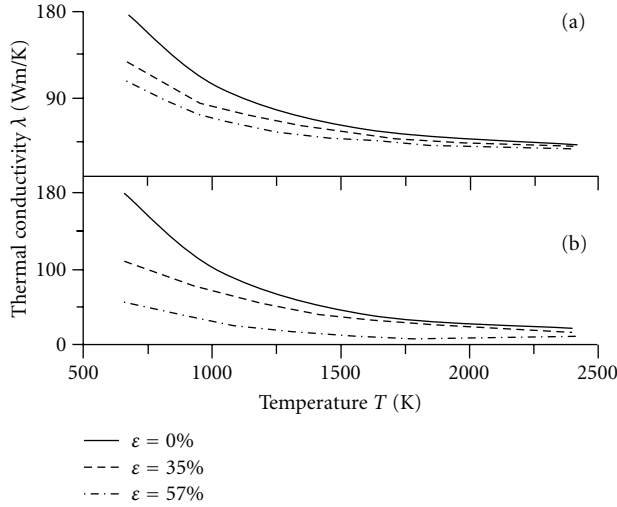


FIGURE 3: The λ - T curves of BN tube under (a) local and (b) whole compression.

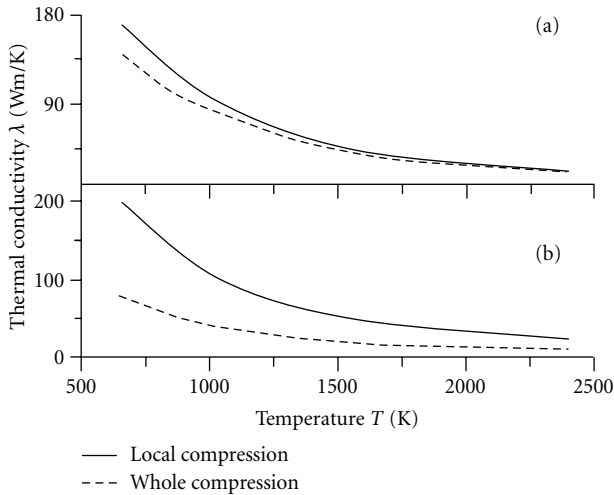


FIGURE 4: The λ - T curves of carbon tube under different compression mode of (a) $\epsilon = 35\%$ and (b) $\epsilon = 57\%$.

strain ϵ is defined as the ratio of the radial compressive deformation to the initial tube diameter D .

From Figures 2 and 3, it can be seen that,

- (1) with the increase of temperature, the thermal conductivity of both the carbon and BN nanotubes decreases, and when temperature $>1,800$ K, their thermal conductivity trends to be constant. What is the reason? It can be explained as the following: due to the increase of temperature, the U scattering process of phonons increases, and the average free range of phonons decreases, which causes the decreases in thermal conductivity of both the carbon and BN nanotubes;
- (2) under the local compression, both the carbon and BN nanotubes have lower thermal conductivity; the

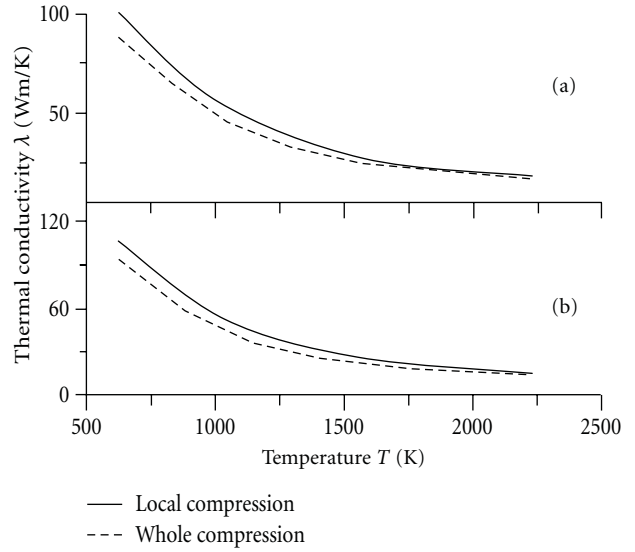


FIGURE 5: The λ - T curves of BN tube under different compression mode of (a) $\epsilon = 35\%$ and (b) $\epsilon = 57\%$.

larger the compressive strain (deformation) is, the lower the thermal conductivity is. The phenomenon can be explained as the following: firstly, the local compression causes local cave-in on the tube wall, that is, the change in local molecular structure, and further the change of the local atoms in vibration mode; secondly, the local cave-in on the tube wall changes the heat exchange path and increases the local phonon U scattering. In a word, the local radial compression makes a bottleneck of heat exchange on the nanotube wall; the larger the compressive deformation is, the worse the thermal conductivity becomes;

- (3) at the same temperature, the whole compression also makes the thermal conductivity of both the nanotubes decrease; the larger the compressive deformation is, the lower the thermal conductivity is. The reason lies in that under whole compression the chemical-bonds are tightened up, and the larger the compressive deformation is, the tighter the chemical-bonds become, which results in the change of atoms in vibration mode, that is, vibration amplitude and frequency, as well as the decrease in thermal conductivity;
- (4) at relatively low temperature, the effect of both the local and whole compression on the thermal conductivity of the carbon and BN nanotubes is remarkable. At high temperature, the effect becomes slight, which is because that the effect of compressive deformation has been inundated by that of high temperature.

According to Figures 4 and 5, it can be observed that, under the same temperature and compressive-deformation, the wholly compressed carbon (or BN) nanotube has lower

thermal conductivity than the locally compressed one. The phenomenon can be explained through the different heat-transfer mechanism of the nanotubes under different compression modes, that is, the tightened up chemical-bonds in the wholly compressed nanotubes results in the change of atom vibration mode as well as the change of thermal conductivity; the bottleneck of heat exchange on the tube wall decreases the thermal conductivity of the locally compressed nanotubes.

The present (10, 10) carbon nanotube without compressive deformation is predicted to have the thermal conductivity of 180 W/mK and 94 W/mK, respectively, at 800 K and 1200 K. The corresponding MD results obtained in [17] are 190 W/mK and 120 W/mK, respectively. Our results are close to those of [17], which implies the effectivity of the MD method in the present paper. In [18, 19], the measurement of the thermal conductivity of single-layer graphenes was reported, and the room temperature values of the thermal conductivity were found to be in the range 3000 to 5300 W/mK. Conceptually, single-wall carbon nanotubes can be considered to be formed by the rolling of a single-layer of graphite/graphene. By the cubic polynomial interpolation of the curves in Figure 2, it is found that the thermal conductivity of the (10, 10) carbon nanotube without deformation is about 430 W/mK at 300 K, lower by one order of magnitude than that of graphenes in [18, 19].

4. Conclusions

As the important components of future NEMs (nanomechanical systems), one-dimensional nano-materials like carbon and BN nanotubes have broad application prospect, and their thermal conductivity and thermal dispersion will directly affect the system operation. In this study the EMD method is used to investigate the effect of local and whole radial compression on the thermal conductivity of carbon and BN nanotubes. It is found that both the local and whole compression can decrease the thermal conductivity of nanotubes. The conclusion will be very helpful for the design of carbon and BN nanotube thermal-conductivity-devices.

References

- [1] A. Balandin and K. L. Wang, "Significant decrease of the lattice thermal conductivity due to phonon confinement in a free-standing semiconductor quantum well," *Physical Review B*, vol. 58, no. 3, pp. 1544–1549, 1998.
- [2] N. G. Chopra, R. J. Luyken, K. Cherrey et al., "Boron nitride nanotubes," *Science*, vol. 269, no. 5226, pp. 966–967, 1995.
- [3] A. A. Balandin, "Thermal properties of graphene and nanostructured carbon materials," *Nature Materials*, vol. 10, no. 8, pp. 569–581, 2011.
- [4] J. Hone, M. Whitney, C. Piskoti, and A. Zettl, "Thermal conductivity of single-walled carbon nanotubes," *Physical Review B*, vol. 59, no. 4, pp. R2514–R2516, 1999.
- [5] C. W. Chang, W. Q. Han, and A. Zettl, "Thermal conductivity of B-C-N and BN nanotubes," *Applied Physics Letters*, vol. 86, no. 17, Article ID 173102, 3 pages, 2005.
- [6] Z. Xu and M. J. Buehler, "Strain controlled thermomutability of single-walled carbon nanotubes," *Nanotechnology*, vol. 20, no. 18, Article ID 185701, 2009.
- [7] K. Bi, Y. Chen, J. Yang, and M. Chen, "Molecular dynamics simulation of thermal conductivity of single-wall carbon nanotubes with different structures," *Journal of Southeast University*, vol. 36, no. 3, pp. 420–422, 2006.
- [8] H. Shen, "Generating carbon nanotube and researching into its mechanics properties by HyperChem," *Computers and Applied Chemistry*, vol. 21, no. 4, pp. 485–488, 2004.
- [9] S. Tian and H. Shen, "Thermal and tensile properties of BN, SiC and Ge nanotubes," *Journal of Materials Engineering & Science*, vol. 26, no. 6, pp. 135–139, 2008.
- [10] D. Lu and P. Jiang, *Solid Physics*, Shanghai Science Press, Shanghai, China, 2003.
- [11] L. Muser, D. Anglos, J. P. Petitet, J. P. Michel, and A. V. Kanaev, "Photoluminescence of hexagonal boron nitride: effect of surface oxidation under UV-laser irradiation," *Journal of Luminescence*, vol. 127, no. 2, pp. 595–600, 2007.
- [12] M. P. Allen and D. J. Tildesley, *Computer Simulation of Liquids*, Clarendon Press, Oxford, UK, 1987.
- [13] R. Pässler, "Basic moments of phonon density of states spectra and characteristic phonon temperatures of group IV, III-V, and II-VI materials," *Journal of Applied Physics*, vol. 101, no. 9, Article ID 093513, 2007.
- [14] J. Tersoff, "Empirical interatomic potential for carbon, with applications to amorphous carbon," *Physical Review Letters*, vol. 61, no. 25, pp. 2879–2882, 1988.
- [15] Y. Chen and H. Shen, "MD simulations of diametrically compressed single-walled and double-walled carbon nanotubes," *Journal of Atomic and Molecular Physics*, vol. 31, pp. 352–356, 2007.
- [16] J. H. Irving and J. G. Kirkwood, "The statistical mechanical theory of transport processes. IV. The equations of hydrodynamics," *The Journal of Chemical Physics*, vol. 18, no. 6, pp. 817–829, 1950.
- [17] H. Chen, Y. Chen, M. Chen, and K. Bi, "Thermal conductivity of single-wall carbon nanotubes filled with argon," *Journal of Southeast University*, vol. 36, no. 3, pp. 416–419, 2006.
- [18] A. A. Balandin, S. Ghosh, W. Bao et al., "Superior thermal conductivity of single-layer graphene," *Nano Letters*, vol. 8, no. 3, pp. 902–907, 2008.
- [19] S. Ghosh, D. L. Nika, E. P. Pokatilov, and A. A. Balandin, "Heat conduction in graphene: experimental study and theoretical interpretation," *New Journal of Physics*, vol. 11, Article ID 095012, 2009.

Research Article

Critical Dispersion Distance of Silicon Nanoparticles Intercalated between Graphene Layers

Shuze Zhu,¹ Jason Galginaitis,¹ and Teng Li^{1,2}

¹Department of Mechanical Engineering, University of Maryland, College Park, MD 20742, USA

²Maryland NanoCenter, University of Maryland, College Park, MD 20742, USA

Correspondence should be addressed to Teng Li, lit@umd.edu

Received 16 October 2011; Accepted 25 January 2012

Academic Editor: Sulin Zhang

Copyright © 2012 Shuze Zhu et al. This is an open access article distributed under the Creative Commons Attribution License, which permits unrestricted use, distribution, and reproduction in any medium, provided the original work is properly cited.

Nanocomposites of silicon nanoparticles (Si NPs) dispersed in between graphene layers emerge as potential anode materials of high-charge capacity for lithium-ion batteries. A key design requirement is to keep Si NPs dispersed without aggregation. Experimental design of the Si NP dispersion in graphene layers has remained largely empirical. Through extensive molecular dynamics simulations, we determine a critical NP dispersion distance as the function of NP size, below which Si NPs in between graphene layers evolve to bundle together. These results offer crucial and quantitative guidance for designing NP-graphene nanocomposite anode materials with high charge capacity.

Rechargeable lithium-ion batteries with high energy capacity and long cycle life are in great demand for applications such as portable devices and electric vehicles [1–3]. Silicon has the highest known theoretical charge capacity, more than ten times higher than the existing graphite anodes [4]. However, the huge volume changes (up to 400%) of silicon upon charging/discharging cause its pulverization and capacity fading, posing a significant challenge to use silicon as anodes [4, 5]. Nanocomposites of silicon nanoparticles (Si NPs) dispersed in between graphene layers are emerging as a novel and promising solution to high-performance Si-based anode materials [6, 7]. Nanoscale silicon materials (e.g., nanoparticles and nanowires) have been shown to be able to sustain much larger volume change without pulverization than their bulk counterpart [6, 8]. The graphene layers of high mechanical flexibility and large surface area serve as a percolating scaffold network to help accommodate the volume change of the Si NPs during charging/discharging and ensure facile electron transport. A key design requirement of such nanocomposite anode materials is to keep the Si NPs evenly dispersed in between the graphene layers [6, 9]. Given their huge surface area over volume ratio, Si NPs that are too close to each other tend to bundle together to reduce surface energy. The aggregations of the Si NPs become more prone to pulverization than dispersed Si NPs. On the other

hand, the charging capacity of the nanocomposite anode material scales with the total volume of the Si NPs that can be dispersed in between the graphene layers. Therefore, the optimal design of Si NP-graphene-based anode materials hinges upon determining the maximum dispersion density of the Si NPs in the graphene layers without Si NP aggregation. Such a critical dispersion of the Si NPs in the graphene layers remains elusive so far, as most experimental studies in this regard are largely empirical [6, 7]. To address such a crucial but large unexplored issue, in this paper we conduct extensive molecular dynamics simulations to determine a critical dispersion distance of the Si NPs as the function of NP size, below which Si NPs in between two graphene layers evolve to bundle together.

The dispersion of the Si NPs in between graphene layers is governed by the energetic interplay between the graphene layers and the Si NPs [10]. The typical size of the Si NPs dispersed in between graphene layers is a few nanometers in diameter, much larger than the equilibrium graphene-graphene interlayer distance (~0.34 nm). As a result, the graphene layers are locally separated by the Si NPs and assume corrugated morphology to wrap around the Si NPs [6]. Such corrugated morphology of the graphene layers results from the following energetic interplay. On the one hand, the graphene-graphene interlayer interaction is

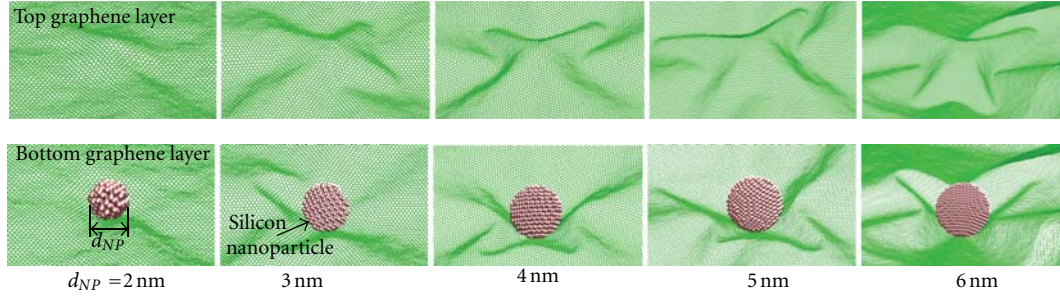


FIGURE 1: The morphology of graphene with the intercalation of a single Si NP of various diameters, d_{NP} . For visual clarity, the top panel shows the top graphene layer, and the bottom one shows the Si NP and the bottom graphene layer (only the portion near the Si NP is shown). Note the ridged morphology formation as d_{NP} increases.

mainly van der Waals type. Therefore, the graphene layers tend to assume their equilibrium distance to reduce the interaction energy. On the other hand, the corrugation of graphene layers due to Si NP intercalation causes the bending and stretching of the graphene, and thus leads to an increase of the graphene strain energy. The tighter the graphene layers wrap around the Si NPs, the higher the resulting graphene strain energy, and the lower the graphene-graphene interaction energy. The equilibrium morphology of the graphene-NP structure is dictated by minimizing the total free energy of the structure, which includes two dominant contributions, that is, the graphene strain energy and the graphene-graphene interaction energy. Given the large in-plane dimension of the graphene (on the order of microns or higher), the weak interaction between the graphene and Si NPs (also van der Waals type) is of secondary significance in the total free energy. So is the strain energy of the Si NPs, which is negligible due to the weak graphene-Si interaction and out-of-plane flexibility of the graphene.

We first conduct molecular dynamics (MD) simulations to determine the equilibrium morphology of the graphene layers with a single Si NP intercalated in between, which corresponds to the limiting case when the Si NPs are widely dispersed in between graphene layers, thus the interaction among Si NPs is negligible. In consideration of the computational cost, we model a graphene bilayer with a Si NP intercalated in between, corresponding to the two closest neighbor graphene layers that wrap around the Si NP in a real material. Such a simplified model can capture the dominant energetic interplay, given that the graphene-graphene interlayer interaction decays quickly as their distance increases, and thus the contribution from the next neighbor graphene layers to the interaction energy is of secondary significance.

In the MD simulations, each graphene layer has a size of 50 nm by 70 nm. Single-crystal Si NPs of various diameters (i.e., 2~6 nm) are used to study the effect of NP size on the corrugated graphene morphology. The carbon-carbon (C-C) covalent bonds in the graphene are described by the adaptive intermolecular reactive bond order (AIREBO) potential [11]. The nonbonded graphene-graphene interlayer interaction and the graphene-Si interaction are described

by two Lennard-Jones pair potentials [12], $V_{C-C}(r) = 4\epsilon_{C-C}(\sigma_{C-C}^{12}/r^{12} - \sigma_{C-C}^{12}/r^6)$ and $V_{C-Si}(r) = 4\epsilon_{C-Si}(\sigma_{C-Si}^{12}/r^{12} - \sigma_{C-Si}^{12}/r^6)$, respectively, where $\epsilon_{C-C} = 0.00284$ eV, $\sigma_{C-C} = 0.34$ nm, $\epsilon_{C-Si} = 0.00213$ eV, and $\sigma_{C-Si} = 0.15$ nm. To reduce the computation cost, the Si NP is assumed to be rigid (i.e., whose bonding energy remains as a constant). In each MD simulation case, the graphene bilayer, with free boundary conditions for both layers, is prescribed with an initial morphology that, near the Si NP, it bulges out into a conical dome in each layer to house the Si NP inside and far away from the Si NP, it remains flat with an interlayer distance of 0.6 nm. The Si NP is first fixed, and the graphene bilayer is equilibrated for 30 ps to minimize the dependence of the final results on the initial prescribed morphology, then the Si NP is set free to evolve with the graphene bilayer until an equilibrium is reached. The MD simulations are carried out using LAMMPS with Canonical Ensemble at temperature 300 K and with time step 1 fs.

Figure 1 shows the simulated morphology of graphene with a single Si NP intercalated in between of various diameters, $d_{NP} = 2$ nm, 3 nm, 4 nm, 5 nm, and 6 nm, respectively. For visual clarity, the top panel in Figure 1 shows the top graphene layer and the bottom one shows the Si nanoparticle and the bottom graphene layer. If the Si NP is small (e.g., $d_{NP} = 2$ nm), each graphene layer bulges out into a dome to wrap around the Si NP. As the size of the Si NP increases, the graphene layers start to form ridged morphology to wrap around the Si NP. The locations of such ridges are approximately complementary in the top and bottom graphene layers. The formation of ridged morphology in the graphene bilayer can be understood as follows. As the size of the Si NP increases, forming a smooth conical dome in each graphene layer to wrap around the Si NP requires accommodating the out-of-plane deflection of the graphene bilayer through the in-plane stretching in radial direction and compressing in hoop direction of the graphene bilayer. Such in-plane deformation of the graphene is energetically unfavorable, given graphene's ultrahigh in-plane stiffness. By contrast, given the much amenable out-of-plane flexibility of graphene, accommodating the out-of-plane deflection of the graphene bilayer by bending each graphene layer to form ridges corresponds to a lower total free energy state, thus is more favorable.

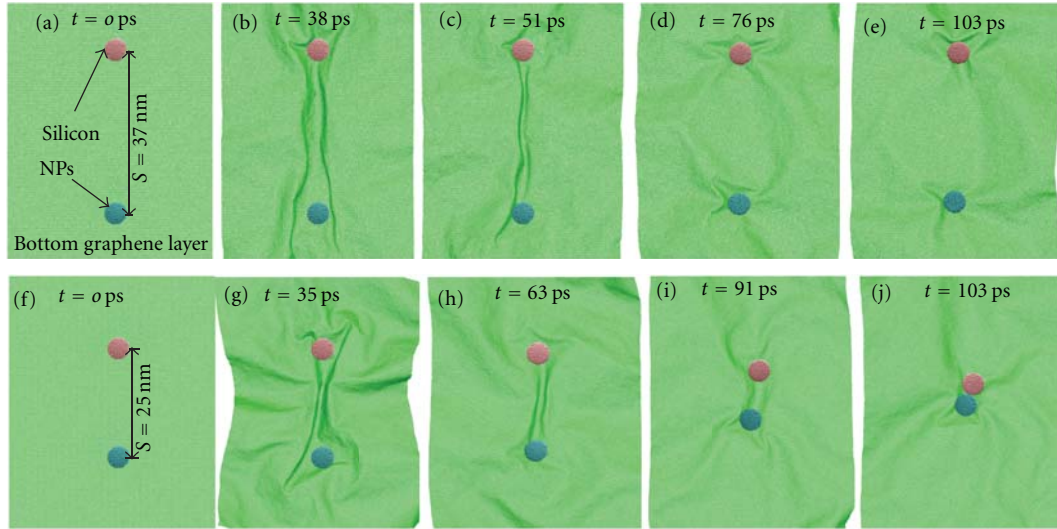


FIGURE 2: (a)–(e) the morphologic evolution of the Si NP-graphene system over simulation time. For visual clarity, only the bottom graphene layer and the Si NPs are shown. When the distance between the two Si NPs is sufficiently large (here $d_{\text{NP}} = 5$ nm, and $S = 37$ nm), the two Si NPs remain dispersed and are wrapped individually by the graphene bilayer. The corrugated graphene morphology near each Si NP is similar to that shown in Figure 1. (f)–(j) when the distance between the two Si NPs is below a critical value (here $d_{\text{NP}} = 5$ nm, and $S = 25$ nm), the two Si NPs evolve to come closer and eventually bundle together. (Supplemental materials: two videos showing the morphologic evolution of the Si NP-graphene system corresponding to (a)–(e) and (f)–(j) are available at <http://ter.ps/dispersed> and <http://ter.ps/bundled>, resp., available online at doi: 10.1155/2012/375289).

We next consider how the structural morphology of the Si NP-graphene nanocomposites evolves as the dispersion distance between the Si NPs varies. To capture the dominant underlying physics of such a morphologic evolution within reasonable computation cost, we model a graphene bilayer with two neighboring Si NPs intercalated in between. Similar materials parameters and numerical strategy as those described above are used in the MD simulations. For a given Si NP size, MD simulations are conducted over a range of Si NP dispersion distance. Two modes of morphologic evolution emerge from the simulations, as illustrated in Figure 2. If the dispersion distance between Si NPs, denoted by S , is sufficiently large (e.g., $S = 37$ nm for $d_{\text{NP}} = 5$ nm), the graphene bilayer in between two neighboring Si NPs is first corrugated to form a long tunnel (Figure 2(b)). The tunnel formation, however, results in increased strain energy in the graphene, therefore is energetically unfavorable. As a result, the long tunnel in the graphene bilayer evolves to disappear, preventing the two Si NPs to migrate toward each other (Figures 2(c) and 2(d)). At equilibrium, the Si NPs remain dispersed and are individually wrapped by the graphene (Figure 2(e)). The corrugated morphology of the graphene near each Si NP is similar to that depicted in Figure 1. If the dispersion distance between the Si NPs is small (e.g., $S = 25$ nm for $d_{\text{NP}} = 5$ nm), the corrugated graphene bilayer between the two neighboring Si NPs can form a short tunnel, which facilitates the migration of the two Si NPs toward each other. As the two Si NPs evolve to come closer, the length of the tunnel becomes shorter (e.g., Figures 2(h) and 2(i)), resulting in a decrease of the strain energy of the graphene, which is thus energetically favorable. Eventually, the two Si NPs evolve to form a bundle, which is wrapped together by the graphene bilayer (Figure 2(j)).

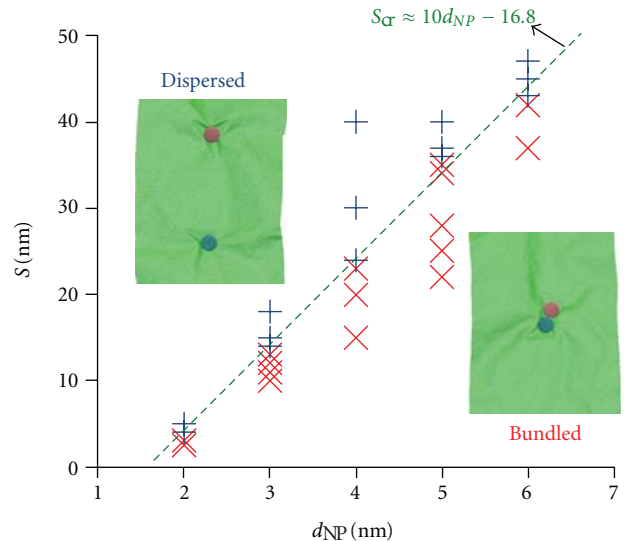


FIGURE 3: A phase diagram of the morphologic evolution of the Si NP-graphene system in the space of NP distance and diameter. “+” denote the MD simulation cases in which Si NPs remain dispersed and “x” denote those in which Si NPs evolve to bundle together. A critical dispersion distance of the Si NPs, S_{cr} , can be determined, which has an approximately linear dependence on d_{NP} .

Also emerging from extensive MD simulations is a critical dispersion distance of Si NPs, S_{cr} , above which the Si NPs remain dispersed and below which the Si NPs evolve to bundle together. Figure 3 plots S_{cr} as a function of the diameter of the Si NP, d_{NP} . There is an approximately linear dependence of S_{cr} on d_{NP} , that is, $S_{\text{cr}} \approx 10d_{\text{NP}} - 16.8$. Results in Figure 3 can serve as guidance for the material

and structural design of Si NP-graphene nanocomposites as anode materials for lithium-ion batteries. For example, for a given design criteria of charging capacity, the maximum volume expansion of the Si NPs upon lithiation can be estimated. The corresponding enlarged size of the Si NPs, instead of the size of pristine Si NPs, should be used to determine a critical dispersion distance to prevent the aggregation of the Si NPs.

In summary, we conduct extensive MD simulations to investigate the morphologic evolution of Si NPs intercalated in between graphene layers, from which a critical dispersion distance of the Si NPs can be determined below which neighboring Si NPs evolve to form a bundle. A roughly linear dependence of the critical distance of the Si NPs on its size is revealed. The ridged morphology of graphene has been observed in recent experiments of substrate-supported graphene with NPs intercalated between the graphene and the substrate [13]. It is further shown that tunneling ridges form between NPs below a critical dispersion distance of the NPs, though the rigid substrate to some extent inhibits the neighboring NPs evolving to bundle together. In our MD simulations, we consider the interaction between two closest neighbor NPs of same size intercalated between graphene layers. In real materials, the variation of the NP sizes and the randomness of the NP distribution render more complex morphologic features that pose significant challenge to be characterized solely by modeling. Nonetheless, results from the present study captures the dominant underlying energetics of NP intercalated in between graphene layers. Furthermore, since the graphene-NP interaction is of secondary importance in determining the corrugated graphene morphology, results from the present study are generally applicable to graphene layers with other anode materials in NP form (e.g., SnO₂ and TiO₂) intercalated in between [14–16]. While the mechanistic understanding and quantitative determination of the critical dispersion distance of Si NPs intercalated between graphene layers shed crucial light on optimizing the design of Si NP-graphene nanocomposites as the high-performance anode materials in lithium-ion batteries, systematic experimental explorations are desirable to validate and further leverage the full potential of the present study.

Acknowledgments

This paper is supported by National Science Foundation (Grants no. 1069076 and no. 1129826) and a UMD GRB Summer Research Award. The authors acknowledge the constructive comments from anonymous reviewers.

References

- [1] M. S. Whittingham, "Lithium batteries and cathode materials," *Chemical Reviews*, vol. 104, no. 10, pp. 4271–4301, 2004.
- [2] K. Kang, Y. S. Meng, J. Bréger, C. P. Grey, and G. Ceder, "Electrodes with high power and high capacity for rechargeable lithium batteries," *Science*, vol. 311, no. 5763, pp. 977–980, 2006.
- [3] J. M. Tarascon and M. Armand, "Issues and challenges facing rechargeable lithium batteries," *Nature*, vol. 414, no. 6861, pp. 359–367, 2001.

- [4] B. A. Boukamp, G. C. Lesh, and R. A. Huggins, "All-solid lithium electrodes with mixed-conductor matrix," *Journal of the Electrochemical Society*, vol. 128, no. 4, pp. 725–729, 1981.
- [5] U. Kasavajjula, C. Wang, and A. J. Appleby, "Nano- and bulk-silicon-based insertion anodes for lithium-ion secondary cells," *Journal of Power Sources*, vol. 163, no. 2, pp. 1003–1039, 2007.
- [6] J. K. Lee, K. B. Smith, C. M. Hayner, and H. H. Kung, "Silicon nanoparticles-graphene paper composites for Li ion battery anodes," *Chemical Communications*, vol. 46, no. 12, pp. 2025–2027, 2010.
- [7] J.-Z. Wang, C. Zhong, S.-L. Chou, and H.-K. Liu, "Flexible free-standing graphene-silicon composite film for lithium-ion batteries," *Electrochemistry Communications*, vol. 12, no. 11, pp. 1467–1470, 2010.
- [8] C. K. Chan, H. Peng, G. Liu et al., "High-performance lithium battery anodes using silicon nanowires," *Nature Nanotechnology*, vol. 3, no. 1, pp. 31–35, 2008.
- [9] Z. Y. Wang, H. Zhang, N. Li, Z. J. Shi, Z. N. Gu, and G. P. Cao, "Laterally confined graphene nanosheets and graphene/SnO₂ composites as high-rate anode materials for lithium-ion batteries," *Nano Research*, vol. 3, no. 10, pp. 748–756, 2010.
- [10] T. Li, "Extrinsic morphology of graphene," *Modelling and Simulation in Materials Science and Engineering*, vol. 19, no. 5, Article ID 054005, 2011.
- [11] D. W. Brenner, O. A. Shenderova, J. A. Harrison, S. J. Stuart, B. Ni, and S. B. Sinnott, "A second-generation reactive empirical bond order (REBO) potential energy expression for hydrocarbons," *Journal of Physics Condensed Matter*, vol. 14, no. 4, pp. 783–802, 2002.
- [12] S. J. Stuart, A. B. Tutein, and J. A. Harrison, "A reactive potential for hydrocarbons with intermolecular interactions," *Journal of Chemical Physics*, vol. 112, no. 14, pp. 6472–6486, 2000.
- [13] M. Yamamoto, W. G. Cullen, and M. S. Fuhrer, Private communication.
- [14] H. Kim, S.-W. Kim, Y.-U. Park et al., "SnO₂/graphene composite with high lithium storage capability for lithium rechargeable batteries," *Nano Research*, vol. 3, no. 11, pp. 813–821, 2010.
- [15] S. M. Paek, E. Yoo, I. Honma et al., "Enhanced cyclic performance and lithium storage capacity of SnO₂/graphene nanoporous electrodes with three-dimensionally delaminated flexible structure," *Nano Letters*, vol. 9, no. 1, pp. 72–75, 2009.
- [16] D. Wang, D. Choi, J. Li et al., "Self-assembled TiO₂-graphene hybrid nanostructures for enhanced Li-ion insertion," *ACS Nano*, vol. 3, no. 4, pp. 907–914, 2009.

Research Article

Effects of Surface Modification of MWCNT on the Mechanical and Electrical Properties of Fluoro Elastomer/MWCNT Nanocomposites

Tao Xu¹ and Jinghui Yang²

¹*Institute of Chemical Materials, Chinese Academy of Engineering Physics, Mianyang 621900, China*

²*Department of Polymer Materials and State Key Laboratory of Polymer Materials Engineering, Sichuan University, Chengdu 610065, China*

Correspondence should be addressed to Tao Xu, xuzhtao@126.com

Received 11 October 2011; Accepted 13 January 2012

Academic Editor: Sulin Zhang

Copyright © 2012 T. Xu and J. Yang. This is an open access article distributed under the Creative Commons Attribution License, which permits unrestricted use, distribution, and reproduction in any medium, provided the original work is properly cited.

Surface modification is a good way to improve the surface activity and interfacial strength of multiwalled carbon nanotubes (MWCNTs) when used as fillers in the polymer composites. Among the reported methods for nanotube modification, mixed acid oxidation and plasma treatment is often used by introducing polar groups to the sidewall of MWCNT successfully. The purpose of this study is to evaluate the effect of different surface modification of MWCNT on the mechanical property and electrical conductivity of Fluoro-elastomer (FE)/MWCNT nanocomposites. MWCNTs were surface modified by mixed oxidation and CF₄ plasma treatment and then used to reinforce the fluoro elastomer (FE, a copolymer of trifluorochloroethylene and polyvinylidene fluoride). FE/MWCNT composite films were prepared from mixture solutions of ethylacetate and butylacetate, using untreated CNTs (UCNTs), acid-modified CNTs (ACNTs), and CF₄ plasma-modified CNT (FCNTs). In each case, MWCNT content was 0.01 wt%, 0.05 wt%, 0.1 wt%, and 0.2 wt% with respect to the polymer. Morphology and mechanical properties were characterized by using scanning electron microscopy (SEM), Raman spectroscopy, as well as dynamic mechanical tests. The SEM results indicated that dispersion of ACNTs and especially FCNTs in FE was better than that of UCNTs. DMA indicated mechanical properties of FCNT composites were improved over ACNT and UCNT filled FE. The resulting electrical properties of the composites ranged from dielectric behavior to bulk conductivities of 10⁻² Sm⁻¹ and were found to depend strongly on the surface modification methods of MWCNTs.

1. Introduction

CNT/polymer nanocomposites hold the promise of delivering exceptional mechanical properties and multifunctional characteristics [1, 2], however, the scope of CNT applications in practical devices has been largely hampered by their poor dispersibility in polymer resin and weak interfacial bonding with polymer matrix. Ineffective interfacial bonding and sliding of individual nanotubes within the ropes inhibit load transfer from the matrix to the fillers in the composite, making the amount of mechanical reinforcement unachievable in polymer composites [3–6]. Therefore, surface modification of carbon nanotubes is a useful approach to improve their surface activity and processibility. Moreover, modification introduces suitable covalent bonds on the sidewalls of CNTs, by which the chemical bondings in the interface

between the CNT and the polymer matrix can be obtained [7–9].

Reported methods for nanotubes modification include chemical and physical treatments [10–14]. Among these methods, mixed acid oxidation and the RF-plasma treatment is often used because both of them can successfully graft polar groups on CNTs [15–20]. For mixed acid oxidation, hydroxyl and carbonyl groups are reported to be grafted on the sidewalls of CNTs. On the other hand, many scientists have reported that the surface of CNTs film can be fluorinated after exposure to CF₄ plasma. The relative amount of functional groups could be controlled by parameter adjustment during CF₄ plasma treatment. Besides semi-ionic/covalent bonding on the surface [21], polymerization of a fluoropolymer around the CNT surface could be also obtained, depending on the reaction conditions. Our previous work [22, 23]

has provided a new way for the homogeneous fluorination of MWCNT powder by using homemade plasma equipment.

As we all know, fluoro-elastomer is quite difficult to be reinforced due to its bad compatibility with the filler and high spatial shielding effect. The fluoro-elastomer we used in the research is a copolymer of trifluorochloroethylene and polyvinylidene fluoride with the volume ratio 1 : 1, which is one of the important materials employed in the aerospace and automotive industries. However, its application is limited by the relatively lower strength. In order to achieve optimal enhancement in the mechanical properties of FE/CNTs nanocomposites, two key issues should be considered: homogeneous dispersion of CNTs in the fluoro-elastomer and strong interfacial bonding between CNT and FE matrix [24]. In order to accomplish these two tasks, surface modification of CNTs is an effective way. But how to select suitable surface modification method is still a challenge for polymer scientists. In this paper, we report on our attempts to understand the relationship between the surface modification of carbon nanotubes and the resulting mechanical property and the electrical conductivity of the nanocomposites. FE/CNTs nanocomposites were fabricated by wet-casting with different kinds of carbon nanotubes including untreated, acid treated, and CF₄ plasma treated. It is shown that fluorinated carbon nanotubes can affect the dispersion in FE rubber and also lead to enhancement behavior on mechanical properties of FE/CNTs composites. In addition, the specific bulk conductivity of the materials was analyzed by DC impedance spectroscopy, and the results showed that the final electrical network depended on the surface modification of CNTs and its weight volume in the matrix. CNTs treated by mixed acid can improve the electrical conductivity of FE/ACNTs with lower percolation threshold. The FE/CNTs composites with improved strength and electrical conductivity are expected to be applied in the fields of automotive and aerospace industry.

2. Experiment

2.1. Samples and Its Modification

2.1.1. Samples. MWCNTs prepared by chemical vapor deposition (CVD) were purchased from the Organic Chemical Limited Company, Chengdu, China. The lengths were about 50 μm , and the outer diameters ranged from 60 to 80 nm. Fluoro-elastomer is the copolymer of trifluorochloroethylene and polyvinylidene fluoride with the molar ratio 1 : 1, which was purchased from the Chenguang Company, Zigong, China.

2.1.2. Mixed Acid Treatment. A raw-MWCNTs sample (4.0 g) was mixed with the concentrated H₂SO₄ (98%) and HNO₃ (65%) mixed solution (3 : 1 by volume) for 24 h at room temperature with stirring. Finally, the solution was filtered through a cellulose nitrate filter (pore size \sim 0.2 μm) and dried at 60°C in a vacuum oven for 24 h. The as-prepared MWCNTs (2.5–3.0 g) with a yield of approximately 60–70% were obtained.

2.1.3. Plasma Treatment. Before being modified by CF₄ plasma, the as-received MWCNT was cleaned by a classical wet method using nitric acid in order to remove the metal catalysts. The inductive coupled plasma was generated in the radio frequency plasma modification equipment (RF-600, Southwest Academy of Nuclear Physics) with a rotating barrel fixed between the two discharge electrodes. A controlled flow of CF₄ gas was introduced into the chamber. The reflective frequency was 13.56 MHz. The diameter of radio-frequency plate electrode was approximately 350 mm, and the spacing of the electrode and samples was 150 mm. The CF₄ plasma treatment conditions for MWCNT powder were as follows: gas flow rate of 80 sccm, operating pressure of 10 Pa, a bias of 200 V, power of 300 W, process duration of 10 minutes, and the average temperature of samples at about 100°C during the CF₄ plasma treatment. Details were presented in the previous papers [22, 23]. The untreated, acid-treated, and plasma-treated carbon nanotubes were abbreviated as CNTs, ACNTs, and FCNTs. And the scheme of modification and mixing in FE is shown in Figure 1.

2.2. Preparation of the FE/CNT Composites. The fabrication of FE/MWCNTs composites is based on a convenient solution process. In brief, FE was first dissolved in the mixture of ethyl acetate and butyl acetate for 2 days till the uniform solution formed. The exact amount of MWCNTs was dissolved in ethyl acetate with continuous ultrasonication for 30 minutes. Then the FE solution was added to the MWCNT solution to obtain a MWCNT-to-polymer weight ratio of 0.05–0.2 wt.% while stirring continually. The solution was then sonicated for 5 min using a high-power sonic tip (200 W) followed by a mild sonication for 2 h in a sonic bath. After careful mixing of FE solution with carbon nanotubes followed by subsequently casting and controlled solvent evaporation, free-standing FE/MWCNTs composite films were obtained by peeling off from Teflon disks. For the control sample, pure FE films were obtained under the same fabrication processing.

2.3. Characterization

2.3.1. X-Ray Photoelectron Spectroscopy (XPS). In order to determine the surface chemical changes during the treatments, XPS measurements were used with a hemispherical electron energy analyzer (ESCALAB250, England). A monochromatized Al K α line ($h\nu = 1486.6\text{ eV}$) was used as the photon source, and the photoelectrons were collected at an angle of 55° relative to the sample surface normal. The energy resolution of system was 0.9 eV. In the spectrum analysis, the background signal was subtracted by Shirley's method. The samples were prepared by attaching carbon nanotube powders to a scotch conductive tape in a form of thin film, in order to avoid dispersion during the pumping. The software Avantage 2.52 was used for peak fitting and quantitative analysis.

2.3.2. Zeta-Potential Measurement. Zeta-potential of different kinds of CNTs was measured by Malvern nanoparticles

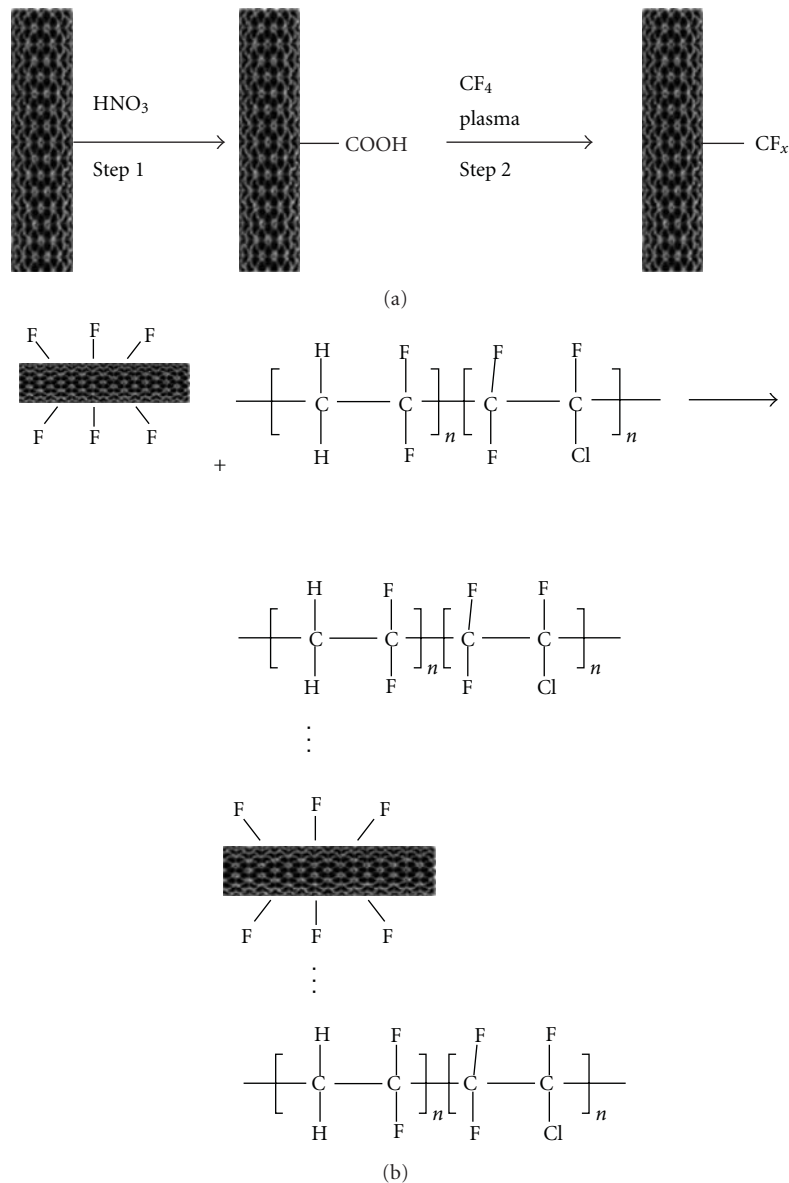


FIGURE 1: Scheme of surface modification and mixing: (a) CF_4 plasma modification of MWCNT; (b) suggested hydrogen bonding of FE with FCNT.

analyzer. CNTs were dispersed in distilled water at the same percent (0.1%) and vibrated for 10 minutes.

2.3.3. Scanning Electron Microscopy (SEM). Samples were fractured in liquid nitrogen, and the fracture surface was observed under an acceleration voltage of 20 kV with a JEOL JSM-5900LV for SEM experiment.

2.3.4. Micro-Raman Spectroscopy. Micro-Raman spectra were recorded on a Renishaw system 2000 micro-Raman spectrometer with Ar (514 nm wavelength) as excitation source. The incident light was introduced to the sample through a 50X objective as a spot less than $2\ \mu\text{m}$ in diameter with the power no more than 1 mW. Three different spots were measured and overlapped.

2.3.5. Mechanical Property. The investigation of the thermo-mechanical behavior was performed by dynamic-mechanical thermal analysis, DMA, using TA RSA3 8500-0001 system. For the measurements, rectangular specimens of 50 mm length, 5 mm width, and 2 mm thickness were prepared. The tests were performed in tensile mode at a frequency of 10 Hz with a static strain of 0.6% and a dynamic strain of 0.1%, in a temperature range between -20°C and 70°C with a heating rate of $2^\circ\text{C}/\text{min}$.

2.3.6. Electrical Conductivity. DC conductivity was measured with a Keithley 6514 Digital Electrostatic Charge Meter in a four-probe setup at room temperature and reported as an average of three readings (see Table 1). The whole measurements were operated under high vacuum conditions in preventing environmental influence.

TABLE 1: Experimental values of the conductivity for FE/CNT nanocomposites.

Sample	Film thickness, μm	Resistivity, $\Omega \cdot \text{m}$	Conductivity, S/m
FE/CNT0.01	102.0	—	—
FE/CNT0.05	13.1	1.13×10^8	8.8×10^{-9}
FE/CNT0.1	73.0	1.27×10^7	8.1×10^{-8}
FE/CNT0.2	69.6	4.03×10^2	2.5×10^{-3}
FE/ACNT0.01	82.7	3.58×10^9	2.8×10^{-10}
FE/ACNT0.05	44.0	4.18×10^3	2.4×10^{-4}
FE/ACNT0.1	30.0	7.96×10^2	1.2×10^{-3}
FE/ACNT0.2	56.3	26.9	3.7×10^{-2}
FE/FCNT0.01	54.0	4.47×10^9	2.2×10^{-10}
FE/FCNT0.05	100.0	4.66×10^8	2.1×10^{-9}
FE/FCNT0.1	210.0	33.8	2.9×10^{-4}
FE/FCNT0.2	180.0	28.3	3.5×10^{-3}

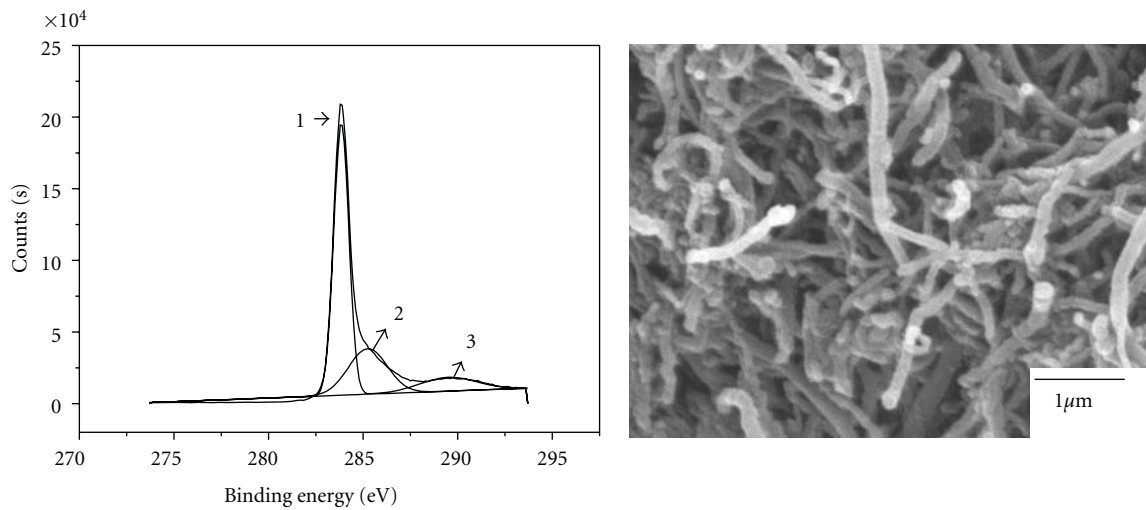
3. Results and Discussion

First, the effects of surface modification on the chemical states and morphology of the MWCNTs were estimated. XPS C1s spectrum of untreated MWCNTs has three chemical states, as shown in Figure 2. The main peak (1) at 283.8 eV corresponds to the sp^2 carbon atoms of original carbon nanotube, similar to the graphite; (2) 284.7 eV matches with the sp^3 carbon atoms indicates the amorphous carbon layer at the surface of CNTs; (3) 289.0 eV is attributed to the oxygen-carbon from air contamination [17, 18]. This is consistent with the fact that nonpurified nanotube powder also contains amorphous carbon and that defects exist at the surface of the nanotubes [5, 14]. After being modified by mixed acid, the CNT main structure survived the irradiation as the chemical state of sp^2 carbon at 283.9 eV remains the same. In addition, a new peak at 286.4 eV appears and is attributed to oxidation carbon of C=O. After being modified by CF_4 plasma, more new peaks appear with higher binding energy and are attributed to fluorinated species: C–C, C–CF, C–O, C–O–F, and C–F, which indicates that CF_4 plasma can induce grafting of CF_x or depositing of a layer of fluorine polymer onto MWCNTs successfully. For a further comparison of different kind of MWCNTs, the SEM is used to observe the morphologies of the carbon nanotube shown in Figure 2 accordingly. The tubes of untreated MWCNTs can be clearly seen, where the amorphous carbon layer is deposited on the surface of CNTs, connecting with each other. No more disordered and amorphous carbon is seen on the surface after mixed acid oxidation. The diameter of the ACNT becomes smaller and the tubes can be more clearly seen. After CF_4 plasma treatment, the tubes of MWCNT expand again and the surface becomes rough. A layer of white substrate coated on the surface of MWCNT powder is observed, suggesting a possible formation of fluoropolymer on the MWCNT surface.

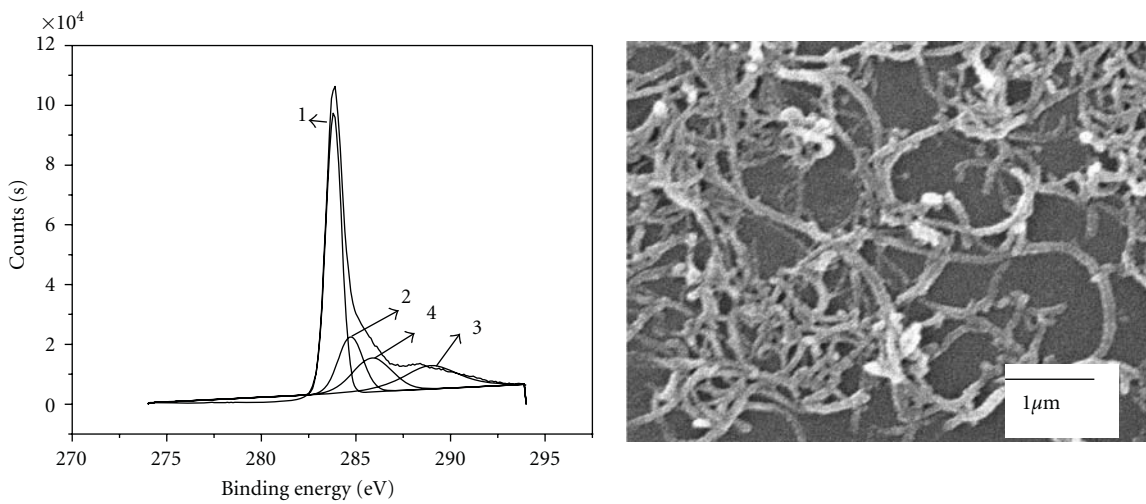
In general, the stability of colloidal particles in solution is important for casting process and is greatly affected by their surface charge density. The electrostatic potential of charged particles dispersed in a liquid medium is governed mainly

by surface functionality, especially by its ionization ability to produce a charged surface, and the preferential absorption of ions of one charge sign from the solution [25]. Therefore, the zeta potentials of CNTs, ACNTs, and FCNTs were measured to understand the effects of surface charge on the dispersion. As we all know, the higher the absolute value of the zeta potential, the more opposite ions will occur in the diffusion layer and the more stable the suspension will be, which indicate the better dispersion of particles in the solvent. Meanwhile, the poorest quality dispersions occur when the magnitude of the zeta potential of particles is near zero. The lowest value is for UCNTs (4.62 V), next the ACNTs (–11.9 V), and the FCNTs have the highest value (–20.2 V). Obviously, FCNTs exhibit negative shift of zeta potentials compared to the CNTs and ACNTs. And also the negative shift can be attributed to the negative surface charges of FCNTs in the solution. Although the values were measured in the distilled water, the results indicated that the surface charge density of CNTs was changed by surface modification. CNTs with C–F groups grafted may reduce the agglomeration effectively by the addition of electron-attracted groups. Therefore, the addition of C–F groups can improve the stability and dispersion of CNTs in the medium, comparing with the pristine CNTs and acid-treated CNTs.

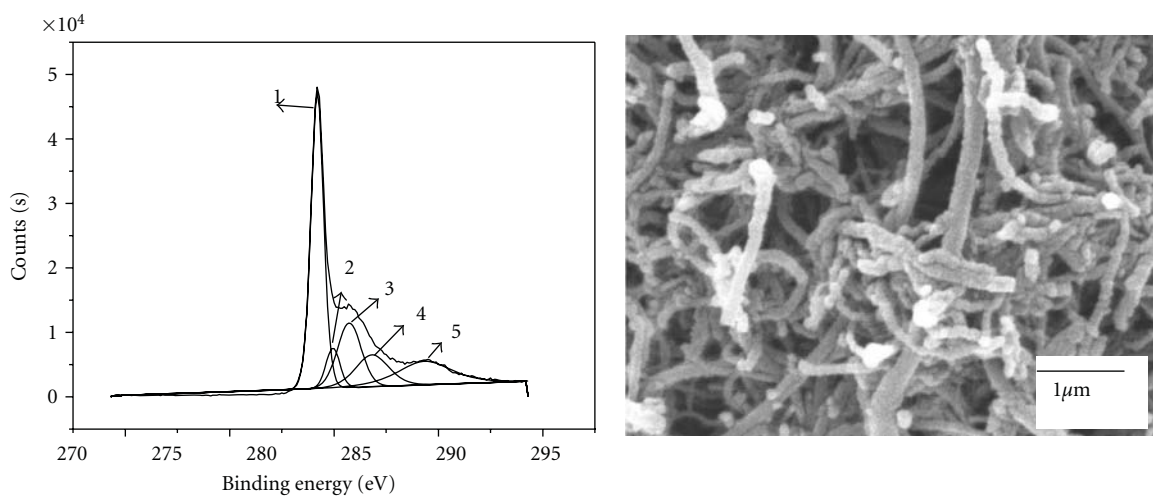
Direct observations of the improved dispersion after adding FCNT are shown in Figure 3, which shows SEM images of the fracture surface of the FE/MWCNT film with MWCNT loading of 0.2 wt%. CNTs without surface modification cannot be dispersed well in the rubber matrix, and most of them are clumped together in aggregates. The dispersion property of ACNT in the FE matrix is a little improved compared with the pristine MWCNT; there are more individual nanotubes scattered in the matrix, while only some of them are clumped together in aggregates in a smaller size. The addition of fluorine functional groups to the CNTs significantly improves the dispersion of the nanotubes in the elastomeric matrix. The different dispersion for three kinds of carbon nanotubes is well consistent with the results of zeta potentials. It is estimated that the addition of containing fluorinated functional group to CNTs surface can effectively



(a)



(b)



(c)

FIGURE 2: XPS C1s spectra: (a) pristine; (b) acid-oxidation-treated MWCNTs; (c) CF₄ plasma-treated MWCNTs. Also shown are the corresponding SEM micrographs.

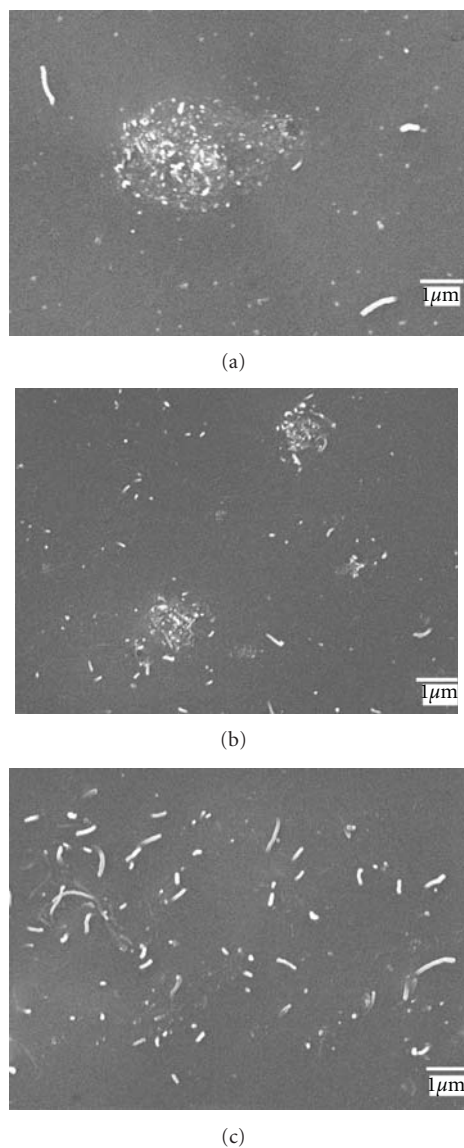


FIGURE 3: SEM photographs of nanocomposite fracture surfaces showing the dispersion state of MWCNT. (a) 0.2 wt% UCNT. (b) 0.2 wt% ACNT. (c) 0.2 wt% FCNT.

eliminate the Van der Waals force of carbon nanotubes due to the exclusive force of F–F bond, finally resulting in the improved dispersion of CNTs in the solvent and in the FE matrix. Noticeably, seen from Figure 3, the FCNTs are not pulled out from the matrix when samples were prepared for SEM observation, indicating strong interfacial adhesions between FCNT and polymer matrix. The strong interfacial interactions may originate from the better compatibility between fillers and polymer matrix. On the other hand, the hydrogen bonding between FCNT and FE may also contribute to the improved interfacial interaction.

For a further study on the interaction between CNTs and polymer matrix, Raman was used to detect the interaction between CNTs and the FE matrix. From Figure 4, all spectra clearly display peaks at 1352 cm^{-1} (D line), 1596 cm^{-1}

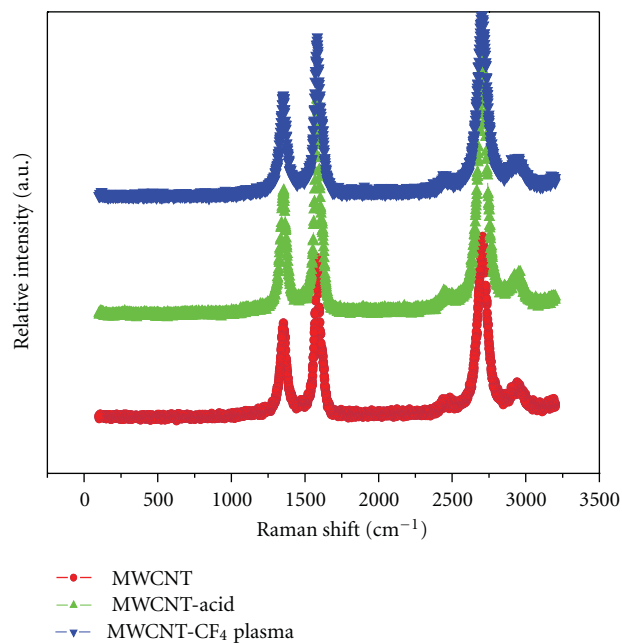


FIGURE 4: Raman spectra for MWCNT under different treatment.

(G line), and 2650 cm^{-1} (G' line). The D line indicates disordered or amorphous carbons, while the G line indicates graphite or ordered carbons in the MWCNTs, and the G' line indicates a second harmonic of the D line [16]. Evaluating the D/G intensity ratio in this Raman spectra, which is frequently used to assess the degree of crystallinity in carbon samples, we can find that a higher ratio exists in the treated MWCNT compared with that of pristine MWCNTs, indicating more defects in the crystal structure (sp^3 carbons as a result of the formation of carboxyl and hydroxyl groups). Among all kinds of CNT, the FCNT has the highest D/G intensity ratio (0.86), next is the ACNT (0.73), and last is the CNT (0.56). The results indicate that the addition of fluorine to the nanotube sidewalls reduces the intensity of the sp^2 C=C stretching mode and increases the intensity of the sp^3 C–C stretching mode. This change is indicative of covalent modification as it reveals sp^3 hybridization or disorder within the nanotube framework. Thus the increase in the relative intensity of the D-band can be attributed to an increased number of sp^3 -hybridized carbons in the nanotube framework and can be taken as a crude measure of the degree of modification. After mixing and casting process, some of the fluorine is removed from the nanotubes, as evidenced by the return of the sp^2 peak at 1596 cm^{-1} seen in Figure 5. The D/G intensity ratio of FE/FCNT decreased comparing with FE/ACNT and FE/MWCNT composites, which indicates the chemical bonding formed between the FCNT and FE.

The DMA properties were measured for neat FE and nanocomposite films, as shown in Figures 6, 7, and 8. The storage modulus of FE/CNTs is enhanced on increasing the content of CNTs to 0.1 wt%, while a decrease in modulus is observed on further increasing the UCNTs and ACNTs content to 0.2 wt%. The decrease of storage modulus for

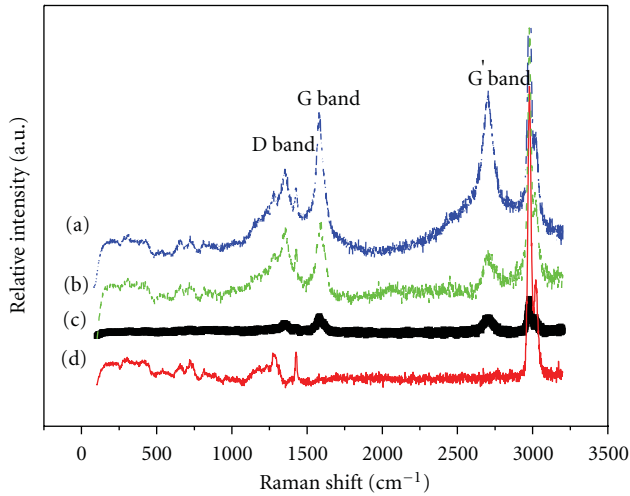


FIGURE 5: Micro-Raman spectra of FE and FE/MWCNT nanocomposites: (a) FE/FCNT, (b) FE/ACNT, (c) FE/MWCNT, and (d) FE.

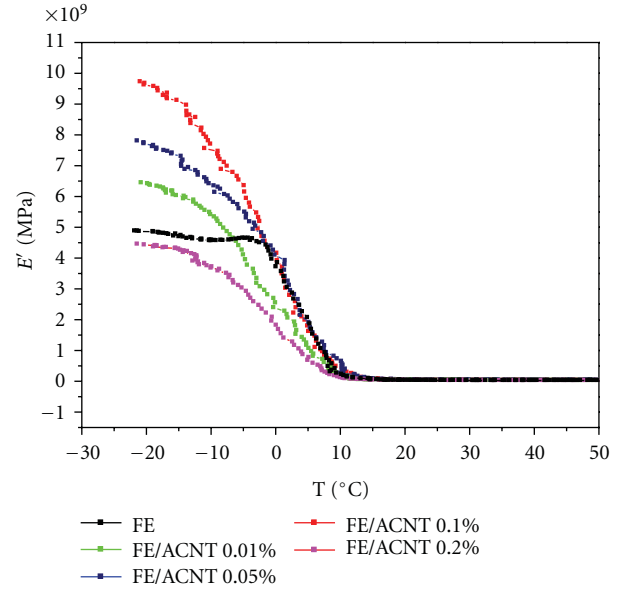


FIGURE 7: The storage modulus as a function of temperature for the FE/ACNT with different ACNT loadings.

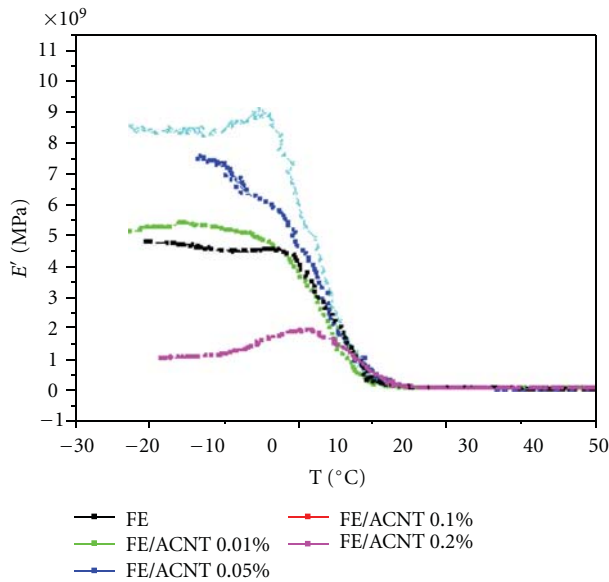


FIGURE 6: The storage modulus as a function of temperature for the FE/MWCNT with different MWCNT loadings.

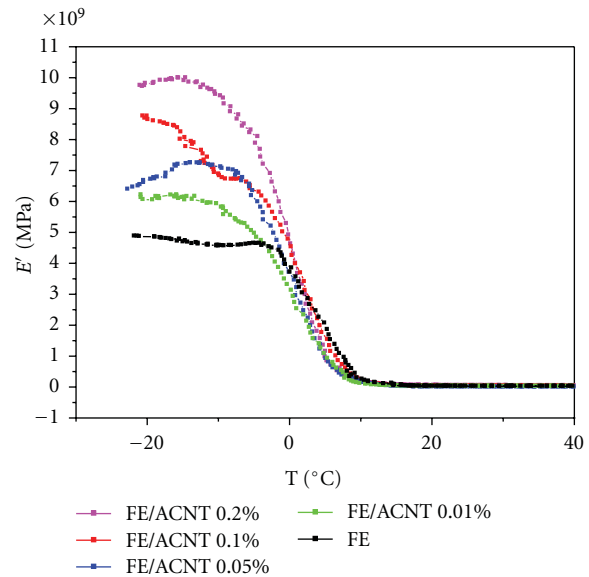


FIGURE 8: The storage modulus as a function of temperature for the FE/FCNT with different FCNT loadings.

the nanocomposites with 0.2 wt% content of UCNTs and 0.2 wt% ACNTs may be due to the agglomeration in the polymer matrix. On the contrary, the storage modulus for FE/FCNTs shows a gradual increase of the FCNTs loadings. Even when the loadings of FCNTs increased to 0.2 wt%, the modulus has reached up to maximum as a result of homogeneous dispersion of FCNTs and good interaction between FCNTs and the matrix. Thus the energy dissipation from the matrix to carbon nanotubes due to the strong interaction which is from the compatibility and hydrogen bonding as described above can be achieved, resulting in the increase of storage modulus.

Figure 9 shows the relationship between the conductivity and the weight fraction of MWCNTs with different surface

modification in the composites. It is obvious that the conductivity of the nanocomposites increases rapidly with increasing MWCNT weight percentage. The electrical properties of the composites ranged from dielectric behavior to bulk conductivities of 10^{-2} Sm^{-1} . The increase in σ as a function of the MWCNT mass fraction is usually due to the introduction of conducting CNT paths to the polymer, indicative of percolative behavior. Moreover, it was found that the electrical property was dependent strongly on the surface modification methods of MWCNTs. Apparently, the conductivity is the highest for ACNT comparing with FCNT and CNT at

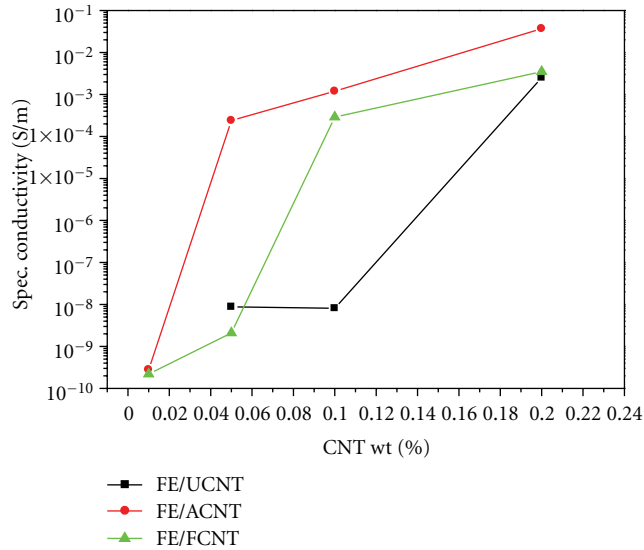


FIGURE 9: The conductivity as a function of CNT loading for CNT/FE composites.

the same weight loading [26]. It is reported that percolation threshold depended on the shape and aspect ratio of fillers. From SEM micrographs (Figure 2), we can find that CNTs after being acid treated exhibits smooth surface compared with UCNT and FCNT by removing amorphous carbon effectively, which increases the aspect ratio at a given weight percent as well. Therefore, electrical percolation threshold for FE/ACNT is the lowest compared with that of FE/CNT and FE/FCNT. On the other hand, there maybe exists a deposited fluoro polymer layer on the surface of CNT after being CF_4 plasma treated, which reduces the electrical conductivity of CNT in the composites. But the conductivity is still higher than that of UCNT, which might be attributed to the improved dispersion state of FCNT in the polymer, and thus reduces percolation threshold of the composite system.

4. Conclusions

Carbon nanotubes modified by CF_4 plasma can reinforce the fluoro elastomer matrix to yield the highest increase in modulus due to better dispersion and enhanced chemical compatibility by introducing electron-rich fluorine atoms. However, for electrical properties, carbon nanotubes modified by mixed acid are predominant in the polymer matrix by removing the amorphous carbon effectively, which results in lower percolation threshold and higher conductivity. This difference in the mechanical and electrical properties would be understood in selecting suitable surface modification.

Acknowledgment

This work was financially supported by the Special Foundation of CAEP (no. 2008B0302029).

References

- [1] S. Iijima, "Helical microtubules of graphitic carbon," *Nature*, vol. 354, no. 6348, pp. 56–58, 1991.
- [2] M. Dresselhaus and Ph. Avouris, *Carbon Nanotubes: Synthesis, Properties and Application*, Springer, Berlin, Germany, 2001.
- [3] W. Tang, M. H. Santare, and S. G. Advani, "Melt processing and mechanical property characterization of multi-walled carbon nanotube/high density polyethylene (MWNT/HDPE) composite films," *Carbon*, vol. 41, no. 14, pp. 2779–2785, 2003.
- [4] M. L. Shofner, V. N. Khabashesku, and E. V. Barrera, "Processing and mechanical properties of fluorinated single-wall carbon nanotube-polyethylene composites," *Chemistry of Materials*, vol. 18, no. 4, pp. 906–913, 2006.
- [5] M. Moniruzzaman and K. I. Winey, "Polymer nanocomposites containing carbon nanotubes," *Macromolecules*, vol. 39, no. 16, pp. 5194–5205, 2006.
- [6] R. Andrews and M. C. Weisenberger, "Carbon nanotube polymer composites," *Current Opinion in Solid State and Materials Science*, vol. 8, no. 1, pp. 31–37, 2004.
- [7] X.-L. Xie, Y.-W. Mai, and X.-P. Zhou, "Dispersion and alignment of carbon nanotubes in polymer matrix: a review," *Materials Science and Engineering R*, vol. 49, no. 4, pp. 89–112, 2005.
- [8] K. L. Strong, D. P. Anderson, K. Lafdi, and J. N. Kuhn, "Purification process for single-wall carbon nanotubes," *Carbon*, vol. 41, no. 8, pp. 1477–1488, 2003.
- [9] H. G. Chae, T. V. Sreekumar, T. Uchida, and S. Kumar, "A comparison of reinforcement efficiency of various types of carbon nanotubes in polyacrylonitrile fiber," *Polymer*, vol. 46, no. 24, pp. 10925–10935, 2005.
- [10] M. Zhang, L. Su, and L. Mao, "Surfactant functionalization of carbon nanotubes (CNTs) for layer-by-layer assembling of CNT multi-layer films and fabrication of gold nanoparticle/CNT nanohybrid," *Carbon*, vol. 44, no. 2, pp. 276–283, 2006.
- [11] M. Abdalla, D. Dean, D. Adibempe, E. Nyairo, P. Robinson, and G. Thompson, "The effect of interfacial chemistry on molecular mobility and morphology of multiwalled carbon nanotubes epoxy nanocomposite," *Polymer*, vol. 48, no. 19, pp. 5662–5670, 2007.
- [12] J. A. Kim, D. G. Seong, T. J. Kang, and J. R. Youn, "Effects of surface modification on rheological and mechanical properties of CNT/epoxy composites," *Carbon*, vol. 44, no. 10, pp. 1898–1905, 2006.
- [13] J. Zhu, J. Kim, H. Peng, J. L. Margrave, V. N. Khabashesku, and E. V. Barrera, "Improving the dispersion and integration of single-walled carbon nanotubes in epoxy composites through functionalization," *Nano Letters*, vol. 3, no. 8, pp. 1107–1113, 2003.
- [14] E. T. Thostenson and T.-W. Chou, "Aligned multi-walled carbon nanotube-reinforced composites: processing and mechanical characterization," *Journal of Physics D*, vol. 35, no. 16, pp. L77–L80, 2002.
- [15] B. Yan, K. Qian, Y. Zhang, and D. Xu, "Effects of argon plasma treating on surface morphology and gas ionization property of carbon nanotubes," *Physica E*, vol. 28, no. 1, pp. 88–92, 2005.
- [16] K. S. Ahn, J. S. Kim, C. O. Kim, and J. P. Hong, "Non-reactive rf treatment of multiwall carbon nanotube with inert argon plasma for enhanced field emission," *Carbon*, vol. 41, no. 13, pp. 2481–2485, 2003.
- [17] K. Yu, Z. Zhu, M. Xu, Q. Li, and W. Lu, "Electron field emission from soluble carbon nanotube films treated by hydrogen plasma," *Chemical Physics Letters*, vol. 373, no. 1-2, pp. 109–114, 2003.

- [18] K. Yu, Z. Zhu, Y. Zhang et al., "Change of surface morphology and field emission property of carbon nanotube films treated using a hydrogen plasma," *Applied Surface Science*, vol. 225, no. 1–4, pp. 380–388, 2004.
- [19] W. Chen and X. Tao, "Production and characterization of polymer nanocomposite with aligned single wall carbon nanotubes," *Applied Surface Science*, vol. 252, no. 10, pp. 3547–3552, 2006.
- [20] L. Valentini, D. Puglia, I. Armentano, and J. M. Kenny, "Side-wall functionalization of single-walled carbon nanotubes through CF_4 plasma treatment and subsequent reaction with aliphatic amines," *Chemical Physics Letters*, vol. 403, no. 4–6, pp. 385–389, 2005.
- [21] Y. W. Zhu, F. C. Cheong, T. Yu et al., "Effects of CF_4 plasma on the field emission properties of aligned multi-wall carbon nanotube films," *Carbon*, vol. 43, no. 2, pp. 395–400, 2005.
- [22] T. Xu, J. Yang, J. Liu, and Q. Fu, "Surface modification of multi-walled carbon nanotubes by O_2 plasma," *Applied Surface Science*, vol. 253, no. 22, pp. 8945–8951, 2007.
- [23] T. Xu, J. Yang, J. Liu, and Q. Fu, " CF_4 plasma-induced grafting of fluoropolymer onto multi-walled carbon nanotube powder," *Applied Physics A*, vol. 90, no. 3, pp. 431–435, 2008.
- [24] C. Vix-Guterl, M. Couzi, J. Dentzer, M. Trinquocoste, and P. Delhaes, "Surface characterizations of carbon multiwall nanotubes: comparison between surface active sites and Raman spectroscopy," *Journal of Physical Chemistry B*, vol. 108, no. 50, pp. 19361–19367, 2004.
- [25] L. Vaisman, G. Marom, and H. D. Wagner, "Dispersions of surface-modified carbon nanotubes in water-soluble and water-insoluble polymers," *Advanced Functional Materials*, vol. 16, no. 3, pp. 357–363, 2006.
- [26] Q. Zhang, S. Rastogi, D. Chen, D. Lippits, and P. J. Lemstra, "Low percolation threshold in single-walled carbon nanotube/high density polyethylene composites prepared by melt processing technique," *Carbon*, vol. 44, no. 4, pp. 778–785, 2006.

Review Article

Fabrication of Microscale Carbon Nanotube Fibers

Gengzhi Sun, Yani Zhang, and Lianxi Zheng

School of Mechanical and Aerospace Engineering, Nanyang Technological University, Singapore 639798

Correspondence should be addressed to Lianxi Zheng, lxzheng@ntu.edu.sg

Received 13 October 2011; Accepted 16 December 2011

Academic Editor: Teng Li

Copyright © 2012 Gengzhi Sun et al. This is an open access article distributed under the Creative Commons Attribution License, which permits unrestricted use, distribution, and reproduction in any medium, provided the original work is properly cited.

Carbon nanotubes (CNTs) have excellent mechanical, chemical, and electronic properties, but realizing these excellences in practical applications needs to assemble individual CNTs into larger-scale products. Recently, CNT fibers demonstrate the potential of retaining CNT's superior properties at macroscale level. High-performance CNT fibers have been widely obtained by several fabrication approaches. Here in this paper, we review several key spinning techniques including surfactant-based coagulation spinning, liquid-crystal-based solution spinning, spinning from vertical-aligned CNT arrays, and spinning from CNT aerogel. The method, principle, limitations, and recent progress of each technique have been addressed, and the fiber properties and their dependences on spinning parameters are also discussed.

1. Introduction

Carbon nanotubes (CNTs) are the stiffest (Yong's modulus) and strongest (yield strength) materials yet measured. Their tensile strength is about 11–63 GPa for individual multiwalled CNTs (MWNTs) and 13–52 GPa for individual single-walled CNTs (SWNTs) [1–3]. They are also good conductors for electricity and heat [4–8]. These extraordinary properties make them attractive for advanced applications. In order to fully utilize their superior properties at practical scale, CNTs need to be prepared into larger size assemblies, such as microscale CNT fibers. Recent progresses [9–12] in neat CNT fibers demonstrate the possibility of retaining CNT's excellent properties at larger-scale and more practicable level. The CNT fibers have been reported to have tensile strength of 1–3 GPa, Young's modulus of 100–260 GPa, toughness of 100–900 J·g⁻¹, and density of 0.2 g·cm⁻³ [9]. These progresses motivate further study of lightweight and high-strength composites for possible structural applications.

Numerous methods have been developed to assemble such fibers [13]. Generally, these techniques could be divided into two groups: solution-spinning methods [14–18] and solid-spinning techniques. In solution-based spinning, CNTs need to be dispersed into a liquid first, and then spun into fibers, by a process similar to that used for polymeric fibers.

In solid-spinning processes, CNT fibers could be spun from vertically aligned CNT arrays [19, 20], cotton-like CNT mats [21, 22], or from an aerogel of CNTs formed in chemical vapor deposition (CVD) reaction zone [23, 24]. The performances of CNT fibers are strongly dependent on processing methods and the detail process parameters. Here in this paper, we will review several key spinning techniques and their recent progress.

2. Solution-Based Spinning

CNT fibers could be produced by using “solution-spinning” method, just like most synthetic fibers created from a concentrated viscous liquid. These processes consist of dispersing the CNTs in solution and then recondensing them in a stream of another solution, which serves as the coagulant. The first critical challenge in development of this method is the difficulty of processing CNTs in liquid state. CNTs are inert in pristine state and tend to bundle together due to the strong van der Waals interactions, making them difficult to disperse uniformly in aqueous or any organic solvents. Some methods have been utilized to overcome this problem through oxidation and grafting with different functionalities [25–29], but these methods normally destroy CNT's intrinsic structures and properties. Thus, they are not favored for fiber spinning. Shaffer and Windle [30] have previously suggested

that CNTs can be viewed as analogous to high-aspect ratio and rigid-rod polymers. According to this analog, CNTs are supposed to be applicable to two types of solution-based spinning methods: coagulation spinning and liquid-crystal solution spinning.

2.1. Surfactant-Based Coagulation Spinning. Generally, the principle of the “coagulation spinning” used for synthetic fiber processing could be depicted as when a polymer solution is extruded through a thin capillary tube and injected into a bath that contains a second liquid in which the solvent is soluble but the polymer is not, the polymer will condense and form a fiber due to the phase separation. Employing this “coagulation spinning” method for CNT fiber fabrication, the CNTs need to be dispersed into a liquid solution at an almost molecule level so that they could be manipulated and aligned well. Surfactants are widely utilized for this purpose because of their ability to absorb/wrap at the surface of individual CNTs and prevent them from rebundling. This spinning approach was initially adopted by Vigolo et al. [14]. In their fabrication process, as shown schematically in Figure 1, arc-discharge-produced SWNTs were firstly dispersed in an aqueous solution by using sodium dodecyl sulfate (SDS) as surfactant, then injected into a rotating bath of aqueous polyvinyl alcohol (PVA) solution, which serves as the coagulant. During this process, PVA displaced the surfactant, causing CNTs collapse and forming ribbon-like elastomeric gel-fibers. These fragile fibers were pulled from the coagulation bath at a rate of about $0.01 \text{ m} \cdot \text{min}^{-1}$ in order to form solid fibers. Such fibers were washed by immersing in successive water container in order to remove excess PVA and surfactant residues and then were dried by pulling them out of water bath.

It is found that one critical parameter to obtain a good dispersion of CNTs is the amount of SDS. When the concentration of SDS is too low, large and dense clusters of the CNTs will still exist in solution even after sonication, which means that the amount of surfactant is too low to produce an efficient coating and induce enough electrostatic repulsion that could counterbalance van der Waals attractions. On the other hand, when the concentration of SDS is too high, the osmotic pressure of the excess micelles causes depletion-induced aggregation. They found that an optically homogeneous solution could be formed with 0.35 wt% CNTs and 1 wt% SDS for CNTs with particular diameter and length. In addition, flow-induced alignment could lead to a preferential orientation of the CNTs in fibers [14, 31] and has a close relationship to relative flow rate between injection solution and coagulant solution, as shown in Figure 2. The coagulant must flow faster than the gel-fiber in order to stretch the fiber along the axis direction and promote alignment of CNTs in the fiber. This could be accomplished by rotating the coagulant container.

This coagulation-based fiber spinning technique is exciting because of its simplicity and ability to produce fibers with very high CNT loadings (60 wt. %). The final CNT/PVA composite fibers exhibited a tensile strength in the order of 0.1 GPa and a Young’s modulus varying between 9 and 15 GPa. In contrast to most ordinary carbon fibers, CNT

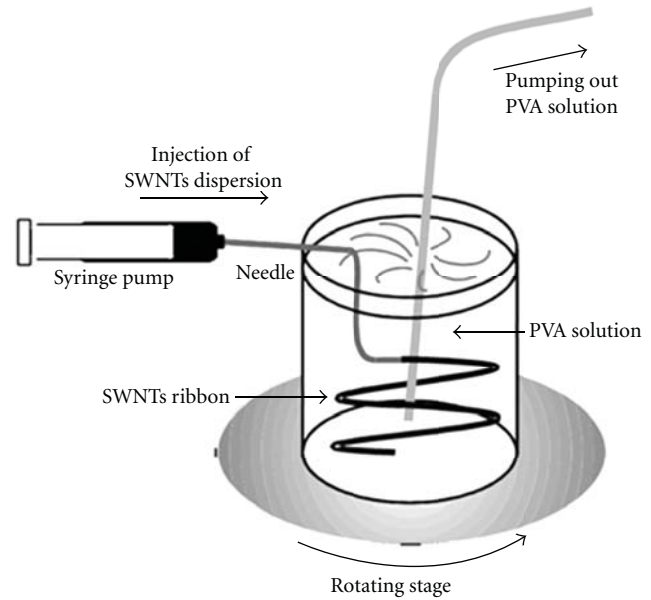


FIGURE 1: Schematic of the experimental setup used to make SWNT ribbons. The capillary tip was orientated so that the SWNT injection was tangential to the circular trajectory of the polymer solution [14].

fibers (shown in Figure 3) can be heavily bent and even tightly tied without breaking.

The main challenges existing in this method include dispersion of SWNTs at high concentrations, low processing rate, and the poor fiber performance. In order to improve the mechanical performance of as-spun CNT fibers, various modified methods have been developed. By drying CNT fibers under load, improved mechanical properties were obtained with a tensile strength of 230 MPa and a Young’s modulus of 45 GPa [32, 33]. By hot drawing the fibers, Miaudet et al. [34] drew such PVA fibers at elevated temperatures, and the fibers yield a strength of 1.8 GPa, a modulus of 45 GPa, and a toughness of $55 \text{ J} \cdot \text{g}^{-1}$ at 11% strain. Dalton et al. [35] further advanced the spinning apparatus to spin fibers continuously by injecting CNT dispersion into a cylinder with the coagulant flowing in the same direction. They were able to spin a reel of CNT gel fibers and then converted it into 100 meters solid CNT-composite fibers, at a rate of more than $0.70 \text{ m} \cdot \text{min}^{-1}$. The final fibers exhibit an increased mechanical performance with a tensile strength of 1.8 GPa and a Young’s modulus of up to 80 GPa. Coagulation spinning has also been done with solutions other than PVA. For example, Lynam et al. [36] produced CNT biofibers based on a wet-spinning process in which biomolecules acted as both the dispersant and coagulant. These fibers possessed strength of 0.17 GPa and modulus of 0.146 GPa.

Since the existence of the second component polymer will add complicity of processing and this second component is usually an insulator, which will compromise the conductive property of as-spun fibers, pure CNT fibers are favorable in some circumstances. Kozlov et al. [17] developed a polymer-free solution spinning method. Pure CNT

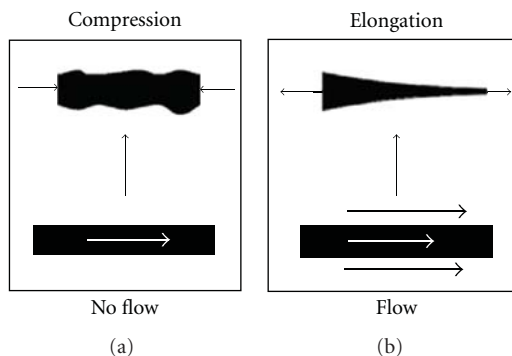


FIGURE 2: (a) When the coagulation bath does not flow or flows slower than injecting rate, a net compressive force acts on the gel-like fiber, compromising the alignment. (b) When the coagulant flows along the extruded fiber and faster than the injecting rate, a net stretching force will be resulted to increase the alignment [14].

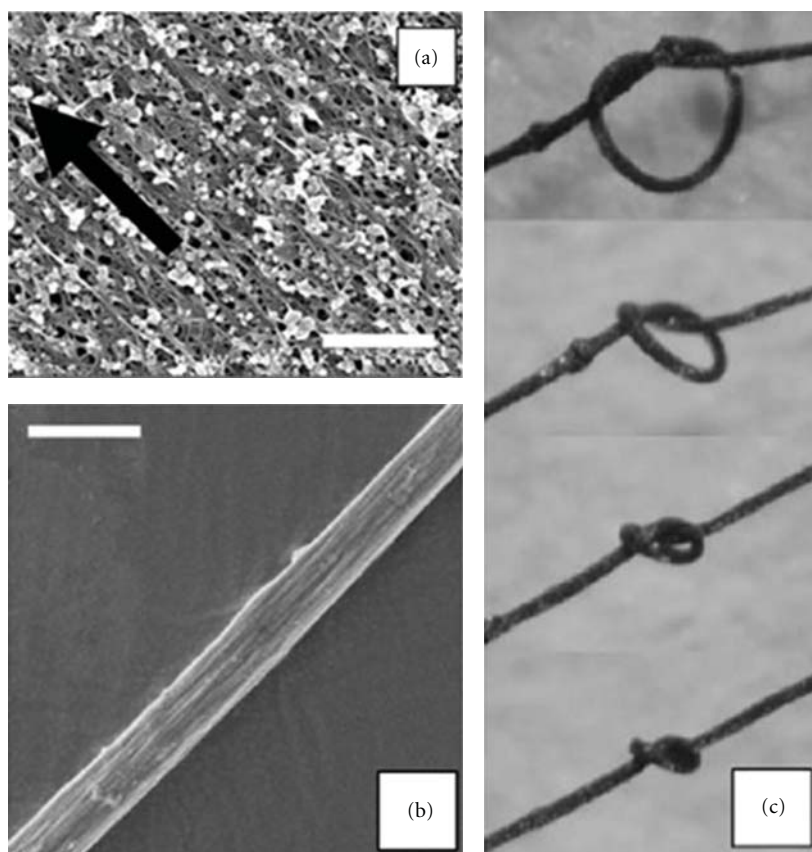


FIGURE 3: (a) A dry ribbon deposited on a glass substrate. (The black arrow indicates the main axis of the ribbon, which corresponds to the direction of the initial fluid velocity.) (b) A CNT fiber. (c) Knots reveal the high flexibility and resistance to torsion of the CNT microfibers. Scale bars: 500 nm and 25 μm for (a) and (b) [14].

fibers can be produced from CNT/surfactant/water solutions. However, the mechanical properties of the as-spun fibers are not impressive, showing a specific strength of $65 \text{ MPa} \cdot \text{g}^{-1} \cdot \text{cm}^{-3}$, specific modulus of $12 \text{ GPa} \cdot \text{g}^{-1} \cdot \text{cm}^{-3}$, and electrical conductivity of $140 \text{ S} \cdot \text{cm}^{-1}$.

2.2. Liquid Crystal-Based Solution Spinning. Spinning from lyotropic liquid-crystalline solution of rigid-rod molecules

is another important method used for fiber production. As shown in Figure 4, CNTs are similar to high-aspect ratio and rigid-rod polymers and exhibit liquid crystallinity feature [37, 38]. Ericson et al. [16] first successfully produced well-aligned macroscopic fibers composed solely of SWNTs from lyotropic solutions in super acids. Fuming sulfuric acid charges SWNTs and promotes them to order into an aligned phase with individual mobile CNTs surrounded by acid

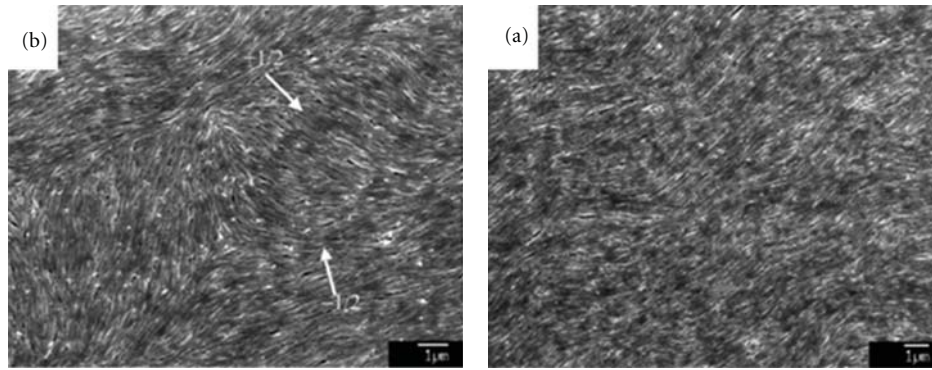


FIGURE 4: Scanning electron microscopy (SEM) images of a dried MWNT film. (a) The director fields around a pair of disclinations of topological strength $+1/2$ and $-1/2$ and (b) the region toward the edge of the film which is free of disclinations [37, 38].

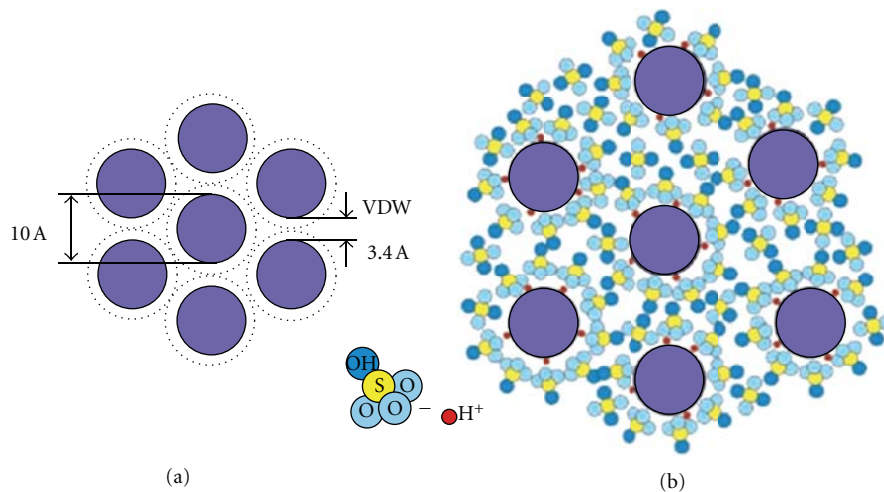


FIGURE 5: A model illustrating the swelling of SWNT ropes in sulfuric acid. (a) A cartoon of SWNTs in van der Waals contact within a neat fiber. (b) The same SWNT fiber after reexposure to sulfuric acid [16].

anions. This ordered dispersion was then extruded into a coagulant bath (either diethyl ether, 5% sulfuric acid, or water) to form continuous macroscopic CNT fibers.

The possible mechanism, that high concentration CNTs could be dispersed in superacid (100 + % sulfuric acid), is the repulsive interaction between CNTs generated in superacids due to the formation of charge-transfer complexes: individual positively charged CNTs surrounded by a finite number of sulfuric acid anions. At very low concentration, such charged tube-anion complexes behave as Brownian rods. At higher concentration, as shown in Figure 5, the CNTs coalesce and form ordered domains, behaving similarly to nematic liquid crystalline.

The CNT fibers spun by such a process have interesting structural and physical properties, including high orientation, good electrical, and thermal conductivities, and reasonable mechanical properties. The alignment of CNTs within these fibers is within $\pm 15.5^\circ$. The strength is 116 ± 10 MPa, and the Young's modulus approaches to 120 ± 10 GPa. However, some protonation of the material occurs

because of prolonged contact with the sulfuric acid. The CNT/acid system is very sensitive to water; the introduction of even minimal moisture causes phase separation and precipitation of discrete needle-like crystal solvates. And superacid route is also found not effective for MWNTs. To address the last problem, Zhang et al. [39] developed a new coagulation process, by which they spun MWNTs from a liquid-crystalline ethylene glycol dispersion. The MWNT fibers have a Young's modulus of 69 ± 41 GPa and a yield strain of 0.3%. Fracture occurs typically at strains below 3% and stresses of 0.15 ± 0.06 GPa.

3. Solid Spinning

3.1. Spinning Fibers from Vertical-Aligned CNT Arrays. In order to eliminate the dispersion problem existing in solution-based spinning methods, spinning CNT fibers directly from as-grown CNT materials seems to be a more convenient way. A breakthrough was made by Jiang et al. [19] in 2002 by simply drawing a neat CNT yarn from a vertically superaligned

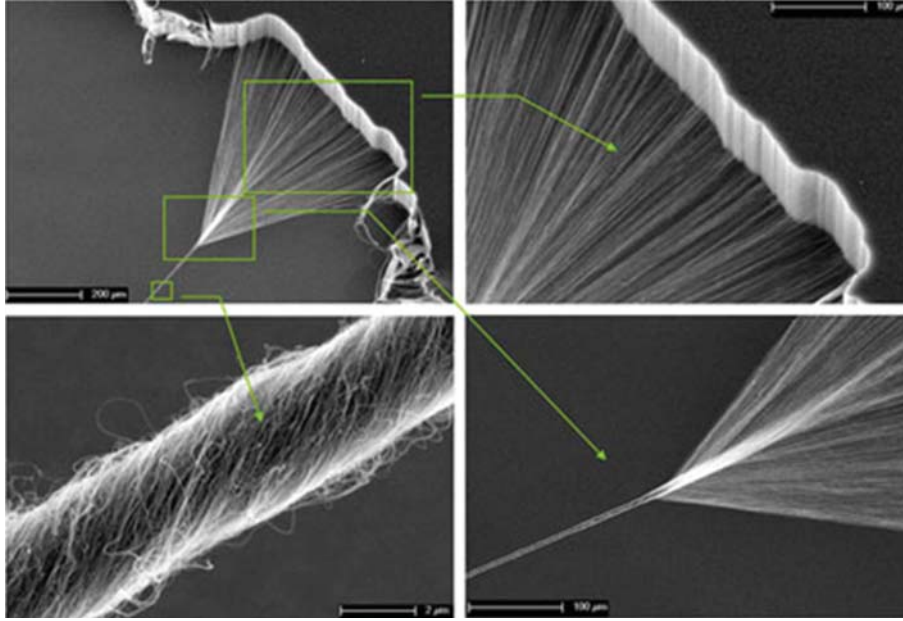


FIGURE 6: SEM images showing the structures formed during the draw-twist process [20].

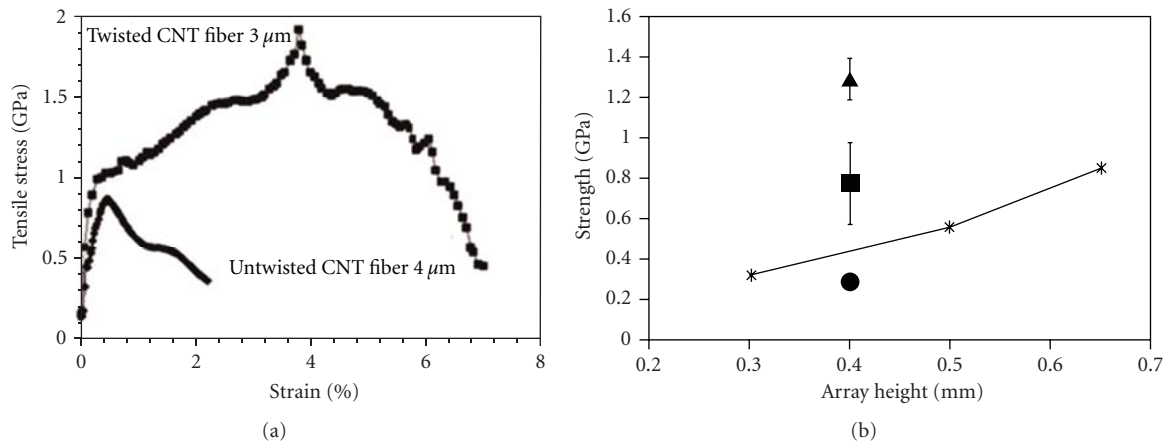


FIGURE 7: (a) As-spun and posttwisted small-diameter CNT fibers spun from a 650 μm array. (b) A comparison of fiber strengths at different array heights. The black line shows that the strength of CNT fibers increases with the array height, and marks show the strength dependence on array morphology (the dot represents the data from oxygen-assisted growth that shows poor CNT alignment, the square represents the data from the normal growth, and the triangle represents the data from the hydrogen-assisted growth that shows good CNT alignment) [10, 12].

CNT array. They found that CNTs could be self-assembled into yarns of up to 30 cm in length. Following that, Zhang et al. [40] produced highly orientated, free-standing CNT transparent sheets using a similar method, and further assemble CNTs into fibers by using a draw-twisting spin method [20]. The typical SEM images of fiber spinning processes are shown in Figure 6.

Many applications of these fibers were proposed and demonstrated [41–44], and different postspinning methods were developed to improve their performances. Jiang et al. [19] found that the strength and conductivity of their yarns could be improved after being heated at high temperatures. By introducing twist during spinning to make multiple,

torque-stabilized yarns, Zhang et al. [20] achieved yarn strength greater than 460 MPa. They emphasized that the load could be transferred effectively between CNTs because of the twisting. In a twisted fiber, individual CNTs are inclined at an angle α with respect to the fiber axis, generating transverse forces which lock the fibers together as a coherent structure. They also found these twisted yarns deformed hysterically over large strain ranges from 0.5% to 8%, providing up to 48% energy damping. These yarns could also retain their strength and flexibility even after being heated in air at 450°C for an hour or being immersed in liquid nitrogen. In addition to using postspinning treatment, Zhang et al. [9–11] found that mechanical properties can

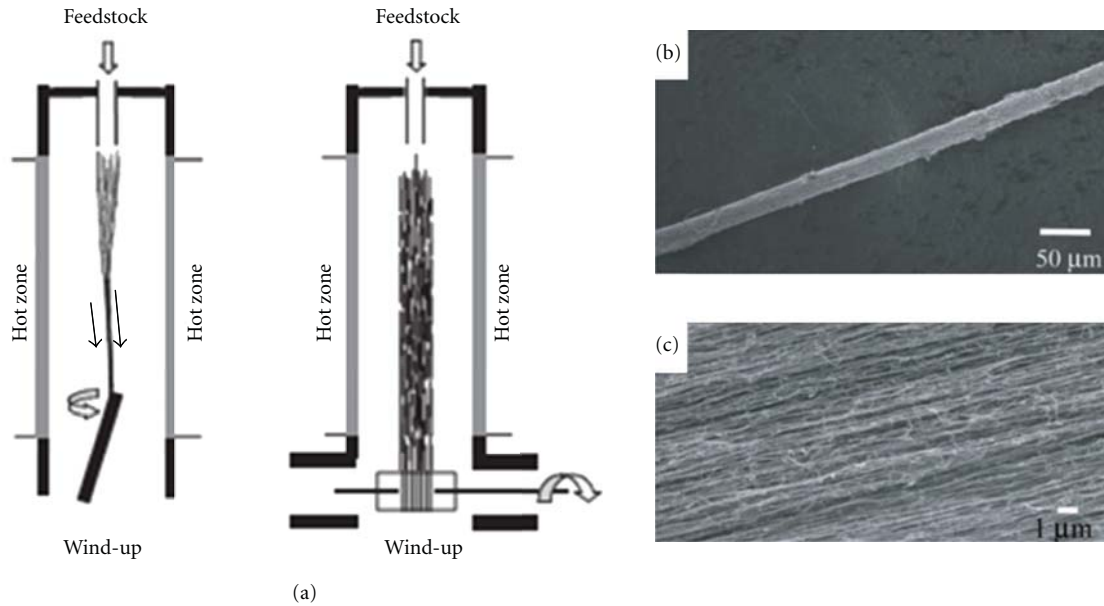


FIGURE 8: (a) Schematic of the direct spinning process. The liquid feedstock, in which small quantities of ferrocene and thiophene are dissolved, is mixed with hydrogen and injected into the hot zone, where an aerogel of CNTs form. This aerogel is captured and wound out of the hot zone continuously as a fiber or film. (b) SEM image of a fiber. (c) Well-aligned MWNTs within the fiber [23].

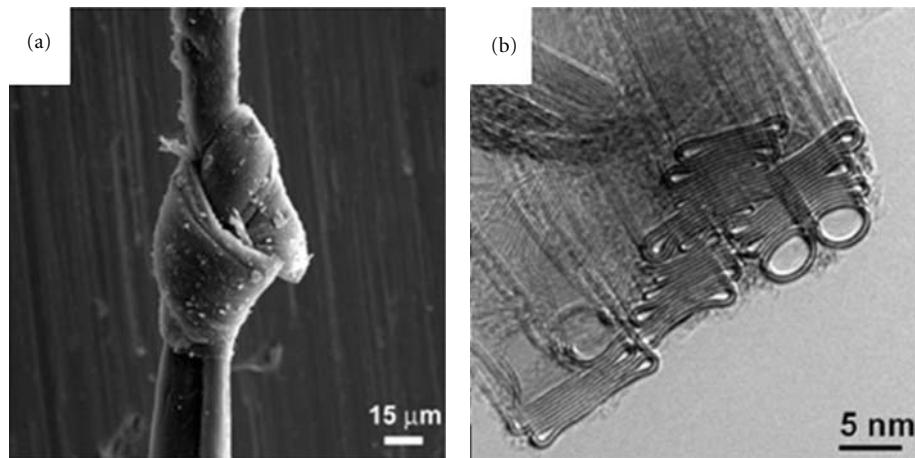


FIGURE 9: Structure of the fiber product. (a) SEM image of knotted fiber. (b) High-resolution transmission electron microscopy (HR-TEM) image of a bundle close to a fiber fracture revealing that the bundles consist, predominantly, of collapsed double-wall nanotubes greater than 5 nm [59].

be significantly improved by using longer CNT arrays. The tensile strength and stiffness of their fibers spun from a 1 mm long CNT array were measured in the range of 1.35–3.3 GPa and 100–263 GPa, respectively, which are many times stronger and stiffer per weight than the best existing engineering fibers and CNT fibers reported previously. It is obvious that the strength of CNT fibers increased with increasing CNT array length which yields a much larger friction between CNTs. Longer CNTs will also introduce fewer mechanical defects (like the ends of CNTs) per unit fiber length [45–48]. Other factors like structure, purity, density, alignment, and the straightness of CNTs [49] have all

been investigated. For instance, in order to get dense packed CNT fibers, surface-tension-driven densification [50, 51] was employed during fiber spinning. Zhang et al. found that after the CNT yarn was pulled through droplets of ethanol, the several centimeters wide yarn shrank into a tight fiber typically 20–30 μm in diameter and the strength of the CNT yarn was dramatically improved. The CNT alignment is found especially crucial for fiber properties [52, 53] and could be measured by Raman and X-ray diffraction [54, 55]. Zheng et al. [12] have observed a strong correlation between the array morphologies (the straightness of CNTs) and the fiber properties: well-aligned arrays yield

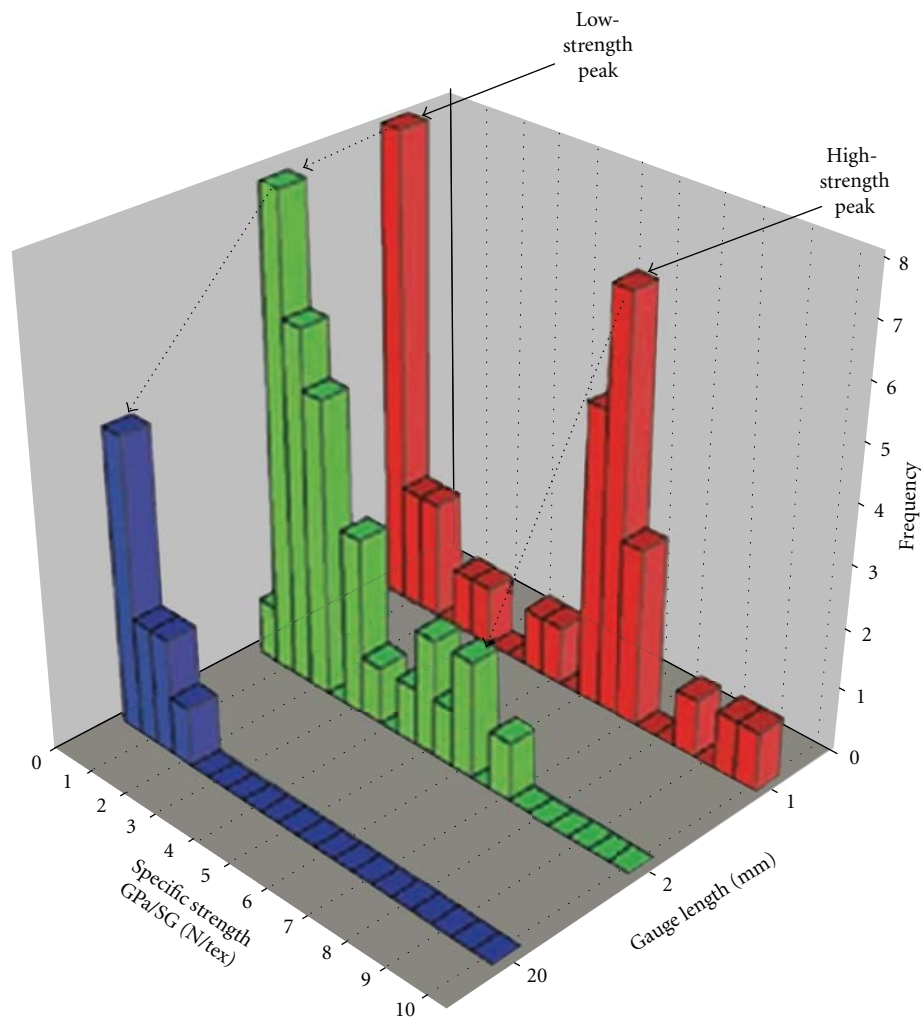


FIGURE 10: specific strength distribution of CNT fibers at different gauge lengths [24].

high performance, while wavy arrays give poor performance. Figure 7 summarizes the influence of several parameters on fibers' mechanical performances.

Since CNTs in a yarn are nearly parallel-aligned, the CNT yarn is intrinsically an anisotropic material and has a special axis along the drawing direction, which demonstrates many fascinating properties and applications. However, some key issues need to be solved in advance to realize their practical applications. Currently the growth of CNT arrays is easy, but not all CNT arrays could be spun into yarns or fibers. Zhang et al. [50] found that strong van der Waals interactions exist between individual CNTs within superaligned arrays, and this van der Waals force makes the CNTs join end to end, thus forming a continuous yarn during pulling. Meanwhile, Zhang et al. [20] claimed that the formation of yarn was due to the disordered regions at the top and bottom of the CNT arrays, which entangled together forming a loop. Further investigation is needed to understand the underlying spinning mechanism.

3.2. Spinning Fiber from Aerogel of CNTs. Zhu et al. [56] have first reported the formation of a 20 cm long CNT thread

after the pyrolysis of hexane, ferrocene, and thiophene. This work shows the possibility of fiber formation directly in a furnace. Based on this phenomenon, a totally different fiber spinning method was developed by Li et al. [23]. They were able to spin neat CNT fibers directly from an aerogel of CNTs formed in CVD reaction zone, as shown in Figure 8. The precursor materials include liquid hydrocarbon feedstock, ferrocene which forms the iron nanoparticles that act as nucleation sites for the growth of CNTs, and thiophene which is an established rate enhancer for vapor grown carbon fibers [57]. The key requirements for continuous spinning are the formation of CNT aerogel and removal of the product from reaction zone. These were realized through the appropriate choice of reactants, control of the reaction conditions, and continuous withdrawal of the products with a rotating spindle used in various geometries.

Recently, systematic studies of this method have been carried out [58, 59]. From the view of reactants and growth conditions, the continuous spinning process is possible with a range of oxygen-containing carbon sources. Aromatic hydrocarbons lead to the deposition of carbon particles and thick fibers, but cannot enable a continuous spinning process

unless they are mixed with another oxygen-containing source. Thiophene is found to be a necessary additive. It was used as an established rate enhancer for vapor growth of carbon fibers [57], but its actual role played in CNT aerogel generation is still open to discussion. However, it is well accepted that sulfur, another additive, plays a major role in promoting carbon-hydrocarbon reactions, especially when associated with iron [57]. Through carefully controlling the growth conditions, the length and diameter of CNT in aerogel could be tuned, and it is found that lower concentrations of iron lead to a greater proportion of SWNTs and double-walled nanotubes (DWNTs) which are favorable for high-performance fibers. For example, it is found that the large diameter DWNTs may collapse within fibers, leading to an increase in friction between individual CNTs, which is beneficial for mechanical performance of CNT fibers [60]. Regarding the processing parameters, it is found that CNT alignment, the density, and microstructures of fibers can be controlled by drawing/winding rate and postprocessing methods. The degree of alignment could be manipulated by adjusting the winding rate as there is a tension introduced into this winding process, which supply a force to align CNTs in the fiber. By introducing the wetting and evaporation of volatile organic liquids such as acetone, the condensation of the CNTs in fibers is greatly increased. Motta et al. [59] have found that the improvement in mechanical strength relates to a unique aspect of fiber microstructure with “dog-bone” shape (shown in Figure 9). They have also shown that the mechanical properties of the fibers directly relate to the type of CNTs, which in turn, can be controlled by the careful adjustment of process parameters.

Through the optimization process, Koziol et al. [24] have found that, by drawing the aerogel at a winding rate of 20 m min^{-1} , the strength of the fiber, mainly containing DWNTs, can reach around 10 GPa, which is the highest value reported so far. As can be seen in Figure 10, it shows the distribution of specific fiber strengths for a range of gauge lengths (the measure length of the sample). The strength of CNT fibers peaks at around 1 GPa in the case of 20 mm gauge lengths. As the gauge length decreases, the strength distribution becomes bimodal with a second peak at 6.5 GPa, which indicates that the distance between “weak points” along the fibers is on the same order as the gauge length. These “weak points” exist inside the fibers without real interlock between individual CNTs, leading to a decrease in mechanical strength when the fiber is long.

4. Summary

In last few years, the development of CNT fibers has shown a sign that superior properties of individual CNTs could be retained at practical size level. A variety of fiber-spinning techniques has been developed, and many posttreatments are utilized to improve the fiber’s mechanical properties. Nevertheless, the fiber’s performance is still poor compared with individual CNTs or small CNT bundles. Future research need to focus on the understanding of the failure mechanism of CNT fibers, aiming at finding key limiting factors and

thus providing reliable and high performance CNT fibers for practical applications.

Acknowledgment

The authors would like to thank the financial support from Singapore DSTA/DIRP Research Grant (no. POD0814218).

References

- [1] M. F. Yu, O. Lourie, M. J. Dyer, K. Moloni, T. F. Kelly, and R. S. Ruoff, “Strength and breaking mechanism of multiwalled carbon nanotubes under tensile load,” *Science*, vol. 287, no. 5453, pp. 637–640, 2000.
- [2] M. F. Yu, B. S. Files, S. Arepalli, and R. S. Ruoff, “Tensile loading of ropes of single wall carbon nanotubes and their mechanical properties,” *Physical Review Letters*, vol. 84, no. 24, pp. 5552–5555, 2000.
- [3] B. G. Demczyk, Y. M. Wang, J. Cumings et al., “Direct mechanical measurement of the tensile strength and elastic modulus of multiwalled carbon nanotubes,” *Materials Science and Engineering A*, vol. 334, no. 1–2, pp. 173–178, 2002.
- [4] P. Nikolaev, H. Dai, P. Petit, H. Dai, P. Petit et al., “Crystalline ropes of metallic carbon nanotubes,” *Science*, vol. 273, no. 5274, pp. 483–487, 1996.
- [5] S. Frank, P. Poncharal, Z. L. Wang, and W. A. de Heer, “Carbon nanotube quantum resistors,” *Science*, vol. 280, no. 5370, pp. 1744–1746, 1998.
- [6] J. Hone, M. Whitney, and A. Zettl, “Thermal conductivity of single-walled carbon nanotubes,” *Synthetic Metals*, vol. 103, no. 1–3, pp. 2498–2499, 1999.
- [7] S. Berber, Y. K. Kwon, and D. Tománek, “Unusually high thermal conductivity of carbon nanotubes,” *Physical Review Letters*, vol. 84, no. 20, pp. 4613–4616, 2000.
- [8] Q. W. Li, Y. Li, X. F. Zhang et al., “Structure-dependent electrical properties of carbon nanotube fibers,” *Advanced Materials*, vol. 19, no. 20, pp. 3358–3363, 2007.
- [9] X. F. Zhang, Q. W. Li, T. G. Holesinger et al., “Ultrastrong, stiff, and lightweight carbon-nanotube fibers,” *Advanced Materials*, vol. 19, no. 23, pp. 4198–4201, 2007.
- [10] X. F. Zhang, Q. W. Li, Y. Tu et al., “Strong carbon-nanotube fibers spun from long carbon-nanotube arrays,” *Small*, vol. 3, no. 2, pp. 244–248, 2007.
- [11] Q. W. Li, X. F. Zhang, R. F. DePaula et al., “Sustained growth of ultralong carbon nanotube arrays for fiber spinning,” *Advanced Materials*, vol. 18, no. 23, pp. 3160–3163, 2006.
- [12] L. X. Zheng, G. Z. Sun, and Z. Y. Zhan, “Tuning array morphology for high-strength carbon-nanotube fibers,” *Small*, vol. 6, no. 1, pp. 132–137, 2010.
- [13] N. Behabtu, M. J. Green, and M. Pasquali, “Carbon nanotube-based neat fibers,” *Nano Today*, vol. 3, no. 5–6, pp. 24–34, 2008.
- [14] B. Vigolo, A. Penicaud, C. Coulon et al., “Macroscopic fibers and ribbons of oriented carbon nanotubes,” *Science*, vol. 290, no. 5495, pp. 1331–1334, 2000.
- [15] A. B. Dalton, S. Collins, J. Razal et al., “Continuous carbon nanotube composite fibers: properties, potential applications, and problems,” *Journal of Materials Chemistry*, vol. 14, no. 1, pp. 1–3, 2004.
- [16] L. M. Ericson, H. Fan, H. Q. Peng et al., “Macroscopic, neat, single-walled carbon nanotube fibers,” *Science*, vol. 305, no. 5689, pp. 1447–1450, 2004.
- [17] M. E. Kozlov, R. C. Capps, W. M. Sampson et al., “Spinning solid and hollow polymer-free carbon nanotube fibers,” *Advanced Materials*, vol. 17, no. 5, pp. 614–617, 2005.

- [18] W. Néri, M. Maugéy, P. Miaudet, A. Derré, C. Zakri, and P. Poulin, "Surfactant-free spinning of composite carbon nanotube fibers," *Macromolecular Rapid Communications*, vol. 27, no. 13, pp. 1035–1038, 2006.
- [19] K. L. Jiang, Q. Q. Li, and S. S. Fan, "Nanotechnology: spinning continuous carbon nanotube yarns—carbon nanotubes weave their way into a range of imaginative macroscopic applications," *Nature*, vol. 419, p. 801, 2002.
- [20] M. Zhang, K. R. Atkinson, and R. H. Baughman, "Multi-functional carbon nanotube yarns by downsizing an ancient technology," *Science*, vol. 306, no. 5700, pp. 1358–1361, 2004.
- [21] L. X. Zheng, X. F. Zhang, Q. W. Li et al., "Carbon-nanotube cotton for large-scale fibers," *Advanced Materials*, vol. 19, no. 18, pp. 2567–2570, 2007.
- [22] L. Ci, N. Punbusayakul, J. Wei, R. Vajtai, S. Talapatra, and P. M. Ajayan, "Multifunctional macroarchitectures of double-walled carbon nanotube fibers," *Advanced Materials*, vol. 19, no. 13, pp. 1719–1723, 2007.
- [23] Y. L. Li, I. A. Kinloch, and A. H. Windle, "Direct spinning of carbon nanotube fibers from chemical vapor deposition synthesis," *Science*, vol. 304, no. 5668, pp. 276–278, 2004.
- [24] K. Koziol, J. Vilatela, A. Moisala et al., "High-performance carbon nanotube fiber," *Science*, vol. 318, no. 5858, pp. 1892–1895, 2007.
- [25] G. Z. Sun, S. W. Liu, K. F. Hua, X. Y. Lv, L. Huang, and Y. J. Wang, "Electrochemical chlorine sensor with multi-walled carbon nanotubes as electrocatalysts," *Electrochemistry Communications*, vol. 9, no. 9, pp. 2436–2440, 2007.
- [26] Y. N. Zhang and L. X. Zheng, "Towards chirality-pure carbon nanotubes," *Nanoscale*, vol. 2, no. 10, pp. 1919–1929, 2010.
- [27] J. B. Xu, K. F. Hua, G. Z. Sun, X. Y. Lv, and Y. J. Wang, "Electrooxidation of methanol on carbon nanotubes supported Pt-Fe alloy electrode," *Electrochemistry Communications*, vol. 8, no. 6, pp. 982–986, 2006.
- [28] P. C. P. Watts, W. K. Hsu, H. W. Kroto, and D. R. M. Walton, "Are bulk defective carbon nanotubes less electrically conducting?" *Nano Letters*, vol. 3, no. 4, pp. 549–553, 2003.
- [29] A. Star, Y. Liu, K. Grant et al., "Noncovalent side-wall functionalization of single-walled carbon nanotubes," *Macromolecules*, vol. 36, no. 3, pp. 553–560, 2003.
- [30] M. S. P. Shaffer and A. H. Windle, "Analogies between polymer solutions and carbon nanotube dispersions," *Macromolecules*, vol. 32, no. 20, pp. 6864–6866, 1999.
- [31] C. Mercader, A. Lucas, A. Derré et al., "Kinetics of fiber solidification," *Proceedings of the National Academy of Sciences of the United States of America*, vol. 107, no. 43, pp. 18331–18335, 2010.
- [32] B. Vigolo, P. Poulin, M. Lucas, P. Launois, and P. Bernier, "Improved structure and properties of single-wall carbon nanotube spun fibers," *Applied Physics Letters*, vol. 81, no. 7, pp. 1210–1212, 2002.
- [33] E. Munoz, A. B. Dalton, S. Collins et al., "Multifunctional carbon nanotube composite fibers," *Advanced Engineering Materials*, vol. 6, no. 10, pp. 801–804, 2004.
- [34] P. Miaudet, S. Badaire, M. Maugéy et al., "Hot-drawing of single and multiwall carbon nanotube fibers for high toughness and alignment," *Nano Letters*, vol. 5, no. 11, pp. 2212–2215, 2005.
- [35] A. B. Dalton, S. Collins, E. Munoz et al., "Super-tough carbon-nanotube fibres—these extraordinary composite fibres can be woven into electronic textiles," *Nature*, vol. 423, no. 6941, p. 703, 2003.
- [36] C. Lynam, S. E. Moulton, and G. G. Wallace, "Carbon-nanotube biofibers," *Advanced Materials*, vol. 19, no. 9, pp. 1244–1248, 2007.
- [37] W. H. Song and A. H. Windle, "Isotropic-nematic phase transition of dispersions of multiwall carbon nanotubes," *Macromolecules*, vol. 38, no. 14, pp. 6181–6188, 2005.
- [38] W. Song, I. A. Kinloch, and A. H. Windle, "Nematic liquid crystallinity of multiwall carbon nanotubes," *Science*, vol. 302, no. 5649, p. 1363, 2003.
- [39] S. J. Zhang, K. K. K. Koziol, I. A. Kinloch, and A. H. Windle, "Macroscopic fibers of well-aligned carbon nanotubes by wet spinning," *Small*, vol. 4, no. 8, pp. 1217–1222, 2008.
- [40] M. Zhang, S. L. Fang, A. A. Zakhidov et al., "Strong, transparent, multifunctional, carbon nanotube sheets," *Science*, vol. 309, no. 5738, pp. 1215–1219, 2005.
- [41] L. Xiao, Z. Chen, C. Feng et al., "Flexible, stretchable, transparent carbon nanotube thin film loudspeakers," *Nano Letters*, vol. 8, no. 12, pp. 4539–4545, 2008.
- [42] C. Feng, K. Liu, J. S. Wu et al., "Flexible, stretchable, transparent conducting films made from superaligned carbon nanotubes," *Advanced Functional Materials*, vol. 20, no. 6, pp. 885–891, 2010.
- [43] Y. H. Sun, K. Liu, J. Miao et al., "Highly sensitive surface-enhanced raman scattering substrate made from superaligned carbon nanotubes," *Nano Letters*, vol. 10, no. 5, pp. 1747–1753, 2010.
- [44] G. Z. Sun, J. Y. Zhou, F. Yu, Y. N. Zhang, J. H. L. Pang, and L. X. Zheng, "Electrochemical capacitive properties of CNT fibers spun from vertically aligned CNT arrays," *Journal of Solid State Electrochemistry*. In press.
- [45] L. X. Zheng, M. J. O'Connell, S. K. Doorn et al., "Ultra-long single-wall carbon nanotubes," *Nature Materials*, vol. 3, no. 10, pp. 673–676, 2004.
- [46] Z. Y. Zhan, Y. N. Zhang, G. Z. Sun, L. X. Zheng, and K. Liao, "The effects of catalyst treatment on fast growth of millimeter-long multi-walled carbon nanotube arrays," *Applied Surface Science*, vol. 257, no. 17, pp. 7704–7708, 2011.
- [47] L. Zheng, B. C. Satishkumar, P. Q. Gao, and Q. Zhang, "Kinetics studies of ultra-long single-walled carbon nanotubes," *Journal of Physical Chemistry C*, vol. 113, no. 25, pp. 10896–10900, 2009.
- [48] S. K. Doorn, L. X. Zheng, M. J. O'Connell, Y. T. Zhu, S. M. Huang, and J. Liu, "Raman spectroscopy and imaging of ultra-long carbon nanotubes," *Journal of Physical Chemistry B*, vol. 109, no. 9, pp. 3751–3758, 2005.
- [49] J. J. Jia, J. N. Zhao, G. Xu et al., "A comparison of the mechanical properties of fibers spun from different carbon nanotubes," *Carbon*, vol. 49, no. 4, pp. 1333–1339, 2011.
- [50] X. B. Zhang, K. L. Jiang, C. Feng et al., "Spinning and processing continuous yarns from 4-inch wafer scale super-aligned carbon nanotube arrays," *Advanced Materials*, vol. 18, no. 12, pp. 1505–1510, 2006.
- [51] Y. Wei, K. L. Jiang, X. F. Feng et al., "Comparative studies of multiwalled carbon nanotube sheets before and after shrinking," *Physical Review B*, vol. 76, no. 4, Article ID 045423, 7 pages, 2007.
- [52] V. K. Rangari, M. Yousuf, S. Jeelani, M. X. Pulikkathara, and V. N. Khabashesku, "Alignment of carbon nanotubes and reinforcing effects in nylon-6 polymer composite fibers," *Nanotechnology*, vol. 19, no. 24, Article ID 245703, 2008.
- [53] L. J. Lantice, Y. Tanabe, K. Matsui et al., "Shear-induced preferential alignment of carbon nanotubes resulted in anisotropic electrical conductivity of polymer composites," *Carbon*, vol. 44, no. 14, pp. 3078–3086, 2006.
- [54] H. H. Gommans, J. W. Alldredge, H. Tashiro, J. Park, J. Magnuson, and A. G. Rinzler, "Fibers of aligned single-walled

- carbon nanotubes: polarized Raman spectroscopy,” *Journal of Applied Physics*, vol. 88, no. 5, pp. 2509–2514, 2000.
- [55] V. Pichot, M. Burghammer, S. Badaire et al., “X-ray microdiffraction study of single-walled carbon nanotube alignment across a fibre,” *Europhysics Letters*, vol. 79, no. 4, Article ID 46002, 2007.
- [56] H. W. Zhu, C. L. Xu, D. H. Wu, B. Q. Wei et al., “Direct synthesis of long single-walled carbon nanotube strands,” *Science*, vol. 296, no. 5569, pp. 884–886, 2002.
- [57] G. G. Tibbetts, C. A. Bernardo, D. W. Gorkiewicz, and R. L. Alig, “Role of sulfur in the production of carbon fibers in the vapor phase,” *Carbon*, vol. 32, no. 4, pp. 569–576, 1994.
- [58] M. Motta, Y. L. Li, I. Kinloch, and A. Windle, “Mechanical properties of continuously spun fibers of carbon nanotubes,” *Nano Letters*, vol. 5, no. 8, pp. 1529–1533, 2005.
- [59] M. Motta, A. Moisala, I. A. Kinloch, and A. H. Windle, “High performance fibres from “dog bone” carbon nanotubes,” *Advanced Materials*, vol. 19, no. 21, pp. 3721–3726, 2007.
- [60] X. H. Zhang and Q. W. Li, “Enhancement of friction between carbon nanotubes: an efficient strategy to strengthen fibers,” *ACS Nano*, vol. 4, no. 1, pp. 312–316, 2010.